Combinatorial Atmospheric Pressure Chemical Vapour Deposition for Optimising the Functional Properties of Titania Thin-Films

Andreas Kafizas

Supervised by Professor Ivan Parkin

Abstract

Titanium dioxide (TiO_2) is the leading material for self-cleaning applications due to its chemical inertness, mechanical robustness, durability to extended photocatalytic cycling, low cost and high photocatalytic activity. There has been a concerted effort to try and improve the material's functional properties through impurity doping; altering the band structure and electronic transport properties. However, any improvements are difficult to optimise using traditional methods.

Thin-film combinatorial methods have heralded the discovery of more than 20 new families of materials since their resurgence in the mid-90's. Such methods enable a high diversity of states to be produced in a single deposition and are now being used more prominently to optimise the functional properties of existing materials. Atmospheric pressure chemical vapour deposition (APCVD) has been applied in a combinatorial fashion to deposit thin-films containing compositional gradients and is also the native method in which thin-films of TiO_2 are mass-produced.

Utilising combinatorial APCVD, we investigated N, Nb and W doped TiO_2 thin-film systems. The N-doped TiO_2 system has been studied most prominently for improved visible light photocatalysis. Nitrogen can either substitute oxygen sites (substitutional doping - N_s) or enter within the TiO_2 framework (interstitial doping - N_i), yet there is little consensus on which type of doping or dopant concentration yields the more active photocatalyst. Using the combinatorial APCVD approach, $TiCl_4$ and ethyl acetate precursors were used to form the host TiO_2 matrix with either NH_3 or t-butylamine used as the N-sources. From three separate investigations we were able to produce combinatorial films with transitional composition/ phase gradients of (i) N_s/ N_i-doped to pure N_i-doped anatase TiO_2 ($0 \leq N_s$: $Ti \leq 8.4$ %, $0.57 \leq N_i$: $Ti \leq 3.3$ %), (ii) N_s-doped anatase TiO_2 and rutile TiO_2 phase mixtures ($0 \leq$

N_s: Ti ≤ 11 %, 0 ≤ anatase TiO_2 ≤ 100 %, 0 ≤ rutile TiO_2 ≤ 41 %) and (iii) pure pseudo-brookite $Ti_{3-\delta}O_4N$ to pure N_i-doped anatase TiO_2 phase mixtures. In tailoring high-throughput screening methods to these systems we were able to characterise large numbers of unique states across each combinatorial system and inter-relate their physical and functional properties. It was found that (i) pure N_i-doped anatase TiO_2 is a more photocatalytically active material than N_s-doped anatase TiO_2 under UVA and visible light (> 420 nm), (ii) un-doped anatase TiO_2 is more photocatalytically active than N_s-doped anatase TiO_2 under UVA light and (iii) pseudo-brookite $Ti_{3-\delta}O_4N$ is a more active photocatalyst than N_i-doped anatase TiO_2 under UVA light. The photocatalytic activity of Nb and W doped TiO_2 solid solutions had not previously been investigated; however, their film resistivities for potential applications as more durable transparent conducting oxide materials had been. Using combinatorial APCVD we were able to produce $Nb_xTi_{1-x}O_2$ ($0.0004 \leq x \leq 0.0194$) and $W_xTi_{1-x}O_2$ ($0.0038 \leq x \leq 0.1380$) anatase TiO_2 thin-film solid solutions with transitional composition gradients. The Nb-doped system was formed from combining $TiCl_4$, ethyl acetate and $NbCl_5$ precursors. By characterising the film with our screening methods were we able to determine the strong functional inter-relationship between the material's bandgap, photocatalytic activity and film resistivity in three dimensions; where an increased photocatalytic activity was associated with a lower bandgap energy and electrical resistance. The importance of oxygen vacancies on increasing charge carrier mobility presided over the number of charge carriers in the system (Nb-doping level). The W-doped system was formed from combining $TiCl_4$, ethyl acetate and WCl_6 precursors. Using high-throughput screening methods once more, the strong physical inter-relationship between the material's Raman shift, unit cell volume and W-doping level were determined; where increased W-doping increasingly expanded the unit cell in the *a/b* axis and caused the prominent Raman active E_g vibrational mode of (144 cm^{-1}) to shift to higher energies. Increased W-doping increasingly disrupted crystallisation, yielding less active photocatalysts. More interestingly however, increased preferred orientation in the (211) plane induced a greater degree of photo-induced surface wetting. Given the mechanism for the photo-induced wetting process in anatase TiO_2 is, to our knowledge, yet to be studied, the trends highlighted the importance of the (211) plane in this process.

Films synthesized by the combinatorial APCVD route, analysed in conjunction with high-throughput characterisation methods, provide a shortcut to understanding and optimising the functional properties of composition/ phase space.

Table of Contents

1. Introduction

In this thesis we aim to explore combinatorial atmospheric pressure chemical vapour deposition (APCVD) as a synthetic method for producing thin-films of TiO_2 with transitional composition/ phase gradients containing a high number of unique states. We will investigate the nitrogen doping of TiO_2 most prominently as well as niobium and tungsten doped systems. In developing tools tailored for quickly screening the physical and functional properties of these systems we will rapidly investigate phase/ composition space. This will lead to a better understanding of the physical and functional properties within these systems and the possible identification of optimal compositions for enhanced functionality.

1.1. The functions of titania thin-films and efforts to improve them

Thin-films of anatase titanium dioxide (TiO_2) have been extensively studied due to their multi-functional applications in self-cleaning,[1,2] water splitting,[3-5] gas sensing[6]and solar-cell devices.[7,8] The majority of TiO_2 thin-film research has focussed on improving the self-cleaning properties of the anatase phase.[9] Anatase TiO_2 is the leading material for self-cleaning applications due to its chemical inertness, mechanical robustness, durability to extended photocatalytic cycling, low cost and high photocatalytic activity.[10] Thin-films of TiO_2 have been shown to photocatalytically oxidise organic pollutants,[1] bacteria,[11] viruses[12] and cancer cells.[13] It is commercially applied in self-cleaning windows and tiles and air/ water purification systems.[14]

TiO_2 is found naturally in three semiconducting polymorphs, anatase, rutile and brookite; the rutile phase being the most thermodynamically stable. As early as 1929 it was known that the pigment “titanium white” (typically mixtures of anatase and rutile TiO_2 powder) was responsible for the chalking of paints. Through subsequent studies in the late 1930’s it was identified that this was due to the photocatalytic degradation of the organic binders.[15] It was not until the late 1960’s that the mechanism by which this operated was better understood.[16] Both anatase TiO_2 and rutile TiO_2 powders show bandgaps of 3.2 and 3.0 eV respectively, falling into the UVC region of the electromagnetic spectrum.[1] When a photon with energy greater than or equal to the bandgap energy is absorbed, a photo-excitation occurs, promoting an electron from the valence band to the conduction band. This creates an excited electronic state (e^-) and concomitant hole (h^+). These photo-generated electrons and holes migrate from the bulk to the lower energy material surface where they become temporarily trapped. Donor molecules in the vicinity of the trapped holes (h_{tr}^+), such as water, react to form radical species. Acceptor molecules, such as di-oxygen, react with trapped electrons (e_{tr}^-) to form super-oxide species. These highly reactive species then oxidise any

organic species in contact with the TiO_2 surface into carbon dioxide, water and mineral acids. The time-scales in which each of these processes occur, shown in Scheme 1.1.1, differ substantially. Interestingly, the time-scales of recombination processes ($h_{tr}^{+} + e^{-}$, $h^{+} + e_{tr}^{-}$ or $h^{+} + e^{-}$) that retard photocatalysis are marginally faster than the di-oxygen reduction process, making the reduction of acceptor species the rate-determining step in many photocatalysis reactions.

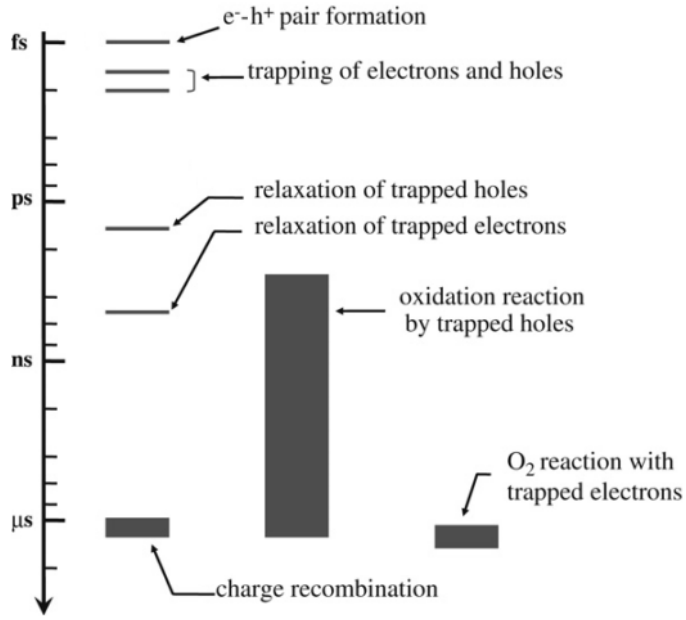

Scheme 1.1.1: *Summary of time-scales for photocatalytic processes in TiO_2. Reproduced from reference 2.*

The rate at which TiO_2 thin-films degrade organic matter under a steady photo-exciting flux follows Langmuir-Hinshelwood kinetics:

$$r_i = (k_s \, x \, A_s \, x \, [O]_i)/(1 + \, A_s \, x \, [O]_i) \qquad (1.1)$$

where r_i is the initial rate of organic degradation, k_s is the photocatalyst reactivity constant, A_s is the absorption constant of the organic to the film surface and $[O]_i$ is the initial concentration of the organic layer. The reactivity constant k_s is dependent on both the rate of light absorption (I_a) and fraction of di-oxygen absorbed at the surface ($f(O_2)$). These constants vary for different TiO_2 samples and therefore display different rates of photocatalysis. They are primarily dependent on four physical characteristics:

(i) *the semiconductor bandgap energy*; determines the region of the photon excitation source that will be absorbed in generating separated electrons and holes.

(ii) *material thickness*; determines the fraction of the photon excitation source that can be absorbed (I_a).

(iii) *surface roughness*; determines the number of active surface sites for radical/ superoxide generation (k_s) and the degree of organic contact ($[O]_i$).

(iv) *film crystallinity*; dictates the transport properties of the photo-generated electrons and holes to the film surface (k_s) as well as the bandgap energy.

Thin-films of TiO_2 develop photo-induced hydrophilicity (PIH) when photo-excited. This phenomenon operates through an entirely different mechanism to photocatalysis. The holes that migrate to the surface of TiO_2 react with bridging oxygens, leading to their ejection. Water molecules in the air then react at these empty bridging sites and form hydroxyl groups at the surface. Through this mechanism, ordered domains of hydroxylated areas on the nanoscale form on the surface of TiO_2. These hydroxylated regions increase the wettability of the surface as they attract water through hydrogen bonding. The mechanism is better understood for the rutile polymorph of TiO_2 as it has been investigated exclusively.[2] In fact, particular facets of the rutile crystal such as the (110) and (100) were found to mediate PIH whereas the (001) facet did not.[17] The PIH effect can be so pronounced in thin-films of TiO_2 that water-droplet contact angles approach 0°.[18] This property has been commercially exploited in anti-fogging mirrors.[14] The effect contributes to the self-cleaning function of TiO_2 thin-films, where it has been shown that this increased wettability helps to dislodge dirt and grime from TiO_2 coated windows and tiles.[14] It was also been demonstrated that TiO_2 thin-films in the PIH state repel airborne pathogens from sticking to the surface and have been applied in hospital environments to hinder the spread of nosocomial infections.[14] The two functions of photocatalysis and PIH operate in tandem, both contributing to the self-cleaning process of TiO_2 thin-films.

The largest avenue of TiO_2 thin-film research is the attempted improvement of the self-cleaning function.[2,10] The most common methods for achieving this improvement are: (i) coupling composites[19-25] (ii) modifying the surface[26-28] and (iii) doping[29-42] (the most popular method).

There are two main strategies in coupling composites. One strategy involves coupling TiO_2 with a semiconductor of lower bandgap energy such as WO_3 (2.8 eV) or CdS (≈ 2.5 eV) for instance.[22-25] Photons incapable of photo-exciting TiO_2 can excite the lower bandgap energy material. Depending on where the band potential of the coupled semiconductor straddles TiO_2, either the photo-excited electron can hop down into the conduction band of TiO_2 (Scheme 1.1.2 (b); CdS-TiO_2) or the hole can jump up into the valence band of TiO_2 (Scheme 1.1.2 (a) WO_3-TiO_2). This increases the separation of the photo-generated electrons and holes and makes recombination less viable. Another strategy involves coupling TiO_2 with a noble metal such as silver,[20] gold[21] or platinum.[19] Photo-generated electrons formed on the TiO_2 semiconductor can hop down into the coupled metal's density of

states, raising the Fermi level (Scheme 1.1.2 (c)). This also increases the separation of the photo-generated electrons and hinders recombination processes.

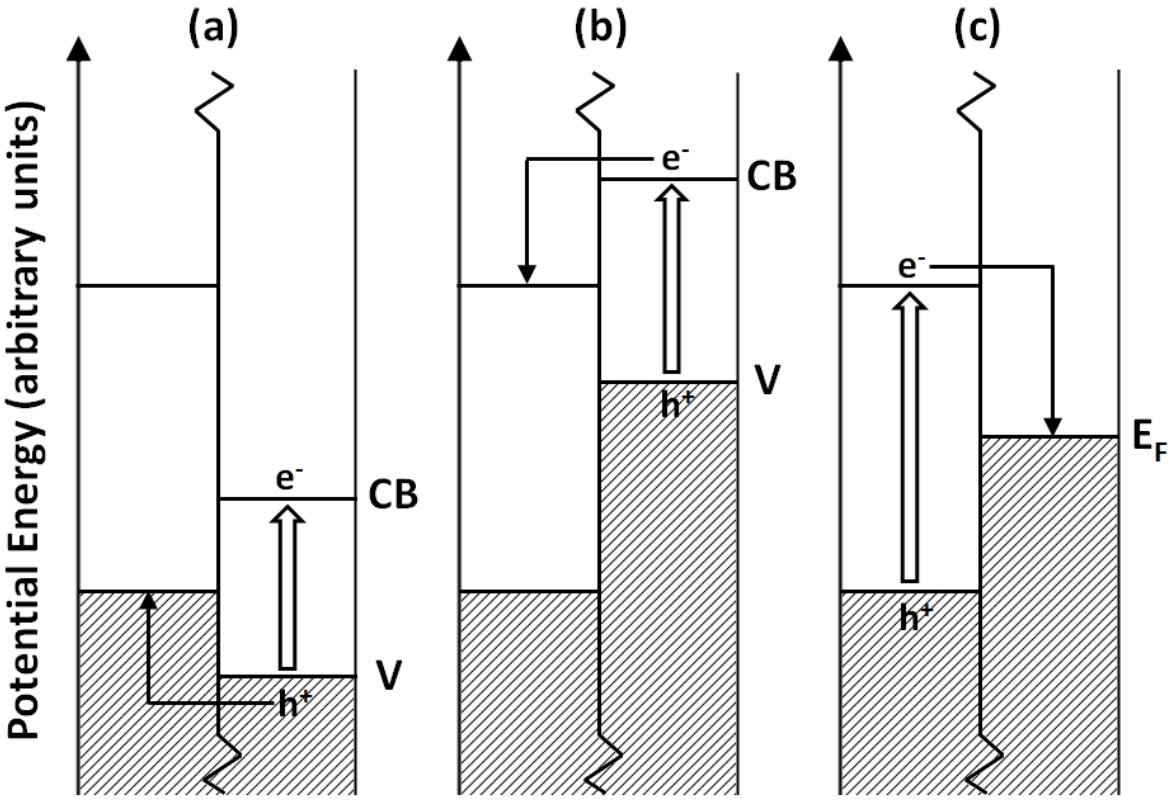

Scheme 1.1.2: *Characteristic density of states diagrams for coupled composites. Coupling with lower energy semiconductors can straddle the (a) valence band or (b) conduction band of TiO_2. (c) Coupling with noble metals can stabilise photo-generated electrons on TiO_2.*

Modifying the surface of TiO_2 is another way of enhancing the photocatalytic activity. By chemically binding molecules to the surface, such as phosphate[27] or carboxylate[26,28] containing compounds, the propensity of the surface to attract or repel specific organic pollutants is altered. This can increase the selectivity of absorption at the surface as well as change the rate of photo-generated electron-hole surface capture and release. In some cases, the rate of hydroxyl radical formation can substantially increase,[27] boosting photocatalytic oxidisation processes.

The bandgap of the more popular studied anatase and rutile TiO_2 polymorphs lie in the UVC region of the electromagnetic spectrum.[9] As a more significant portion of light is contained in the visible region of the solar spectrum, modifying the band structure to produce more red-shifted materials has become the most pursued course for improving the photocatalytic activity of TiO_2 thin-films to sunlight.[2,10] The most common method for achieving this is through doping TiO_2. Computational density of states calculations (DOS) have shown how the band structure of TiO_2 consists of a valence band made primarily of O 2p orbitals and a conduction band made primarily of

Ti 3d orbitals. TiO_2 thin-films have been doped with a range of non-metals such as boron,[41] carbon,[42] nitrogen,[30] fluorine,[40] phosphorus[39] and sulphur[29] in order to alter the band structure. These dopants typically substitute oxygen (O^{2-}) sites, but can also enter interstitially within the titanium-oxygen framework. Through computational modelling, it is generally found that such non-metal dopants in substitutional positions interact and mix strongly with O 2p orbitals, pushing the valence band from the DOS higher in energy and lowering the bandgap (Scheme 1.1.3 (b)).

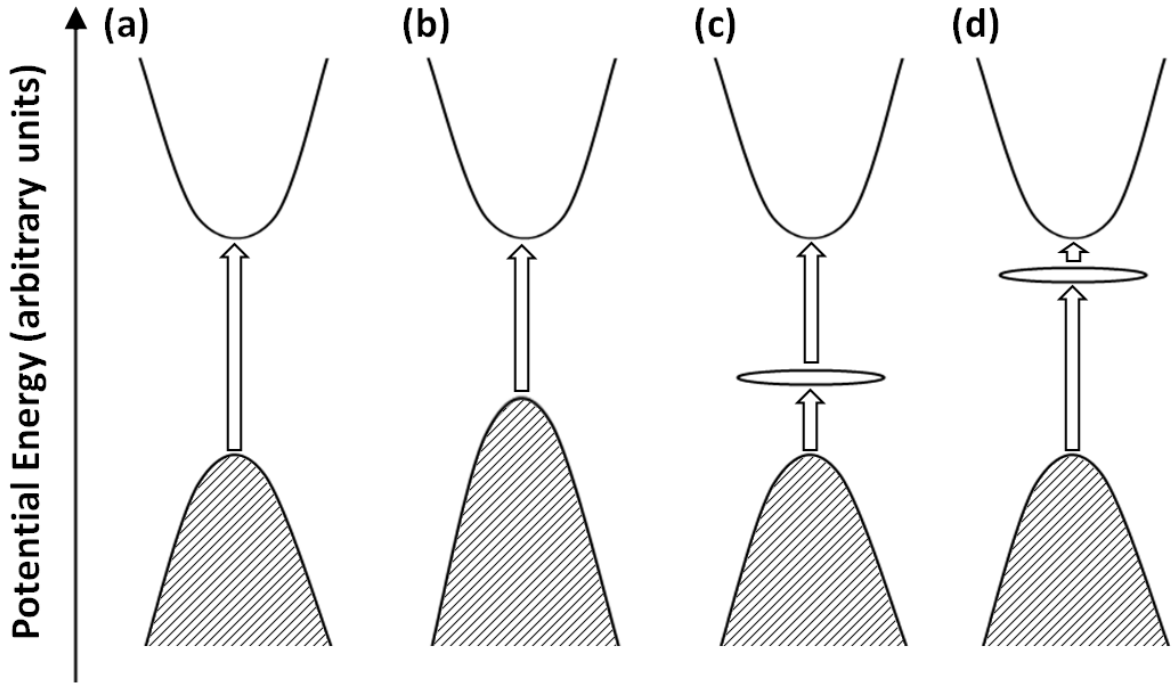

Scheme 1.1.3: *Characteristic density of states diagrams for (a) TiO_2 (b) non-metal doped TiO_2 (c) non-metal interstitial doped TiO_2 /transition metal doped TiO_2 and (d) oxygen deficient TiO_2.*

However, the DOS of interstitial dopants typically show inter-band states between the valence and conduction band (Scheme 1.1.3 (c)). TiO_2 thin-films have also been doped with a range of transition metals such as vanadium,[31] chromium,[33] manganese,[36] iron,[35] cobalt,[34] nickel,[37] copper[32] and molybdenum.[38] These metals dopants replaced Ti sites and DOS calculations indicated the formation of intra-bandgap energy levels between the TiO_2 valence and conduction bands (Scheme 1.1.3 (c)).[10] In most such studies, a more pronounced visible light photocatalytic activity was observed. For the case of non-metal anionic dopants substituting O^{2-} sites, the improvements were attributed to the direct lowering of the bandgap energy. However, for interstitial doped and transitional metal doped systems with inter-band states, a multi-electron excitation mode was suggested.[2] In some cases, the visible light enhancements were attributed to the formation of O^{2-} vacancies that formed inter-band states below the conduction band (Scheme 1.1.3 (d)).[2] Of the numerous dopants that have shown improvements in the visible light photocatalytic activity of TiO_2, there is little consensus on which is the most effective and what the optimum doping level is. Because there is no standard protocol for

measuring photocatalysis, the organic material tested varies as well as the units in which the photocatalytic degradation rate is presented. Greater sense could be made of the vast amounts of data generated in this field if the photocatalytic rates were presented as formal quantum efficiencies (FQE) or yields (FQY), making results far more comparable:

$$FQE = \frac{rate\ (molecules\ degraded\ cm^{-2}\ s^{-1})}{flux\ (photon\ cm^{-2}\ s^{-1})} \quad FQY = \frac{rate\ (molecules\ degraded\ cm^{-2}\ s^{-1})}{flux\ absorbed\ (photon\ cm^{-2}\ s^{-1})} \tag{1.2}$$

Most thin-films studies of TiO_2 have utilised the sol-gel synthetic route. Although the sol-gel method can form smooth, robust and strongly adhered TiO_2 thin-films on a variety of substrates, the film is inherently homogenous. Previous attempts to find the most effective dopant or optimal dopant level for improved photocatalytic performance involved the synthesis of catalytic arrays of individual samples. Given a separate sol is required for each sample, the number of possible examinable states is highly limited by the synthetic method and has made finding the optimum composition time consuming. In the next section we therefore present the benefits of using the combinatorial thin-film approach to optimise functional properties. We will discuss how such methods have developed since their resurgence in the mid-90's and highlight some landmark examples.

1.2. Thin-film combinatorial chemistry for optimising functional properties

Combinatorial chemistry involves the study of all possible combinations and arrangements of atoms. The use of combinatorial methods has taken hold most prominently in the pharmaceutical industry, where attempts to optimise the medicinal activity of new drugs has led to more than 100,000 new compounds being synthesised and screened each year.[43] Combinatorial chemistry has also been extensively applied in the inorganic field, chiefly in the area of thin-film science, and has led to the discovery of more than 20 new families of materials since their resurgence in the mid-90's.[44-47] As such methods enable a high diversity of states to be produced in a single deposition they are now being used more prominently to optimise the functional properties of existing materials.

Combinatorial methods were first demonstrated through the pioneering work of Boettcher *et. al.* in 1955.[48] It was a unique approach to rapidly identify the vast number of ternary and quaternary metallic phases that had not been investigated by traditional methods. By vaporising metal sources through a rotating mask, a thin-film of a continuously graded Ag-Sn-Pb alloy was formed. A detailed

ternary phase diagram was compiled from this lone sample and demonstrated the simplicity of their approach. By the early 1970's, the concept of thin-film combinatorial methods had reached the wider research community through the studies of ceramic and metal oxide films by Hanak *et. al.*[49,50] For the first time the functional properties of combinatorial films were being mapped and related to their composition and phase. However, the progress of this methodology was hampered by the speed in which samples could be analysed.

It was not until the mid 90's that the concept re-emerged, when technological advances in the precision of physical vapour deposition (PVD) processes and screening techniques made combinatorial methods more attractive. This was demonstrated by Xiang, Schultz *et. al.* in 1995 with their discovery of a new class of Co-based giant magneto-resistance compounds.[51] Using a radio frequency magnetron sputtering method, La_2O_3, Y_2O_3, $BaCO_3$, $SrCO_3$, CaO, and Co targets were ablated through a series of physical masks to form a library of 128 unique members containing different compositions and stoichiometries of $Ln_xM_yCoO_\delta$; where Ln = Y or La and M = Pb, Ca, Sr, or Ba. The largest magneto-resistances were found in the $La_x(Ba,Sr,Ca)_yCoO_6$ region, whereas Y-based samples exhibited much smaller magneto-resistive effects. The magneto-resistance of this new class of material was found to increase as the size of the alkaline earth ion increased and was in sharp contrast to colossal magneto-resistance Mn-based perovskites.[52]

This work was followed by Danielson *et. al.* in 1997 with the combinatorial investigation of luminescent materials and the discovery of a new red phosphor $Y_{0.845}Al_{0.070}La_{0.060}Eu_{0.025}VO_4$.[53] They applied radio frequency magnetron sputtering to 12 targets to produce over 25,000 unique samples over a 3" wide silicon wafer. The phosphor library was designed to include combinations of host lattice cations from groups IIA and IIIA, with a VO^{-n}_{m} counter ion (m = 3, 4; n = 1, 3) and from the group IIIB and IVB elements with Eu, Tb, Tm and Ce activator ions. Four columns of SnO_2, V, Al_2O_3: V (15 : 8 molar ratio) and Al_2O_3 were first deposited with constant thickness. Four rows with linearly increasing thickness of La_2O_3, Y_2O_3, MgO and $SrCO_3$ were then layered over the columns to divide the substrate into 16 sub-regions. Finally, within each sub-region, columns of rare earths Eu_2O_3, Tb_4O_7, Tm_2O_3 and CeO_2 were deposited, again with linearly varying thickness. Annealing the entire combinatorial array ensured the complete inter-diffusion of the components to their equilibrium structures. The level of photo-luminescence was screened using a simple photographic method. By photo-exciting the entire combinatorial library at once, a photograph of the ensuing luminescence was taken (Figure 1.2.1). After pre-calibrating the camera to industrial standards, the chromaticity of each library member was quantified from a single image. The most highly efficient luminescent materials with desirable chromaticity were observed in the Eu^{3+} doped $Y_{1-m}Al_mVO_4$ region. The

luminescence was optimised by depositing another combinatorial library focussed specifically on combinations of these elements with La. From their photographic screening method, the composition with optimal luminescence intensity and chromaticity for commercial applications corresponded to $Y_{0.82}Al_{0.07}La_{0.06}Eu_{0.05}VO_4$. Yet again, this system was further optimised, designing a combinatorial deposition that linearly varied the Eu^{3+} concentration in $Y_{0.87-m}Al_{0.07}La_{0.06}Eu_mVO_4$ ($0 \leq m \leq 0.2$). By screening this library, a 2.5 % Eu (m = 0.025) optimal loading was identified and showed improved red chromaticity to the more orange-red commercial standard $Y_{1.95}O_3Eu_{0.05}$ that was then available.

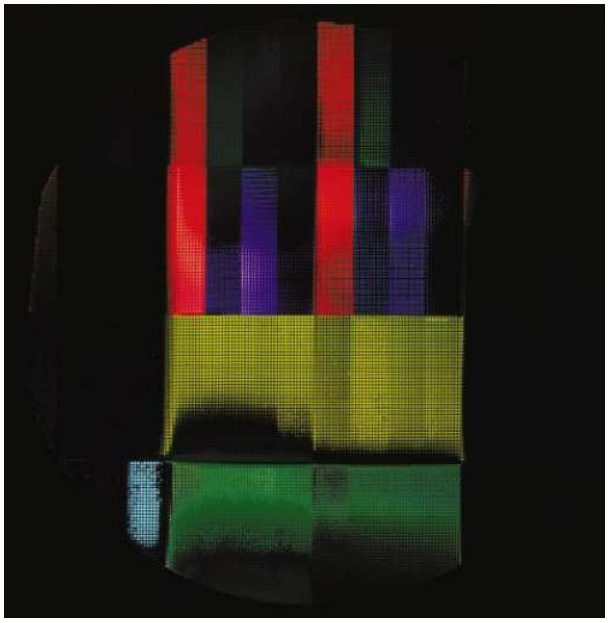

Figure 1.2.1: *Digital photograph of luminescent phosphors taken in situ. The set of 25,000+ unique compositions were formed by a combinatorial radio frequency magnetron sputtering deposition and their luminescence quantified from this single image. Reproduced from reference 53*.

In 1998, Van Dover *et. al.* used thin-film combinatorial methods to discover a high-specific capacitor material $Zr_{0.2}Sn_{0.2}Ti_{0.6}O_2$ with applications in what were "new-age" dynamic random-access memory.[54] Given most oxide systems with high dielectric constants typically incorporate one or more early transition metals, 30 quaternary combinatorial systems, containing two early transition metals, were deposited using a radio frequency magnetron co-sputtering process and screened. The three metallic targets were positioned at a different central edge to the square substrate and sputtered off-axis; forming continuous compositionally graded thin-films. A high-throughput screening tool capable of rapidly assessing the capacitance across these systems was developed. This consisted of a Hg filled capillary that could be translated across the surface forming a capacitor. Each position analysed took just a few seconds to assess and ≈ 4000 positions were screened within each system. From their extensive search, a Zr-Sn-Ti oxide system appeared to show the most promising properties; with moderately high specific capacitance and low leakage in the $Zr_{0.2}Sn_{0.2}Ti_{0.6}O_2$ region.

An optimised uniform thin-film of $Zr_{0.2}Sn_{0.2}Ti_{0.6}O_2$ was tested against the leading materials in industry and was the only material to meet the basic requirements of high-specific capacitance, scalable deposition, high-breakdown field and low leakage for DRAM applications.

In 2001, Koinuma *et. al.* applied thin-film combinatorial methods to the TiO_2 system in their search for transparent ferromagnets.[55,56] Using molecular beam epitaxy, pure TiO_2 targets and a series of transition metal co-doped M-TiO_2 targets (M = Sc, V, Cr, Mn, Fe, Co, Ni, Cu or Zn) were ablated through synchronised masks to form a library of discrete and unique samples with varying dopant levels. By screening the magnetic properties it was found that solely $Ti_{1-x}Co_xO_2$ samples showed ferromagnetic behaviour and were the first transparent materials to show room temperature ferromagnetism. As a number of Co-doped TiO_2 samples were produced, it was elucidated that 8 % metal doping (x = 0.08) produced the maximum ferromagnetic effect. To the best of our knowledge, the functional properties of any TiO_2 based system have not since been investigated using combinatorial methods.

From such examples it is clear that combinatorial methods could be applied to thin-film systems to investigate extensive combinations of elements and phase space and further optimise regions of promising functionality. Each study encompassed the simultaneous formation of up to several thousand unique positions that were then rapidly screened using high-throughput characterisation methods to find the optimum functionality. With the vast number of unique states that could be deposited, the limiting factor was indeed the speed of characterisation. The methodology was soon applied in new areas of research. This was after the development of high-throughput screening methods, tailored to the analysis of specific functions, increased the breadth of investigation.[44-47] Now, thin-film combinatorial methods are regularly applied in at least 14 key areas of functional materials development, spanning dielectric,[57-59] ferroelectric,[60,61] H_2 storage,[62-65] fuel cell anode and cathode,[66-72] hardness,[73-76] Li-ion battery electrode, [77-79] luminescence,[80,81] transparent ferromagnetic,[55,56] photovoltaic,[82-85] transparent conducting oxide,[86-91] shape-memory[92-95] and thermoelectric[96-100] materials optimisation. However, thin-film combinatorial methods were yet to be applied in the field of photocatalysis.

Within the field of thin-film combinatorial optimisation, PVD techniques are applied in predominance over CVD or wet-chemical methods. This has led to huge advances in shadow masking methods[45] and sputter prediction control of PVD depositions.[49,50] Nevertheless, more cost-effective and innovative synthetic methods have also been developed, such as ink-jet printing for the investigation of electron donor/ acceptor blends in hetero-junction solar cells[101] and ferroelectric lead-zirconium titanate materials.[102] Automated robotic dispensing methods, used primarily in the

pharmaceutical industry for investigating drug libraries,[103] have also been used in combinatorial thin-film polymer studies.[104,105] However, when combinatorial methods are used to optimise the functional properties of a commercial material, it is important to use a deposition method suitable to scale-up. An interesting example of this is found in Dahn *et. al.*'s study of Si-Sn alloys for negative electrodes in Li-ion batteries.[106] By depositing an array of Si-Sn alloys using PVD, it was found that $Si_{0.6}Sn_{0.4}$ alloys were the best candidates for negative electrodes as they showed the highest stabilities to recharge and discharge. However, the synthesis was impractical to scale-up as the electricity costs alone for producing these materials by PVD sputtering far outweighed the marginal functional benefits.[77] Research now favours doping Sn/ Si based materials with transition metals to induce an amorphous phase formation without the need of forced kinetic equilibrium through sputtering. Commercial products containing TiO_2 thin-films are typically produced by either a sol-gel or CVD process. For instance, the TiO_2 layer on Pilkington Activ™ self-cleaning glass is deposited using an atmospheric pressure CVD (APCVD) process.[107] Given the incompatibility of sol-gel for combinatorial investigations, we chose APCVD, the native method in which self-cleaning thin-films of TiO_2 are mass-produced, to investigate combinatorial TiO_2 systems.

In the next section we will discuss all examples in which the combinatorial thin-film method has been applied using CVD. We will present the basic layout of the combinatorial APCVD apparatus used throughout this thesis and explain the basis in which thin-films with compositional/ phase gradients are formed by this route.

1.3. Combinatorial atmospheric pressure chemical vapour deposition

Chemical vapour deposition (CVD) is a synthetic method used to produce high-purity and high-performance solid materials.[108] The process involves transporting gaseous precursor vapours over a heated substrate, which chemically react and/or decompose at the substrate surface to produce the desired product. Combinatorial CVD involves the combination of two or more precursor vapours over the substrate surface at different locations; invoking transitional composition/ phase gradients.

Combinatorial CVD has been previously used to investigate and optimise the functional properties of a number of systems.[57-60,109-111] The first such application of combinatorial CVD was demonstrated in 2002 by Gladfelter *et. al.* who used it to investigate the dielectric properties of continuous compositional spreads of Zr-Hf-Sn and Ti-Hf-Sn oxides.[57-59] By adding Sn into these systems, Gladfelter *et. al.* purposed that film crystallisation would be reduced and the high dielectricity of the Zr, Hf and Ti oxides would be maintained. The continuous compositional spreads were deposited

using a low pressure CVD synthesis by arranging precursor inlets equilaterally. The vapours from $Zr(NO_3)_4$, $Sn(NO_3)_4$ and $Hf(NO_3)_4$ / $Ti(NO_3)_4$ sources were carried over the heated silicon substrates using an inert N_2 carrier gas. Extending from the screening method applied by Van Dover *et. al.*,[54] a pre-wired grid of 100 capacitors were used to simultaneously screen the capacitance and leakage current across both systems. The chemical composition of each system was mapped using X-ray photoelectron spectroscopy. The dielectric functional properties were then related to their composition. An example is shown in Figure 1.3.1 of their Ti-Hf-Sn oxide system. The optimum composition was observed in the Ti-Hf-Sn system and corresponded to $Ti_{0.76}Hf_{0.10}Sn_{0.14}O_2$.

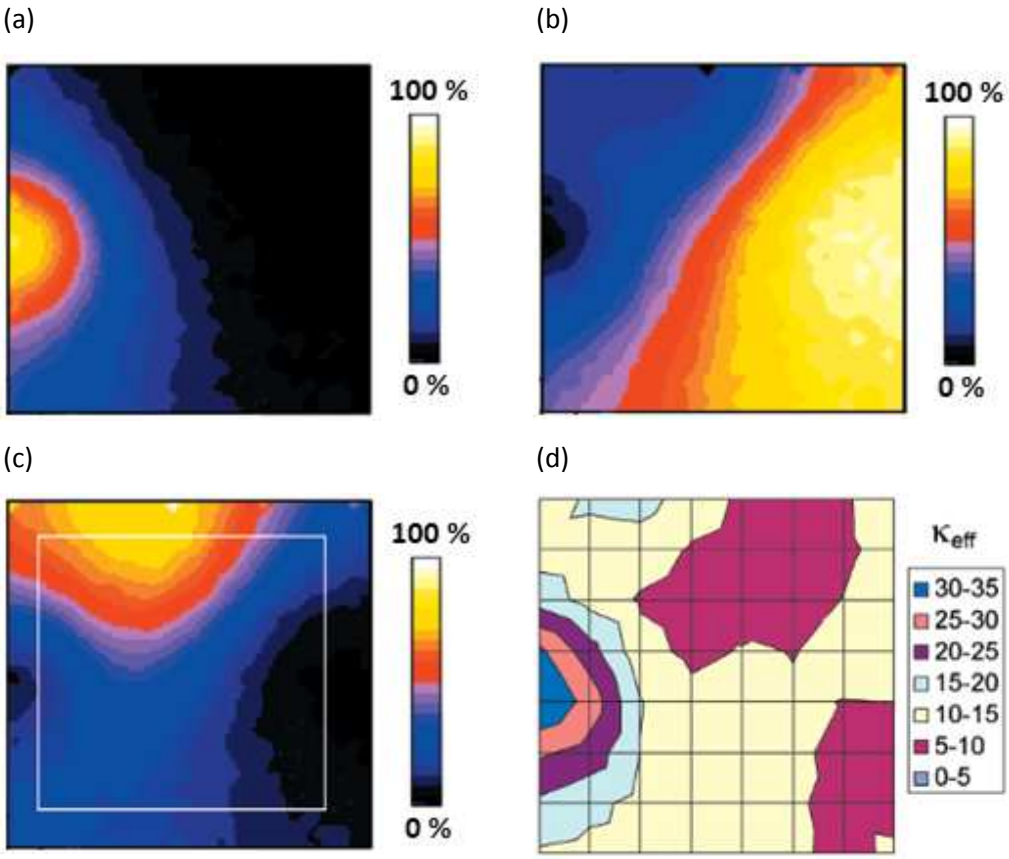

Figure 1.3.1: *Metallic content (X-ray photoelectron spectroscopy mapping) of (a) Ti (b) Hf (c) Sn within a combinatorial Ti-Hf-Sn oxide thin-film produced by low-pressure CVD and (d) the dielectric constants determined from high-throughput screening. Reproduced from reference 57.*

In 2007, Kim *et. al.* used a combinatorial misted liquid source CVD method to deposit mixed Bi-La titanates doped with Ce and investigate the remnant polarisation of these ferroelectric materials.[60] Vapours from nebulised Bi-La and Bi-Ce titanate containing solutions were transported through computer guided shutters and onto the heated substrate, inducing a compositional gradient in the La/ Ce concentration. The optimum remnant polarisability was found at the composition $Bi_{3.75}La_{0.21}Ce_{0.04}Ti_3O_{12}$ with the trend coinciding with preferred orientation in the (117) plane. In the same year, Kuykendall *et. al.* used a combinatorial APCVD process to produce the full range of In_xGa_{1-}

$_x$N materials in a single deposition and investigate the change in bandgap energy.[109] In fact, it was the first time in which indium had been introduced into an $In_xGa_{1-x}N$ system above x = 0.2 without phase segregation. $InCl_3$ and $GaCl_3$ metal precursors were introduced at opposite ends to the substrate within a tube furnace and the NH_3 nitrogen source at the centre. The process induced the growth of nano-wires that showed a near continuum of photo-luminescence colours from the In rich to Ga rich ends (Figure 1.3.2(a)). These photo-luminescence energies, as well as optical absorption and electron energy loss spectroscopy were used to calculate the direct bandgap of the alloy with changing composition (Figure 1.3.2(b)). The study demonstrated how the bandgap energy of materials could be tailored to their composition. Combinatorial APCVD was used again that year, this time by Hyett *et. al.*, in their investigation of titanium oxynitrides and led to the discovery of a new material, pseudo-brookite $Ti_{3-\delta}O_4N$ ($0.06 < \delta < 0.25$).[112] In 2008, Hyett *et. al.* used the same synthetic technique to investigate the heat-mirror properties of $Ti_xV_{1-x}N$ alloys.[111] By introducing the three precursors at separate points over their substrate ($TiCl_4$ top, NH_3 middle and VCl_4 bottom) they were able to produce a comprehensive range of alloys from $0.29 < x < 0.94$. Through investigating the changes in IR reflectance across the material, the detriment to the heat-mirror properties of mixed Ti-V nitrides was established.

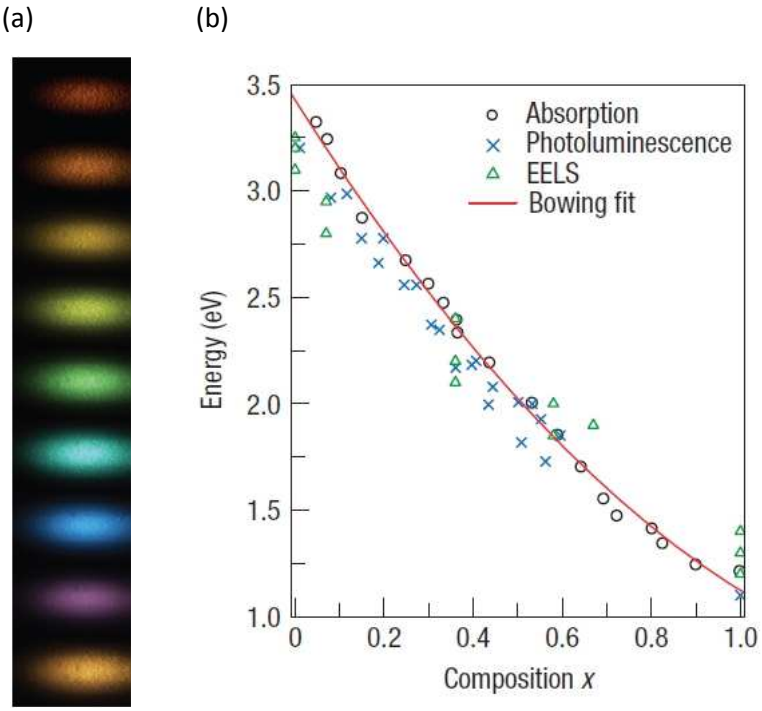

Figure 1.3.2: *(a) Photo-luminescence emission across a compositionally graded $In_xGa_{1-x}N$ ($0 \leq x \leq 1$) thin-film produced by APCVD and (b) the relationship of In content with bandgap energy. Reproduced from reference 109.*

Cold-walled APCVD depositions of TiO_2 inherently produce thin-films with thickness and preferred orientation gradients and in some cases, phase gradients too. This was demonstrated by

Hyett *et. al.* in their deposition of TiO_2 on glass from $TiCl_4$ and ethyl acetate precursors.[110] The anatase TiO_2 film deposited at 450 °C ranged in thickness from 75 – 310 nm and showed varying degrees of preferred orientation of crystallites across the film, most prominently in the (200) and (112) planes. The changes in thickness were related to the slight heating gradient (≈ 25 °C) induced by the cold-walled arrangement and explained why the film was thickest at the centre. However, preferred orientation varied with distance from where the precursors entered the reactor, where the changes were related to the variation in precursor concentration across the substrate during the deposition. The same deposition was conducted at 600 °C. In addition to the thickness and preferred orientation variations observed at 450 °C, an anatase TiO_2 - rutile TiO_2 phase gradient was also induced. In the middle section of the film, where the substrate was hottest, rutile TiO_2 formation was dominant. The photocatalytic activity of four characteristic spots was assessed to the oxidation of stearic acid under 254 nm radiation. Interestingly, sections more highly composed of anatase TiO_2 displayed higher activities.

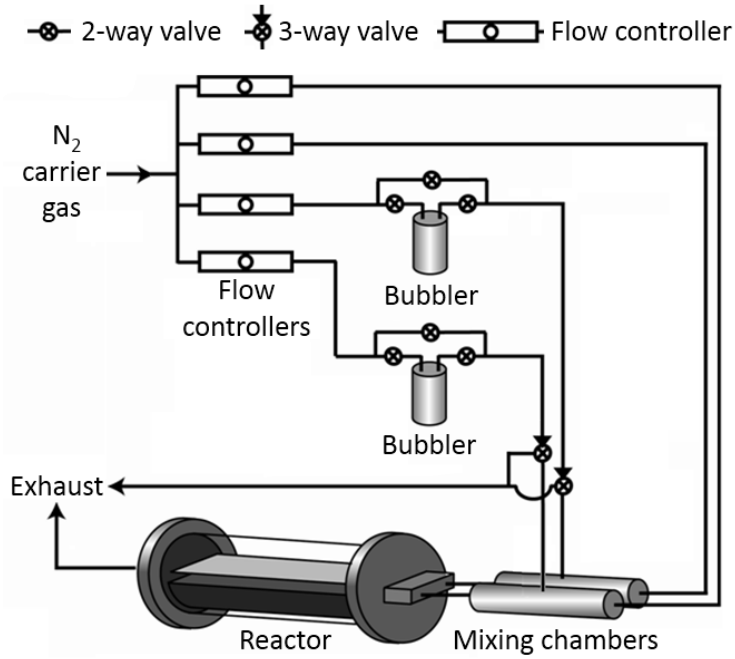

Figure 1.3.3: *Schematic of a typical arrangement of the APCVD apparatus used to deposit combinatorial thin-films of doped TiO_2 in this thesis.*

Using a similar cold-walled combinatorial APCVD set-up to Hyett *et. al.*,[110-112] we investigated the functional properties of doped TiO_2 systems on barrier glass substrates. These substrates, provided by Pilkington NSG, are used commercially for the mass-production of their self-cleaning windows. A typical combinatorial APCVD set-up, used throughput our investigations, is shown in Figure 1.3.3. Precursors placed inside the bubblers can be heated to increase their volatilities. An inert N_2 gas, with a controlled rate of flow, can be passed through each bubbler and carry the vapours to the

mixing chamber. In our combinatorial depositions, the vapours from up to two bubblers are carried to any mixing chamber. In this chamber, the vapours are pushed by plain flows of the carrier gas through a baffle manifold and into the reactor. The manifold contains a series of cavities that invoke laminar flow. More importantly, the baffle manifold has two separate entry and exit points from each mixing chamber into the reactor. This induces a gradient in the carrier gas flows and a concentration gradient in the precursor vapours; creating the combinatorial aspect of this work. Precursors are absorbed on the surface of the heated barrier glass substrate inside the reactor. They subsequently diffuse to growth sites, react and nucleate to produce epitaxial thin-films.[108] The volatile by-products produced in these reactions are removed by the continuous carrier gas stream out from the exhaust.

When producing combinatorial thin-films with the potential to contain vast numbers of unique states it is important to have suitable high-throughput characterisation methods in place to cope with such volumes - otherwise the benefit of the rapid synthesis is lost. In Hyett *et. al.*'s study of TiO_2 thin-films produced by cold-walled APCVD, a rapid X-ray diffraction mapping technique was presented.[110] They demonstrated how the phase composition and preferred orientation of 165 unique positions across the film could be mapped in just one day of analysis. Several novel high-throughput screening tools were thus developed to increase the speed of characterisation of our combinatorial systems and are reported in Chapter 2 of this thesis.

Using a combinatorial APCVD synthesis, we investigated nitrogen (Chapter 3), niobium (Section 4.3) and tungsten (Section 4.4) doped TiO_2 thin-film systems. The N-doped TiO_2 system has been studied most prominently for improved visible light photocatalysis.[30,113-118] Nitrogen can either substitute oxygen sites (substitutional doping - N_s) or enter within the TiO_2 framework (interstitial doping - N_i), yet there is little consensus on which type of doping or dopant concentration yields the more active photocatalyst. Using the combinatorial APCVD approach, $TiCl_4$ and ethyl acetate precursors will be used to form the host TiO_2 matrix with either NH_3 or t-butylamine used as N-source. The photocatalytic activities of Nb and W doped TiO_2 solid solutions have not previously been investigated; however, their resistivities for potential applications as more durable transparent conducting oxide materials have been. The Nb-doped and W-doped systems will be formed from combining $TiCl_4$, ethyl acetate and $NbCl_5$/ WCl_6 precursors respectively. In applying our high-throughput screening tools (Chapter 2), tailored to the systems under study, we show how large numbers of unique states across each combinatorial system can be characterised and their physical-functional properties inter-related, demonstrating a rapid method for the functional property optimisation of composition/ phase space.

2. Developing high-throughput analysis methods

2.1. Introduction

Combinatorial thin-films have the potential to contain large numbers of diverse states. It is therefore essential to have an array of high-throughput screening methods alongside such films in order to characterise these states with appreciable speed, otherwise the benefit of rapidly generating large numbers of diverse states is lost. Several novel characterisation methods were developed to cope with assessing large numbers of states and are discussed in this chapter.

We were not the first to develop new methods of screening combinatorial thin-films. In fact, their development has led to the progression of the combinatorial methodology into new fields. A fine example of this was demonstrated by Olk *et. al.*[62,63] In realising that the emissivity properties of metallic alloys alter upon absorbing hydrogen,[119] a tool for rapidly monitoring the hydrogen storage properties of thin-films was developed. By monitoring changes in the IR region, the comparative levels of hydrogen sorption and desorption were rapidly determined. Later, this method was further developed by Gremaud *et. al.*[64,65] As a material's transmittance changes upon hydrogen absorption and desorption, the level of light that passes through the material can be simply assessed from digital photographs. This allowed the hydrogen storage properties of large areas of unique states to be simultaneously monitored *in situ* as a function of hydrogen pressure or temperature, increasing the speed of analysis. Digital photography was also applied by Danielson *et. al.* in their study of 25,000+ unique states of phosphorescent materials.[53] By photo-exciting the entire phosphor array with UV light, the ensuing light emissions were photographed. After calibrating the intensity of the red-green-blue components of digital colour of images from the camera to standard phosphor materials, the photograph of the 25,000+ discrete materials was simultaneously assessed. This methodology became the method of choice for studying large numbers of unique states in this field.[81,120]

Numerous screening probes that could be translated across the surface of combinatorial films were further developed or adapted. For instance, a scanning electron microscopy probe was adapted by Lu *et. al.* to simultaneously assess the catalytic oxidation of H_2 over a continuous library of Pt-Ru-(WC/ Co) alloys for anodic fuel cell applications.[66] In applying a bias voltage at the tip, a diffusion-limited reduction of protons was induced. If the sample was an active catalyst, the H_2 generated at the tip would diffuse to the surface and be re-oxidised. This continuous cycle of oxidation-reduction produced an additional current at the tip, where the magnitude was wholly dependent on the activity of the catalyst. Atomic force microscopy (AFM) was also adapted by Rende *et. al.* as a way of screening the remnant polarisability of ferro-electric thin-films materials.[121] As a material's

piezoelectricity and remnant polarisability are generally proportional characteristics, the AFM probe was used to screen the piezoelectricity of material libraries which were then related to their polarisability.

The progress and application of such screening tools for thin-film combinatorial applications is extensive, with several reviews written on the topic.[44-47] Nevertheless, a number of novel screening methods had to be developed in order to investigate the thin-film combinatorial systems studied in this thesis. For example, the photocatalytic activities of compositionally graded combinatorial systems were yet to be investigated, so a tool capable of mapping photocatalysis needed to be developed (Chapter 2.5). Films of TiO_2 formed on glass by combinatorial APCVD inherently display variation in their preferred orientation and thickness and at certain temperatures can also show phase gradients.[110] As the preferred orientation of such films can lie in a number of planes it is difficult, near impossible, to fit crystallography patterns to a Rietveld refined model with defined phase contributions. For this reason, Raman spectroscopy was developed to decipher the contribution of each phase in multi-phased materials (Section 2.1) in addition to a simple X-ray diffraction based method for normalising the degree of preferred orientation in a given plane (Section 2.2). A method originally developed by Swanepoel *et. al.*[122] was manipulated so that the thickness at any position on the combinatorial film could be determined (Section 2.3). And finally, given the extensive analysis of N-doped systems, a method less laborious than X-ray photoelectron analysis for determining the N concentration in TiO_2 was developed through deconvoluting wavelength dispersive X-ray patterns (Section 2.4).

2.2. Phase mapping

Traditionally, the phase compositions of the large numbers of crystalline states generated in thin-film combinatorial depositions have been mapped using X-ray diffraction methods.[44-47] In some cases, neutron diffraction from a synchrotron source has been used to more rapidly identify such large numbers of states.[123] However, thin-films formed from chemical vapour depositions suffer from substrate/ reaction induced preferred orientation growth. As such effects typically mediate growth in a number of planes by differing degrees, fitting the diffraction pattern to a truly accurate Rietveld refined model[124] can be difficult, near impossible. When applying preferred orientation constraints[125] to this model, several combinations in multiple planes tend to fit, so it is impossible to know which combination is true from the X-ray diffraction pattern alone. Additional information from side-on

scanning electron microscopy or transmission electron microscopy might reveal the true nature of the preferred orientation growth, but would be highly laborious if applied on a combinatorial scale.

Raman spectroscopy is regularly used to identify the phase of TiO_2 thin-films.[126] As the phases of TiO_2 are such strong Raman scatterers, the phase can be identified on the minute time-scale and is typically at least one order of magnitude faster than X-ray diffractometry. The Raman Effect occurs when plane polarised light interacts with the electron clouds of atoms within bonds.[127] If the mode of interaction leads to a change in polarisability the bonds are excited from the ground state to a virtual energy state. These bonds eventually relax and return to a rotational or vibrational state different from before excitation, releasing energy shifted photons. If the final state of the molecule is more energetic than its initial state, the photon released will be of a lower energy and is defined as a Stokes shift. The reverse case is defined as an anti-Stokes shift. As the polarisability change of bonds in TiO_2 is high, the intensity of in-elastically scattered light due to the Raman Effect is also high. Also, the energy shifts of emitted photons differ substantially for each phase of TiO_2, making TiO_2 a simple material to be rapidly phase characterised using Raman spectroscopy.

Raman spectroscopy has been used in the past to determine the concentration of small amounts of anatase TiO_2 in anatase TiO_2 - rutile TiO_2 powder mixtures.[128,129] The technique was developed to identify low concentrations of anatase TiO_2 more accurately than modelled X-ray diffraction data. The method was also applied in mineralogy, to determine low levels of anatase TiO_2 in kaolinite clays because of the strong degree of X-ray diffraction peak overlap.[130] However, to our knowledge, the technique has not been applied to thin-films nor used to determine higher levels of anatase TiO_2 in anatase TiO_2 -rutile TiO_2 phase mixtures. It has certainly not been used in any case to determine the relative concentrations in phase mixtures of anatase TiO_2 and pseudo-brookite $Ti_{3-\delta}O_4N$. From our combinatorial investigations of N-doped titania phase space, we encountered systems with anatase TiO_2 - rutile TiO_2 phase gradients (Chapter 3.2) as well as anatase TiO_2 -pseudo-brookite $Ti_{3-\delta}O_4N$ phase gradients (Chapter 3.3). In order to rapidly determine the contribution of each phase in composite mixtures, a method utilising Raman spectroscopy was developed.

Anatase TiO_2, rutile TiO_2 and pseudo-brookite $Ti_{3-\delta}O_4N$ show distinctly different Raman patterns due to their different structures, as shown in Figure 2.1.1. The anatase TiO_2 structure is comprised of TiO_6 octahedra that each share four of their edges with four neighbouring TiO_6 polyhedra whereas rutile TiO_2 is comprised of a structure based on edge-sharing chains of TiO_6. When phase mixtures are analysed, the peaks characteristic of each phase can be separated by deconvolution. This operation can be performed accurately if the nature of each peak is known i.e. its typical shape and width. However, each Raman active mode varies in intensity depending on the magnitude of the

polarisability change. Therefore, in order to convert these separated peaks into phase contributions an array of phase-mixed composite standards, of known concentration, were first investigated. For anatase TiO_2 and rutile TiO_2 mixtures this was easy, as the powders were commercially available. However, pseudo-brookite $Ti_{3-\delta}O_4N$ is a newly discovered material with no current industrially applied use and therefore had to be synthesised. Following the same combinatorial APCVD method used by Hyett *et. al.* in its original discovery,[112] pseudo-brookite $Ti_{3-\delta}O_4N$ was deposited onto a thin steel substrate. As the steel bent on cooling from the elevated temperatures of the deposition, the thin-film deposited at the surface began to flake. These pseudo-brookite $Ti_{3-\delta}O_4N$ flakes could be simply brushed off the surface and ground into a fine powder.

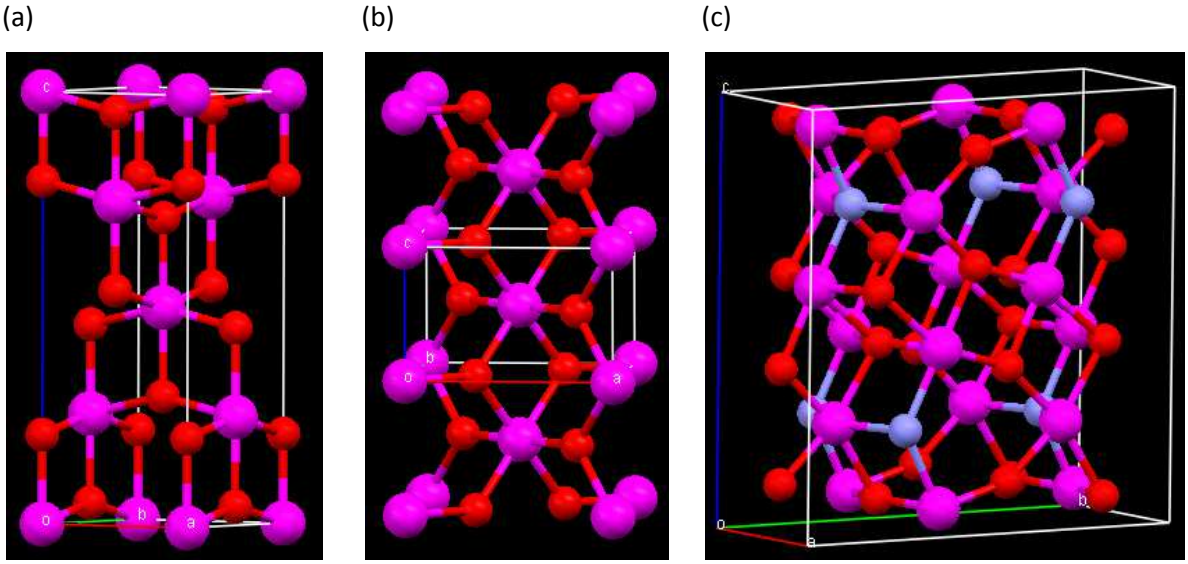

Figure 2.1.1: *Crystallographic arrangements of (a) anatase TiO_2 (b) rutile TiO_2 and (c) pseudo-brookite $Ti_{3-\delta}O_4N$; the box encapsulates one unit cell.*

A series of standards were made by mixing specified ratios of anatase TiO_2 -rutile TiO_2 and anatase TiO_2 - pseudo-brookite $Ti_{3-\delta}O_4N$ powders. The powder mixtures were mixed under vortex and ground several times to achieve homogenous pastes. The Raman pattern of each paste was then taken using a Renishaw 1000 spectrometer with its laser calibrated to the emission lines of a graphite standard. A red laser (633 nm) excitation source produced the most intense spectra from anatase TiO_2 -rutile TiO_2 pastes and a green laser (532 nm) produced the most intense spectra from and anatase TiO_2 - pseudo-brookite $Ti_{3-\delta}O_4N$ pastes. A stack of the spectral patterns generated from each series is shown in Figure 2.1.2.

To deconvolute each and every peak in patterns of phase-mixtures patterns would be challenging. As the intensity change in any lone band can be related to changes in phase concentration, it was decided that a single prominent mode of each phase be chosen and separated instead. In addition, if

the separation included a prominent mode from each phase involved, merely a single deconvolution would necessitate phase determination of each sample.

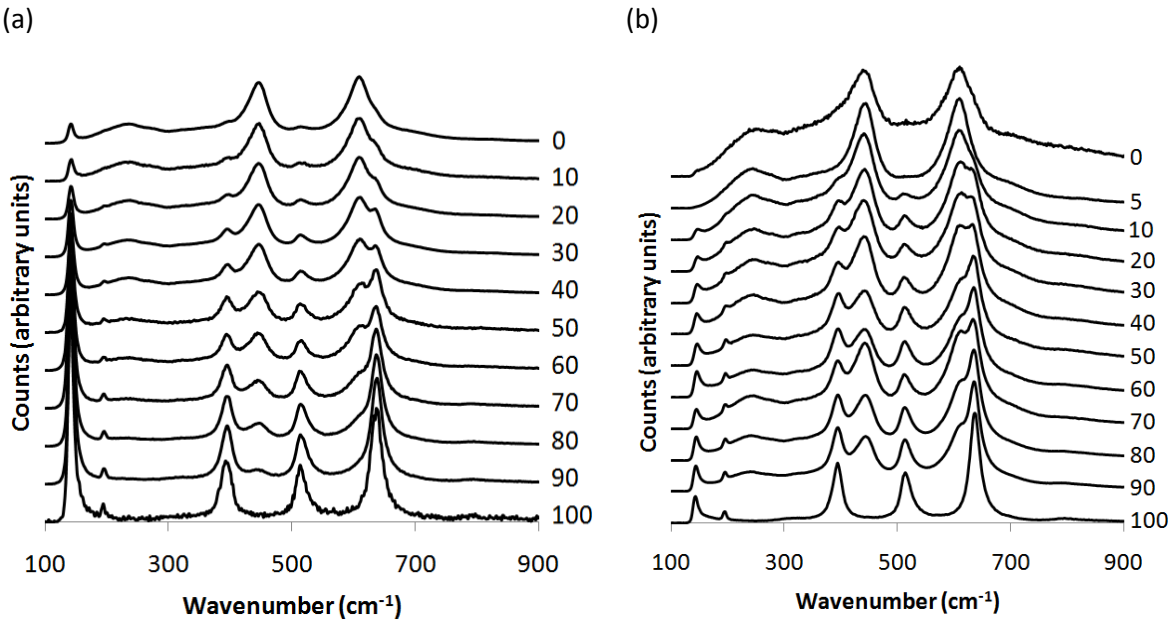

Figure 2.1.2: *Stacked Raman patterns of pre-formulated powder mixtures of (a) anatase TiO_2 and rutile TiO_2 using a red laser (633 nm) and (b) anatase TiO_2 and pseudo-brookite $Ti_{3-\delta}O_4N$ using a green laser (532 nm). Numbers indicate the percentage composition of anatase in each standard mixture.*

In comparing anatase and rutile TiO_2, the two most prominent and separable modes occur at 639 cm^{-1} (E_g mode) and 612 cm^{-1} (A_{1g} mode) respectively. For anatase TiO_2 and pseudo-brookite $Ti_{3-\delta}O_4N$, the two most prominent and separable modes occur at 639 cm^{-1} (E_g mode) and 620 cm^{-1} respectively. By first looking at the pure phase powders, we were able to model the shape, width and location of each of these prominent peaks using Casa XPS software.[131] With this knowledge, we were then able to model and separate these prominent peaks within phase mixtures. Some examples from within each series is shown in Figure 2.1.3. The peak area of each mode for all compositions tested was then converted into a ratio where for the anatase TiO_2 - rutile TiO_2 series:

$$rutile\ ratio\ (\%) = \left[\frac{Area\ rutile\ (612\ cm^{-1})}{Area\ rutile\ (612\ cm^{-1}) + \ Area\ anatase\ (639\ cm^{-1})}\right] x\ 100 \quad (2.1)$$

and for the anatase TiO_2 and pseudo-brookite $Ti_{3-\delta}O_4N$ series:

$$pseudo\ brookite\ ratio\ (\%) = \left[\frac{Area\ pseudo\ brookite\ (620\ cm^{-1})}{Area\ pseudo\ brookite\ (620\ cm^{-1}) + \ Area\ anatase\ (639\ cm^{-1})}\right] x\ 100 \quad (2.2)$$

For each series, these ratios were plotted against their corresponding anatase compositions (%) as shown in Figure 2.1.4.

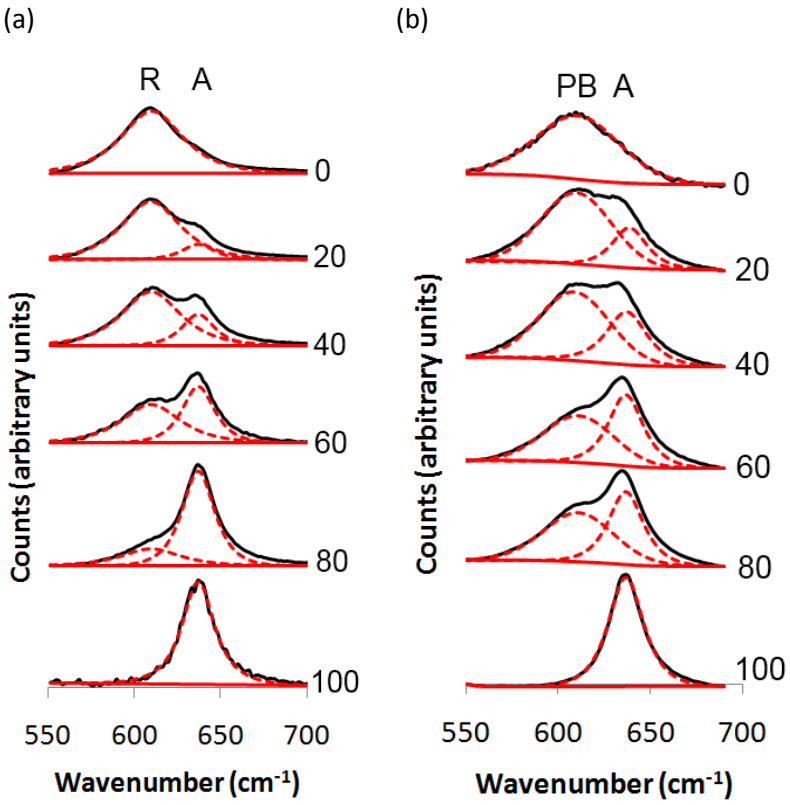

Figure 2.1.3: *Stacked deconvoluted Raman patterns focused on the prominent modes of choice for the pre-formulated mixtures of (a) anatase TiO_2 and rutile TiO_2 and (b) anatase TiO_2 and pseudo-brookite $Ti_{3-\delta}O_4N$ powder standards. A = anatase 639 cm^{-1} (E_g mode), R = rutile 612 cm^{-1} (A_{1g} mode) and PB = pseudo-brookite 620 cm^{-1} prominent peaks.*

For the anatase TiO_2 - rutile TiO_2 series an almost linear relationship between the rutile peak area ratio (Equation 2.1) and composition was observed. This fit a first order exponential model best, with excellent fit (r^2 = 0.989). With this relationship now established, if the peak area ratio of the prominent rutile TiO_2 (Equation 2.1) is known, the phase composition can be derived. We were now able to determine the composition of any unknown anatase TiO_2 - rutile TiO_2 phase mixture by first acquiring the Raman pattern over the range of these prominent modes (500 – 700 cm^{-1}) and then separating each mode through a modelled deconvolution. This was also true for the anatase TiO_2 - pseudo-brookite $Ti_{3-\delta}O_4N$ series as the peak area ratio of the prominent pseudo-brookite $Ti_{3-\delta}O_4N$ (Equation 2.2) formed a strong Boltzmann-type relationship with phase composition (r^2 = 0.993).

When applying this phase mapping method one must make some assumptions. For instance, we must assume that the phases of the sample being tested are both equally crystalline. This is because the degree of Raman inelastic scattering is proportional to the degree of crystallinity. One simple way of checking that this is true is through X-ray diffraction. By measuring the line-width of X-ray

diffraction peaks we can derive the average degree of crystallinity of each phase (average crystallite size) through application of the Scherrer equation[132] and works regardless of preferred orientation effects.

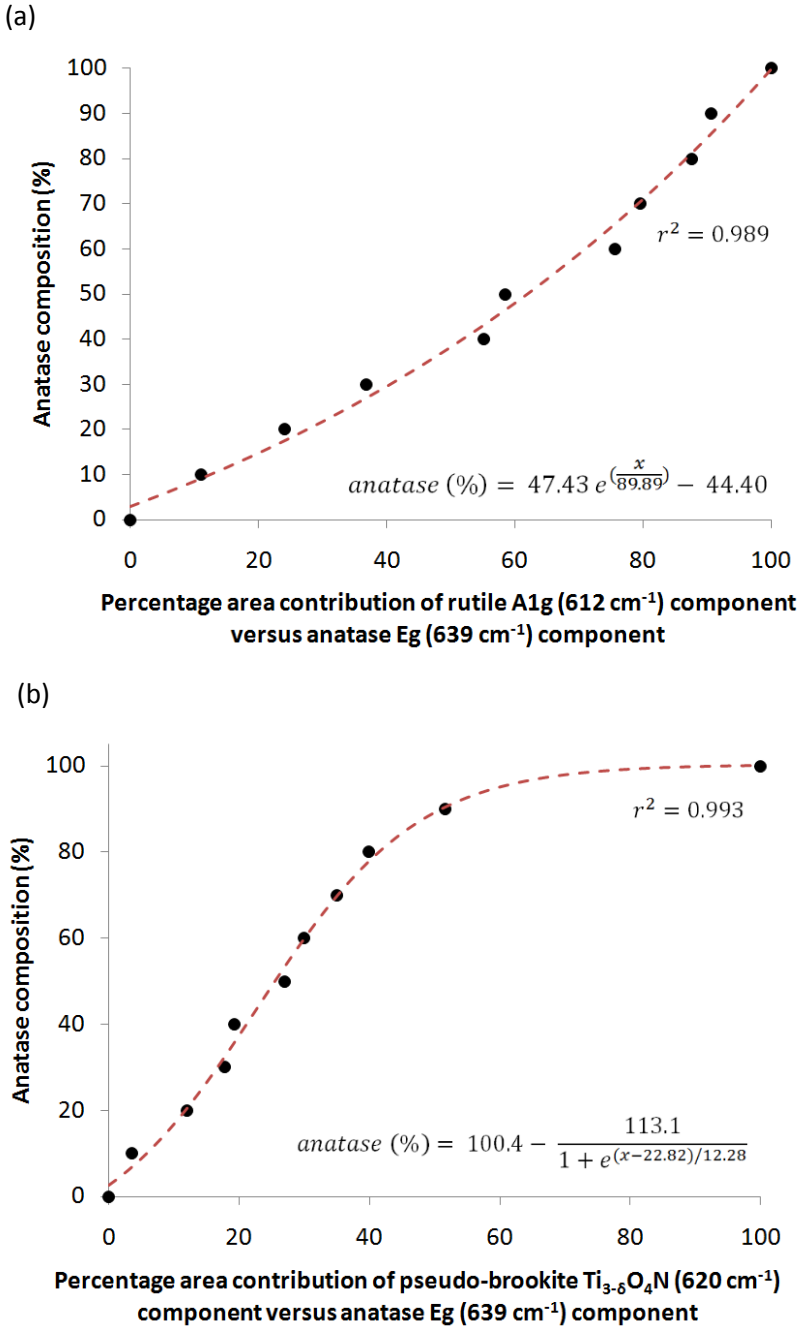

Figure 2.1.4: *Plots of the percentage area contribution of (a) the rutile TiO_2 Raman mode at 612 cm^{-1} and (b) the pseudo-brookite $Ti_{3-\delta}O_4N$ Raman mode at 620 cm^{-1} against pre-formulated anatase phase composition for the (a) anatase TiO_2 and rutile TiO_2 and (b) anatase TiO_2 and pseudo-brookite $Ti_{3-\delta}O_4N$ series of mixed phase powder standards.*

Although the speed at which the phase composition of anatase TiO_2 - rutile TiO_2 or anatase TiO_2 - pseudo-brookite $Ti_{3-\delta}O_4N$ systems can be determined is slowed by the deconvolution stage, there was no conceivable alternative except extended X-ray absorption fine structure (EXAFS)

measurements. As EXAFS gives detailed information on the local environment of each element in the sample, it can be used to accurately and rapidly determine the phase composition regardless of the degree of crystallinity of each phase.[133] However, EXAFS is not a freely available technique as it requires a synchrotron to generate the tuneable X-rays for exciting the sample. Therefore, this highly accessible Raman-based phase mapping method was developed instead.

2.3. Preferred orientation mapping

Through the studies of Hyett *et. al.,* the multitude of preferred orientation environments in combinatorial APCVD deposited TiO_2 thin-films on glass is well established;[110,134] however, a method for rapidly quantifying the degree of preferred orientation of the large number of unique states is not. Being able to quantify or determine the most preferential plane of growth is important when studying the functional properties of thin-film materials. For example, it has been found that different facets of crystal planes of TiO_2 absorb certain types of organic material more readily than others.[135,136] Such facets have showed more enhanced degrees of photocatalysis in thin-film TiO_2[137,138] as well as other systems.[139,140] A study of rutile TiO_2 single crystals found the photo-induced wetting (PIH) wetting mechanism to be most prominent in the (110) and (100) faces and least prominent in the (001) face.[17] This has lead to the design of nano-structured materials with constrained growth in certain planes to induce enhanced functionality.[141]

Some groups have applied magnetic anisotropy to quantify the preferred orientation in rocks.[142] Other groups have simply assessed the intersection-lines on different sections of rock using computer software.[143] However, both methods, used commonly in the field of mineralogy, were designed to investigate large 3-dimensional bodies. The preferred orientation of thin-films, or texturing as some call it, is regularly investigated using X-ray diffraction instead. The most common and precise way of doing this involves scanning the sample at a fixed angle of diffraction at a large number of different angular orientations to produce a pole figure.[144] The probability of finding a given crystal plane as a function of specimen orientation can thus be derived. When the pole figures of several diffractions are combined, a complete orientation distribution function of the crystallites can be extracted that precisely quantifies the degree of preferred orientation. Given the typically lower diffraction counts achieved from thin-film samples, such tilt analysis might take several hours to characterise just one sample, making it highly impractical for screening large numbers of unique states in combinatorial samples. A more simple way of quantifying differences in the preferred orientation had to be developed.

In processing regular X-ray diffraction patterns of thin-film samples we were able to quantify the degree of preferred orientation change versus a single crystal. The general principle underpinning X-ray diffraction is the ability of an electron cloud that surround an atom to scatter X-ray radiation. When a crystalline sample, which consists of a highly ordered arrangement of atoms, is bombarded with monochromatic X-rays in phase, the diffracted X-rays can only be detected at specific angles of incidence. This effect is explained by Bragg's law[145] with a diagrammatic example shown in Figure 2.2.1. When X-ray *i* encounters an atom in a crystal plane at an angle θ it is diffracted. When X-ray *ii*, in phase with X-ray *i*, encounters the atom at a distance of *d* below the first atom, it is also diffracted. The diffracted X-rays can either still be in phase, leading to constructive interference and detection or out of phase, leading to destructive interference and no detection. The case where the diffracted X-rays are in phase occurs only at specific angles of incidence θ. From the diagram we can see that X-ray *ii* must travel a greater distance of 2d.sinθ. We also know that this distance must be equal to an integer number of wavelengths or the X-rays will destructively interfere. Therefore:

$$n\lambda = 2d.sin\theta \tag{2.3}$$

where *n* is any integer, *λ* is the X-ray wavelength, *d* is the spacing between atomic planes and θ the angle of incidence.

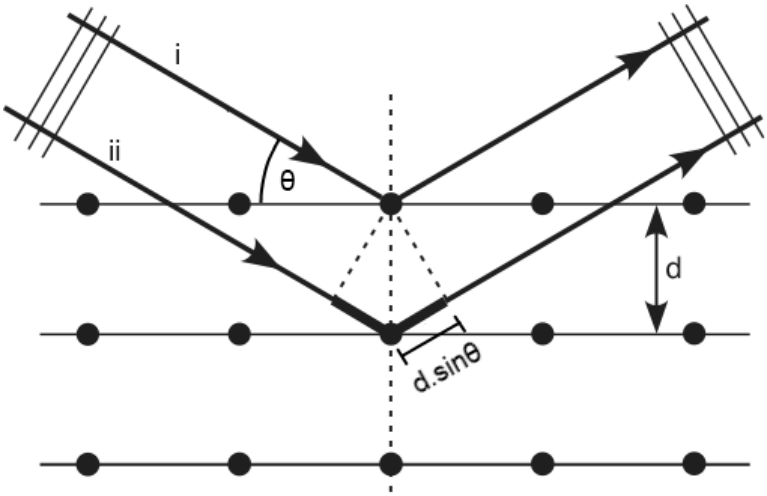

Figure 2.2.1: *Schematic to explain the requirement for in phase diffraction of X-rays from crystal planes for a detection to be observed at a given angle of incidence; in accordance with Bragg's law.*

Thin-film samples are typically analysed at low angles of incidence using glancing angle X-ray diffractometers. In our experiments we used a Bruker-Axs D8 general area diffraction detector system (GADDS) and an incident beam angle of 5°. This instrument utilizes a large 2D area X-ray detector to record large sections of multiple Debye-Scherrer cones simultaneously at 34° in both θ and perpendicular in ω with 0.01° resolution without moving the detector. After collection, the

Debye-Scherrer cones can be integrated across ω to produce a standard one-dimensional plot of 2θ against intensity. The instrument utilizes a monochromated Cu X-ray source (λ = 1.5406 Å) collimated such that only a small area of the sample (≈ 3-4 mm^2) is studied at any one time. Despite the small sample illumination, diffraction patterns with acceptable signal-to-noise ratios can still be recorded in very short time-frames (≈ 10 mins) due to the large amount of data that the area detector can simultaneously collect. The sample itself is placed on a flat stage that is motorized to automatically move in x, y, and z directions. This combination of abilities (i) small illumination area, (ii) rapid collection and (iii) moveable sample stage makes the diffractometer ideal for recording the diffraction patterns of a multitude of different positions across the surface of a thin-film. This makes the method ideal for analysing the changes in preferred orientation of combinatorial thin-film samples.

By comparing the X-ray diffraction pattern of an anatase single crystal ($I4_1/amdz$, a = 3.7848 Å, c = 9.5124 Å)[146] with an example from our combinatorial studies that shows preferred orientation, as shown in Figure 2.2.2, we will demonstrate the development of our simple and rapid method for quantifying preferred orientation. When comparing the relative heights of peaks we find that the thin-film example shows little growth in the (103), (004) and (105) planes and quite a strong preference for growth in the (211) plane.

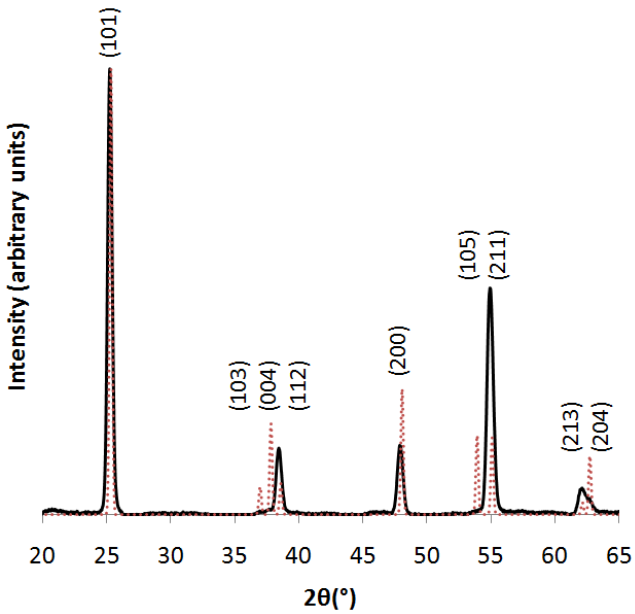

Figure 2.2.2: *X-ray diffraction pattern of an anatase TiO_2 single crystal (red dotted line) and an example of an anatase TiO_2 thin-film (black solid line) with preferred orientation. Heights of the (101) diffraction peaks are normalised to be equivalent in height.*

In order to quantify this observed preferred orientation effect we first determined the percentage contribution of each peak compared with total peak intensity:

$$\left[I_{hkl} \Big/ \sum_{hkl} I_{hkl} \right] \times 100 \qquad (20° \leq 2\theta \leq 65°)$$

(2.3)

This was performed for each diffraction peak in both thin-film and single crystal samples. The percentage increase in growth of a particular plane compared to a randomly oriented single crystal could thus be derived:

$$\left(\left[I^f_{hkl} \Big/ \sum_{hkl} I^f_{hkl} \right] - \left[I^c_{hkl} \Big/ \sum_{hkl} I^c_{hkl} \right] \Big/ \left[I^c_{hkl} \Big/ \sum_{hkl} I^c_{hkl} \right] \right) \times 100$$

(2.4)

where I^f and I^c are the X-ray diffraction intensities of a preferentially orientated sample and the single crystal respectively. The percentage changes for the example are shown in Figure 2.2.3(a). The planes of preferred growth observed by eye were quantified, with the largest comparative increase in preferred growth in the (211) plane and the biggest decreases in the (103), (004) and (105) planes.

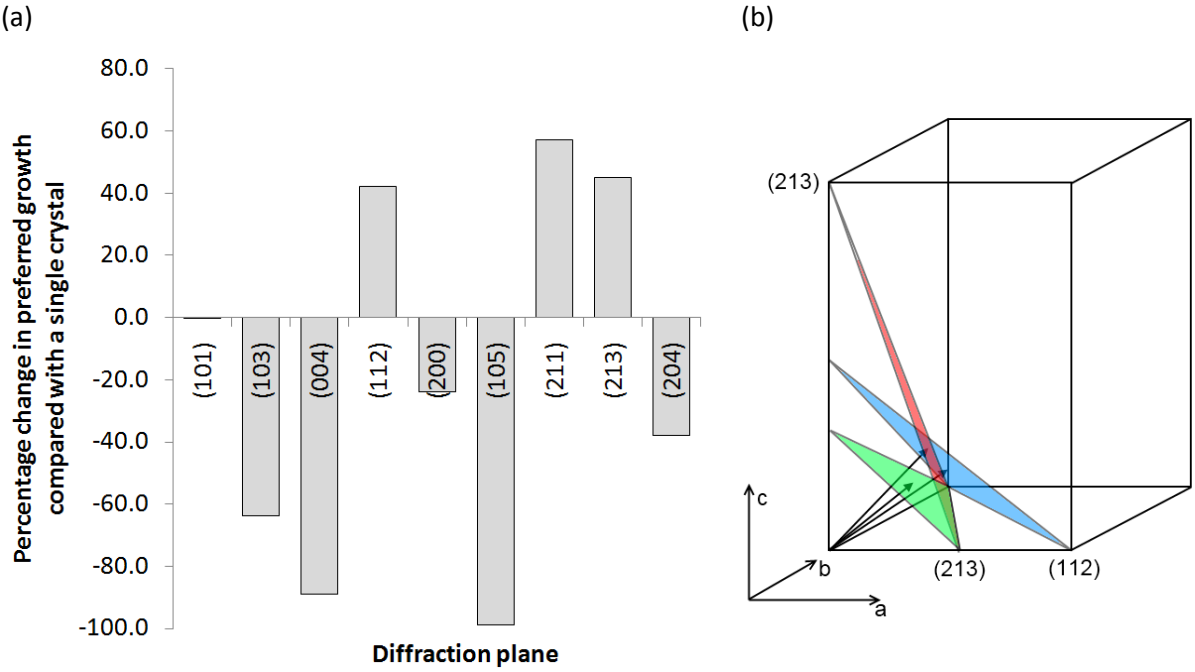

Figure 2.2.3: *(a) Percentage change in preferred growth of an example anatase TiO_2 thin-film versus a randomly oriented single crystal of anatase TiO_2 for the planes of diffraction over 20° ≤ θ ≤ 65° range and (b) the projections of the Miller planes of maximum preferred growth.*

In most literature combinatorial thin-film studies where the preferred orientation of crystallites has been observed, preferred growth typically occurs in a single plane and most prominently in the direction of the *c* axis (multiples of the (001) plane).[55,147,148] However, this was due to the use of

crystalline substrates with matched lattice spacing to the thin-film being deposited, which invoked strain-free directional growth. In the example outlined in this section of a thin-film grown from a combinatorial APCVD process, preferred orientation was observed in several directions, be it the (211), (213) and (112) planes. By drawing their Miller planes (Figure 2.2.3(b)) we see the similarity in their direction and when we form a weighted average in these directions of preferred growth, we find they lie approximately in the direction of the (323) plane.

2.4. Film-thickness mapping

The functional properties of TiO_2 thin-films are directly related to its thickness. This is because thicker films have the capacity to absorb more UV light, thereby generating more photo-generated electrons and holes that are the foundation of photo-induced wetting or photocatalysis self-cleaning mechanisms. The film conductivity of TiO_2 can also be altered through doping.[149,150] The conductivity through a thin-film is highly dependent on the number of charge flow pathways, where thicker films typically increase conductivity. In order to make values unilaterally comparable, the resistivity is determined by multiplying sheet-resistance by film-thickness. Knowing the thickness of TiO_2 is therefore imperative if these functional properties are to be appropriately compared.

There are a number of approaches in measuring the thickness of thin-films. For instance, one popular method is profilometry.[151] This has been particularly applied in films synthesised by PVD.[45,52] By either masking an area of the substrate from film deposition or introducing a lithographic mask that can be later removed,[120] a step between the thin-film and the substrate is formed. Typically, a surface profiling stylus is dragged across the surface of the step and the difference in height measured.[86] Atomic force microscopy is also employed for such a task, with the capacity to measure step-heights with greater precision.[77] Film thickness can also be measured by tilting the sample perpendicular to their plane of growth and imaging using either scanning or transition electron microscopy.[152] More conveniently, the thickness of transparent thin-films can also be determined by spectroscopy and was developed by Swanepoel *et. al.* in their study of amorphous silicon thin-films.[122] They noticed that thin-films with high refractive indices would show colour due to its interference with visible light. By modelling the effect from first principles, they realised two certain conditions must be met for this effect to be observed in highly refractive thin-film materials: (i) the thickness must be uniform over an appreciable area for the human eye to observe this effect and (ii) the films must be in the sub-nanometre to micron range or the light reflected through the material will not reach the surface for constructive/ destructive effects to occur. The minimum thickness where the interference wave-pattern effect is observed for TiO_2 is ≈ 100 nm and above 1000 nm the

effect is obscured as films turn white and opaque. A model for the interference of light through a thin-film of thickness *d* is shown in Figure 2.3.1.

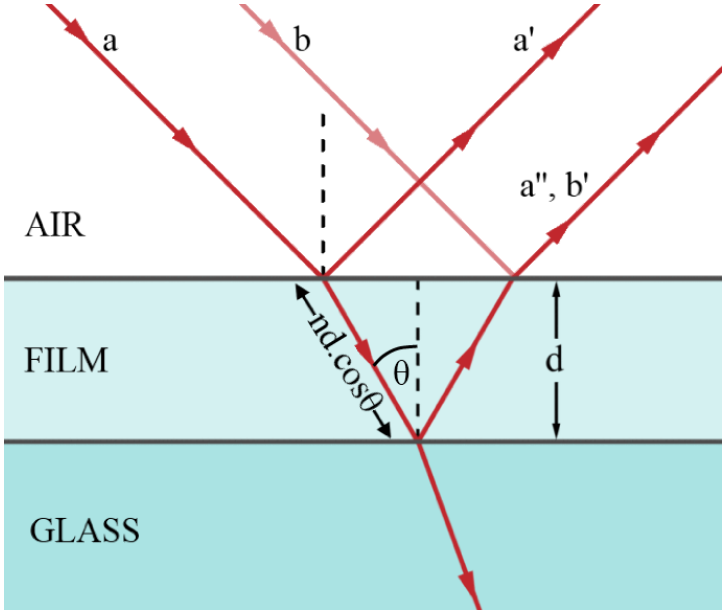

Figure 2.3.1: *Model for the interference of light through a thin-film material deposited on glass.*

Let us consider the case where photons *a* and *b* are of equal wavelength. When photon *a* reaches the air-film interface it can either be reflected (photon *a'*) or travel through the medium. Depending on the refractive index (*n*) of the material, the direction of the photon is altered (θ). The photon then travels a distance *nd*.cosθ to reach the next film-glass interface where it can either transmit through or be reflected. If reflected, the photon travels a distance of *nd*.cosθ back to the air-film interface. This can again be reflected or transmitted through the medium. Let us consider the case where it transmits through (photon *a''*). If the wavelength of this photon (*λ*) meets the following condition:

$$2nd.cos\theta = m\lambda \qquad where\ m = 1, 2, 3, 4\ ....$$

(2.5)

then photon *a''* will constructively interfere with the reflected photon *b'*. If, however, photon *a''* meets the following condition:

$$2nd.cos\theta = m\lambda \qquad where\ m = \frac{1}{2}, \frac{3}{2}, \frac{5}{2}, \frac{7}{2} ...$$

(2.6)

then photon *a''* will destructively interfere with the reflected photon *b'*. Increasingly thicker samples can accommodate the interference of increasingly wider wavelengths, increasing the maximum order

of interference *m*. Swanepoel *et. al.* spectroscopically investigated the transmittance of light (500 - 900 nm wavelength range) through amorphous silicon on glass.[122] In their case, light was directed perpendicular to the sample (θ = 0°), negating the $cos\theta$ term. A transmittance wave-pattern consisting of a series of maxima and minima was observed over the range of photon wavelengths examined. They realised that the condition for constructive interference was being met at transmittance maxima and the condition for destructive interference was being met at transmittance minima. The condition for constructive (m_1 = integer)/ destructive (m_1 = non-integer) interference could be re-written as:

$$2nd = \left(m_1 - {}^{l}/_{2}\right)\lambda_1 \qquad where\ l = 0, 1, 2, 3 \ldots$$

(2.7)

If the refractive index (*n*) of the thin-film material at each transmittance maximum/ minimum is known, a plot of *l*/2 versus λ/2 yields a straight line with a slope of 2*d* and intercept of $-m_1$; revealing the order (*m*) of interference. The thickness can thus be calculated for every transmittance maximum and minimum from the interference relationship in its simplest form:

$$2nd = m\lambda$$

(2.8)

where the average yields a precise value for film thickness with less than 1% error.[122]

The Swanepoel method for calculating film-thickness has already been applied in the field of combinatorial science. Using a high specification fibre optic cable with the unique capacity to measure the UV-visible-IR spectrum of thin-film samples in just one second, Perkin *et. al.* determined the thickness of compositionally graded Cd-Sn oxide libraries.[153] However, the use of such high-end equipment may not be a necessity when investigating TiO_2 thin-film libraries formed by cold-walled combinatorial APCVD. For instance, when Hyett *et. al.* applied this synthetic method, a TiO_2 thin-film with alternating purple and green interference bands was formed with transitionally graded thickness from 75 nm at the edges to 310 nm at the centre.[110] As TiO_2 thin-films formed by combinatorial APCVD have (i) inherently smooth changes in thickness across the film and (ii) wide and clearly identifiable interference colour bands, the thickness of each band can be measured. We will illustrate this with a plain anatase TiO_2 thin-film formed by combinatorial APCVD in our studies, as shown in Figure 2.3.3(a). The film displayed a series of interference colour bands, primarily oscillating from purple to green that peaked where the film was thickest in the bottom-middle section. It was proposed by Hyett *et. al.* that such thickness gradients were invoked by the slight heat

gradient in the underlying substrate.[110,134] This was primarily caused by the cold-walled reactor arrangement, where the centre of the reactor was better insulated and maintained a higher temperature than at the edges. As the reaction of the $TiCl_4$ and ethyl acetate reagent vapours were reaction-rate limited, rather than mass-transport limited, more rapid film growth occurred where it was hottest. As the heat gradient was transitional, so was film-thickness. By measuring the reflectance spectrum on a Helios double beam instrument relative to a rhodium mirror from 300 – 2500 nm at each interference colour band, the wavelength at which each oscillating maximum and minimum was found. An example reflectance spectrum is shown in Figure 2.3.2(a). The position where a reflectance maximum occurs, due to constructive interference, was analogous to the position where a transmittance minimum occurs. This simply demonstrates that the transmittance or reflectance spectrum of a transparent thin-film material can be used to determine film thickness using Equation 2.7. As the spectral dependence of the refractive index for anatase TiO_2 has previously been determined, we could then plot $l/2$ against $\lambda/2$ (Figure 2.3.2(b)). The line of best fit made an intercept at ≈ -1.5, therefore the initial order of interference m_1 = 1.5. The thickness at each maximum and minimum could thus be derived using Equation 2.8. The average film-thickness at the position analysed was 535 nm with a standard deviation of 3.09 nm. If we assume the error to be within two standard deviations of the mean, then with > 95 % confidence we can say that the error in the value is ≈ 1 %.

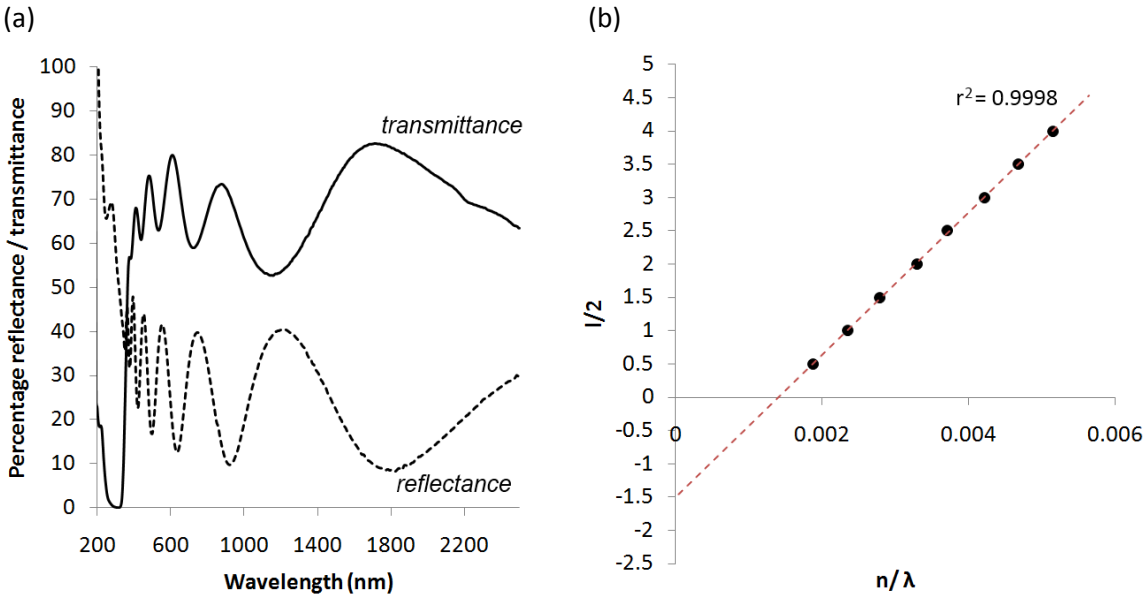

Figure 2.3.2: *(a) The reflectance-transmittance pattern of an interference colour band on an anatase TiO_2 thin-film formed by a combinatorial APCVD synthesis and (b) a plot of the refractive index (n) divided by the positions of maximum and minimum wave interference (nm) against l/2.*

The thickness of each interference colour band across the anatase TiO_2 thin-film was calculated using the same method (Figure 2.3.3(a)).

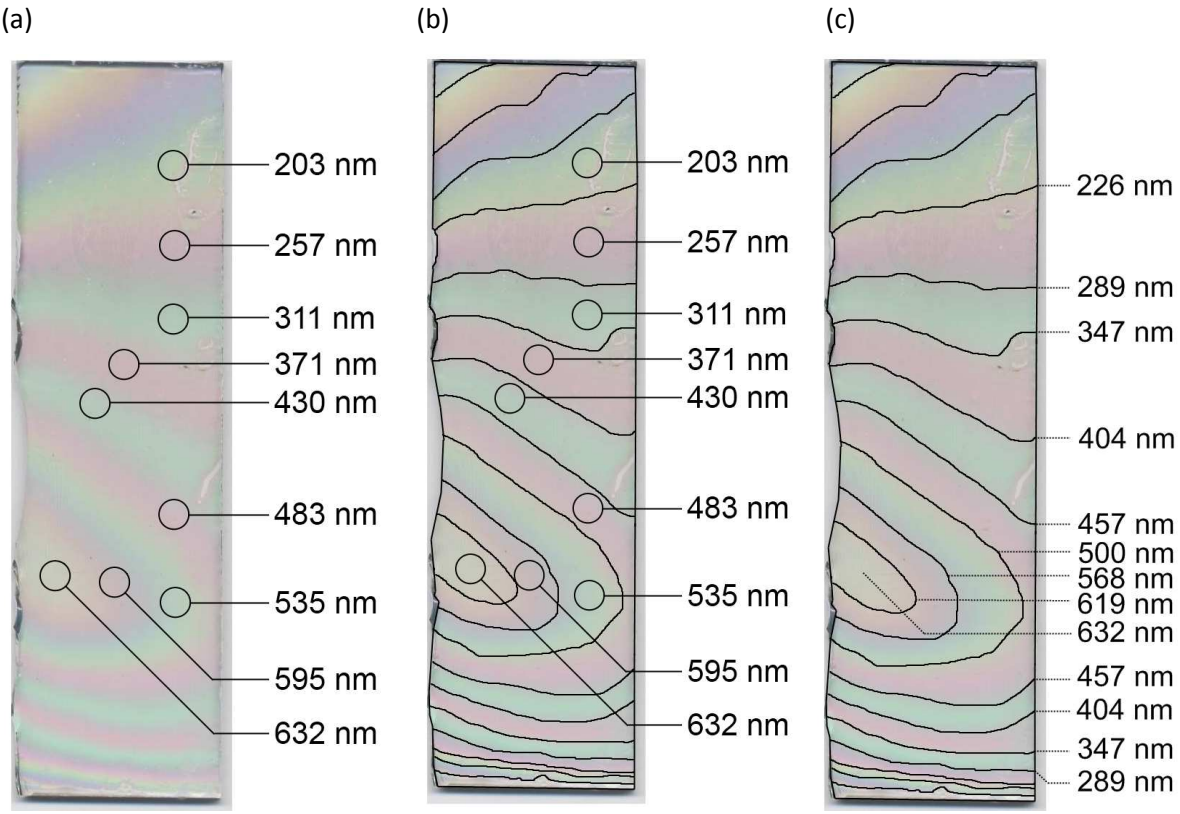

Figure 2.3.3: *A diagram showing (a) the film thickness at colour bands, (b) the drawing of contours and (c) the film-thickness at these contours from application of the Swanepoel method on an example anatase TiO_2 thin-film formed by a combinatorial APCVD synthesis.*

The spectrum at each band was analysed through circular holes, where the determined thickness describes the average over the area of analysis. As the variation in thickness was smooth, the average thickness determined through the circular hole would equate to the thickness at the centre of the hole. From Figure 2.2.3(a) we can seen that the thickness between each successive colour band was approximate constant ($\langle d \rangle$ = 55 nm, 2σ = 6.5 nm). The width between each contour band varied, however, it was typically of the centimetre scale. The incline of growth was therefore incredibly shallow (θ = 0.0003° from the above assumptions) so assuming the mode of growth across the film to be linear was fair. With this assumption in mind, we could first draw the boundaries at which the interference colours changed (Figure 2.2.3(b)) and then determine the thickness of each contour (Figure 2.2.3(c)) through the simple law of weighted averages:

$$d_{ab} = \frac{b}{a+b}\, d_a + \frac{a}{a+b}\, d_b \qquad (2.9)$$

where d_{ab} is the thickness at a position between d_a and d_b a distance of b from d_b and a from d_a. The law of weighted averages can then be applied more broadly in deriving film thickness at any position

between two contours, effectively allowing film-thickness to be mapped. For the example demonstrated, the film was of uniform phase. In our combinatorial studies, we encountered anatase TiO_2 – rutile TiO_2 and anatase TiO_2 – pseudo-brookite $Ti_{3-\delta}O_4N$ composite thin-films. When applying this method of thickness mapping, the non-anatase TiO_2 phased sections were avoided in the initial analysis of the interference colour bands. Given the transitional nature of film growth induced by the cold-walled combinatorial APCVD process, the thickness at the interference boundaries can be extrapolated to any position between them for as many unique positions warranted.

2.5. Nitrogen/ titanium concentration mapping

Of all areas of TiO_2 thin-film research, no avenue has been investigated with more vigour than its nitrogen doping.[2,10] In determining the level of nitrogen doping, X-ray photoelectron spectroscopy (XPS) is the method of choice.[154,155] The technique involves exciting samples with monochromatic X-rays (typically Al K_α = 1486.6 eV) and monitoring the kinetic energy of the electrons ejected from the surface. As the energy of the incident photons is high, it has the capacity to eject electrons from core-shells. The process can be summarised as follows:

$$A + hv \rightarrow A^+ + e^-_{core} \tag{2.10}$$

where *A* is any atom, A^+ is the ionised atom and e^-_{core} is the ejected core electron. Conservation of energy requires that:

$$E(A) + hv = E(A^+) + E(e^-_{core}) \tag{2.11}$$

The difference in energy between the ionised and non-ionised atom is termed the binding energy. As the electron's energy is solely kinetic, this equation can be rearranged to:

$$binding\ energy = hv - KE(e^-_{core}) \tag{2.12}$$

The binding energy is specific to the atom, orbital of electron ejection and chemical environment. For instance, attempting to eject a core-electron from a cationic species requires more energy than attempting to eject a core-electron from the element due to the greater effective nuclear charge. The reverse case is true for anionic species. The binding energies of nitrogen 1s electrons range from 394 eV (N^{3-}) to 408 eV (N^{5+}) depending on chemical environment. From the area underneath each binding energy peak observed in an XPS spectrum, the relative atomic concentration can be determined. As lighter elements are less likely to catch the incident X-rays, sensitivity factors specific to each atom are applied in this calculation.

XPS is an excellent method for determining the chemical environment of dopant species, particularly that of nitrogen dopants in TiO_2.[154,155] Given the controversy in the literature as to which mode of nitrogen doping, be it substitutional (N^{3-} replace O sites) or interstitial (N^0 inserts between Ti-O bridges), yields the more effective photocatalyst, XPS has recently helped shed some light on this issue.[30] In the literature it seems only electron paramagnetic resonance (EPR) can determine the nature of nitrogen dopant as well, yet can only realistically be applied to powders.[113,156] XPS is an incredibly surface sensitive technique. This is because the ejected electrons can only escape near the sample's surface, typically 10 nm deep at best.[157] In order to get a good idea of nitrogen levels in the bulk requires a series of surface etches and re-analysis. This is typically achieved through argon-ion sputtering. To make matters worse, the number of nitrogen counts is normally quite low due to the lightness of the atom. This means that XPS cannot precisely determine concentrations below 1 at. % in nitrogen-doped TiO_2. Rutherford back-scattering has also been used to determine nitrogen concentrations in doped TiO_2 thin-films, however, the technique also suffers from low sensitivity of the light elements.[158] Although wavelength dispersive X-ray (WDX) analysis is used regularly in the field of materials science for quantifying elemental concentrations it has been altogether discarded for investigating nitrogen and titanium containing samples because of the overlap of nitrogen K-shell lines (392.4 eV) and titanium L-shell lines (395.3 eV).[159] However, due to the technological improvements in WDX apparatus, the resolution in emission spectra have substantially increased. Similar to XPS studies, where merged peak-shapes from elements in multiple chemical environments are regularly deconvoluted, we developed a technique for separating the overlapped nitrogen K-shell and titanium L-shell lines; where such an idea was applied by Leite *et. al.* in separating titanium L-lines from oxygen K-lines in energy dispersive X-ray (EDX) patterns of mixed anatase TiO_2 and α-Fe_2O_3.[160]

WDX analysis involves bombarding a sample with high energy electrons (typically 10 – 20 keV) and measuring the photo-emission spectrum over the X-ray region of the electromagnetic spectrum. As the incident electrons probe several microns deep into the sample, the emission spectrum describes the properties of the material bulk. Similar to XPS, the bombardment invokes an ejection of core-shell electrons. However, in WDX analysis, we measure the energy of the X-ray photon released when a valence shell electron relaxes to the core. As the photo-emissions are characteristic of the difference in energy between the two electron shells and the atomic structure of the element from which they were emitted, an emission spectrum that is unique to each element is produced. What separates WDX analysis from EDX analysis is the photo-detection method. Where EDX measures all emitted photons using an energy dispersive spectrometer, WDX angles a single crystal diffraction grating to detect individual wavelengths in turn, yielding sharper and better separated peaks. In

comparing the peak areas of an element's emission against that of a calibrated standard, the weight concentration can be determined:

$$W_x = \frac{A_x}{A_s} \times \frac{[ZAF]_x}{[ZAF]_s} \times W_s \tag{2.13}$$

where *x* is the sample, *s* is the standard, *W* is the percentage weight, *A* is the peak area and [*ZAF*] corrects backscattering and electron retardation effects that depend on the atomic number (*Z*), photo-emitted re-absorption effects (*A*) and photo-emitted fluorescence effects (*F*).

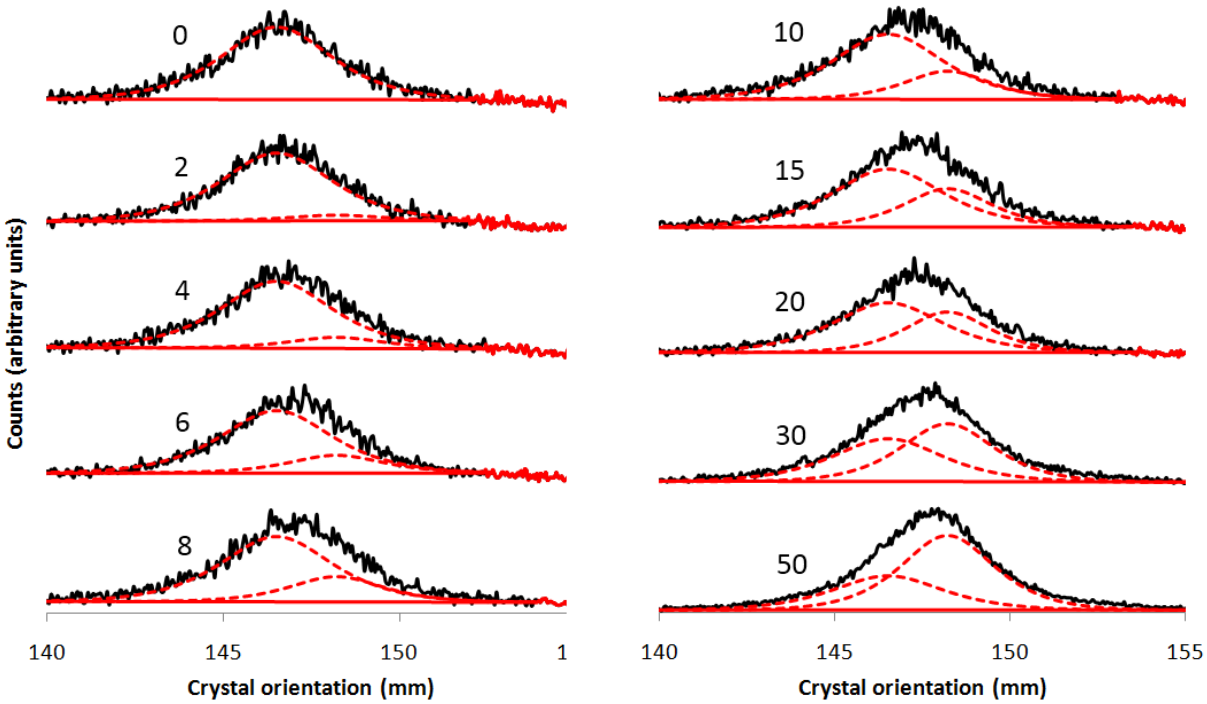

Figure 2.4.1: *A stacked plot of the separation of nitrogen K-lines (148.2 mm) from titanium L-lines (146.5 mm) through WDX analysis of a set of pre-formulated TiB_2 – TiN pellets ranging in N: Ti molar ratio from 0 – 50.*

A series of pre-formulated mixtures of TiB_2 and TiN powders were tested in order to verify if deconvoluting nitrogen K-lines from titanium L-lines was feasible. The powders were mixed to form N: Ti molar ratios of 0, 2, 4, 6, 8, 10, 15, 20, 30 and 50. They were ground and mixed under vortex numerous times to form smooth pastes, which were then pressed into pellets. The nitrogen K-line and titanium L-line energy region of all pellets were investigated using a Joel Superprobe JXA-8600 instrument by rotating a LDE1 crystal through 138 - 160 mm for 2 s per 5 µm interval. Pure Ti metal and BN pellets were used as calibration standards. By first modelling the peak shape and position of the titanium L-line from the titanium metal standard and the nitrogen K-line from the boron nitride

standard, the combined emission lines from the TiB_2 – TiN mixtures could then be deconvoluted (Figure 2.4.1).

The respective weight percentage nitrogen and titanium for each pellet, relative to the standards, was then determined using equation 2.13 and then converted into N: Ti molar ratios using:

$$N{:}\,Ti\ molar\ ratio = \left[\frac{W_N/m_{a_N}}{\left(W_N/m_{a_N} + W_{Ti}/m_{a_{Ti}}\right)}\right] \times 100 \qquad (2.14)$$

where m_a is the atomic mass. The derived molar ratios are listed in Table 2.1. Only slight differences between pre-formulated and calculated molar ratios were observed. This could be attributed to (i) an inhomogeneous mixing of the powders when making the TiB_2 – TiN pellets or (ii) errors in the deconvolution stage. Nevertheless, the deviations were nominal (σ = 0.5) legitimising the technique.

	N : Ti molar ratio									
Pre-formulated	0.0	2.0	4.0	6.0	8.0	10.0	15.0	20.0	30.0	50.0
Calculated	0.0	2.5	3.8	6.8	8.6	10.6	15.8	19.7	28.4	51.6
Difference	0.0	0.5	0.2	0.8	0.6	0.6	0.8	0.3	1.6	1.6

Table 2.1: *Table showing the difference in pre-formulated and calculated N: Ti molar ratios; determined by deconvoluting the nitrogen K-lines from titanium L-lines acquired through WDX analysis of a series of TiB_2 – TiN pellets.*

This method of deriving the bulk nitrogen concentration in co-titanium containing samples was subsequently applied in our combinatorial investigations of nitrogen-doped TiO_2. As sample analysis can be relatively fast (≈ 10 minutes), in addition to most WDX equipment coming fitted with a manoeuvrable stage, it is well suited for combinatorial analysis.

2.6. Photocatalytic activity mapping

Thin-films of TiO_2 have been shown to photocatalytically degrade a variety of organic pollutants,[1] bacteria,[11] viruses[12] and cancer cells;[13] however, when an accurate measure of the photocatalytic activity is warranted, the most popular method is the stearic acid test.[161] The method first involves coating a relatively thick layer (several microns) of stearic acid onto the semiconductor photocatalyst. This is normally achieved through spin[22] or dip-coating[11] a methanolic solution of stearic acid. After the solvent has evaporated a white and waxy stearic acid overlayer forms. The underlying photocatalyst is photo-irradiated with light ≥ bandgap that leads to the eventual

formation of radical species at the surface. These radical species continually oxidise any stearic acid in their vicinity leading to the eventual mineralisation of the organic material as summarised:

$$C_{17}H_{35}COOH + 26O_2 \rightarrow 18CO_2 + 18H_2O \quad (2.15)$$

The rate of this photocatalysis reaction can be measured in several ways. For instance, the rate can be indirectly measured by monitoring the level of carbon dioxide/ water generated through gas chromatography[162] or directly measured by monitoring the change in thickness of the stearic acid overlayer by ellipsometry.[163] However, monitoring the disappearance of the IR active C–H vibrations of stearic acid (3000 – 2800 cm^{-1}) is the preferred method in the literature, as the absorption area can be simply translated into the number of molecules present using a pre-determined conversion factor (9.7 x 10^{15} molecules ≡ 1 cm^{-1}).[161] The reaction kinetics are zero-order if the stearic acid coverage is greater than a monolayer.[164] This means that the rate of photocatalysis is independent of stearic acid loading (as long as it is sufficiently thick) so efforts do not have to be made to load specific quantities for fair testing. Although the photocatalytic activities attained from stearic acid testing are (i) accurate and (ii) highly reproducible, the rate of mineralisation is quite slow, involving the effective transfer of 104 e^- per molecule degraded.[165]

The measurement of the photocatalytic rate by monitoring the photocatalytic oxidation of aqueous organic dyes can be orders of magnitude faster than the stearic acid test. This is because it takes less electron transfers to destroy the bonds responsible for colouration. The most popular dye in the literature employed for this task is methylene blue.[166-168] Although the complete photocatalytic mineralisation of methylene blue is an 102 e^- process:

$$2C_{16}H_{18}N_3S^+ + 51O_2 \rightarrow 32CO_2 + 6HNO_3 + 2H_2SO_4 + 2H^+ + 12H_2O \quad (2.16)$$

the initial step in the photo-oxidation process is the cleavage of the R-S^+=R' functional group by a photo-generated hydroxyl radical.[169] A second oxidative attack on the sulfoxide produces an unstable sulfone that dissociates into two separate benezenic rings and causes a complete loss in solution colour; meaning the dye colour can be lost in as little as 2 e^- transfers. In measuring the decrease in the dye's absorption maximum (≈ 660 nm) the rate can be determined simply using the Beer-Lambert law:

$$A = \varepsilon \times [c] \times l \quad (2.17)$$

where ε is the extinction coefficient of the dye (*ca.* 7.3 x 10^5 dm^3 mol^{-1} cm^{-1} at 660 nm), [*c*] is the concentration of the dye in solution and *l* is the optical path length. The test is not without its detractors however. For instance, its aqueous photocatalytic degradation on TiO_2 thin-films shows

first-order kinetics, making comparisons difficult unless initial solution concentrations were equivalent. In addition, methylene blue solutions are susceptible to forming *leuco*-methylene blue, a colourless dimer, under anaerobic or slightly acidic conditions.[170] The intermediate is colourless but can revert to methylene blue when re-exposed to di-oxygen, increasing the absorbance at 660 nm and confusing rate calculations. Nevertheless, Mills *et. al.* found that by continuously stirring slightly basic methylene blue solutions in air, the formation of *leuco*-methylene blue was inhibited.[161] They also developed a simple and fast method for analysing thin-film samples. By replacing one face of a spectrophotometer cell with the semiconductor photocatalyst film, the photocatalysis reaction could be monitored *in situ*. Although being a useful method for simultaneously assessing a nominal number of films (≈ 10), the test is relatively labour intensive and realistically could not be applied to the simultaneous analysis of a much larger series (i.e. > 100).

Rather than assessing the photocatalysis of thin-films submerged in aqueous environments, dyes have been incorporated in inks to directly stain the surface of the semiconductor photocatalyst. The first such application involved the study of Acid Blue 9 dye in a PVA binder on TiO_2 thin-films by Doushita *et. al*.[171] However, the mineralisation kinetics was quite slow and comparable to the photo-oxidation of stearic acid. This problem was counteracted by Mills *et. al.* by placing redox indicators, such as resazurin[172,173] or di-chloroindophenol,[174] and a sacrificial electron donor (glycerol) within inks that functioned through a novel photo-reductive mechanism. The ink consisted of 4 mg of resazurin/ 5 mg of di-chloroindophenol redox indicator, 0.3 g of glycerol and 0.05 g of a hydroxyl-ethyl cellulose thickener dissolved in 3 ml of distilled water. When such an ink, deemed “intelligent ink”, is placed on a semiconductor photocatalyst and then photo-excited, the holes that migrate to the surface are scavenged by the sacrificial electron donor, inhibiting electron-hole recombination. The electrons that remain consequently reduce the redox dye, where the resazurin redox dye reaction proceeds through a two-step mechanism to reach its colourless intermediate:

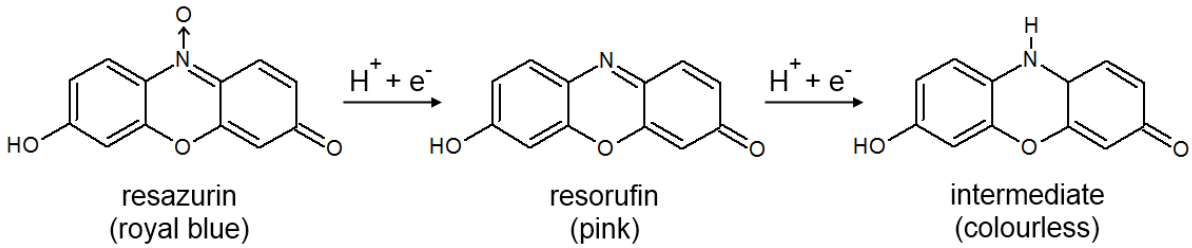

(2.18)

and the di-chloroindophenol redox dye proceeds directly to its colourless intermediate:

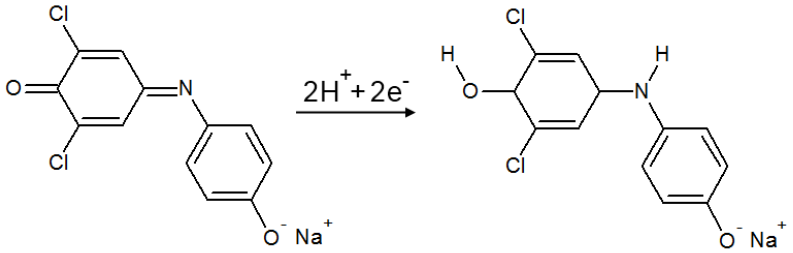

di-chloroindophenol (light blue) — intermediate (colourless)

(2.19)

The rate of the redox dye's colour change, induced by this forced photo-reductive mechanism, is on the second-minute time scale and typically orders of magnitude faster than dyes that are discoloured by a traditional photo-oxidative mechanism.[172] For instance, a layer of intelligent ink containing resazurin redox dye cast onto commercially available Activ™ self-cleaning glass, considered to have moderate photocatalytic activity due to its thin TiO_2 layer (≈ 15 nm thick),[164] was rapidly reduced upon UVA irradiation (365 nm, 7.2 $mW.cm^{-2}$) from royal blue to pink in just 3 minutes.[172] Although the overall reaction kinetics for these novel intelligent inks are first-order,[173] the initial rate of reaction is approximately independent of concentration and directly proportional to the rate of photo-oxidation of stearic acid,[175] one of the most accurate and reliable determinants of photocatalytic activity.

Since the photocatalytic reductions of intelligent inks invoke such marked colour changes, it was proposed by Mills *et. al.* that the naked eye is sufficient for a semi-quantitative assessment of rate.[175] We therefore decided to monitor the photo-reduction kinetics of both resazurin and di-chloroindophenol intelligent inks on Activ™ self-cleaning glass by UV-visible spectroscopy and digital photography (Epson Perfection 1200 Photo Scanner) in tandem. By eye, the resazurin containing ink turned from royal blue to pink after just 5 minutes irradiation, signifying the formation of resorufin (365 nm, 1.75 $mW.cm^{-2}$). Prolonged irradiation (≈ 50 mins) led to a colour change from pink to colourless, indicating a full conversion to its bleached intermediate. A stack of the UV-visible spectra for this photo-reduction reaction against a colour boundary background are shown in Figure 2.5.1(a), where the colour of each stack is the inks colour observed in digital photographs. A transition is observed from resazurin (0 min, royal blue, λ_{max} = 608 nm) to a spectrum more characteristic of resorufin (5 min, pink, λ_{max} = 584 nm) and was in agreement with what was seen by eye. This spectrum, more characteristic of resorufin, decreased in absorbance after subsequent irradiations, signifying the photo-reduction to its colourless intermediate (Equation 2.18). A systematic movement of the peak shoulder of resazurin from inside the red colour region to lower wavelengths occurred as

it was converted to resorufin. It was intuitive that the red component of RGB colour from the digital images recorded in tandem should also signify this transition. The absorption decrease at the red boundary (630 nm) was subsequently plotted with the red component of RGB colour against time, shown in Figure 2.5.1(b).

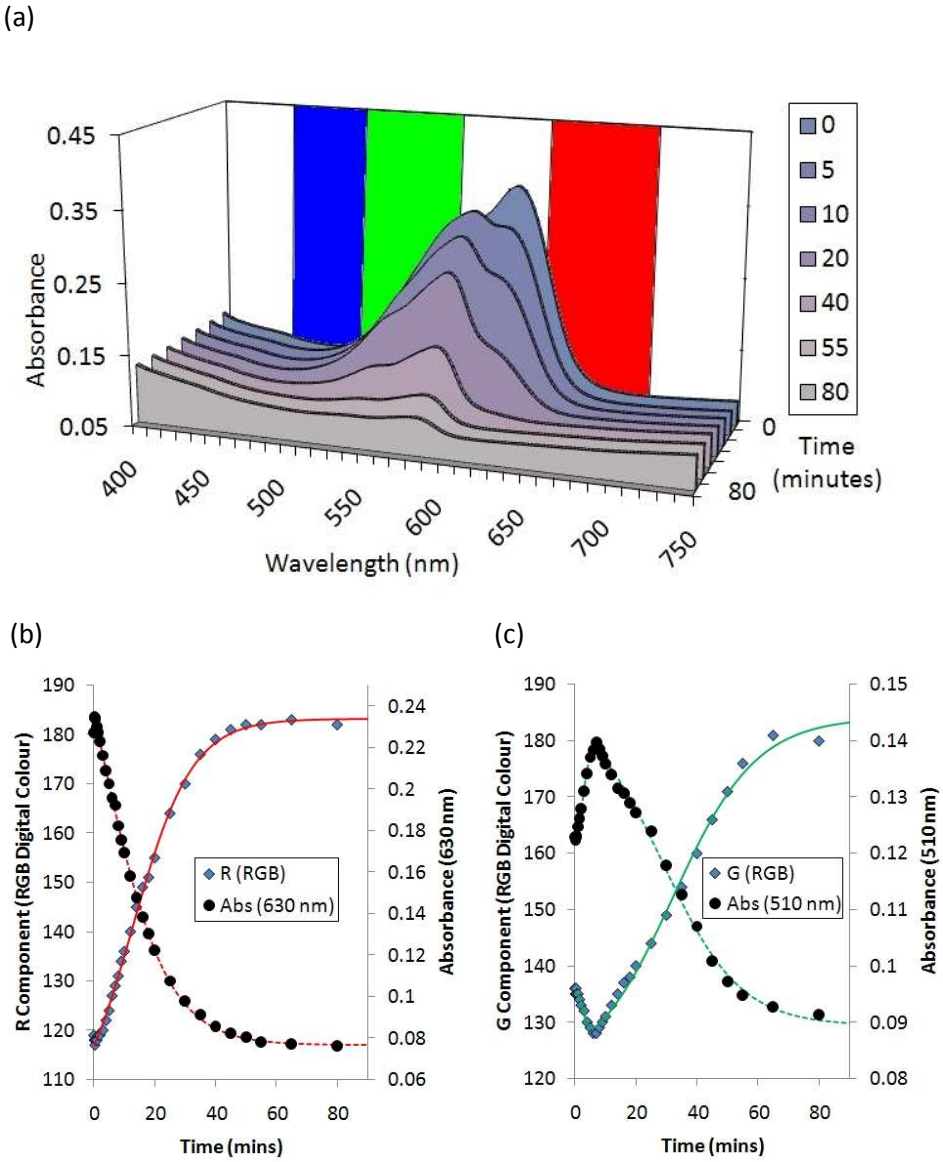

Figure 2.5.1. *(a) Stacked UV–visible absorption spectra against a colour boundary background following the photo-reduction (365 nm, 1.75 mW.cm^{-2}) of a resazurin intelligent ink on Activ^{TM} self-cleaning glass. (b) The absorbance at 630 nm was plotted with the red component of RGB colour and (b) the absorbance at 510 nm was plotted with the green component of RGB colour from digital images recorded in tandem, fitting Boltzmann and Biphasic models respectively ($r^2 \geq 0.99$).*

The relationship was inversely proportional as digital scanners measure the amount of light that can transmit through a material against a white background whereas the UV-visible spectrum was measured in absorbance. Intriguingly, the time at which the absorbance at 630 nm plateaued, signifying the complete photo-reduction of resazurin, occurred at an almost analogous time for

which the red component of digital colour plateaued. Looking at the UV-visible spectral stack we can see how the absorbance near the green increases from t = 0 mins to t = 5 mins, and then decreases from t = 5 mins to t = 80 mins. In plotting the absorbance at the green boundary (510 nm) with the green component of RGB colour from the digital images recorded in tandem against time, an inversely proportional relationship is again observed (Figure 2.5.1(c)). The point at which the absorbance at 510 nm maximises, signifying the time at which the maximum concentration of resorufin is formed, was again analogous to the point at which the green component of digital colour minimised. In addition, the absorbance at 510 nm and green component of digital colour plateaued at almost the same time and signified the complete photo-reduction of resorufin. This demonstrated how the reaction kinetics for the photo-reduction of resazurin intelligent ink could simply be followed using digital photography, summarised by:

$$t(R_{\text{plateau}}, RGB) \equiv t([resazurin] = 0) \tag{2.20}$$

$$t(G_{\text{minimum}}, RGB) \equiv t([resorufin] = max) \tag{2.21a}$$

$$t(G_{\text{plateau}}, RGB) \equiv t([resorufin] = 0) \tag{2.21b}$$

where *t* is time. For the intelligent ink containing di-chloroindophenol, a more rapid colour change from pale blue to colourless was observed by eye after ≈ 35 minutes irradiation (365 nm, 1.75 mW.cm^{-2}). A stack of the UV-visible spectra for this photo-reduction reaction against a colour boundary background are shown in Figure 2.5.2(a).

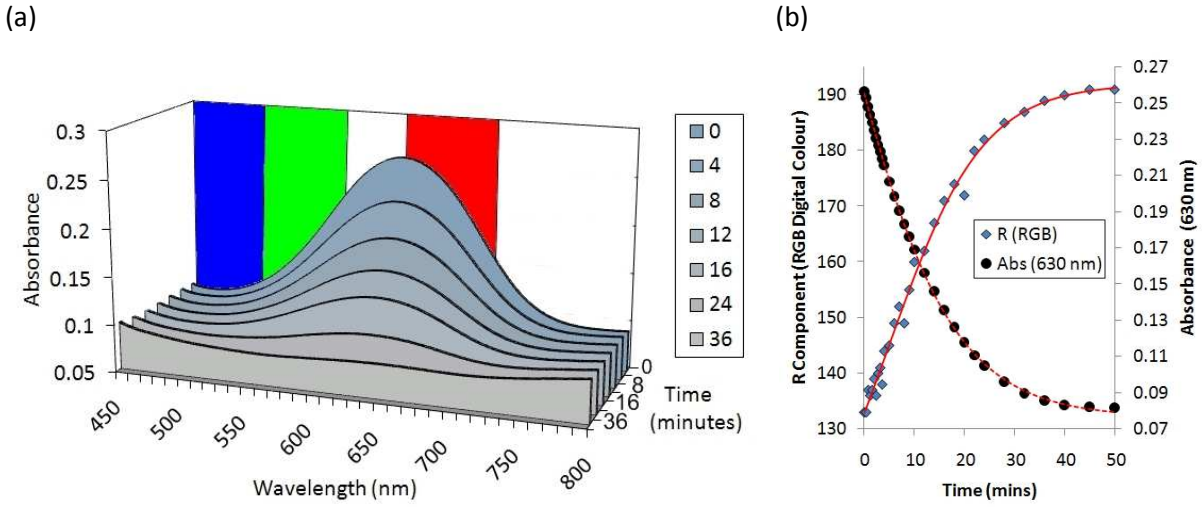

Figure 2.5.2. *(a) Stacked UV–visible absorption spectra against a colour boundary background following the photo-reduction (365 nm, 1.75 mW.cm^{-2}) of a di-chloroindophenol intelligent ink on Activ™ self-cleaning glass. (b) The absorbance at 630 nm plotted with the red component of RGB colour from digital images recorded in tandem and fit Boltzmann models ($r^2 \geq 0.99$).*

A systematic decrease in the absorbance maximum (0 min, blue, λ_{max} = 632 nm) that bordered the red colour boundary was observed. The UV-visible absorbance at 630 nm, representing the red region of the spectrum, was plotted with the respective red component of RGB colour from the digital images recorded in tandem against time (Figure 2.5.2(b)). Once again, an inversely proportional relationship, similar to that of the resazurin photo-reduction reaction, was observed. The time at which the absorbance maximum plateaued was again analogous to the time at which the red component of digital RGB colour plateaued, meaning the photo-reduction of di-chloroindophenol intelligent ink could also be followed by digital photography, where:

$$t(R_{\text{plateau}}, RGB) \equiv t([dichloroindophenol] = 0) \tag{2.22}$$

Since it was now established that the photo-reduction kinetics of both resazurin and di-chloroindophenol intelligent inks on a semiconductor photocatalyst thin-film could be monitored by digital photography, we now needed methods for:

(i) depositing the intelligent ink evenly over a large number of unique positions,
(ii) photographing the large combinatorial samples with high consistency,
(iii) software that could rapidly extract the RGB colour data for each unique position in these digital photographs and
(iv) software that could fit changes in the red component of digital colour to a Boltzmann model and changes in green component of digital colour to a Biphasic model in an automated fashion

in order to simultaneously and rapidly assess the photocatalytic activity across combinatorial arrays.

From changes in the RGB colour of digital images we could either find the time at which the redox dye had reacted to completion (Equations 2.20, 2.21b and 2.22) or more specific to resazurin, the time at which the maximum concentration of the resorufin intermediate was formed (Equation 2.21a). The magnitude of change in RGB colour could not simply be related to the rate of reaction nor the original concentration of the intelligent ink layer deposited, as this was sample independent. This negated the benefit of the initially zero-order reaction kinetics these intelligent inks display. For instance, if a red tinged thin-film sample was tested, the magnitude of change in the red component of digital colour would be masked compared to that of a transparent sample. However, if the red component of digital colour plateaued at the same time for both samples of equal intelligent ink loadings, then the rate of photocatalysis was equivalent. As the concentration of the intelligent ink layer could not be determined from digital images alone, we needed a method for casting equivalent loadings of intelligent ink on top of large numbers of unique positions, thus allowing the end-point of each photocatalysis reaction to be compared fairly.

Intelligent ink has been cast in a number of ways, including spin-coating, dip-coating, sandwich spreading between the film and a watch glass or even drawn using a felt-tipped pen.[161] Although dip-coating seemed like a promising method for coating our combinatorial thin-films the technique failed. This was because the ink beaded on the surface rather than forming a smooth ink layer upon extraction. Our samples were also too large to have even intelligent ink layers spread over the surface by spin-coating. Sandwiching large numbers of unique positions with intelligent ink droplets and watch glasses was not time-effective either. However, intelligent ink could be applied from a felt-tipped pen to a large number of positions relatively quickly. This was achieved by drawing grids with a ruler and applying an even pressure throughout. The number of analysable positions was limited to the number of crossings on the grid where:

$$lines\ in\ x\ direction \times lines\ in\ y\ direction = number\ of\ crossings \qquad (2.23)$$

For instance, if a 7 by 8 grid was drawn, there would be 56 points of crossing. An example of this is for a resazurin intelligent ink is shown in Figure 2.5.3(a).

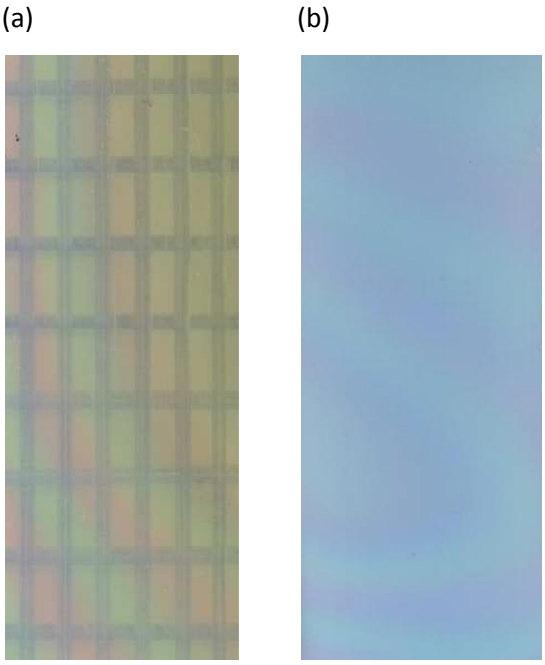

Figure 2.5.3: *Examples of resazurin intelligent ink coated combinatorial TiO_2-based thin-films either (a) drawn by hand using a felt-tipped pen or (b) deposited using an aerosol spray gun.*

By eye it can be seen that the drawn intelligent ink grid was evenly thick and spaced. However, this involved prior practice and high levels of concentration to apply an even force when stroking the pen along a steadily held ruler. The technique held too much room for human error, where any slip of the hand could smudge the grid. It was also difficult to ensure the crossings on the grid overlaid the unique positions one wished to characterise.

Although the technique was applied in two of our combinatorial investigations (Chapters 3.1 and 3.2), it was a little laborious, so we investigated other ways of depositing even layers of intelligent ink. The most reliable and simplest way we found involved depositing the ink layer using an aerosol-spray gun (SIP Emerald Spray Gun/ Halfords Plc). An optimal balance between aerosol generation and reduced surface spatter was found at an air-pressure feed of 3.5 bar and sample to spray-head distance of ≈ 15 cm. Combinatorial films were first wall-mounted before being coated in stages; spraying vertically from top to bottom in each action for each shift, in short even steps, across the surface from left to right. The process was repeated several times until a pale coating of the intelligent ink was discernable, where an example spray-coating of a resazurin intelligent ink onto a combinatorial film is shown in Figure 2.5.3(b). The evenness of the ink layer from such spray depositions was assessed by UV-visible spectroscopy for a plain float glass example (the material used as our substrate in all our syntheses). The piece of glass (10 × 10 x 0.32 cm; length × breadth × thickness) was coated using the aerosol-spray method with a di-chloroindophenol intelligent ink layer. The level of maximum absorbance (di-chloroindophenol, λ_{max} = 632 nm) was assessed for 25 unique locations spaced equally apart over the ink-coated glass (Figure 2.5.4).

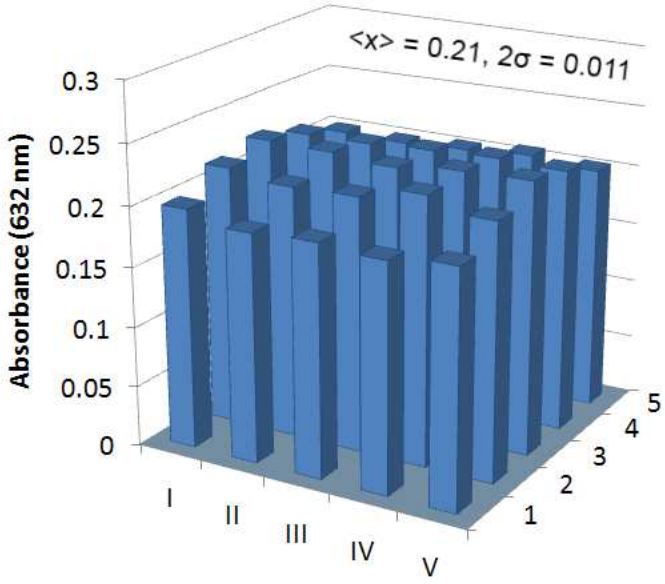

Figure 2.5.4: *The absorbance maximum (632 nm) of an aerosol-spray coated di-chloroindophenol intelligent ink layer for 25 unique and equally spaced positions over the 10 x 10 cm float glass substrate; the average absorbance <x> was 0.21 with two standard deviations σ of 0.011.*

An average absorbance of 0.21 was observed with two standard deviations of 0.011. This roughly equated to a 5 % deviance (with > 95 % confidence) and demonstrated the high degree of smoothness in which the intelligent ink layer could be deposited. The aerosol-spray method was far from perfect and required good user practice to ensure samples were coated evenly. This problem may have been avoided if a robotic arm was used instead. However, implementing such apparatus

would certainly take away the cost-effectiveness and accessibility of the assessment technique, which required no expensive analytical equipment.

By employing a flat-bed digital scanner, photographing the large combinatorial samples with consistency was simple. However, extracting the RGB values from these images was painstakingly slow when performed manually. Some software was developed in house using Visual Basic 6.0 software,[176] which we entitled RGB Extractor[(c)]. The program allowed the user to create a grid of boxes of any size in the x and y directions. These square boxes represented the positions at which the RGB colour would be extracted on the image of the film. The size of each box could be altered to include a greater number of pixels. When the operation was permitted by the user, the RGB values within each box were averaged and an output file was generated containing the colour data of all allotted grid squares. The program allowed a series of images to be uploaded together in which any operation made in the first image would be applied to the series. Quite simply, once the positions were allocated by the user and the number and size of grid squares defined, the colour data for even thousands of positions could be simultaneously extracted in just a few seconds per digital image.

The kinetics of the photo-reduction reaction could be subtly followed by finding the times at which the red and green components of RGB colour plateaued and minimised. Changes in the red component of digital colour for both resazurin and di-chloroindophenol intelligent ink photo-reduction reactions fit a Boltzmann model. Changes in the green component of digital colour for resazurin intelligent ink photo-reduction reactions fit a Biphasic model. The mathematical characteristics of each model are shown in Table 2.2. By computationally fitting the colour data to an appropriate model, these times could be found with consistency and precision. Origin 8.0 software[177] was capable of doing this in a semi-automated fashion. The colour data of up to ≈ 20 unique positions could be uploaded at a time and simultaneously fitted to their respective model in ≈ 30 seconds. Using a computer cluster would certainly have increased the speed at which this colour data could be modelled but was not implemented in our studies.

The advantages of analysing digital images over spectroscopic methods are two-fold: (a) no expensive analytical equipment or technician is required and (b) a picture of the entire film is taken whereby the photocatalytic activity of any number of positions, limited only by the number of pixels in the image, could be intra-comparatively assessed. Indeed, in two of our combinatorial studies (Chapters 4 and 5) where the photocatalytic activity was photographically assessed, the thickness of the aerosol-spray deposited resazurin intelligent ink layer was also determined. This meant that the time it took the resazurin redox dye to be completely photo-degraded (i.e. times of plateau in red component of RGB colour) could be converted into inter-comparable photocatalytic rates.

	Equation	Depiction
Boltzmann	$R_{component}, RGB = \frac{A_2 - A_1}{1 + e^{(t-t_0)/dt}} + A_2$ $A_1 = minimum\ value\ of\ R_{component}$ $A_2 = maximum\ value\ of\ R_{component}$ $t_0 = value\ of\ "t"\ at\ the\ curve's\ centre$ $dt = time\ constraint$ $t = time$	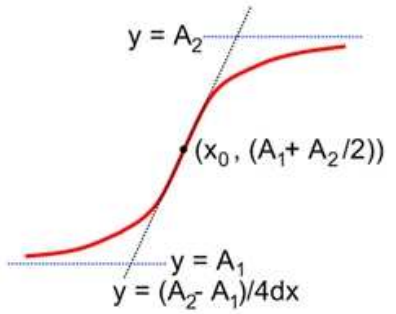
Biphasic	$G_{component}, RGB = A_{min} + \frac{(A_{max1} - A_{\min})}{(1+10^{((t-t_1)h_1)})} + \frac{(A_{max2} - A_{\min})}{(1+10^{((t-t_2)h_2)})}$ $A_{min} = minimum\ value\ of\ G_{component}$ $A_{max1} = initial\ G_{component}\ maximum\ asymptote$ $A_{max2} = final\ G_{component}\ maximum\ asymptote$ $t_1, t_2 = first, second\ top\ medians$ $h_1, h = primary, secondary\ slope$	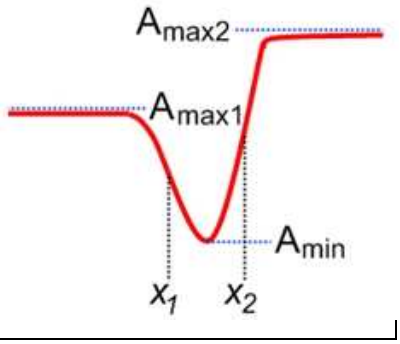

Table 2.2: *Table showing the mathematical characteristics of the Boltzmann and Biphasic models in which the changes in RGB colour from digital images following the photo-reduction reaction of intelligent inks were fit.*

This was not the first case in which digital photography was applied in screening the functional properties of combinatorial thin-films, which was first demonstrated by Danielson *et. al.* in their combinatorial study of phosphors.[53] By photo-exciting the library altogether, a photograph of the ensuing luminescence was taken and compared against pre-calibrated industrial standards (Figure 1.2.1). Digital photography was also used by Gremaud *et. al.* in assessing the hydrogen storage capacity of combinatorial libraries, exploiting the fact that the transmittance properties of a thin-film material alters upon hydrogen absorption and desorption.[65] However, our use of digital photography in assessing the rate of photocatalysis of combinatorial thin-films is to the best of our knowledge the first of its kind. Although, Zhou *et. al.* did apply digital photography to assess the rate of photocatalysis of mesoporous powders.[178-180] By immersing TiO_2-WO_3-Nb_2O_5 composite libraries in aqueous fluorescamine derivative solutions, the photocatalysis that ensued upon photo-excitation caused a decrease in fluorescence, which was photographically assessed. The photocatalytic activities over a combinatorially graded thin-film have also been indirectly assessed by Koinuma *et. al.* in their study of Sr-V-Cr-Ti oxides.[181] In submerging the combinatorial film in an aqueous solution of $AgNO_3$ salt, photo-irradiation induced the photo-assisted deposition of Ag on the film's surface. The level of Ag deposited was quickly assessed through energy dispersive X-ray area analysis, where the areas of highest silver loading corresponded to the areas of greatest photo-reduction; a good indicator of photocatalytic activity. However, such a method of photocatalytic screening was not used in our combinatorial studies for the simple reason that samples become permanently modified,

with silver islands bound chemically to the material's surface. Our method wanted to focus on testing combinatorial thin-film libraries from the outset, so that regions of high activity can be identified and later characterised; possibly leading to photocatalytic materials discovery.[182] We believe the method we present is a better solution for screening the photocatalysis of a number of homogenous materials simultaneously or numerous positions across a single film. This can be extremely useful in assessing the homogeneity of a film or in determining the best combination of elements in a catalytic array.

With the screening methods discussed in this chapter, developed specifically for rapidly assessing large numbers of diverse states, we were now able to characterise our combinatorial thin-film systems. Using a combinatorial APCVD synthesis, nitrogen (Chapter 3), niobium (Section 4.3) and tungsten (Section 4.4) doped TiO_2 thin-film systems were investigated. We will demonstrate how large numbers of unique states across each combinatorial system can be characterised and their physical-functional properties inter-related, demonstrating a rapid method for the functional property optimisation of composition/ phase space.

3. Nitrogen doped titania

3.1. Introduction

The combination of photo-induced surface wetting and superior photocatalytic properties has made TiO_2 thin-films the most suited candidates for self-cleaning coatings.[9] Although a range of products extending the use of anatase TiO_2 (bandgap ≈ 3.2 eV) in water and air purification systems, sanitary-ware and deodorizing products have been commercially introduced,[183] their use is limited to environments where sufficient UV-light is available for them to function. Although the thermodynamic rutile phase of TiO_2 has a lower associated bandgap energy (3.0 eV),[184] commercial TiO_2 products have predominantly featured the anatase phase. It has been a matter of considerable debate as to whether phase pure anatase TiO_2, rutile TiO_2 or composite mixtures provide a more effective photocatalyst.[1] For instance, many argue that a synergistic photocatalytic effect exists in anatase-rutile TiO_2 composites,[185] such as in commercially available Degussa P25 powder composed of anatase and rutile in roughly a 3: 1 ratio.[186] However, it has yet to be conclusively proven that the pronounced photocatalysis observed in cases such as Degussa P25 powder is due to a synergistic effect and has otherwise been attributed to differences in surface areas and powder crystallinity.[187] Through a combinatorial APCVD process, Hyett *et. al.* recently demonstrated how a range of anatase and rutile TiO_2 composite mixtures ($0 \leq$ anatase ≤ 100 %, $0 \leq$ rutile ≤ 80 %) could be deposited within a single thin-film.[110] Monitoring the rate of stearic acid degradation under a UVC source (254 nm) indicated the pure anatase TiO_2 region was a more effective photocatalyst than any of the composite regions tested. However, the photocatalytic activities of only 5 positions were tested and any possible changes in film-thickness and crystallinity were not accounted for. Through our combinatorial APCVD approach to investigating nitrogen doped titania, we will encounter a range of anatase TiO_2 -rutile TiO_2 composites ($0 \leq$ anatase ≤ 100 %, $0 \leq$ rutile ≤ 41 % - Section 3.3). By applying our photocatalytic activity mapping method as well as other screening methods for characterising large numbers of unique states we will shed some light on the legitimacy of the proposed synergistic effect. In addition, through our unique application of combinatorial APCVD, we formed the full spread of composites of the newly discovered material pseudo-brookite $Ti_{3-\delta}O_4N$[112] and anatase TiO_2 ($0 \leq$ anatase ≤ 100 %, $0 \leq$ pseudo-brookite ≤ 100 %) and investigated the possibility of a synergistic effect in this system as well (Section 3.2).

As a more significant portion of sunlight is contained in the visible region of the electromagnetic spectrum compared with UV-light,[188] it has become an important goal for many research groups to develop red-shifted TiO_2 materials in an effort to enhance their capacity to perform solar photocatalysis. As such, there have been a large number of studies aimed at modifying TiO_2, primarily

though doping and composite formation.[189-193] The inclusion of dopants can alter the band structure of TiO_2 and narrow the bandgap to more visible wavelengths whereas composites of TiO_2 coupled with lower energy bandgap semiconductors can increase the separation of photo-generated electrons and holes, decreasing the likelihood of recombination as well as increasing quantum efficiency. No dopant within TiO_2 has been investigated more so than nitrogen, however there is little consensus on which type of insertion, be it interstitial (N atoms insert between Ti-O bridges – N_i) or substitutional (N atoms replace O sites – N_s), yields the more effective visible light photocatalyst.[113-118] In contrast to this, some groups have suggested that it is the indirect formation of oxygen vacancies (V_O) upon nitrogen doping TiO_2 that is fundamental to the pronounced visible light activity.[194] However, nitrogen doping has been experimentally shown to introduce lower energy sites for electron-hole recombination processes to occur.[117] Therefore a trade-off exists in N-doped TiO_2 between the positive effect of bandgap narrowing and the detrimental effect of recombination, leading research groups to seek the optimum balance. Through our combinatorial APCVD approach we synthesised both a N_s-doped TiO_2 system ($0 \leq N_s$: Ti ≤ 11 % - Section 3.3) and mixed N_s/ N_i -doped anatase TiO_2 system ($0 \leq N_s$: Ti ≤ 11 %, $1.0 \leq N_i$: Ti ≤ 4.3 % - Section 3.4) and rationalised the variations in photocatalytic activity with our screening methods.

Using a combinatorial APCVD approach, we will explore the chemistry of either NH_3 (Section 3.3 & 3.4) or t-butylamine (Section 3.2) as sources for nitrogen doping TiO_2 thin-films formed from $TiCl_4$ and ethyl acetate precursors. The details on how each experiment was conducted are described in the following section.

3.2. Experimental methods

All chemicals were purchased from Sigma-Aldrich Chemical Co; dichloroindophenol 98.0%, resazurin 92%, hydroxyethyl cellulose (HEC) [average $M_v \approx 90{,}000$], glycerol 99.5%, stearic acid 99%, methylene blue powder (99%), isopropanol 99.98%, acetone 99%, anatase powder 99.8%, rutile powder 99.8%, titanium nitride powder (99.9%), titanium diboride powder (99.9%), ethyl acetate (MeCOOEt) 99%, t-butylamine (Me_3CNH_2) 99% and titanium chloride ($TiCl_4$) 99.9%. Di-nitrogen and ammonia (NH_3) gas cylinders were supplied by BOC. The glass blank, consisting of a piece of standard 3.2 mm thick float glass coated with a 50 nm SiO_2 barrier layer was supplied by the Pilkington NSG Group. The stainless steel substrate (austenic grade 304L - 225 x 90 x 0.7 mm; length × breadth × thickness) was supplied by Corus.

3.2.1. Physical characterisation

Phase mapping was conducted using a Renishaw 1000 Raman spectrometer using either a green (532 nm) or red (633 nm) laser. Samples were analysed over the 100 - 1200 cm^{-1} energy range. The phase composition at each position analysed could then be determined in accordance with our deconvolution method described in Section 2.2. X-ray diffraction mapping was carried out using a micro-focus Bruker GADDS powder X-ray diffractometer, with a monochromated Cu K_α (1.5406 Å) source and a CCD area X-ray detector, capable of 0.01° resolution in 2θ with an automated X–Y movable stage. The degree of preferred orientation was assessed using our preferred orientation mapping method described in Section 2.3. The wavelength where a transmittance maxima occurs is analogous to where a reflectance minima occurs (Figure 2.3.2(a)), therefore reflectance spectra recorded over the 300 - 2500 nm range on a Helios double beam instrument (standardised relative to a rhodium mirror) allowed the thickness to be determined at any allotted grid position in accordance with our thickness-mapping method described in Section 2.4. The level of nitrogen doping was investigated by wavelength dispersive X-ray (WDX) analysis on a Joel Superprobe JXA- 8600. The overlapping N K-lines and Ti L-lines were acquired by reflecting an X-ray beam over an LDE1 crystal rotated through 138–160 mm. The circular beam was focussed over a 10 µm diameter analysis area. Each sample was analysed for 2 seconds per 5 µm rotation of the crystal. The problem of N K-line and Ti L-line overlap was solved by deconvoluting models relative to BN and Ti metal standards using CASA software[131] and allowed the nitrogen/ titanium concentration to be mapped (Section 2.5). X-ray photoelectron spectroscopy (XPS) was performed at Cardiff University using a Kratos Axis Ultra - DLD photoelectron spectrometer with monochromatic Al K_α radiation. Survey scans of the binding energy were collected from 0 – 1100 eV at a pass energy of 160 eV. Higher resolution scans encompassing the principal peaks of Ti (2p), O (1s), N (1s), C (1s) and Si (2p) were collected at a pass energy of 40 eV. For compositional depth profiling, an Ar-ion gun was used to etch away the surface layers of samples for a sputtering time of 30s per etch. The peaks of each contributing oxidation state were modelled using CasaXPS.[131] The peak positions were adjusted to adventitious graphite present at the surface (284.5 eV) and peak areas were converted using appropriate sensitivity factors[157] to determine the concentration of each state. Transmittance spectra were recorded over the 300 - 2500 nm range on a Helios double beam instrument to determine bandgap energies through Tauc plots.[195] The surface topography was investigated by atomic force microscopy (AFM) using a Veeco Dimension 3100 in air with a contact operating mode and a silicon tipped cantilever for 1 x 1 µm sample areas. Scanning electron microscopy (SEM) was used to investigate the surface topography and to directly measure film-thickness. Gold-sputtered cuts were mounted side-on for determining the thickness

and top-down for investigating the topography on a JOEL-6301F field emission instrument with secondary electron imaging.

3.2.2. Photocatalysis

3.2.2.1. Intelligent ink

Intelligent ink was used to map the photocatalytic activity for a large number of positions simultaneously across a combinatorial thin-film. The method by which the relative rates of photocatalysis were determined is described in Section 2.6. The combinatorial film was first washed with distilled water, rinsed with isopropanol and then placed under UVC irradiation (254 nm, 2 x 8W - Vilber Lourmat VL-208G) for 1 hr to ensure the surface was free from contaminants. Either an intelligent ink grid was drawn using a felt-tipped pen using a ruler and even pressure throughout or an even layer was applied using an aerosol-spray gun (SIP Emerald Spray Gun/Halfords Plc) at an air-pressure feed of 3.5 bar. The ink consisted of either the di-chloroindophenol (5 mg) or resazurin (4 mg) redox dye in an aqueous solution (3 ml) with glycerol (0.3 g) and hydroxyl-ethyl cellulose (0.05 g). The photocatalysis reaction was conducted using UVA irradiation (365 nm, 2 x 8W - Vilber Lourmat VL-208BL) and monitored solely by digital photography (Epson Perfection 1200 Photo Scanner) at intervals. For each digital image acquired, the red-green-blue components of digital colour were extracted at each position on the grid, specified in each study. The time it took for the red component of digital colour to plateau for each location analysed was determined by fitting the colour data to a Boltzmann model. This time represented the complete photo-reduction of the original redox dye, be it di-chloroindophenol (Equation 2.22) or resazurin (Equation 2.20). In studies involving resazurin intelligent ink, the time it took for the green component of digital colour to minimise for each location analysed could also determined by fitting the colour data to a bi-phasic model. This represented the time at which a maximum concentration of resorufin, the pink coloured intermediate of resazurin, was formed (Equation 2.21(a)).

3.2.2.2. Methylene blue

The photocatalytic oxidation and discolouring of methylene blue (MB) was assessed using UV-visible spectroscopy over the 400 – 800 nm range on a PerkinElmer Lambda 25 UV/VIS spectrometer. Samples were affixed to a custom-made measurement cell that consisted of a plastic cuvette transparent on three sides and holed on the fourth. The hole, centred on the test position, was 25 mm high and 8 mm wide; exposing a 2 cm^2 area to the MB solution. An aluminium frame held the sample and the cuvette together with a silicon seal providing a water tight boundary. A stirrer bead was used to ensure uniform dispersion and aeration of the system. This resulted in a reservoir of MB

solution in contact with the photocatalyst surface. The concentration of MB solution was made up such that the maximum absorbance (≈ 660 nm) was approximately 1 absorption unit ([MB] ≈ 14 μM). Any surface-dye absorption was first allowed to reach equilibrium in the dark for 1 hr before beginning the photocatalysis reaction, where a 1-2 % drop in the absorbance was typically observed. The photocatalysis reaction was conducted using UVA irradiation that was shone through the solution onto the semiconductor photocatalyst exposed at the back of the holed cuvette. The destruction of MB was then followed as a function of time by the change in height of the dye's absorbance maximum in 30 minute intervals for a total of 6 hrs UVA irradiation.

3.2.2.3. Stearic acid

The photocatalytic oxidation of a stearic acid overlayer was investigated using Fourier transform infrared (FTIR) spectroscopy over the 2980-2800 cm^{-1} range on a Perkin Elmer RX-I instrument. Samples were affixed to measurement cells centred on the test position; exposing a 1 cm^2 area. The films were washed with propan-2-ol and then placed under UVC irradiation for 1 hr to ensure the surface was free from contaminants. Samples were coated with a waxy stearic acid over-layer (0.02 M solution in methanol) by depositing a few solution droplets onto the film's surface. After spinning the samples at 1000 rpm for 10 s, the samples were oven dried for 1 hr at 50 °C to ensure the complete evaporation of the methanol solvent. The samples were then irradiated under a white light source (GE lighting 2D fluorescent GR10q- 835 white, 28W [15,000 lux]) masked with a UV filter (Optivex^{TM}). The decrease in absorbance of C-H symmetric/anti-symmetric stretches in the infra-red region investigated signified the photocatalytic oxidation of the stearic acid overlayer. The absorbance area could be related to the concentration of the stearic acid overlayer by a conversion factor (9.7 x 10^{15} molecules ≡ 1 cm^{-1}).[161] The change in absorbance area, and thus a decrease in the number of stearic acid molecules, was followed as a function of time for 50 hrs white light irradiation.

3.3. Pseudo-brookite $Ti_{3-\delta}O_4N$ and N_i-doped anatase TiO_2 composite mixtures

3.3.1. Introduction

Pseudo-brookite $Ti_{3-\delta}O_4N$ ($0.06 \leq \delta \leq 0.25$) was recently discovered by Hyett *et. al.* though a combinatorial APCVD exploration of nitrogen doped TiO_2 phase space.[112] In combining $TiCl_4$, ethyl acetate and NH_3 precursor vapours through separated points over a glass substrate heated to 630 °C, a thin-film with a green-brown colour gradient was formed. The entire film was composed of the new

pseudo-brookite $Ti_{3-\delta}O_4N$ phase, where the differences in colour were due to slightly varying anion/metal ratios of 1.70 within the brown section and 1.78 within the green. The photocatalytic activity of the green and brown sections in this film were tested against thin-films of anatase-rutile TiO_2 composites also formed at 630 °C by APCVD to the photo-oxidation of a stearic acid overlayer under UVC (254 nm) light.[196] The activity of the pure pseudo-brookite $Ti_{3-\delta}O_4N$ ($0.06 \leq \delta \leq 0.25$) material was found to be significantly greater than the anatase-rutile TiO_2 composites tested; however, only two unique composite concentrations were assessed (85: 15 and 45: 55 anatase TiO_2: rutile TiO_2). The possibility of a synergistic effect on the photocatalytic activity between anatase-rutile TiO_2 composites is well documented in the literature.[185] Taking Hyett *et. al.*'s recent findings into account, there may be potential for a greater synergistic effect between composites of pseudo-brookite $Ti_{3-\delta}O_4N$ and anatase/ rutile based TiO_2.

Thin-films of interstitial nitrogen (N_i) doped TiO_2 have been previously synthesised by Dunnill *et. al.* by combining $TiCl_4$, ethyl acetate and t-butylamine (Me_3CNH_2) precursors on glass at 500 °C.[30] The films were shown to be strong photocatalysts in the photo-oxidation of stearic acid under a visible light source. The N_i-type doping was encouraged by reacting low concentrations of the nitrogen source relative to the Ti source (≈ 0.2: 1, N: Ti ratio). When higher concentrations of the nitrogen source were introduced (> 0.5: 1, N: Ti ratio) a mixed interstitial and substitutional (N_s) nitrogen doped material was formed that showed slightly hampered visible light photocatalysis. This was still considerably lower than the N: Ti source concentrations used by Hyett *et. al.* in forming pseudo-brookite $Ti_{3-\delta}O_4N$ (≈ 1.5: 1 ratio).[112]

Dunnill *et. al.* used the t-butylamine precursor over NH_3 as a nitrogen source as it encouraged N_i-doping in TiO_2 below a threshold concentration.[30] This was also explained by the reaction chemistry of the compound, where it was proposed that a thermal decomposition to NH_3 first takes place before nitrogen insertion can occur:

$$Me_3CNH_2 \rightarrow CH_2 = C(Me)_2 + NH_3 \quad (3.1)$$

This decomposition barrier hindered nitrogen insertion compared with the reaction of pure NH_3 in Hyett *et. al.*'s study, with approximately one in thirty t-butylamine molecules leading to a single nitrogen insertion compared with one in five for NH_3.

Given the decomposition of t-butylamine yields NH_3, one should consider the possibility of forming pseudo-brookite $Ti_{3-\delta}O_4N$ if the reaction was exposed to high enough levels of t-butylamine at the required temperature of 630 °C. We therefore investigated this reaction from a combinatorial perspective in aid of forming pseudo-brookite $Ti_{3-\delta}O_4N$ and TiO_2 composites that had not previously

been synthesised. In this section we describe the combinatorial APCVD synthesis of such a film with the full range of composite concentrations from pure orthorhombic pseudo-brookite $Ti_{3-\delta}O_4N$ at one end to pure tetragonal N_i-doped TiO_2 at the other. This was formed using a triple source of precursors; with $TiCl_4$ as the titanium source, ethyl acetate as the oxygen source and t-butylamine as the nitrogen source. The phase composite variation of 42 unique positions across the film was quantified using our phase mapping method described in Section 2.2. The thickness at each of these 42 unique positions was also determined using our film-thickness mapping method described in Section 2.4. X-ray photoelectron spectroscopy (XPS) confirmed the transition from N_s-type insertion at the pure pseudo-brookite $Ti_{3-\delta}O_4N$ end to N_i-type insertion at the pure N_i-doped TiO_2 end. The possibility of a synergistic effect on photocatalysis was then investigated by applying our photocatalytic activity mapping method described in Section 2.6.

3.3.2. Experimental combinatorial film synthesis

A combinatorial thin-film with the full range of smoothly graded composite concentrations from pure pseudo-brookite $Ti_{3-\delta}O_4N$ at one end to pure N_i-doped anatase TiO_2 at the other was formed by combinatorial APCVD. The combinatorial film was formed on float glass (90 × 225 × 3.2 mm; length × breadth × thickness) that contained an ≈ 50 nm thick barrier layer of SiO_2 at the substrate's surface to inhibit the diffusion of ions from the glass into the film. A schematic of the apparatus is shown in Figure 3.3.1. The combinatorial film was synthesised from volatised precursors stored and carried from bubblers. Bubbler 1 contained t-butylamine (N source), bubbler 2 contained $TiCl_4$ (Ti source) and bubbler 3 contained ethyl acetate (O source). The volatility of the precursor could be altered by adjusting the temperature of the bubbler. The reagent vapours were transported from their bubblers by an inert N_2 gas to their respective mixing chamber. The vapours from the t-butylamine precursor were carried to mixing chamber A. The vapours from the $TiCl_4$ and ethyl acetate precursors were carried to mixing chamber B. At each mixing chamber, the vapours were combined with a plain line flow of inert N_2 gas and carried into the cold-walled reactor (630 °C) through separate points of entry. This created a gradient in the oxygen: nitrogen source concentration horizontally across the substrate and a range of deposition conditions in a single experiment. The parameters used to achieve the combinatorial film in this study are displayed in Table 3.3.1. A reference system showing the exact locations of the positions analysed across the combinatorial film produced is shown in Figure 3.3.2. The methods of characterisation that were applied to each grid position are shown in the key. Further details of the experimentation and apparatus can be found in the experimental methods, Section 3.2.

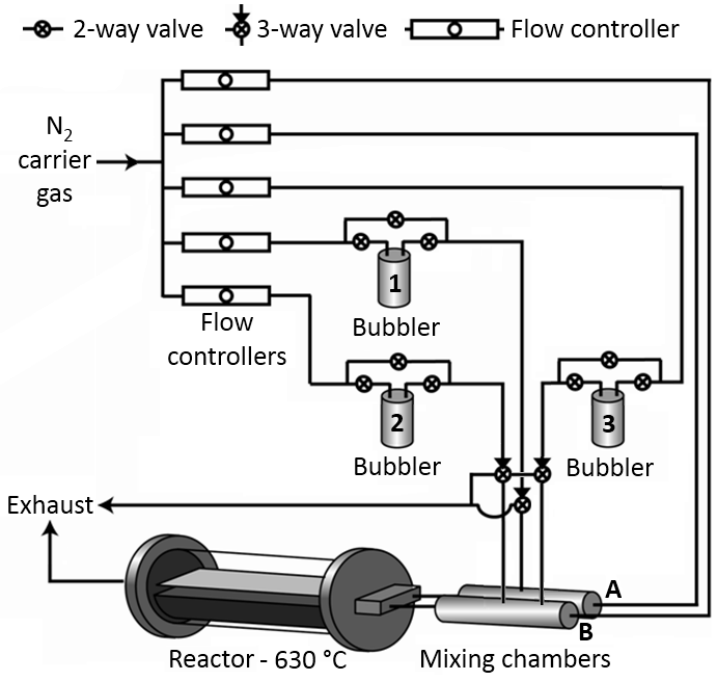

Figure 3.3.1: *Schematic of the combinatorial APCVD apparatus. The combinatorial film was synthesised from volatised precursors carried from bubblers; where bubbler 1 contained t-butylamine (cooled by an iced water bath), 2 contained $TiCl_4$ and 3 contained ethyl acetate. Of particular importance are the two separate entry points into the reactor, where $TiCl_4$ and ethyl acetate entered the reactor via mixing chamber B and t-butylamine entered the reactor via mixing chamber A. This created a gradient in the nitrogen source concentration horizontally across the substrate and a range of deposition conditions in a single experiment.*

	Mixing Chambers		Bubblers		
			1	2	3
	A	B	t-butylamine	$TiCl_4$	ethyl acetate
Temperature (°C)	100	250	10.0	70.0	40.0
Flow rate (L min^{-1})	1.0	6.0	0.30	0.50	0.50
Vapour pressure (mm Hg)	-	-	189	96.3	189
Mass flow rate (mol min^{-1})	-	-	4.1×10^{-3}	3.0×10^{-3}	6.8×10^{-3}
Molar ratios	-	-	1.4	1.0	2.3

Table 3.3.1: *Temperatures (°C) of components and N_2 carrier gas flow rates (L min^{-1}) in the combinatorial APCVD synthesis of a thin-film containing the full range of graded composites from pure pseudo-brookite $Ti_{3-\delta}O_4N$ at one end to pure N_i-doped anatase TiO_2 at the other. The carbon block inside the reactor was maintained at 630 °C during the 30 s deposition. Mass flow rates (mol min^{-1}) were derived from vapour pressure (mm Hg) curves to yield the molar ratio of each precursor relative to $TiCl_4$.*

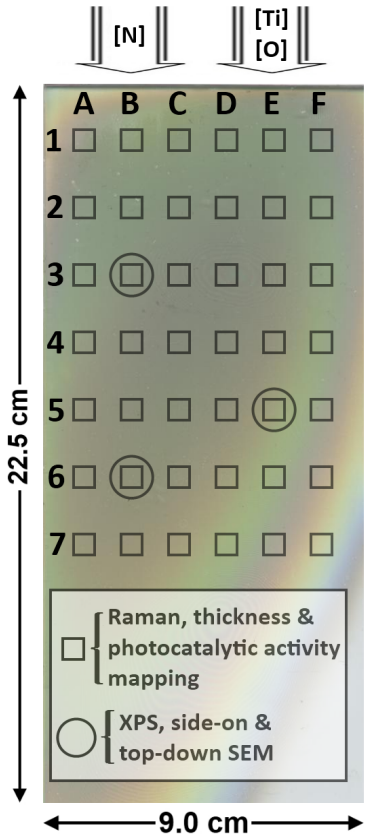

Figure 3.3.2: *Picture of the combinatorial thin-film and super-imposed grid reference system used throughout this section with the type of characterisation for each of the 42 unique positions analysed stated in the key. The positions of the gas inlets relative to the glass substrate when the deposition took place inside the reactor are shown; with Row 1 lying closest to the gas inlets and Row 7 lying closest to the exhaust. Positions are spaced 2.0 cm apart in rows and 1.0 cm apart in columns.*

3.3.3. Results

3.3.3.1. Appearance

A composite thin-film with graded composite phase from pure pseudo-brookite $Ti_{3-\delta}O_4N$ at one end to pure N_i-doped anatase TiO_2 at the other was formed by combinatorial APCVD from reaction of $TiCl_4$, ethyl acetate and t-butylamine at 630 °C. Interference fringes, characteristic of thin-film materials with high refractive indices were observed (Figure 3.3.2). This showed how the thickness varied across the combinatorial film. The contours of the fringes peaked within the middle section of the film. This indicated the film was thickest towards the centre. The film also displayed a yellowish tint, characteristic of nitrogen doping in TiO_2.[30] The film was adhesive and impervious to prolonged immersion in common solvents (water, acetone and isopropanol). From the accumulated thicknesses determined by our film-thickness mapping method the average growth rate was 8.0 $nm.s^{-1}$.

3.2.3.2. Phase mapping

The phase was mapped using Raman spectroscopy, as described in Section 2.2. Some Raman patterns are shown in Figure 3.3.3(a) to demonstrate the smooth transition from spectra characteristic of orthorhombic symmetry (pure pseudo-brookite $Ti_{3-\delta}O_4N$ – position A1) to spectra characteristic of tetragonal symmetry (pure anatase TiO_2 – position F6).

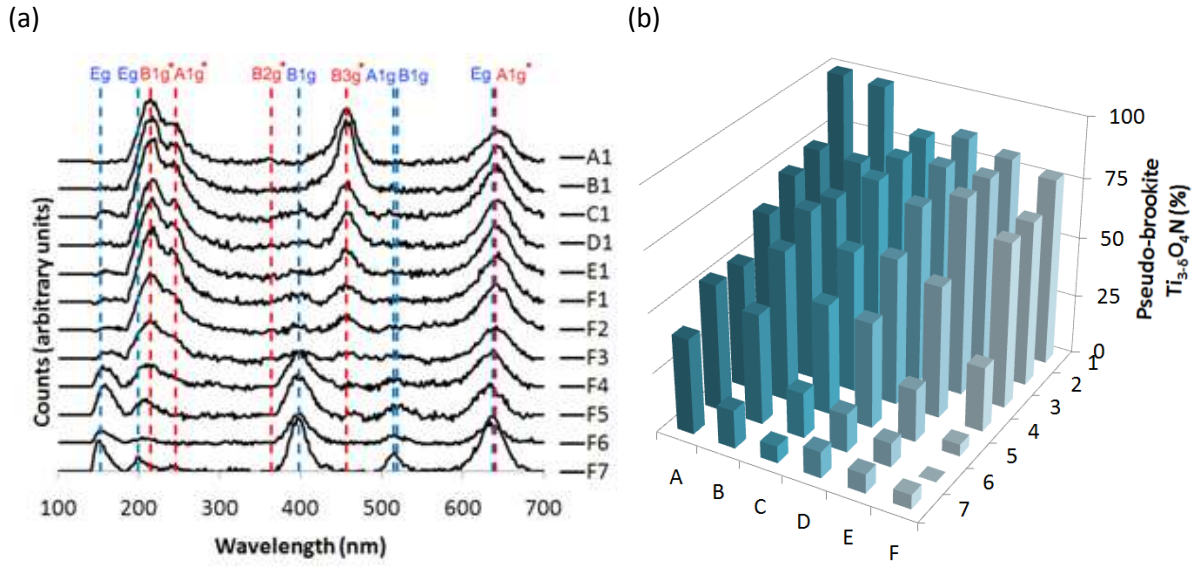

Figure 3.3.3: (a) *Raman spectra of all positions across Row 1 and Column F; stacked from A1 to F1 to F7. If asterisked, the vibrational modes represent orthorhombic pseudo-brookite $Ti_{3-\delta}O_4N$ symmetry and tetragonal anatase TiO_2 symmetry if not. (b) 3-dimensional bar chart of percentage contribution of pseudo-brookite $Ti_{3-\delta}O_4N$ across the combinatorial composite thin-film determined by our phase mapping method described in Section 2.2.*

The phase contribution was determined by separating the two most prominent modes at 639 cm^{-1} (anatase TiO_2) and 620 cm^{-1}(pseudo-brookite $Ti_{3-\delta}O_4N$) by a systematic deconvolution and then applying an equation determined from pre-formulated powder standards:

$$anatase\ TiO_2\ (\%) = 100.4 - \frac{113.1}{1 + e^{(x-22.82)/12.28}} \tag{3.2}$$

where x = the percentage area contribution of the pseudo-brookite $Ti_{3-\delta}O_4N$ mode (620 cm^{-1}) versus the anatase TiO_2 mode (639 cm^{-1}). After separating the peaks of all 42 locations, Equation 3.2 was applied. The quantified phase contributions are shown in Figure 3.3.3(b) as a 3-dimensional bar chart for the pseudo-brookite $Ti_{3-\delta}O_4N$ phase:

$$anatase\ TiO_2\ (\%) = 100 - pseudo.brookite\ Ti_{3-\delta}O_4N\ (\%) \tag{3.3}$$

The smooth phase transition seen in Raman spectra (Figure 3.2.3(a)) was now quantified (Figure 3.3.3(b)), decreasing smoothly from pure pseudo-brookite $Ti_{3-\delta}O_4N$ at position A1 in a diagonal fashion to pure anatase TiO_2 at position F6.

3.3.3.3. Film-thickness mapping

The reflectance spectrum of each colour band due to interference was recorded from 300 – 2500 nm at the positions designated in Figure 3.3.4(a).

(a) (b)

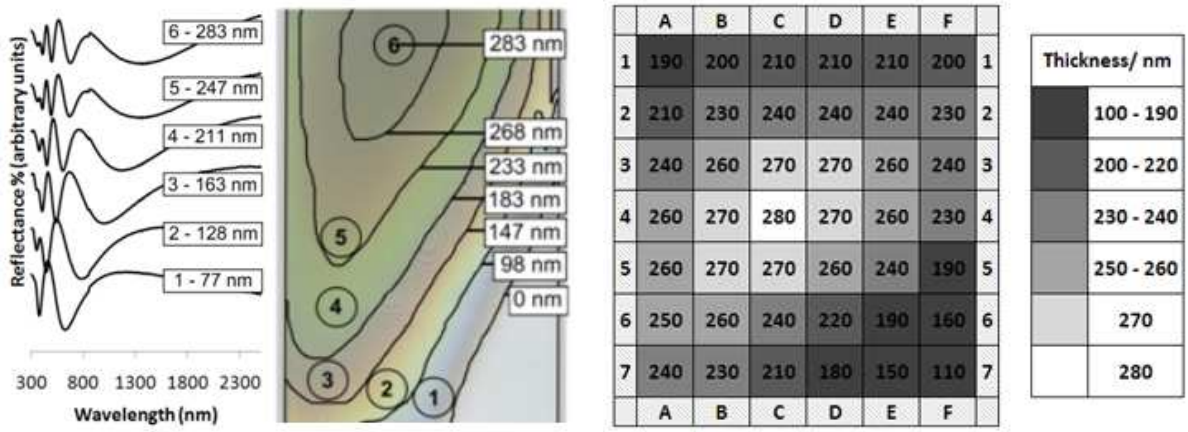

Figure 3.3.4: *(a) Stacked reflectance spectra at the centre of each of the 6 colour bands observed, with film-thicknesses determined by the Swanepoel method and (b) a colour coded film-thickness map of all 42 allotted grid positions across the combinatorial film, calculated by approximating linear growth in accordance with our film-thickness mapping method described in Section 2.4.*

As the position of a transmittance maximum is analogous to where a reflectance minimum occurs, the Swanepoel method for determining the thickness of thin-films could be applied.[122] The method can determine film-thickness if the wavelengths at which maximum and minimum interference occur is known as well as the spectral dependence of the refractive index. However, the combinatorial thin-film is composed of a range of composite concentrations. As the change of refractive index over the wavelength range analysed is known for pure anatase TiO_2 and pure pseudo-brookite $Ti_{3-\delta}O_4N$ as well as the contribution of each phase at each interference colour band analysed from phase mapping (Section 3.3.3.2), the spectral dependence of the refractive index was determined through a weighted average of each contributing phase. The error in this assumption was made lower by the fact that the spectral dependence of the refractive index of anatase TiO_2 (tetragonal symmetry) and brookite TiO_2 (orthorhombic symmetry) are quite similar[197] in addition to the high degree of fit ($r^2 >$ 0.99) of our Swanepoel plots (Figure 2.3.2(b)). With the thickness at the centre of each colour band known, the thickness at the colour boundaries and then the 42 designated grid positions (Figure 3.3.2) were calculated by approximating linear growth (Section 2.4). A colour coded map of film-

thickness for the 42 grid positions was constructed, shown in Figure 3.3.4(b), and quantified the variation in thickness observed by eye across the combinatorial film.

3.3.3.4. X-ray photoelectron spectroscopy

The oxidation state and environment of the constituent elements were investigated by X-ray photoelectron spectroscopy (XPS) at three locations across the combinatorial film; B3, B6, and E5. Peak positions were calibrated to adventitious graphite impurities on the surface (284.5 eV).[157] The presence of titanium, oxygen and nitrogen was confirmed at each of the three positions analysed. Deconvoluting peaks within the N (1s) binding energy range revealed three distinct nitrogen environments (Figure 3.3.5).

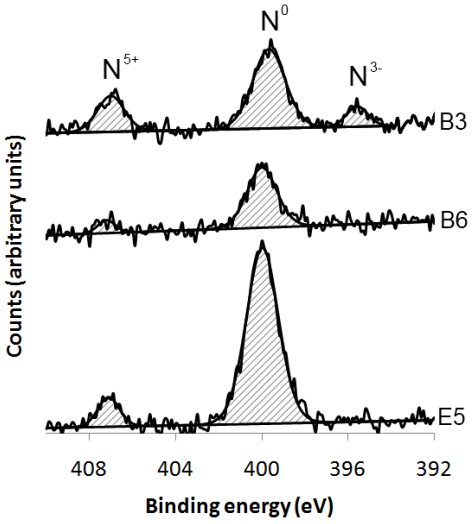

Figure 3.3.5: *Stacked N (1s) X-ray photoelectron spectra conducted at grid positions B3, B6 and E5. Deconvoluting peak areas revealed three distinct nitrogen environments; substitutionally doped N_s (N^{3-}), interstitially doped N_i (N^0) and surface bound nitrate NO_3^- (N^{5+}).*

One of these environments was seen only at position B3 with a binding energy of 395.6 eV and corresponded to an N_s environment (N^{3-}) within pseudo-brookite $Ti_{3-\delta}O_4N$.[112] Although phase mapping (Section 3.3.3.2) showed at least some contribution of the pseudo-brookite $Ti_{3-\delta}O_4N$ phase at B3, B6 and E5, it was only observed though XPS at the most phase-rich pseudo-brookite $Ti_{3-\delta}O_4N$ environment of the three (B3). However, position B3 was only ≈ 1.5 times richer in pseudo-brookite $Ti_{3-\delta}O_4N$ than at position B6 and hinted that pseudo-brookite $Ti_{3-\delta}O_4N$ formation at the surface may have been somewhat discouraged compared with the bulk. The two remaining N (1s) environments were present at all three locations, seen at binding energies of 399.7 eV and 407.0 eV and corresponded to an N_i environment (N^0) within anatase TiO_2[198] and surface NO_3^- species (N^{5+})[157] respectively. The binding energy of the N_i environment also falls within the region of surface bound γ-N_2.[199] This can make identifying N_i-doping confusing if the surface of the material is not sputtered

clean of the surface bound γ-N_2 species. However, a correlation between the concentration of the N^0 environment and phase contribution of anatase TiO_2 was observed. As the level of surface bound γ-N_2 should be similar in both pseudo-brookite $Ti_{3-\delta}O_4N$ and anatase TiO_2 materials, this variation was attributed to the presence of N_i-doping in the anatase TiO_2 regions of the composite. The most highly concentrated N^0 environment was observed at E5. As this position was also the richest in anatase TiO_2, this suggested N_i dopants formed solely within anatase TiO_2 sites. The relatively consistent occurrence of the surface NO_3^- species was inherent with the synthetic method, where nitrogen exposed at the surface of the film is fully oxidised upon exposure to air.

3.3.3.5. Scanning electron microscopy

Scanning electron microscopy (SEM) imaging of the film's surface at positions B3, B6 and E5 showed similar grainy topography with crystallites less than 100 nm in diameter. Off-cuts at each position were turned side-on to investigate film thickness. These thicknesses compared well with those determined more simply by our film-thickness mapping method (Section 2.4). A table accumulating the physical data for positions B3, B6, and E5 is shown in Table 3.3.2.

	SEM	Swanepoel	XPS		Raman
	Film-thickness (nm)		N_i-doping (N:Ti ratio)	N_s-doping (N:Ti ratio)	Pseudo-brookite $Ti_{3-\delta}O_4N$ (%)
B3	260 (15)	260 (10)	0.07 (1)	0.02 (1)	68 (5)
B6	260 (30)	260 (10)	0.08 (1)	0.00 (1)	46 (5)
E5	240 (30)	240 (10)	0.16 (1)	0.00 (1)	22 (5)

Table 3.3.2: *Grouped physical data for positions B3, B6 and E5 containing information on film-thickness (nm), nitrogen concentration (N: Ti ratio) and pseudo-brookite $Ti_{3-\delta}O_4N$ phase contribution (%) within the composite.*

3.3.3.6. Reaction chemistry

A composite thin-film with graded phase concentration from pure pseudo-brookite $Ti_{3-\delta}O_4N$ at one end to pure N_i-doped anatase TiO_2 at the other was formed by a combinatorial APCVD process. Such APCVD processes afford precise reaction control as the precursor temperature and carrier gas flow rate can be adjusted to provide specific reagent mass flow rates.[200] Given the conditions used in this combinatorial study, the mass flow rates and molar ratios were determined (Table 3.3.1). From our phase mapping experiments, the average phase contribution over the 42 positions analysed was found to be 47: 53 anatase TiO_2: pseudo-brookite $Ti_{3-\delta}O_4N$. This corresponded to an average O: Ti ratio of 1.6: 1. As the molar ratio of the oxygen source (ethyl acetate): titanium source ($TiCl_4$) was 2.3: 1, the titanium source was the limiting reagent. In mapping the contribution of each phase (Figure

3.3.3(b)) as well as film-thickness (Figure 3.3.4(b)), the reaction rate of each precursor at each of the 42 grid positions (over a 1cm^2 area) could be derived (Figure 3.3.6). Several assumptions were made in order to determine the reaction rate. For instance, the densities of pseudo-brookite $Ti_{3-\delta}O_4N$ (4.30 g.cm^{-3}) and anatase TiO_2 (3.89 g.cm^{-3}) were required, so values were taken from the literature.[112,201] In addition, the level of N_i-doping could not be incorporated into the calculation as it was unknown for all but three positions (XPS analysis of B3, B6 and E5). However, as the N_i-doping capacity of anatase TiO_2 is significantly lower than the N-concentration in pseudo-brookite $Ti_{3-\delta}O_4N$,[30,112] such an omission should only marginally effect the reaction rate calculation of the nitrogen source t-butylamine.

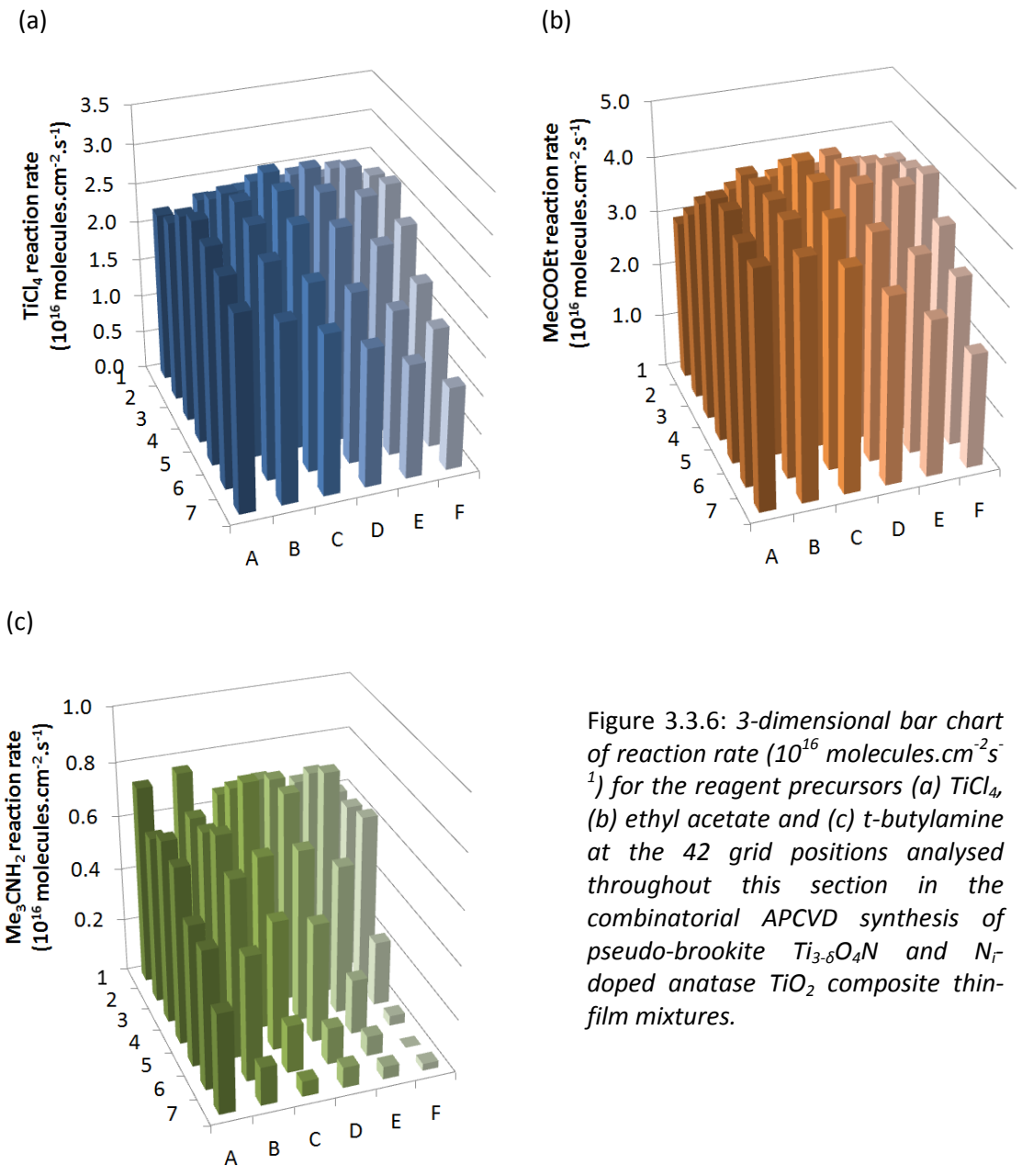

Figure 3.3.6: *3-dimensional bar chart of reaction rate (10^{16} molecules.cm^{-2}s^{-1}) for the reagent precursors (a) $TiCl_4$, (b) ethyl acetate and (c) t-butylamine at the 42 grid positions analysed throughout this section in the combinatorial APCVD synthesis of pseudo-brookite $Ti_{3-\delta}O_4N$ and N_i-doped anatase TiO_2 composite thin-film mixtures.*

The trend in reaction rates of $TiCl_4$ and ethyl acetate were quite similar, peaking at the centre of the film. As the reaction was conducted in a cold-walled reactor, the substrate was marginally hotter in the centre of the film (*c.a.* 25 °C hotter than at the edges). Therefore, the reactions of both $TiCl_4$ and ethyl acetate were reaction rate limited processes.[108] However, the trend in reaction rate for t-butylamine was quite different to that of $TiCl_4$ and ethyl acetate, peaking near the top-left section of the film and decreasing almost steadily in a diagonal fashion to the bottom-right. As the t-butylamine nitrogen source entered the reactor in the vicinity of the top-left section, such a trend was unsurprising. Nevertheless, this indicated that the reaction of t-butylamine was a mass-transport limited process. It also showed us how pseudo-brookite $Ti_{3-\delta}O_4N$ formation was encouraged over anatase TiO_2 formation when the nitrogen source concentration was high.

By culminating reaction rate data, the overall combinatorial APCVD reaction for the formation of this composite thin-film with graded N_i-doped anatase TiO_2: pseudo-brookite $Ti_{3-\delta}O_4N$ could be written as follows:

$$TiCl_4 + MeCOOEt + Me_3CNH_2 \rightarrow (N_i - TiO_2)_x : (Ti_{3-\delta}O_4N)_{1-x} + \text{by products} \ (17\ \%) \quad (3.4)$$

where $0 \leq x \leq 1$ ($\langle x \rangle = 0.47$, $\sigma = 0.30$). An average $TiCl_4$: MeCOOEt: Me_3CNH_2, 1.0: 2.3: 1.4 molar ratio was introduced in this combinatorial reaction over a glass substrate held at 630 °C (± 25 °C). As the reaction chemistry of 42 cm^2 over a total of 202 cm^2 of combinatorial film-space was investigated (Figure 3.3.6), the reaction efficiency (17 %) could be determined in terms of the limit reagent ($TiCl_4$).

Little is known on the mechanism by which $TiCl_4$ reacts with ethyl acetate to form TiO_2 thin-films through APCVD.[202] However, it has been suggested that ethyl acetate decomposes to produce oxidant species. At 630 °C, ethyl acetate can decompose to ethanol which in turn could dehydrate to evolve water and ethane. With water present, the reaction could then proceed by a simple hydrolysis reaction with $TiCl_4$:

$$TiCl_4 + 2H_2O \rightarrow TiO_2 + 4HCl \quad (3.5)$$

As our t-butylamine nitrogen source also decomposes to form NH_3 at such temperatures (Equation 3.1), the insertion of nitrogen may also proceed by a simple hydrolysis reaction.

The nitrogen and titanium sources introduced into this combinatorial reaction were in a 1.4: 1 molar ratio. For a similar APCVD reaction of $TiCl_4$, ethyl acetate and t-butylamine performed at 500 °C, as opposed to 630 °C in this study, it was found that a N: Ti source ratio greater than 0.5: 1 encouraged the formation of N_s-doped TiO_2.[30] As no evidence for N_s-doped TiO_2 was observed in this study, one can deduce that pseudo-brookite $Ti_{3-\delta}O_4N$ formation is encouraged over N_s-doped TiO_2 at

elevated temperatures. Our N: Ti source ratio was in fact quite similar to that used by Hyett *et. al.* in their discovery of pseudo-brookite $Ti_{3-\delta}O_4N$ (N: Ti ≈ 1.5: 1) through a combinatorial APCVD process conducted at the same temperature (630 °C).[112] However, an NH_3 nitrogen source was used as opposed to the t-butylamine nitrogen source used in this study. Pseudo-brookite $Ti_{3-\delta}O_4N$ was formed exclusively in their study whereas a mixture of pseudo-brookite $Ti_{3-\delta}O_4N$ and N_i-doped anatase TiO_2 was formed in this study. This was attributed to the mass-transport limited movement of the bulkier t-butylamine nitrogen source.

When comparing the relative mass flows of each precursor into the reactor (Table 3.3.1) against the average reaction rate, it was found that $TiCl_4$ reacted most efficiently and as expected given it was the limiting reagent. However, the reaction of t-butylamine was ≈ 7 times less efficient than $TiCl_4$ and ≈ 5 times less efficient than ethyl acetate. This was attributed to two factors: (i) the decomposition barrier to ammonia (Equation 3.1) and (ii) competition with the oxygen source ethyl acetate that was, on average, present in almost double the concentration of t-butylamine.

3.3.3.7. Photocatalytic activity mapping

A grid was drawn using a felt-tipped pen filled with a di-chloroindophenol-based intelligent ink on top of the combinatorial film. 6 vertical lines and 7 horizontal lines were drawn so that the 42 points of crossing overlaid the 42 grid positions that were physically characterised. An example of such a style can be observed in Figure 2.5.3(a). After photographing the film and ink layer it was subjected to UVA-irradiation to initiate photocatalysis. At set time intervals, the film and photo-reducing ink layer were photographed until the colour was completely bleached. A non-homogenous yet smooth transition from blue to colourless was observed. The top-left section of the film was, by eye, the most active region of the combinatorial film, decolouring the redox dye most rapidly after approximately 500 seconds UVA exposure (365 nm, 2 x 8W). Sections progressively further from the top-left region took longer to discolour the dye, with a smooth change in colour occurring outwardly in a diagonal fashion from the top-left section to the bottom-right section. After approximately 1000 seconds of UVA irradiation, most of the ink grid had been discoloured. By this point however, the bottom-right section of the grid was yet to fully lose its colour and it was clear that the underlying film at this point was of lower photocatalytic activity. The red component of digital colour at each grid position was extracted using the software we developed (RGB Extractor$^{(c)}$). All positions showed an increase in the red component of digital colour until a point of plateau. This represented the point of complete photo-reduction of di-chloroindophenol to its colourless intermediate (Equation 2.22). The time at which the plateau was reached differed across the combinatorial film, as varying degrees of photocatalysis was observed. The red component of digital colour was fit to a Boltzmann model

(Table 2.2) and the time taken to reach each plateau extracted. These times are displayed in a 3-dimensional bar chart in Figure 3.3.7(a).

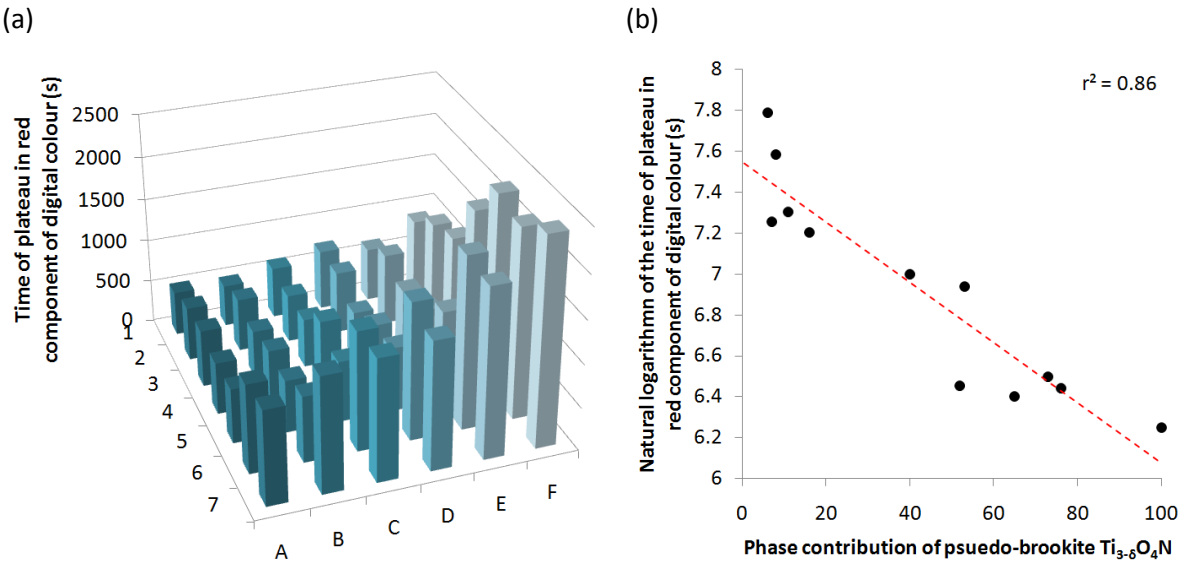

Figure 3.3.7: *(a) 3-dimensional bar chart of the time taken for the red component of digital colour to reach a plateau for all 42 grid positions analysed, thereby indicating the complete photo-reduction of a di-chloroindophenol intelligent ink overlayer using UVA light and (b) a plot of the natural logarithm of the time taken for the red component of digital colour to reach a plateau against pseudo-brookite $Ti_{3-\delta}O_4N$ phase contribution for the positions along Row 1 and Column F (A1 to A7 to F7), where a strong linear correlation was observed (r^2=0.86).*

The numbers quantified the trend observed by eye, with the quickest times, indicative of a more rapid photocatalyst, observed in the top-left region of the combinatorial film. Through phase mapping (Section 3.3.3.2), this region was found to be primarily composed of the pseudo-brookite $Ti_{3-\delta}O_4N$ phase. The slowest times were observed in the bottom-right region where the film was mainly composed of N_i-doped anatase TiO_2. The times were subsequently plotted against phase composition for the 12 positions across Row 1 and Column F (A1 to A7 to F7). A first order exponential dependence was observed so the natural logarithm of the times were re-plotted against phase composition, as shown in Figure 3.3.7(b), where a strong degree of linear correlation was observed (r^2 = 0.86). The plot showed how an increasing phase contribution of pseudo-brookite $Ti_{3-\delta}O_4N$ phase produced an increasingly more active photocatalyst. This was not too dissimilar from Hyett *et. al.*'s investigation of the photocatalysis of pure pseudo-brookite $Ti_{3-\delta}O_4N$ and TiO_2 thin-films.[196] They found that thin-films of pure pseudo-brookite $Ti_{3-\delta}O_4N$ were almost twice as active in the photocatalytic oxidation of a stearic acid overlayer under UVC (254 nm) light than either 85: 15 and 45: 55 anatase TiO_2: rutile TiO_2 composites. Although a UVC source was used by Hyett *et. al.* in their photocatalysis study,[196] Mills *et. al.* had previously shown the rate of photocatalysis of intelligent ink to a UVA (365 nm) source was directly proportional to the rate of photocatalysis of stearic acid to a UVC source;[172] validating comparisons between Hyett *et. al.*'s study and our own. In

addition, Hyett *et. al.* tested films of approximately equivalent thickness, so formal quantum efficiencies did not have to be taken into account to make fair comparisons within their study. To be sure that our correlation between composite phase contribution and photocatalytic activity was real, the effect of film-thickness was also compared. A poor correlation was observed with a low degree of fit to either a linear (r^2 = 0.62) or first order exponential (r^2 = 0.46) model. This indicated the changes in film-thickness were not the majority cause for the large variations in photocatalysis observed. This could also be observed by comparing the median and standard deviations of each data set, where film-thickness (μ = 240 nm, σ = 37 nm) did not vary anywhere near as strongly as the time for complete photocatalysis to occur (μ = 760 nm, σ = 540 nm).

3.3.4. Conclusions

A new route to forming the recently discovered pseudo-brookite $Ti_{3-\delta}O_4N$ phase was established through the combinatorial APCVD of $TiCl_4$, ethyl acetate and t-butylamine precursors at 630 °C on glass. By introducing the precursors at different points inside the reactor, a N: O source concentration gradient was imposed, creating a range of deposition conditions in a single experiment. This induced the formation of the full range of pseudo-brookite $Ti_{3-\delta}O_4N$ and N_i-doped anatase TiO_2 composites over a single film and is the first case, to our knowledge, in which any such composite has ever been formed. Our high-throughput methods for characterising combinatorial thin-films was applied to 42 allotted positions over a 6 x 7 grid (vertical x horizontal). The phase, thickness and photocatalytic activity at each of the 42 grid positions across the combinatorial film were rapidly deduced. By correlating the physical properties of the film against the rates of photocatalysis it was found that pure pseudo-brookite $Ti_{3-\delta}O_4N$ material was most photocatalytically active to UVA light. No evidence for a synergistic enhancement of photocatalysis within the comprehensive range of composite phase space tested was observed, where increasing phase contributions of N_i-doped anatase TiO_2 caused a comparative detriment to the photocatalytic activity.

In the following section we will use combinatorial APCVD in conjunction with our characterisation mapping methods to investigate the UVA photocatalysis of a N_s-doped TiO_2 system with graded levels of nitrogen doping ($0 \leq N_s$: Ti $\leq$ 11 %) and composite phase contribution ($0 \leq$ anatase $TiO_2 \leq$ 100 %, $0 \leq$ rutile $TiO_2 \leq$ 41 %). The effects of N_s-doping on UVA photocatalysis and the validity of the proposed synergistic model for anatase TiO_2 and rutile TiO_2 composites will then be discussed.

3.4. N_s-doped TiO_2; anatase and rutile phase composite mixtures

3.4.1. Introduction

The photocatalysis of un-modified TiO_2 functions with UVA light. As a greater portion of photons from the sun and most indoor lamps are present in the visible region of the electromagnetic spectrum there has been a strong drive to narrow the bandgap of this material. Since the visible light photocatalytic activity of nitrogen doped TiO_2 was reported by Asahi *et. al.* in 2001,[118] it has been studied more extensively than any other modified TiO_2 system.[2] The material has been prepared through many routes including sol-gel,[116] sputtering,[203] ion implantation,[204] atomisation,[115] pyrolysis,[205] CVD[30] etc. Most groups have assigned the enhancement in visible light photocatalytic activity to N_s-doping given the experimental evidence for a strong band narrowing.[205] Theoretical studies have complemented these results and explained how such a band narrowing comes about through the effective overlap of the N (2p) and O (2p) states that increase the height of the valence band (Scheme 1.1.3(b)).[206] The degree of photocatalytic enhancement for N_s-doped TiO_2 thin-films under visible lighting has been studied against a range of organic materials.[116,118,207-209] Although several studies have also mentioned the detriment that these materials show to UVA photocatalysis,[117,210,211] little work has been done to quantify this. If such materials are to be applied in solar conditions, both the UVA and visible light photons present will have the capacity to produce photo-excitations. Therefore, depending on the level of detriment that N_s-doping might cause to UVA photocatalysis its overall photocatalytic activity under solar conditions might not actually yield an improvement. Given the capacity of our photocatalytic activity mapping method to rapidly screen UVA photocatalysis, we investigated the N_s-doping of TiO_2 from a combinatorial approach.

In this section we describe the combinatorial APCVD synthesis of a N_s-doped TiO_2 system with graded levels of nitrogen doping ($0 \leq N_s$: Ti ≤ 11 %) as well as composite phase contribution ($0 \leq$ anatase $TiO_2 \leq 100$ %, $0 \leq$ rutile $TiO_2 \leq 41$ %). This was formed using a triple source of precursors, with $TiCl_4$ as the titanium source, ethyl acetate as the oxygen source and NH_3 as the nitrogen source. The properties of 247 unique positions were investigated across the combinatorial film. X-ray photoelectron spectroscopy confirmed the presence of N_s-doping. The level of N_s-doping for a large number of states was found by applying our nitrogen/ titanium concentration mapping method (Section 2.5). The large variance in preferred growth seen in X-ray diffraction patterns was quantified by preferred orientation mapping (Section 2.3). The phase contributions and film-thicknesses were also found by phase mapping (Section 2.2) and film-thickness mapping (Section 2.4) respectively. Scanning electron microscopy was used to investigate the surface topography across a section of the combinatorial film as well as verify thicknesses determined by our film-thickness mapping method.

Our photocatalytic activity mapping method was then applied to screen the degree of UVA photocatalysis. The contributing effects of both N_s-doping and phase contribution on UVA photocatalysis are then discussed as well as the validity of the proposed synergistic model for anatase TiO_2 and rutile TiO_2 composites.

3.4.2. Experimental combinatorial film synthesis

A combinatorial N_s-doped TiO_2 system with graded levels of nitrogen doping ($0 \leq N_s$: Ti ≤ 11 %) as well as composite phase contribution ($0 \leq$ anatase $TiO_2 \leq 100$ %, $0 \leq$ rutile $TiO_2 \leq 41$ %) was formed by combinatorial APCVD. The film was deposited on float glass (225 × 90 × 3.2 mm; length × breadth × thickness) that contained an ≈ 50 nm thick barrier layer of SiO_2 at the substrate's surface to inhibit the diffusion of ions from the glass into the film. A schematic of the apparatus is shown in Figure 3.4.1.

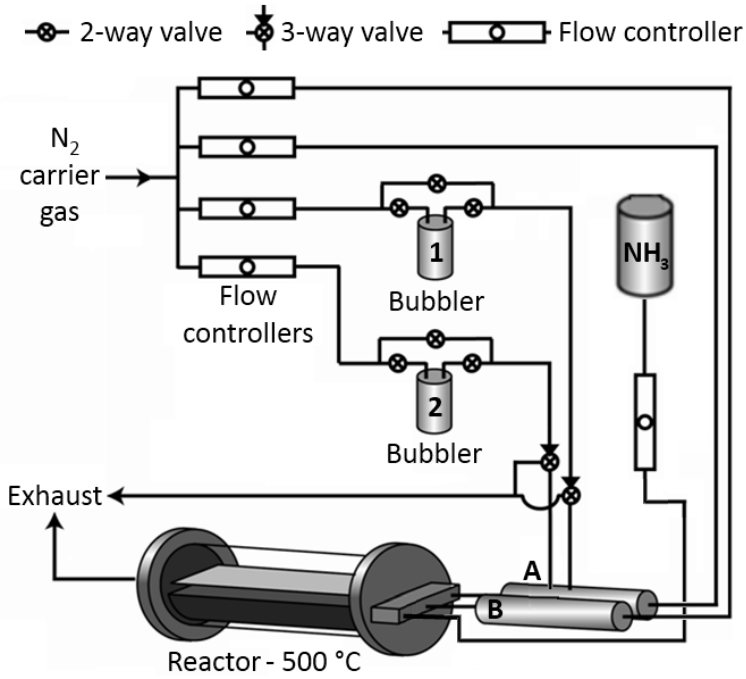

Figure 3.4.1: *Schematic of the combinatorial APCVD apparatus. The combinatorial film was synthesised from a combination of NH_3 gas direct from a cylinder and volatised liquid precursors carried from bubblers, where bubbler 1 contained $TiCl_4$ and 2 contained ethyl acetate. Of particular importance are the two separate entry points of the precursors into the reactor, where $TiCl_4$ and ethyl acetate entered the reactor via mixing chamber A and NH_3 entered the reactor at the opposite end. This created a gradient in the nitrogen source concentration horizontally across the substrate and a range of deposition conditions in a single experiment.*

The combinatorial film was synthesised from a combination of NH_3 gas direct from a cylinder (N source) and volatised precursors stored and carried from bubblers, where bubbler 1 contained $TiCl_4$

(Ti source) and bubbler 2 contained ethyl acetate (O source). The volatility of each precursor could be altered by adjusting the temperature of the bubbler. The reagent vapours were transported from their bubblers by an inert N_2 gas to mixing chamber A where they were then combined with a plain line flow of inert N_2 gas and carried into the cold-walled reactor (500 °C). The NH_3 gas was pumped directly into the reactor at the opposing side. This created a gradient in the oxygen: nitrogen source concentration horizontally across the substrate and a range of deposition conditions. An additional plain line flow of N_2 gas was carried through mixing chamber B to increase the spread of precursor flow across the substrate. The parameters used to achieve the combinatorial film in this study are displayed in Table 3.4.1.

	Mixing Chambers		Bubblers		Gas cylinder
			1	2	
	A	B	$TiCl_4$	ethyl acetate	NH_3
Temperature (°C)	225	240	69	41	-
Flow rate (L min^{-1})	2.0	5.0	2.0	0.80	0.02
Vapour pressure (mm Hg)	-	-	92.7	197	-
Mass flow rate (mol min^{-1})	-	-	1.14×10^{-2}	1.15×10^{-2}	0.83×10^{-2}
Molar ratios	-	-	1.0	1.0	0.73

Table 3.4.1: *Temperatures (°C) of components and N_2 carrier gas flow rates (L min^{-1}) in the combinatorial APCVD synthesis of a N_s-doped TiO_2 system with graded levels of nitrogen doping ($0 \leq N_s$: Ti ≤ 11 %) as well as composite phase contribution (0 ≤ anatase TiO_2 ≤ 100 %, 0 ≤ rutile TiO_2 ≤ 41 %). The carbon block inside the reactor was maintained at 500 °C during the 60 s deposition. Mass flow rates (mol min^{-1}) were derived from vapour pressure (mm Hg) curves to yield the molar ratio of each precursor relative to $TiCl_4$.*

A reference system that shows the exact locations of the positions analysed by each characterisation method is shown in Figure 3.4.2. The methods of characterisation that were applied to each grid position in this combinatorial system are shown beside the image. Further details of the experimentation and apparatus can be found in the experimental methods, Section 3.2.

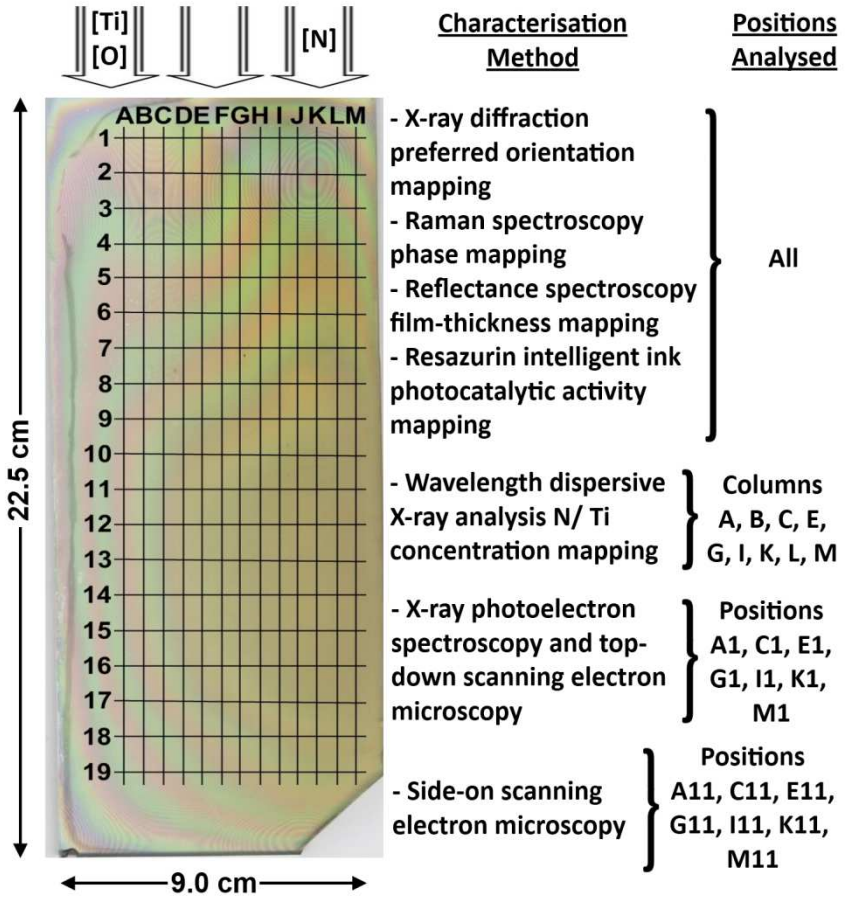

Figure 3.4.2: *Picture of the combinatorial thin-film and super-imposed grid reference system used throughout this section. The type of characterisation for each of the 247 unique grid positions is stated. The positions of the gas inlets relative to the glass substrate when the deposition took place inside the reactor are shown; with Row 1 lying closest to the gas inlets and Row 19 lying closest to the exhaust. Positions are spaced 1.0 cm apart in rows and 0.5 cm apart in columns.*

3.4.3. Results

3.4.3.1. Appearance

A combinatorial N_s-doped TiO_2 thin-film with graded levels of nitrogen doping ($0 \leq N_s$: Ti ≤ 11 %) as well as composite phase contribution ($0 \leq$ anatase $TiO_2 \leq 100$ %, $0 \leq$ rutile $TiO_2 \leq 41$ %) was formed by combinatorial APCVD from reaction of $TiCl_4$, ethyl acetate and NH_3 at 500 °C. Interference fringes, characteristic of thin-film materials with high refractive indices were observed (Figure 3.4.2). This showed how the thickness varied across the combinatorial film. The contours of the fringes peaked within the middle-right section of the film where the film was thickest. The film also displayed a yellowish tint, characteristic of nitrogen-doped TiO_2.[30] The yellowish tint was most prominent in the top-right section of the film, decreasing outwards in a diagonal fashion, to a more transparent looking film in the bottom-left. This hinted at the graded nature of N_s-dopant concentration across

the combinatorial film that was later confirmed by nitrogen/ titanium concentration mapping. The greatest concentrations of N_s-doping coincided with the region of most prominent yellowish tint. The film was adhesive and impervious to prolonged immersion in common solvents (water, acetone and isopropanol). From the accumulated thicknesses determined by our film-thickness mapping method the average growth rate was 9.2 $nm.s^{-1}$ (standard deviation = 2.2 $nm.s^{-1}$) at a substrate temperature of 500 °C.

3.4.3.2. Preferred orientation mapping

All 247 X-ray diffraction patterns acquired from the locations specified on the grid (Figure 3.4.2) featured anatase TiO_2 ($I4_1/amdz$, a = 3.785 Å, c = 9.512 Å)[146] as the predominant phase. X-ray diffraction patterns of the bottom-right section of the combinatorial film showed combinations of anatase TiO_2 and rutile TiO_2 ($P4_2/mnm$, a = 4.594 Å, c = 2.959 Å)[212] phases. Diffraction patterns with wider peaks and of lower overall intensity were observed near the top-edge of the film and signified this region was of lower crystallinity. Marked differences in the relative intensities of particular peaks were also seen across the film due to changes in preferred orientation growth. Four distinct types of pattern were observed. These were placed into groups arbitrarily labelled A, B, C and D. In stacking the X-ray diffraction patterns acquired from Column L we can observe an example from each group as the phase preference and preferred orientation changes down the film (Figure 3.4.3).

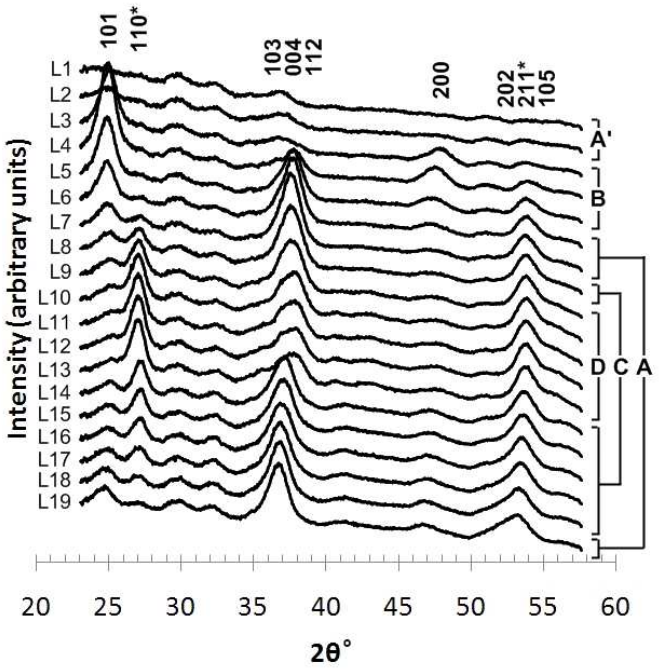

Figure 3.4.3: *A stack of the X-ray diffraction patterns acquired from Column L. The letters on the right represent the group in which each pattern was placed. Asterisked and non-asterisked indices represent rutile TiO_2 and anatase TiO_2 diffraction peaks respectively.*

Patterns in Group A contained little or no rutile TiO_2 component and had a strong preference for growth in the (004) plane; representing the bulk of phase-space across the combinatorial film. Group A could also be further sub-categorised in low crystallinity (A') or high crystallinity (A) patterns (Figure 3.4.3). Patterns in Group B also contained little or no rutile TiO_2 component but had a strong preference for growth in the (101) plane. Patterns that were placed in Group C contained a small rutile TiO_2 component, distinguished by the principle (110) rutile TiO_2 peak at $2\theta = 27.6°$. Patterns placed in Group D contained larger rutile TiO_2 components and a lower degree of preferred orientation of its anatase TiO_2 component in the (004) plane.

As the anatase phase of TiO_2 was in majority, our preferred orientation mapping method (Section 2.3) was applied to its principle (101) peak. The percentage contributions were calculated using Equation 2.3. A colour coded map of the percentage contribution of the anatase TiO_2 (101) peak was constructed (Figure 3.4.4).

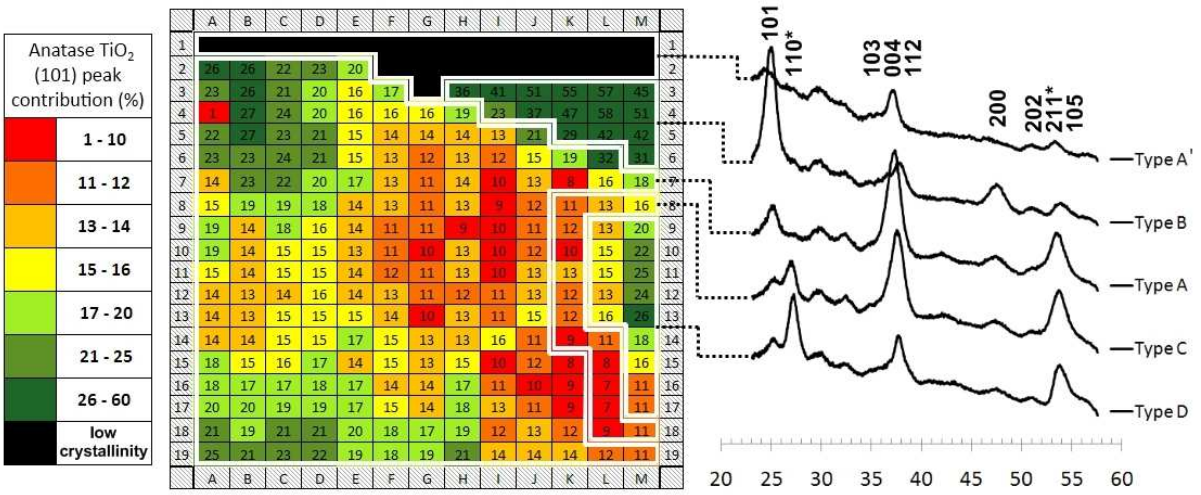

Figure 3.4.4: *A colour coded map showing the percentage contribution of the (101) principle peak intensity area for the anatase TiO_2 component. Sectioned areas contain X-ray diffraction patterns of a particular group (Groups A, B, C and D) with example patterns of each type displayed on the right. Asterisked and non-asterisked indices represent rutile TiO_2 and anatase TiO_2 peaks respectively.*

The colour coded map quantified the smooth transition in preferred orientation seen across the combinatorial film for the (101) plane of the anatase TiO_2 (101) component. The lowest degrees of preferred orientation in the (101) plane were observed in the bottom-right and middle sections of the film. Medium levels of preferred orientation in the (101) plane were observed in the bottom-left and top-left sections of the film. High degrees of preferred orientation growth in this plane were observed in the top-right section of the film, forming Group B. Given the changing degree and direction of preferred orientation across the combinatorial film, the contribution of each phase could not be simply extracted through fitting patterns to Rietveld refined models.[124] The level of phase contribution was instead quantified using Raman spectroscopy.

3.4.3.3. Phase mapping

Raman spectroscopy was conducted on all 247 specified locations on the grid (Figure 3.4.2). The Raman patterns predominantly featured peaks relating to anatase TiO_2 symmetry. Phase mixtures composed more strongly in rutile TiO_2 were observed on movement towards the bottom-right section of the combinatorial film; analogous to X-ray diffraction studies. Positions along the top-edge of the film were the weakest Raman scatterers. This was attributed to their low degree of crystallinity observed in X-ray diffraction studies. Raman patterns across Row 11 are shown in Figure 3.4.5(a) and demonstrate the smooth transition from spectra characteristic of pure anatase TiO_2 symmetry (position A11) to those characteristic of composite mixtures (position M11).

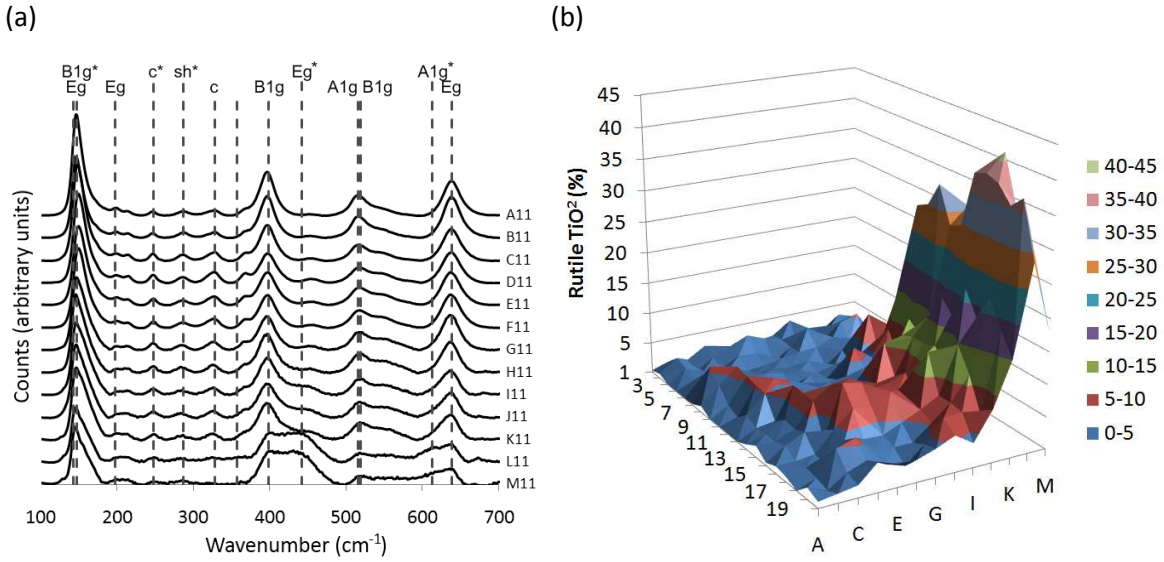

Figure 3.4.5: (a) *Raman spectra of all positions across Row 11; stacked from A1 to M11. Asterisked and non-asterisked vibrational modes represent rutile TiO_2 symmetry and anatase TiO_2 symmetry respectively and (b) a 3-dimensional contour map of percentage contribution of rutile TiO_2 across the combinatorial film, determined by our phase mapping method described in Section 2.2.*

The phase contribution was mapped using Raman spectroscopy as described in Section 2.2. The phase contribution was determined by first separating out the prominent mode for anatase TiO_2 at 639 cm^{-1} (E_g mode) and 612 cm^{-1} (A_{1g} mode) for rutile TiO_2 by a systematic deconvolution and then by applying the equation determined from assessment of pre-formulated powder standards:

$$anatase\ TiO_2\ (\%) = 47.7e^{\left(\frac{x}{89.9}\right)} - 44.4 \quad (3.6)$$

where x = the percentage area contribution of the rutile TiO_2 mode (A_{1g} - 612 cm^{-1}) versus the anatase TiO_2 mode (E_g - 639 cm^{-1}). After separating the peaks of all 247 locations, Equation 3.6 was applied. The quantified phase contributions are shown in Figure 3.4.5(b) as a 3-dimensional contour

map for the contribution of the rutile TiO_2 phase, which was determined by the simple relationship expressed in Equation 3.7:

$$anatase\ TiO_2\ (\%) = 100 - rutile\ TiO_2\ (\%) \quad (3.7)$$

The smooth phase transition seen in Raman spectra (Figure 3.3.5(a)) was now quantified (Figure 3.4.5(b)). The greatest degree of rutile TiO_2 phase formation was seen in the bottom-right section of the film, corroborating with observations from X-ray diffraction. The rutile TiO_2 phase component maximised at position M15, consisting of a 59: 41 anatase TiO_2: rutile TiO_2 composite mix. A relatively small region of phase-space contained substantial levels of rutile TiO_2, with just 14 % of the positions analysed containing ≥ 10 % rutile TiO_2 component. An almost pure anatase TiO_2 region was observed along Columns A and B and Rows 1 and 2, where no more than a 4 % presence of rutile TiO_2 component was derived.

3.4.3.4. Film-thickness mapping

The reflectance spectrum of each colour band due to interference was recorded from 300 – 2500 nm at the positions designated in Figure 3.4.6(a). As the position of a transmittance maximum is analogous to where a reflectance minimum occurs (Figure 2.3.2(a)), the Swanepoel method for determining the thickness of thin-films could be applied.[122] The method determines film-thickness with knowledge of the positions at which interference maxima and minima occur, combined with the spectral dependence of the refractive index of the material. However, the combinatorial thin-film under investigation was composed of a range of composite concentrations as well as band modified N_s-doped states. By avoiding the analysis of colour bands at positions containing high levels of N_s-doping, the spectral dependence of the refractive index could be estimated through a weighted average of each contributing phase. This could simply be determined using the spectral dependencies of pure anatase TiO_2 and pure rutile TiO_2 from the literature in conjunction with the phase contributions determined from our phase mapping experiments (Section 3.4.3.3). The error in this assumption was low for several reasons: (i) the colour bands analysed contained N_s-dopant levels lower than 1.0 at. % with the exception of the thickest position at L13 where N_s: Ti = 1.9 at. % (Section 3.4.3.5), (ii) all colour bands analysed were primarily composed of the anatase TiO_2 phase, (iii) the spectral dependence of the refractive index of the anatase TiO_2 and rutile TiO_2 polymorphs are quite similar due to their similar tetragonal symmetries[197] and (iv) a high degree of fit ($r^2 > 0.99$) was observed in all of our Swanepoel plots (Figure 2.3.2(b)). With the thickness at the centre of each colour band known, the thickness at the colour boundaries and then the 247 designated grid positions (Figure 3.4.2) were calculated by approximating linear growth (Section 2.4). A contour map

of film-thickness was constructed, shown in Figure 3.4.6(b), and quantified the variation in thickness observed by eye across the combinatorial film. The thickest point was found to lie at grid position L13 (743 nm). The thinnest point within the allotted grid positions was found to lie at position D1 (240 nm) and was more than 3 times thinner than the thickest point.

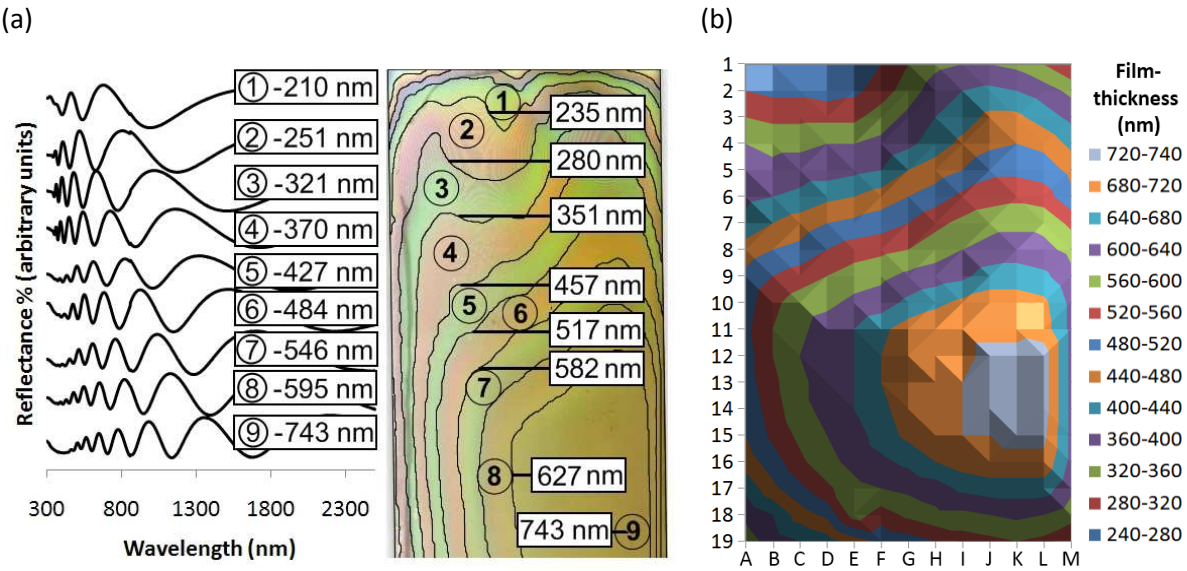

Figure 3.4.6: *(a) Stacked reflectance spectra at the centre of each of the 9 colour bands observed, with film-thicknesses determined by the Swanepoel method and (b) a film-thickness contour map of all 247 designated grid positions over the combinatorial film, calculated by approximating linear growth using our film-thickness mapping method described in Section 2.4.*

3.4.3.5. Nitrogen/ titanium concentration mapping

The overlapping emission of N K-lines and Ti L-lines of all positions along Columns A, B, C, E, G, I, K, L and M were recorded using high resolution wavelength dispersive X-ray (WDX) analysis. Each contributing component then was separated in accordance with modelled Ti metal and BN standards through a deconvolution, as described in our section on nitrogen/ titanium concentration mapping (Section 2.5). Some examples of peak separated data are shown in Figure 3.4.7(a) for positions along Row 1. We can see that both positions A1 and C1 have no contributing N K-line peak and were therefore free from nitrogen doping. A small contribution was observed on movement to position E1 (N: Ti = 3.4 at. %) and increased steadily to position I1 where it maximised (N: Ti = 11.0 at. %). This N K-line contribution then fell steadily to position M1 (N: Ti = 3.1 at. %). A colour coded map of the N: Ti concentration was constructed for all grid positions analysed across the combinatorial film (Figure 3.4.7(b)). A trend was observed whereby the N : Ti (%) maximised toward the top-right section of the film at position I1; decreasing smoothly from top to bottom and more sharply from right to left. Given the proximity of position I1 to the NH_3 (N source) gas inlet during the deposition, it was not surprising that the greatest concentration of nitrogen was incorporated at this point. However, large

portions of the film contained little or no nitrogen doping such as Columns A, B and C, which incorporated no discernable levels of nitrogen.

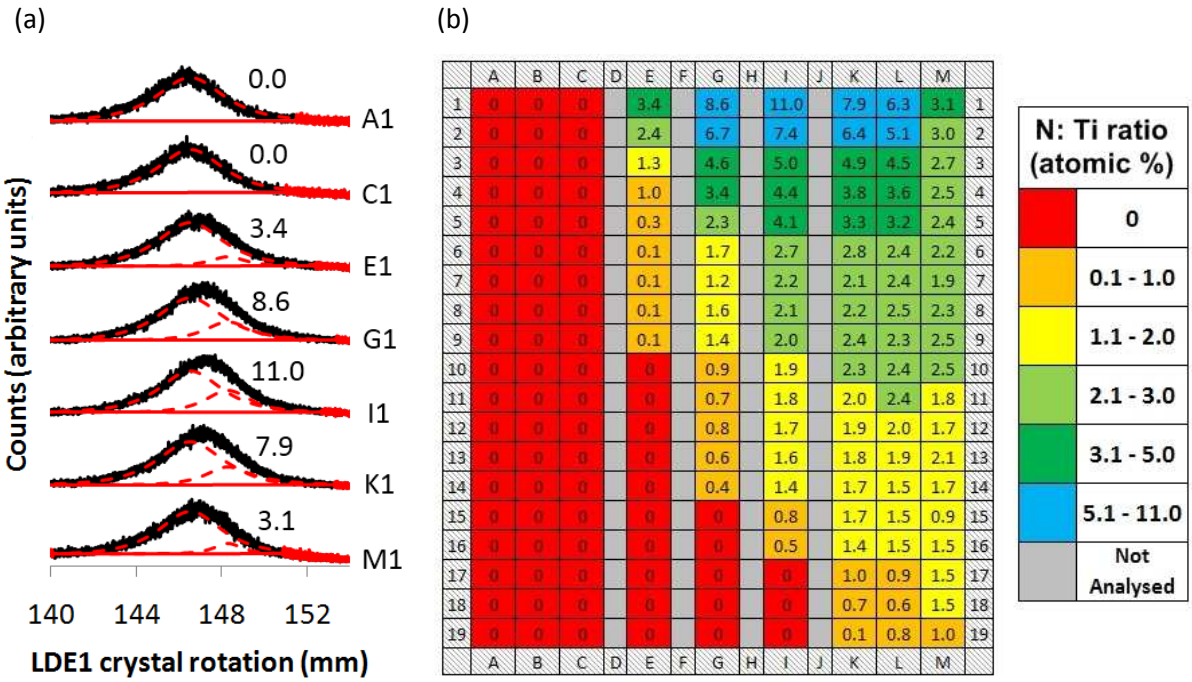

Figure 3.4.7: *(a) A stacked plot of the separation of nitrogen K-lines (148.2 mm) from titanium L-lines (146.5 mm) through wavelength dispersive X-ray (WDX) analysis for some example positions across Row 1 where values indicate the N: Ti at. % derived from Equation 2.14 and (b) a colour coded map of the N: Ti at. % derived for all positions analysed by this technique.*

3.3.3.6. X-ray photoelectron spectroscopy

The oxidation state and environment of constituent elements were investigated by X-ray photoelectron spectroscopy (XPS) at 7 locations distributed evenly across the top row of the film at positions A1, C1, E1, G1, I1, K1 and M1. Peak positions were calibrated to adventitious graphite impurities on the surface (284.5 eV).[157] The technique confirmed the presence of titanium, oxygen and nitrogen. Deconvoluting peaks within the N (1s) binding energy range revealed three distinct nitrogen environments (Figure 3.4.8). Two of these environments were present at all positions analysed; centred at binding energies of 399.7 eV and 407.0 eV. The species with a binding energy of 399.7 eV has been attributed in the literature to either the presence of surface-bound γ-N_2[199] or N_i-dopants.[198] Nitrogen/ titanium concentration mapping experiments using wavelength dispersive X-rays (Section 3.4.3.5) showed no presence of nitrogen at positions A1 and C1. Wavelength dispersive X-rays probe several microns deep into samples whereas X-ray photoelectron spectroscopy is a highly surface sensitive technique that probes the first few nanometres of a sample at best. It was therefore most probable that a thin layer of surface-bound γ-N_2 (N^0) was present at the surface. Such species are commonly found on thin-film samples that have been handled in air. Its presence was

made more plausible by the fact that the level of surface-bound γ-N_2 present was relatively constant across the samples analysed. The species with a binding energy of 407.0 eV was attributed to the presence of surface-bound NO_3^- species. It was present in relatively equal concentrations across the samples analysed, similar to the surface-bound γ-N_2 species. Such formation of NO_3^- (N^{5+}) species at the film surface is inherent with the synthetic method, where nitrogen exposed at the surface of the film is fully oxidised upon exposure to air.

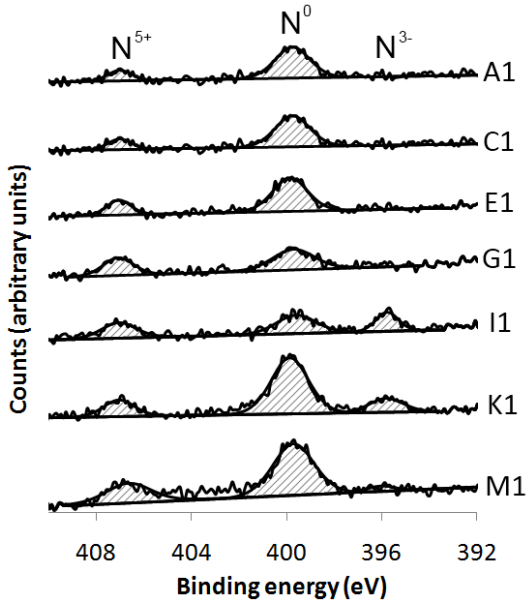

Figure 3.4.8: *Stacked N (1s) X-ray photoelectron spectra conducted at grid positions A1, C1, E1, G1, I1, K1 and M1. Deconvoluting peak areas revealed three distinct nitrogen environments; substitutionally doped N_s (N^{3-}), surface-bound γ-N_2 (N^0) and surface-bound nitrate NO_3^- (N^{5+}).*

The last environment was observed only at positions I1, K1 and M1 at a binding energy of 395.6 eV. This was attributed to the presence of N_s-doped (N^{3-}) species[118] as no formal presence of a separate cubic TiN[213] or pseudo-brookite $Ti_{3-\delta}O_4N$[112] phase was observed in either XRD patterns or Raman spectra. The N: Ti concentrations (at. %) were determined by multiplying XPS environment peak areas with corresponding sensitivity factors.[157] These N: Ti concentrations were listed alongside those acquired from WDX analysis for comparison (Table 3.4.2).

	N_s: Ti concentration (at. %)						
	A1	C1	E1	G1	I1	K1	M1
XPS Analysis	0.0	0.0	0.0	0.0	7.4	6.3	5.5
WDX Analysis	0.0	0.0	3.4	8.6	11.0	7.9	3.1

Table 3.4.2: *N_s: Ti concentration (at. %) determined from X-ray photoelectron spectroscopy (XPS) analysis at grid positions A1, C1, E1, G1, I1, K1 and M1 compared alongside those determined from wavelength dispersive X-ray (WDX) analysis.*

The levels of N_s-doping (N^{3-}) seen in XPS studies were typically lower than those seen in WDX studies. Although this may have been due to the lower detection sensitivity of XPS, especially for the lighter elements such as nitrogen, this result also suggested that N_s-doping may have been more favoured in the bulk due to surface segregation effects.

3.4.3.7. Scanning electron microscopy

Scanning electron microscopy (SEM) was conducted at the surface of grid positions A1, C1, E1, G1, I1, K1 and M1. Grainy morphologies were observed, where the average particle size decreased transitionally from position A1 to M1 (Figure 3.4.9). This indicated that film-crystallinity decreased across the row from A1 to M1.

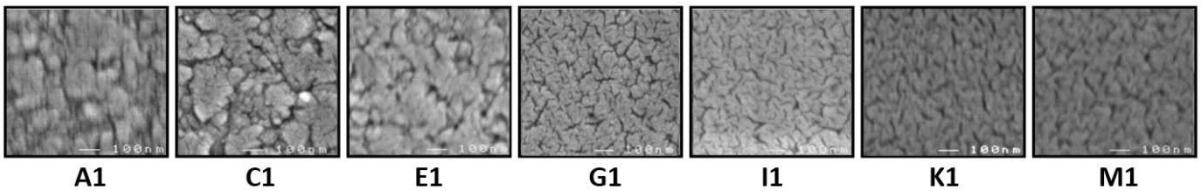

Figure 3.4.9: *Scanning electron microscopy (SEM) images of the film-surface at grid positions A1, C1, G1, I1, K1 and M1. Each image represents a width of 800 nm.*

Of-cuts at grid positions A11, C11, E11, G11, I11, K11 and M11 were mounted side-on for further investigation by SEM. Crystallites were oriented primarily in one direction, concurring with the preferred orientation growth demonstrated by X-ray diffraction analysis (Section 3.4.3.2). The film thickness was also determined at each grid positions analysed and compared with those acquired through our film-thickness mapping method (Table 3.4.3). A strong degree of linear correlation was observed ($r^2 = 0.92$).

	Film-thickness (nm)						
	A11	C11	E11	G11	I11	K11	M11
Mapping method	510 (10)	590 (10)	640 (10)	700 (10)	710 (10)	710 (10)	630 (10)
SEM	520 (20)	570 (30)	630 (50)	680 (30)	710 (30)	740 (30)	660 (40)

Table 3.4.3: *Film-thicknesses (nm) determined from scanning electron microscopy (SEM) analysis of side-mounted off-cuts at grid positions A1, C1, E1, G1, I1, K1 and M1 compared alongside those determined from our film-thickness mapping method (Section 3.3.3.4) .*

3.4.3.8. Reaction chemistry

A combinatorial N_s-doped TiO_2 thin-film with graded levels of nitrogen doping ($0 \leq N_s$: Ti ≤ 11 %) as well as composite phase contribution ($0 \leq$ anatase $TiO_2 \leq 100$ %, $0 \leq$ rutile $TiO_2 \leq 41$ %) was formed by combinatorial APCVD. The precursor temperature and carrier gas flow rate was adjusted to achieve the reagent mass flow rates specified in Table 3.4.1.[200] From our phase mapping (Section 3.4.3.3) and

nitrogen/ titanium concentration mapping (Section 3.4.3.5) experiments the average phase contribution was found to be 93: 7 anatase TiO_2: rutile TiO_2 and 1.4 at. % nitrogen doping respectively. This corresponded to an average O: Ti ratio of 1.98. As the molar ratio of the oxygen source (ethyl acetate): titanium source ($TiCl_4$) was in a 1.0: 1.0 ratio, the oxygen source was the limiting reagent in the formation of the TiO_2 matrix. This was fundamental to the quality of the films produced, as higher levels of ethyl acetate can cause carbon contamination.[214] In mapping the nitrogen dopant level (Figure 3.4.7(b)), the anatase TiO_2: rutile TiO_2 phase contribution (Figure 3.4.5(b)) and film-thickness (Figure 3.4.6(b)), the reaction rate of each precursor at 171 grid positions (over a 0.5.cm^2 area) could thus be derived (Figure 3.4.10).

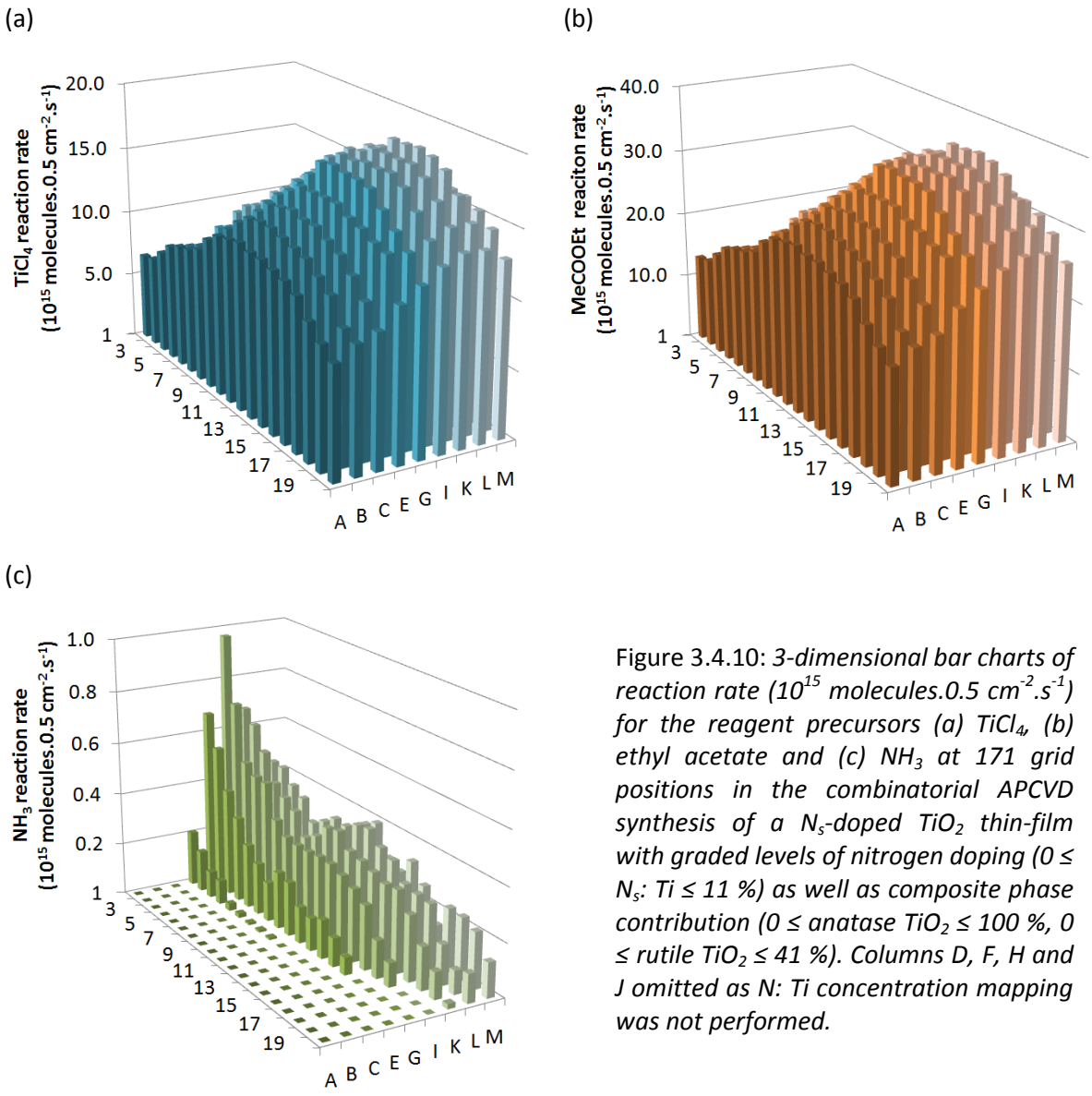

Figure 3.4.10: *3-dimensional bar charts of reaction rate (10^{15} molecules.0.5 cm^{-2}.s^{-1}) for the reagent precursors (a) $TiCl_4$, (b) ethyl acetate and (c) NH_3 at 171 grid positions in the combinatorial APCVD synthesis of a N_s-doped TiO_2 thin-film with graded levels of nitrogen doping ($0 \leq N_s$: Ti $\leq$ 11 %) as well as composite phase contribution (0 $\leq$ anatase $TiO_2 \leq$ 100 %, 0 $\leq$ rutile $TiO_2 \leq$ 41 %). Columns D, F, H and J omitted as N: Ti concentration mapping was not performed.*

We assumed anatase TiO_2 and rutile TiO_2 to have densities of 3.89 g.cm^{-3} and 4.23 g.cm^{-3} respectively in order to determine these reaction rates.[201] As nitrogen/ titanium concentration mapping was not

performed down Columns D, F, H and J, the reaction rates could not be determined at these positions.

The reaction rates of $TiCl_4$ and ethyl acetate showed a similar trend, peaking near the middle-right section. As the reaction was conducted in a cold-walled reactor, the substrate was marginally hotter at the centre of the film than at the edges by ≈ 25 °C. Film growth was most rapid near the centre of the film, peaking at position L13 with a growth rate of 12.4 $nm.s^{-1}$; more than 1.5 times more rapid than the average growth rate of 8.0 $nm.s^{-1}$. As the reactions of $TiCl_4$ and ethyl acetate were most rapid where the film was hottest and not local to their point of entry, the formation of TiO_2 was a reaction rate limited process.[108] However, the trend in reaction rate of NH_3 was very different to those of $TiCl_4$ and ethyl acetate, peaking near the top-right section of the film at position I1 (N: Ti = 11.0 at. %); decreasing sharply from left to right and more steadily from top to bottom the film. The sharp decrease in the level of N_s-doping across the combinatorial film from right to left was attributed to two factors: (i) the relatively slow speed at which the NH_3 precursor filled the reactor as 0.02 $L.min^{-1}$ was passed into a 0.25 L reactor cavity and (ii) the high flow of plain N_2 carrier gas (5.0 $L.min^{-1}$) that was pushed down the middle strip of the film. Although the plain N_2 flow served to increase the coverage of precursor reagents by pushing gas flows more rapidly down the substrate this would certainly have inhibited NH_3 gas flows from diffusing laterally across the substrate.

N_s-doped TiO_2 thin-films have been produced in a number of ways, where the main routes include ion bombardment[215] or gas-phase impregnation[216] of existing TiO_2 thin-films or complete growth from sol-gel liquids[217,218] or gaseous precursors.[219] Thin-films of N_s-doped TiO_2 have also been achieved by APCVD using a variety of precursors.[209,220] However, the APCVD of N_s-doped TiO_2 through the reaction of $TiCl_4$, ethyl acetate and NH_3 (the same set of precursors used in our combinatorial study) was first demonstrated by Yates *et. al.*[221] In their reactions, the nitrogen and titanium sources were introduced in a range of concentrations ranging from N: Ti = 7.5: 1 to 9.2: 1. In our combinatorial formation of N_s-doped TiO_2, the nitrogen and titanium sources were introduced in a 0.7: 1 ratio. However, the highest level of N_s-doping achieved by Yates *et. al.* was only 4.59 at. %, which was far lower than the highest level of N_s-doping of 11.0 at. % (grid position I1) achieved here. Nevertheless, when comparing the reaction of a combinatorial film with that of a homogenous study, one should compare averages. In fact, the average level of N_s-doping observed across our combinatorial film was 1.35 at. %. This was still comparatively high given Yates *et. al.* used, at the very least, more than 10 times the level of NH_3 in their depositions. It was mentioned by Yates *et. al.* that their nitrogen source was introduced into the reaction at the same location as their titanium and oxygen sources. Although this produced a well-mixed flow of precursor vapours and the formation of

homogenous N_s-doped TiO_2 thin-films, it also allowed the precursors to react in the gas phase before entering the reactor and may have accounted for the discrepancies in the level of N_s-doping observed across both studies. Using a similar APCVD reaction of $TiCl_4$, ethyl acetate and t-butylamine as the nitrogen source (rather than NH_3) it was observed by Dunnill *et. al.* that a N: Ti source ratio above 0.5: 1 encouraged the formation of N_s-doped TiO_2,[30] which was also observed in our study. Although Hyett *et. al.* used analogous precursors to our own in their combinatorial APCVD synthesis of pure pseudo-brookite $Ti_{3-\delta}O_4N$ thin-films, no such phase formation was observed in our study and was attributed to their use of a higher N: Ti source ratio (1.5: 1) and deposition temperature (630 °C).[112]

When comparing the relative mass flows of each precursor into the reactor (Table 3.4.1) against the average reaction rate it was found that ethyl acetate reacted most efficiently. However, the reaction of NH_3 was ≈ 60 times less efficient than $TiCl_4$ and ≈ 110 times less efficient than ethyl acetate. This was in stark contrast to the reaction of t-butylamine with $TiCl_4$ and ethyl acetate investigated in the previous section (Section 3.3.3.6), where the reaction of the nitrogen source was, at most, only 7 times less efficient than any other precursor. As nitrogen insertion using t-butylamine occurs *via* thermal decomposition to NH_3 (Equation 3.1),[30] the difference in efficiency could not be attributed to a different precursor chemistry. However, the reaction of t-butylamine with $TiCl_4$ and ethyl acetate was conducted at a higher temperature of 630 °C, suggesting the insertion of nitrogen in TiO_2 held a relatively high activation energy barrier compared with the formation of TiO_2 alone.

Our phase mapping experiments quantified the contribution of the anatase TiO_2 and rutile TiO_2 phase composites for each of the 247 grid positions analysed. It was found that the bottom and middle-right sections of the combinatorial thin-film contained the highest contributions of the rutile TiO_2 phase, maximising at 41 % at grid position M15. This coincided with the region where the combinatorial film was most thick. As the formation of TiO_2 from $TiCl_4$ and ethyl acetate precursors is a reaction rate limited process, the rate of TiO_2 film formation should be most rapid where the substrate was hottest. Indeed, the formation of the more thermodynamically stable rutile phase of TiO_2 is favoured at more elevated temperatures[110] and would explain why a higher rutile TiO_2 composition was observed in the thickest regions of the combinatorial film.

By culminating reaction rate data, the overall combinatorial APCVD reaction for the formation of the N_s-doped TiO_2 thin-film with graded levels of nitrogen doping ($0 \leq N_s$: Ti ≤ 11 %) and composite phase contribution (0 ≤ anatase TiO_2 ≤ 100 %, 0 ≤ rutile TiO_2 ≤ 41 %) could be written as follows:

$$TiCl_4 + MeCOOEt + NH_3 \rightarrow TiO_{2-x}N_x\left(\text{anatase}_y\text{: rutile}_{1-y}\right) + \text{by products}\ (9.0\ \%) \quad (3.8)$$

where $0 \leq x \leq 0.11$ ($\langle x \rangle = 0.014$, $\sigma = 0.019$) and $0 \leq y \leq 0.41$ ($\langle y \rangle = 0.066$, $\sigma = 0.089$). An average molar ratio of $TiCl_4$: MeCOOEt: NH_3 = 1.0: 1.0: 0.73 was introduced in this combinatorial reaction over a glass substrate held at 500 °C (± 25 °C). As the reaction chemistry of 86 cm^2 over a total of 202 cm^2 of combinatorial film-space was investigated (Figure 3.4.10), the overall reaction efficiency in terms of the limit reagent was determined (9.0 %). This reaction efficiency, dominated by the formation of TiO_2, was almost half the efficiency compared with our combinatorial APCVD investigation of t-butylamine with $TiCl_4$ and ethyl acetate (Section 3.3.3.6). This reaction efficiency difference was attributed to the difference in reaction temperatures, where the reaction was more efficient at a higher deposition temperature. Although it has been suggested that the APCVD reaction of $TiCl_4$ and H_2O precursors is a lower activation energy process than the APCVD reaction of $TiCl_4$ and ethyl acetate,[202] thin-films formed from $TiCl_4$ and H_2O are notoriously blotchy and have a tendency to flake. This is due to the greater propensity for the reaction of $TiCl_4$ and H_2O to proceed in the gas phase to TiO_2 rather than at the substrate surface. Ethyl acetate was chosen as the oxygen source in our APCVD reactions over H_2O as it forms robust and strongly adhered transparent thin-films when reacted with $TiCl_4$. It is also very volatile and cheap; ideal for up-scaled APCVD applications.

3.4.3.9. Photocatalytic activity mapping

A grid was drawn using a felt-tipped pen filled with a resazurin-based intelligent ink on top of the combinatorial film. 13 vertical lines and 19 horizontal lines were drawn so that the 247 points of crossing overlaid the 247 grid positions that were physically characterised, as shown in Figure 3.4.11.

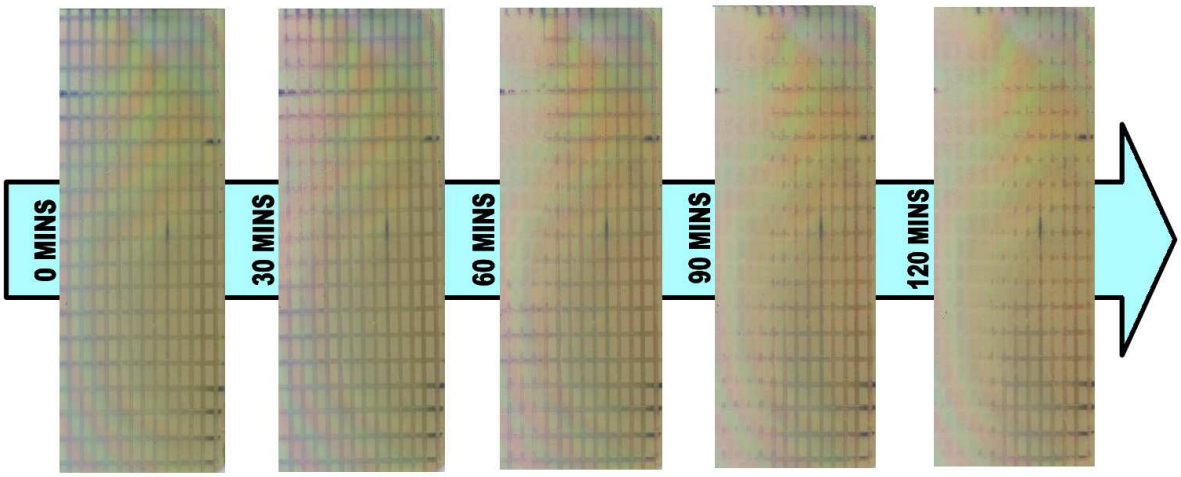

Figure 3.4.11: *A time-line of the photo-reduction reaction of a resazurin-based intelligent ink grid to a UVA (365 nm, 2 x 8W) light-source. The grid was drawn so that the 247 crossing points overlaid the 247 grid positions that were physically characterised across the combinatorial film (Figure 3.3.2).*

The combinatorial film and ink overlayer were photographed between periods of UVA-irradiation (365 nm, 2 x 8 W) that initiated and propagated photocatalysis until most of the ink overlayer had been bleached. A non-homogenous yet smooth transition from royal blue to pink to colourless was observed and represented the photo-reduction of the redox dye from resazurin to resorufin to its colourless intermediate respectively. The top-left section of the film was, by eye, the most photocatalytically active region of the combinatorial film, turning the dye pink after ≈ 30 mins and completely decolouring it after ≈ 60 mins exposure to UVA. The bottom-left and top-right sections of the film were successively slower in bleaching the dye, with the bottom-left section bleaching the dye after ≈ 90 mins and the top-right section bleaching the dye after ≈ 120 mins. However, the bottom-right section of the film was exceedingly the least photocatalytically active region of the film and only just began to turn the dye pink after 120 mins of UVA exposure.

The red component of digital colour at each of the 247 grid positions was extracted using the software we developed (RGB Extractor$^{(c)}$). Most grid positions, except for those within the bottom-right section of the film, showed an increase in the red component of digital colour until a point of plateau. This represented the point of complete photo-reduction of resazurin to resorufin (Equation 2.20). The time at which the plateau was reached varied with the differing degrees of photocatalysis seen by eye. These red components of digital colour were fit to a Boltzmann model (Table 2.2) and the time taken for each grid position to reach a plateau was determined. The longer it took for the red component to plateau, the less active the photocatalyst was. An example of this fitting for positions along Row 6 is shown in Figure 3.4.12(a). Across Row 6, the time taken for the red component of digital colour to plateau generally increased from 47 mins at A6 to 182 mins at L6; quantifying the trend seen by eye. After fitting the change in red component of digital colour to a Boltzmann model for all 247 grid positions ($\langle r^2 \rangle$ = 0.98, σ = 0.01), a contour map of all of the times taken to reach a plateau was constructed (Figure 3.4.12(b)).

The numbers quantified the trends observed by eye with: (i) the quickest times (≈ 60 mins), indicative of a more rapid photocatalyst, seen in the top-left region of the combinatorial film, (ii) the next quickest times (≈ 100 mins) seen in the bottom-left region, (iii) the next quickest times (≈ 150 mins) seen in the top-right region and (iv) the slowest regions seen in the bottom-right region, where the full photo-reduction of resazurin did not occur within the time-frame of the experiment. Through phase mapping, the bottom-right region was found to be most highly composed of rutile TiO_2 (Figure 3.4.5(b)). High components of rutile TiO_2 were local to the region where the rate of photocatalysis was slowest. Contrastingly, the left region of the combinatorial film was primarily composed of the anatase TiO_2 phase where the highest rates of photocatalysis were observed. However, some level of

N_s-dopant was also present in the bottom-right region, which may have adversely contributed to the material's photocatalytic function.

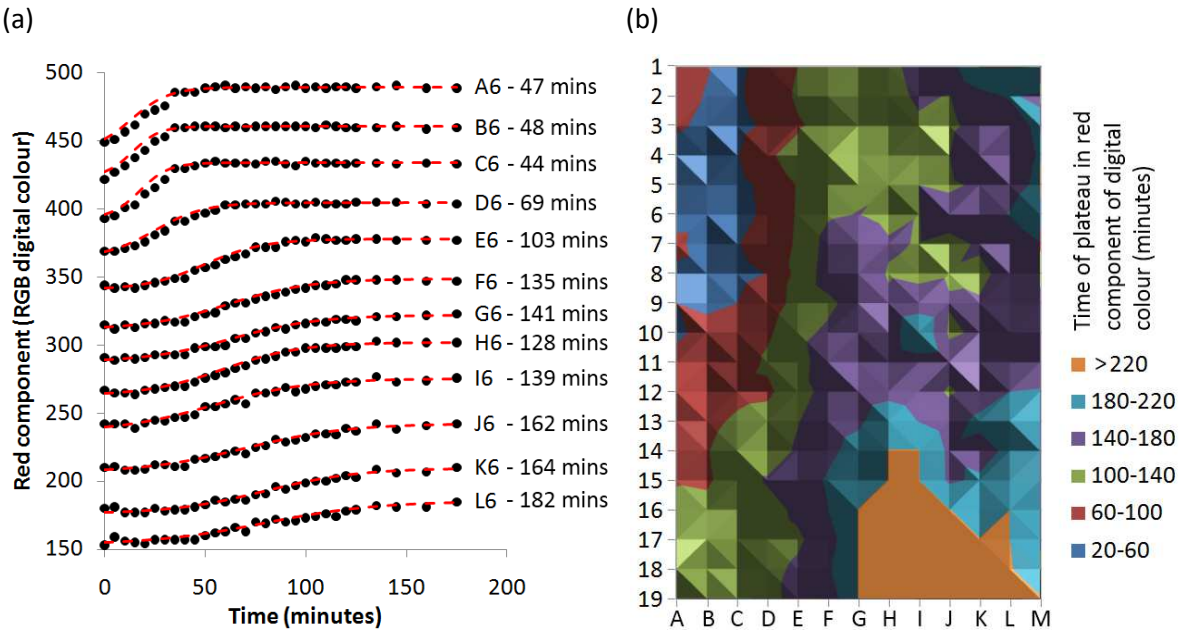

Figure 3.4.12: *(a) Stacked plot of red components of digital colour (arbitrary units) extracted for positions along Row 6 that have also been fit to a Boltzmann model (<r^2> = 0.99, σ = 0.01) to precisely extract the times in which a plateau was reached and (b) contour map of the time taken (minutes) for the red component of digital colour to reach a plateau for all 247 grid positions analysed, thereby indicating the complete photo-reduction of a resazurin-based intelligent ink overlayer to UVA light.*

In order to make a fair comparison on the effect of phase contribution on the rate of photocatalysis, positions from Row 15 to Row 19 were investigated as they contained very low levels of N_s-doping or none at all where 1.7 ≤ N_s: Ti (at. %) ≤ 0.0, <N_s> = 0.40, σ = 0.59. The rutile TiO_2 component was plotted against the time taken to reach a plateau in the red component of digital colour (Figure 3.4.13(a)). As the rutile TiO_2 component increased, a general trend for an increasing length of time for the red component of digital colour to reach a plateau was observed. At positions with low levels of rutile TiO_2 (0 – 5 %), the red component plateaued in ≈ 100 mins. At higher levels of rutile TiO_2 phase component (> 10 %), the red component generally plateaued in ≈ 200 mins or above. In fact, in this region there were several occasions where the red component of digital colour did not yet reach a plateau (marked as red dots in 3.4.13(a)). From these trends we can see that the rate of photocatalysis of almost phase pure anatase TiO_2 was generally double that of composites with just 10 % or more rutile TiO_2 component. To verify that this observed trend had nothing to do with the variation in film-thickness, the film-thickness of each grid position in Rows 15 to 19 were again plotted against the time taken to reach a plateau in the red component of digital colour. No discernable effect of film-thickness was observed. This was unsurprising given film-thickness

(<thickness> = 590 nm, σ = 99 nm) did not vary any near as much as rutile TiO_2 component (<rutile TiO_2> = 11 %, σ = 13 %) within this region. The trend in decreasing photocatalytic activity with increasing rutile TiO_2 component, where phase pure anatase TiO_2 was most active (Figure 3.4.13(a)), gave little credit to the proposed synergy of anatase TiO_2: rutile TiO_2 composites.

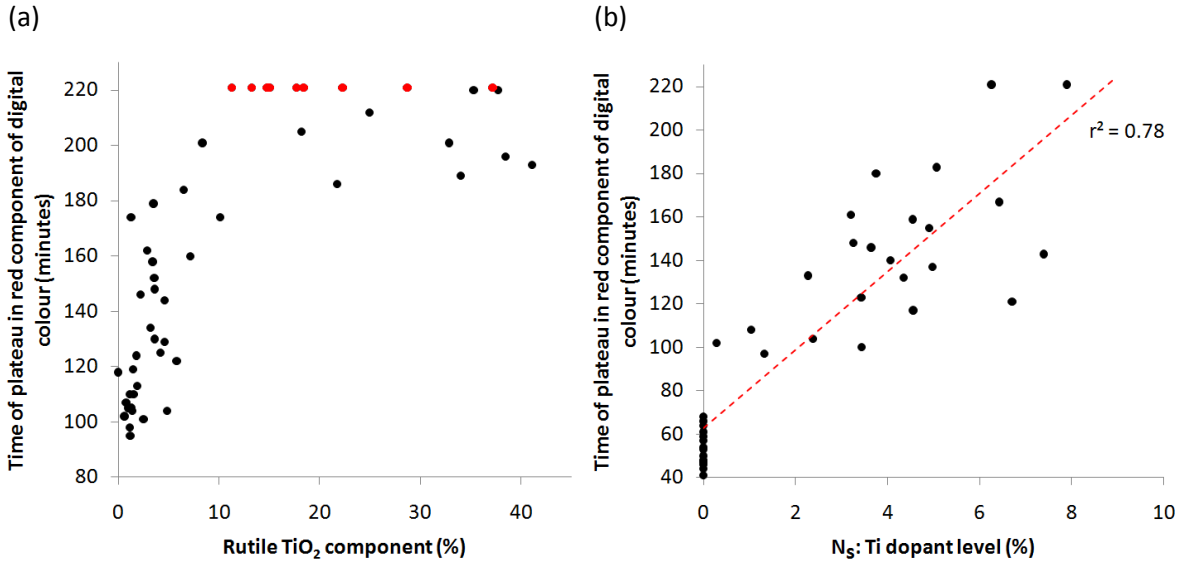

Figure 3.4.13: *Plots of the time taken to reach a plateau in the red component of digital colour (minutes) thereby indicating the complete photo-reduction of a resazurin intelligent ink overlayer to UVA light against (a) rutile TiO_2 component (%) for Rows 15 to 19; dots coloured red did not reach a plateau in the time-frame of the photocatalysis experiment and each represent some number above 220 minutes and (b) N_s: Ti dopant level (%) for Rows 1 to 5; where a linear relationship was observed with a reasonable degree of fit (r^2 = 0.78).*

To establish the effect of N_s-doping on the degree of UVA photocatalysis positions containing low levels of rutile TiO_2 component were investigated to avoid misconstruing any relationship. Therefore, grid positions within Rows 1 to 5, which contained no more than 5 % rutile TiO_2 at any point analysed (<rutile TiO_2> = 1.9 %, σ = 1.3 %), were assessed. The N_s-dopant level was subsequently plotted against the time taken to reach a plateau in the red component of digital colour (Figure 3.4.13(b)) for these positions. A general trend was observed whereby as the level of N_s-doping increased, the time taken to reach a plateau in the red component of digital colour also increased. The relationship held a linear correlation with a reasonable degree of fit (r^2 = 0.78). Therefore N_s-doping was shown to adversely affect the degree of photocatalysis within a primarily anatase TiO_2 doping regime. The time taken to reach a plateau in the red component of digital colour was plotted against film-thickness for the grid positions within Rows 1 to 5 to verify that this trend was strictly due to N_s-dopant levels. Once again, no relationship between film-thickness and photocatalysis was observed for the positions investigated, where a weak correlation factor of r^2 = 0.20 was observed. It is widely accepted that N_s-doping of TiO_2 induces a narrowing of the bandgap and shifts the energy required for photo-excitation toward the visible.[2] However, this bandgap narrowing would not have

necessarily given the N_s-doped portion of our combinatorial TiO_2 thin-film any advantage over the un-doped TiO_2 portions (E_{bg} = 3.0 – 3.2 eV) as a UVA light source (≈ 3.4 eV) was used. In fact, the light source carried enough energy to photo-excite any region of compositional/ phase-space. It was therefore the subtle balance between the photo-generation of electrons and holes and their recombination processes that affected the rate of photocatalysis in this case. Beranek *et. al.* recently demonstrated that the photo-generated electrons and holes in N_s-doped TiO_2 thin-films almost instantaneously recombine when placed in the dark, whereas those of pure anatase TiO_2 are stable for longer periods of time.[205] Duminica *et. al.* also found that nitrogen sites within N-doped TiO_2 thin-films provide a lower energy pathway for the recombination of electrons and holes.[220] With these factors in mind, it was not unexpected that the rate of photocatalysis should decrease with increasing levels of N_s-doping, as was observed in this combinatorial study (Figure 3.4.13(b)). Given the visible light induced enhancement of N_s-doped TiO_2 thin-films,[208,209,218] finding the optimum N_s-dopant level, where the best trade-off between the benefit of bandgap narrowing against the detriment of electron and hole recombination pathways would certainly be of interest. However, our photocatalytic activity mapping method did not work when applied to this combinatorial film using a white light source (GE lighting 2D fluorescent GR10q-835 white, 28 W) masked with an UV-filter (Optivex^{TM}). In fact, all positions across a hand-drawn intelligent ink grid bleached simultaneously after several hours irradiation (≈ 10 hours). This was attributed to two factors: (i) the intelligent ink was absorbing a significant portion of the visible light rather than the underlying semiconductor photocatalyst and (ii) the rate of air oxidation of the redox dye was most probably far more rapid than any visible light induced photo-reduction process.

The possible effects of preferred orientation were assessed in regards to the combinatorial film's photocatalytic activity. The degree of preferred orientation growth in the (101) plane of the anatase TiO_2 phase (Figure 3.4.4) maximised in the top-right section at 58 % (position L4), then had a region of next highest growth in the top-left section and minimised in the bottom-right and middle sections of the film. These changes in preferred growth did not seemingly match any trends in the changing photocatalytic activity across the combinatorial film. They did not match physical changes such as the variation in nitrogen/ titanium concentration and phase contribution either, however, a slight correlation between film-thickness was observed (r^2 = 0.59). The relationship was such that as the film-thickness increased, the degree of preferred orientation in the (101) plane decreased. This may have been due to some surface directional effect from the substrate that became less pronounced as films grew thicker.

Through characterising a combinatorial thin-film with our mapping techniques two physical-functional property relationships were established where both:

(i) increased N_s-doping of predominantly anatase TiO_2 phase materials and

(ii) increased rutile TiO_2 phase component in anatase TiO_2: rutile TiO_2 composites

cause detriment to UVA light photocatalysis. An approximately linear correlation was established for the detriment N_s-doping anatase TiO_2 whereby ≈ 2 at. % insertion halves the rate of photocatalysis relative to the unmodified region and ≈ 8 at. % insertion halves this furthermore. In fact, looking at the relative effects both properties had on photocatalysis, an increased rutile TiO_2 phase component caused a greater detriment to UVA photocatalysis than increased N_s-doping over the regimes investigated ($0 \leq N_s$: Ti (at. %) ≤ 11, $0 \leq$ rutile TiO_2 (%) ≤ 41).

3.4.4. Conclusions

A combinatorial N_s-doped TiO_2 thin-film with graded levels of nitrogen doping ($0 \leq N_s$: Ti ≤ 11 %) as well as composite phase contribution ($0 \leq$ anatase $TiO_2 \leq 100$ %, $0 \leq$ rutile $TiO_2 \leq 41$ %) was formed by the combinatorial APCVD of $TiCl_4$, ethyl acetate and NH_3 precursors at 500 °C on glass. By introducing the precursors at different points inside the reactor, a N: O source concentration gradient was imposed, creating a range of deposition conditions in a single experiment. This induced the formation of a graded range of N_s-doping levels. The slight variation in reactor temperature, which is a nature of cold-walled depositions, induced a heating gradient across the substrate and the formation of a film with graded thickness and anatase TiO_2: rutile TiO_2 phase composition. We applied our high-throughput characterisation methods to 247 allotted positions over a 13 x 19 grid (vertical x horizontal). The preferred orientation, phase, thickness, nitrogen/ titanium concentration and photocatalytic activity at each of the 247 grid positions across the combinatorial film were rapidly deduced. By correlating the physical properties of the film against the rates of photocatalysis it was identified that: (i) increased N_s-doping within anatase TiO_2 imposes detriment to UVA light photocatalysis and (ii) increased rutile TiO_2 phase component in anatase TiO_2: rutile TiO_2 composites imposes further detriment to UVA light photocatalysis over the dopant and phase contribution ranges investigated. Our results gave little credit to the proposed synergistic effect of anatase TiO_2: rutile TiO_2 composites. The mode for worsened UVA photocatalysis through the N_s-doping of TiO_2 was attributed to the lower energy pathway these dopant centres provide for the recombination of photo-generated electrons and holes.

In the following section we will use combinatorial APCVD in conjunction with our characterisation mapping methods to investigate the UVA and visible light photocatalysis of a mixed N_s/ N_i-doped to pure N_i-doped anatase TiO_2 thin-film with graded levels of nitrogen doping ($0 \leq N_s$: Ti ≤ 8.4 %, $0.57 \leq N_i$: Ti ≤ 3.3 %). As there is little consensus on which type of nitrogen dopant produces the more active photocatalyst, the effect that either type of nitrogen dopant imposes on the material's UVA and visible light photocatalysis will be thoroughly assessed and the type of dopant that produces the more photocatalytically active material suggested.

3.5. N_s and N_I-doped anatase TiO_2

3.5.1. Introduction

Although the visible light photocatalysis of nitrogen doped TiO_2 was first reported by Sato *et. al.* in 1986,[207] little attention was paid to this material until its unique function was reported once again by Asahi *et. al.* in 2001.[118] Since then, nitrogen doped TiO_2 has been studied more than any other modified TiO_2 system.[2] Nevertheless, there is still little consensus in the literature as to the mode of improvement. For instance, many argue that substitutional (N_s) doping is the sole reason for the improvements in visible light photocatalysis whereas others argue that it is due to nitrogen dopants that lie in interstitial (N_i) sites.[30,209] More recently some have argued that it is due to the oxygen vacancies that form through nitrogen doping.[222] This is because, more often than not, nitrogen-doped TiO_2 photocatalysts contain some amount of both N_s and N_i dopants and it is difficult to distinguish which mode is the main or sole contributor to the observed improvement.[118,223,224] The situation is further worsened because determining the nature of the nitrogen dopant is not simple. Although electron paramagnetic resonance (EPR) has be used to determine the nature of the dopant, it can realistically only be applied to powders.[113,156] X-ray photoelectron spectroscopy (XPS) can be used to distinguish between N_s and N_i environments, but should be used in conjunction with sputtering tools to ensure the surface of the sample is free from γ-N_2 species absorbed at the surface, or false positives for the presence of N_i doping will result.[30]

To try and clarify which mode of bonding is responsible for the visible light photocatalysis observed in nitrogen doped TiO_2, the density of states for each mode of doping was investigated computationally.[206,222] The calculations showed how N_s-doping raises the valence band energy due to the overlap between nitrogen (2p) and oxygen (2p) orbitals and narrows the bandgap. The computational study of N_i-doping showed the formation of an inter-band state ≈ 0.74 eV above the valence band. When oxygen vacancies were introduced into the model, mid-gap states formed 0.14

eV below the conduction band.[225] The propensity to form oxygen vacancies (V_O) in nitrogen doped TiO_2 was also shown to increase relative to un-modified TiO_2, where the formation energy decreased by a factor of 7. In Di Valentin *et. al.*'s computational study of N_s-doped anatase TiO_2, the bandgap was shown to narrow by just 0.14 eV to 3.06 eV.[206] However, several experimental studies of N_s-doped TiO_2 have reported significantly lower bandgaps, ranging from 3.17 to 2.46 eV.[226-229] A summary of the changes to the density of states through nitrogen doping anatase TiO_2 is shown in Scheme 3.4.1.

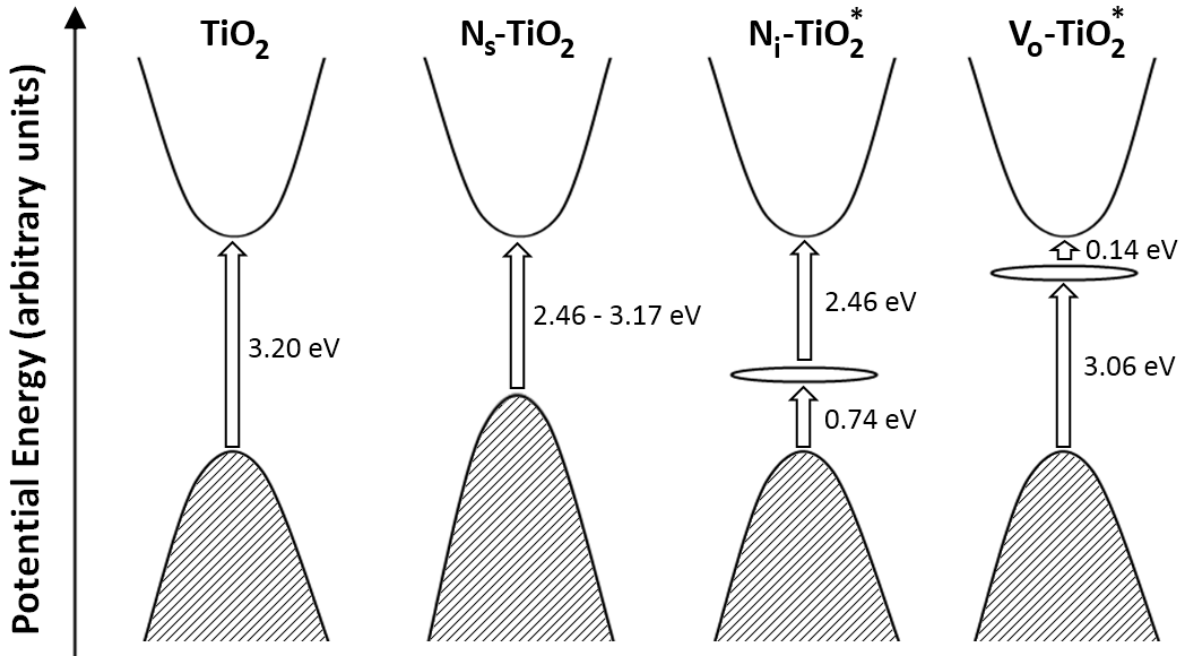

Scheme 3.4.1: *A summary of changes to the density of states of anatase TiO_2 upon introducing a nitrogen dopant. The shaded regions at the bottom represent valence bands and un-shaded regions at the top represent conduction bands. Materials marked with asterisks present energies reported from computational studies whereas those not marked were from experimental studies.*

In the case of N_s-doping, the associated bandgap narrowing allows lower energy light to produce photo-excitations in the material. However, for the case of N_i-doping, a dual-electron excitation process was suggested, where electrons are initially excited to the inter-band state (0.74 eV) and subsequently to the conduction band (2.46 eV).[230] Computational studies showed that either N_s or N_i doping of TiO_2 produced materials with the potential for visible light photocatalysis and did not quell the argument as to which mode was in fact responsible for the improvements observed experimentally.

A contrasting range of visible light photocatalytic activities have been reported for nitrogen-doped TiO_2 thin-film photocatalysts, from comparatively extensive improvements[118] to moderate[210,211] to even no activity at all.[221] Some have attributed this to the fact that no universal method is used to test the visible light photocatalytic activity. Although methylene blue solution was

tested more frequently than other test organics, it has been argued that methylene blue is not such a good indicator.[224] This is because of the dye's capacity to be discoloured not just through warranted photo-oxidation processes but also by reacting with photo-generated holes,[231] absorbing to the surface of the photocatalyst[161] and by forming a colourless dimer in slightly anaerobic or acidic conditions.[170] It is therefore of tantamount importance that samples be tested in the same manner for fair comparisons to be made.

Thin-films of N_s and N_i doped TiO_2 have been prepared in a variety of ways. Primarily N_i-doped TiO_2 has traditionally been achieved through sol-gel,[207,224] yet primarily N_s-doped TiO_2 is achieved in a number of ways including sputtering,[203] ion implantation,[204] atomisation[115] and pyrolysis.[205] However, both N_i and N_s-doped TiO_2 have also been achieved by APCVD.[30,221] Purely N_s-doped TiO_2 thin-films have been prepared by APCVD in two ways using either $Ti\{OCH(CH_3)_2\}_4$ and N_2H_4 as the nitrogen source[220] or $TiCl_4$, ethyl acetate precursors and NH_3 as the nitrogen source.[221] Purely N_i-doped TiO_2 thin-films have been prepared using $TiCl_4$, ethyl acetate and t-butylamine.[30] From these synthetic routes it would seem the type of nitrogen source plays a major role in the type of nitrogen doping achieved. For instance, t-butylamine is relatively more bulky than the other nitrogen sources that were applied and yielded primarily N_i-doped TiO_2, where it has been suggested that t-butylamine undergoes a thermal decomposition to NH_3 before insertion. It was therefore our belief that if a NH_3 precursor was diluted, N_i-doping might be achieved.

In this section we describe the combinatorial APCVD synthesis of a mixed N_s/ N_i-doped to pure N_i-doped anatase TiO_2 thin-film ($0 \leq N_s$: Ti ≤ 8.4 %, $0.57 \leq N_i$: Ti ≤ 3.3 %). This was formed using a triple source of precursors, with $TiCl_4$ as the titanium source, ethyl acetate as the oxygen source and NH_3 as the nitrogen source. The properties of up to 528 unique positions were investigated across the combinatorial film. The large variance in preferred growth, seen in X-ray diffraction patterns, was quantified by our preferred orientation mapping method (Section 2.3). The Scherrer equation was then applied to map film-crystallinity. Phase mapping confirmed the solitary presence of the anatase TiO_2 phase throughout the combinatorial film. The variation in film thickness was quantified by our film-thickness mapping method (Section 2.4). Atomic force microscopy (AFM) was used to map the degree of surface roughness and topography. Our photocatalytic activity mapping method (Section 2.6) was then used to identify regions of interest that were then investigated more thoroughly. The rate of photocatalytic oxidation of methylene blue in solution for each of the identified regions was first examined to confirm trends observed from our photocatalytic activity mapping method. The visible light photocatalysis of these regions where then investigated through their photocatalytic oxidation of a stearic acid overlayer. The mode (N_s/ N_i) and level of nitrogen doping within each

region was determined by X-ray photoelectron spectroscopy (XPS) depth profiling and their bandgap energies by UV-visible spectroscopy. The contributing effects of N_s and/ or N_i doping on the material's UVA and visible light photocatalysis are discussed and the more beneficial mode of doping proposed.

3.5.2. Experimental combinatorial film synthesis

A mixed N_s/ N_i-doped to pure N_i-doped anatase TiO_2 combinatorial thin-film ($0 \leq N_s$: Ti ≤ 8.4 %, $0.57 \leq N_i$: Ti ≤ 3.3 %) was formed by combinatorial APCVD. The film was deposited on float glass (225 × 40 × 3.2 mm; length × breadth × thickness) that contained an ≈ 50 nm thick barrier layer of SiO_2 at the substrate's surface to inhibit the diffusion of ions from the glass (i.e. Na, Mg, Ca) into the film. A schematic of the apparatus is shown in Figure 3.4.1.

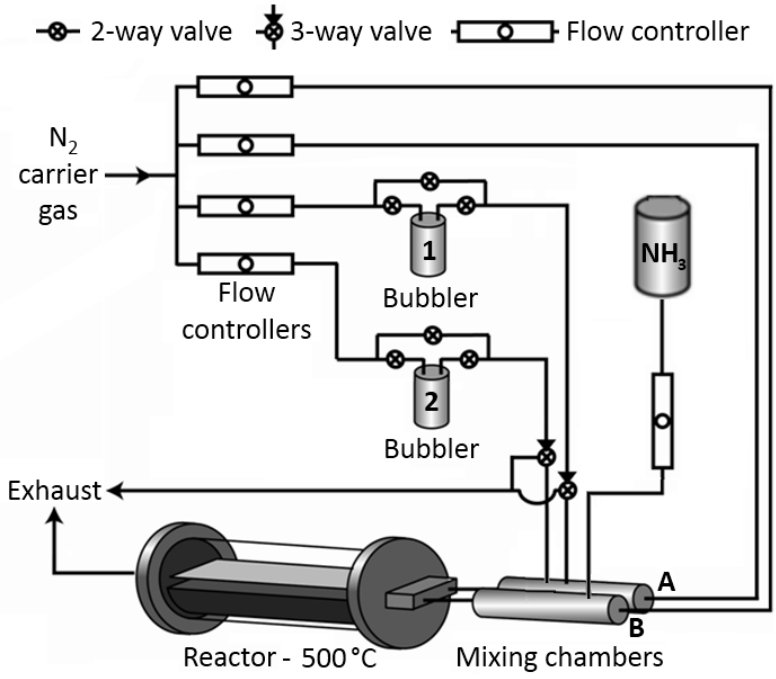

Figure 3.4.1: *Schematic of the combinatorial APCVD apparatus. The combinatorial film was synthesised from a combination of NH_3 gas direct from a cylinder and volatised liquid precursors carried from bubblers, where bubbler 1 contained $TiCl_4$ and bubbler 2 contained ethyl acetate. Of particular importance are the two separate entry points of the precursors into the reactor, where $TiCl_4$ and ethyl acetate entered the reactor via mixing chamber A and NH_3 entered the reactor via mixing chamber B. This created a gradient in the nitrogen source concentration horizontally across the substrate and a range of deposition conditions in a single experiment.*

The combinatorial film was synthesised from a combination of NH_3 gas direct from a cylinder (N source) and volatised precursors stored and carried from bubblers, where bubbler 1 contained $TiCl_4$ (titanium source) and bubbler 2 contained ethyl acetate (oxygen source). The volatility of each

precursor could be altered by adjusting the temperature of the bubbler. The vapours were transported from their bubblers by an inert N_2 gas to mixing chamber A, where they were then combined with a plain line flow of inert N_2 gas and carried into the cold-walled reactor (500 °C). The NH_3 gas (nitrogen source) was pumped directly into mixing chamber B where it was combined with a plain line flow of N_2 before being carried into the reactor. The separate entries of the nitrogen and oxygen sources created a horizontal gradient in the oxygen: nitrogen source concentration across the substrate and a range of deposition conditions in a single experiment. The parameters used to achieve the combinatorial film in this study are displayed in Table 3.4.1.

	Mixing Chambers		Bubblers		Gas cylinder
			1	2	
	A	B	$TiCl_4$	ethyl acetate	NH_3
Temperature (°C)	226	245	45	43	-
Flow rate (L min^{-1})	2.0	1.0	2.0	0.80	0.02
Vapour pressure (mm Hg)	-	-	32.9	215	-
Mass flow rate (mol min^{-1})	-	-	0.37×10^{-2}	1.29×10^{-2}	0.83×10^{-2}
Molar ratios	-	-	1.0	3.5	2.2

Table 3.4.1: *Temperatures (°C) of components and N_2 carrier gas flow rates (L min^{-1}) in the combinatorial APCVD synthesis of a mixed N_s/ N_i-doped to pure N_i-doped anatase TiO_2 thin-film ($0 \leq N_s$: $Ti \leq 8.4$ %, $0.57 \leq N_i$: $Ti \leq 3.3$ %). The carbon block inside the reactor was maintained at 500 °C during the 40 s deposition. Mass flow rates (mol min^{-1}) were derived from vapour pressure (mm Hg) curves to yield the molar ratio of each precursor relative to $TiCl_4$.*

A reference system that shows the exact locations of the positions analysed by each characterisation method is shown in Figure 3.5.2. The methods of characterisation that were applied to each grid position in this combinatorial system are shown beside the image. Further details of the experimentation and apparatus can be found in the experimental methods, Section 3.2.

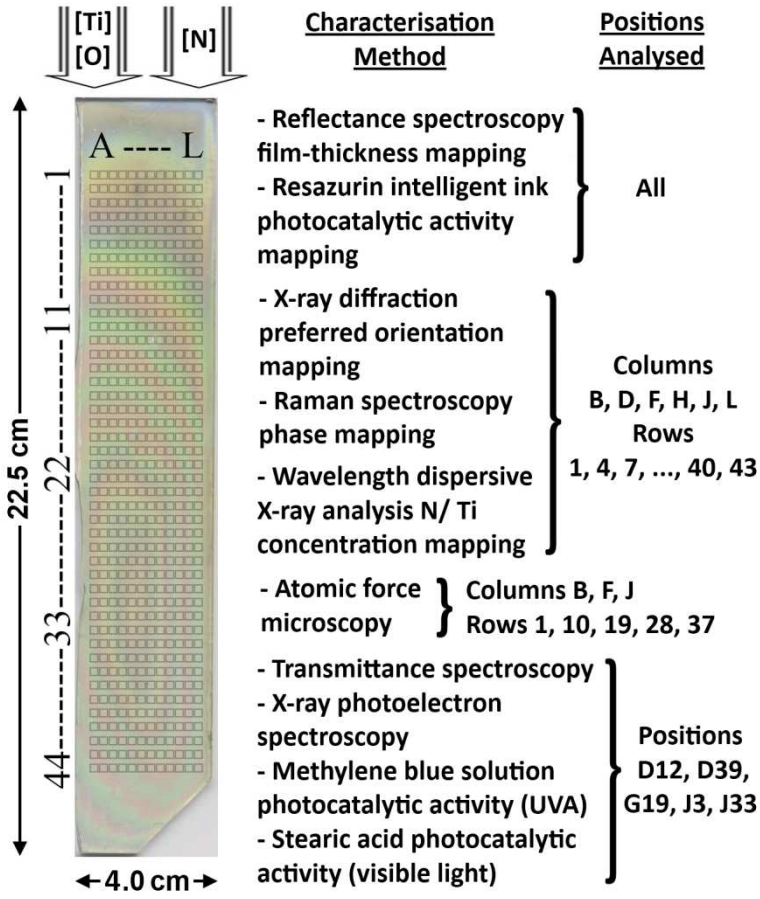

Figure 3.5.2: *Picture of the combinatorial thin-film and super-imposed grid reference system used throughout this section with the type of characterisation stated next to the image for each of the 528 unique grid positions (12 x 44; horizontal x vertical). The positions of the gas inlets relative to the glass substrate when the deposition took place inside the reactor are shown; with Row 1 lying closest to the gas inlets and Row 44 lying closest to the exhaust. Positions are spaced 0.4 cm apart in rows and 0.3 cm apart in columns.*

3.5.3. Results

3.5.3.1. Appearance

A mixed N_s/ N_i-doped to pure N_i-doped anatase TiO_2 combinatorial thin-film ($0 \leq N_s$: Ti ≤ 8.4 %, $0.57 \leq N_i$: Ti ≤ 3.3 %) was formed by combinatorial APCVD from reaction of $TiCl_4$, ethyl acetate and NH_3 at 500 °C. Interference fringes, characteristic of thin-films with high refractive indices were observed (Figure 3.5.2). This showed how the thickness varied across the combinatorial film. The contours of the fringes peaked within the middle-bottom section of the film and indicated the film was thickest in this region. The film also displayed a yellowish tint, characteristic of nitrogen doping in TiO_2.[30] The yellowish tint was visually most prominent in the top-right section of the film, decreasing smoothly in strength to a more transparent looking film in the bottom-right section of the film. This hinted at the

graded nature of nitrogen doping across the combinatorial film that was later confirmed by nitrogen/ titanium concentration mapping and X-ray photoelectron spectroscopy. The greatest levels of nitrogen doping coincided with the region of most prominent yellow tint. The film was adhesive and impervious to prolonged immersion in common solvents (water, acetone and isopropanol). The films all passed the Scotch$^{(R)}$ tape test and were impervious to scratching with a stainless steel stylus. However, the film and glass substrate could be scratched with a diamond tip. From the accumulated thicknesses determined by our film-thickness mapping method the average growth rate was 11.7 nm.s^{-1} (standard deviation = 4.5 nm.s^{-1}) at a substrate temperature of 500 °C.

3.5.3.2. Preferred orientation and phase mapping

Raman spectroscopy was performed at 90 unique locations spaced equally across the combinatorial film (Figure 3.5.2). All Raman patterns signified the presence of anatase TiO_2. Therefore, there was no need to apply our phase mapping method described in Section 2.2 for separating out individual phases. However, the degrees of preferred orientation and crystallinity were investigated at the same locations by X-ray diffraction. It should first be stated that all X-ray diffraction patterns featured solely the anatase TiO_2 phase ($I4_1/amdz$, a = 3.785 Å, c = 9.512 Å),[146] corroborating with evidence from Raman spectroscopy. Both Raman spectroscopy and X-ray diffraction indicated that films were highly amorphous in the top few rows of the combinatorial film, as the patterns were very weak. However, going down the combinatorial film, the intensity of patterns increased. An example of this phenomenon for the positions analysed in Column F is shown in Figure 3.5.3. The intensity of Raman patterns increased significantly from position F1 to F43. It is well known that the intensity of a Raman pattern depends on both the thickness[232] and crystallinity[233] of the sample. However, the width of a Raman active mode has been found to be entirely dependent on film-crystallinity, where, analogous to X-ray diffraction patterns, more narrow peaks indicate a more crystalline sample.[233] A closer inspection of our Raman patterns revealed a trend where the peaks narrowed going down the combinatorial film from Row 1 to Row 43. The most prominent E_g vibrational mode (147 cm^{-1}) for each Raman pattern was fit to a Lorentzian model to quantify this narrowing. It is well known that the average crystallite size of a material can be determined from the full width at half maximum of any diffraction peak by applying the Scherrer equation:[132]

$$\tau = \frac{K.\lambda}{\beta.\cos\theta} \qquad (3.9)$$

where τ is the average crystallite size, K is the shape factor (typically 0.9 for spherical crystallites), λ is the wavelength of the X-ray beam used, β is the full width at half maximum and θ is the Bragg angle of the diffraction peak.

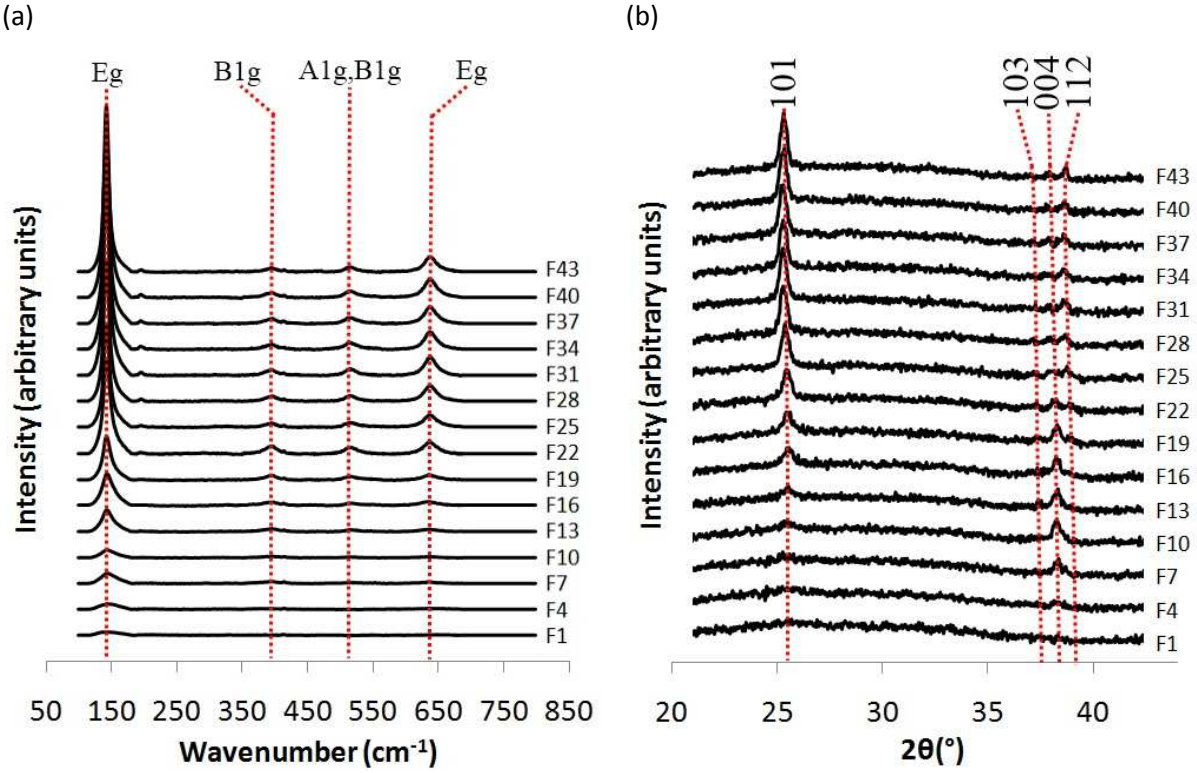

Figure 3.5.3: *Stacked (a) Raman spectra and (b) X-ray diffraction patterns of the 15 unique grid positions analysed along Column F.*

For the X-ray diffraction patterns that showed a peak in the most prominent (101) plane of diffraction in anatase TiO_2 (i.e. those diffraction patterns that were not of amorphous material), the peaks were fit to a Gaussian model to accurately determine their full width at half maximum and the average crystallite size by applying the Scherrer equation (Equation 3.9). A 3-dimensional bar chart of the average crystallite sizes for all positions analysed by X-ray diffraction is displayed in Figure 3.5.4(a). Positions within Rows 1 to 7 were too amorphous for their average crystallite sizes to be determined. A general trend was observed where crystallinity increased down the film, quantifying observations by eye (Figure 3.5.3(b)). From Rows 10 to 31 the average crystallite size increased steadily from ≈ 10 nm to ≈ 20 nm. From Rows 31 to 43, the average crystallite size did not significantly increase and had seemingly reached a plateau. Marginally higher film-crystallinity was observed in the bottom-left section of the film, peaking at 21.6 nm at position D43. These average crystallite sizes were plotted against their corresponding full width at half maximum attained by modelling the prominent E_g Raman vibrational mode (Figure 3.5.4.(b)). An approximately linear trend was observed with a reasonable degree of correlation ($r^2 = 0.79$).

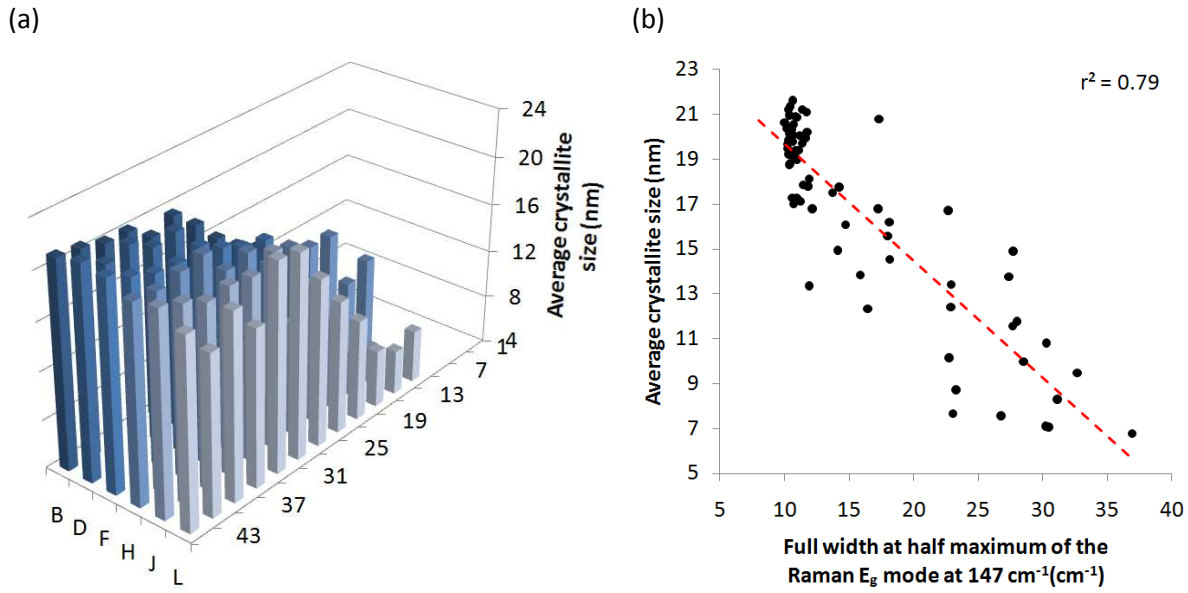

Figure 3.5.4: *(a) 3-dimensional bar chart displaying the average crystallite sizes (nm) determined by application of the Scherrer equation*[132] *to the (101) diffraction peaks of anatase TiO_2 and (b) a plot of the full width at half maximum of the prominent E_g vibrational mode (149 cm^{-1}) acquired from Raman spectroscopy against the corresponding average crystallite size (nm).*

Although it is well known that the widths of Raman vibrational modes are dependent on the crystallinity of the sample,[233] it is rarely used to determine film-crystallinity. This is because the widths have little physical meaning unless they are somehow calibrated to a direct measure of crystallinity in a sample. For instance, in their study of amorphous to microcrystalline transitions in silicon thin-films, Ledinsky *et. al.* used atomic force microscopy (AFM) to calibrate film-crystallinity to the widths of Raman vibrational modes.[234] There is certainly some benefit in knowing such relationships, as the time taken to acquire a Raman pattern, especially for strong Raman scatterers such as TiO_2, is minimal compared with the length of time required to acquire an X-ray diffraction pattern. The equation relating the width of the prominent E_g Raman vibrational mode (147 cm^{-1}) to the average crystallite size determined from this combinatorial study is shown below:

$$\tau\,(nm) = -0.52\,\gamma + 24.9 \qquad (3.10)$$

where τ is the average crystallite size (nm) and γ is the full width at half maximum (cm^{-1}).

Alternations in the relative heights of X-ray diffraction peaks were also observed. This was due to variations in the planes of preferred growth across the combinatorial film. For example, a transition from preferred growth in the (004) plane (positions F7 to F19) to preferred growth in the (101) plane (positions F22 to F43) was seen along Column F (Figure 3.5.3(b)). As the (101) plane was most intense and varied in height quite extensively across the film, the degree of preferred orientation was quantified for this plane using our preferred orientation mapping method (Section 2.3). The

percentage preference for growth in the (101) plane was determined using Equation 2.3. The results were normalised to a percentage scale and are shown as a 3-dimensional bar chart in Figure 3.5.5(a).

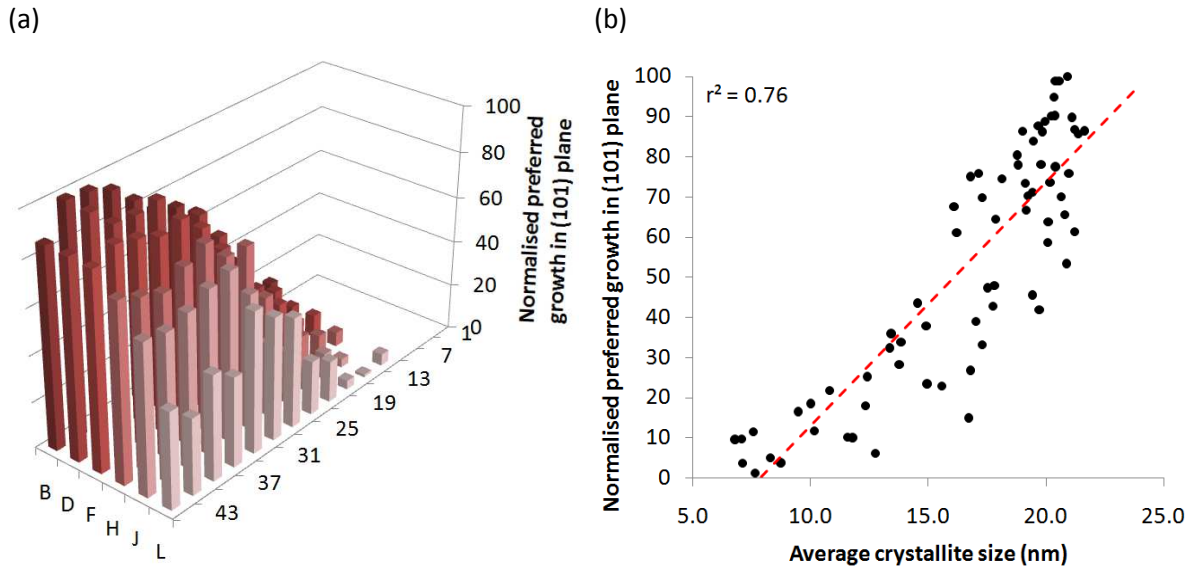

Figure 3.5.5: *(a) 3-dimensional bar chart displaying the normalised preferred growth in the (101) diffraction plane of anatase TiO_2 and (b) a plot of average crystallite size (nm) versus normalised preferred growth in the (101) plane (r^2 = 0.76).*

The greatest preference for film growth in the (101) plane was seen in the bottom-left section of the film, maximising at position B40. The preference for growth in this plane decreased smoothly in a diagonal fashion from the bottom-left toward the top-right section of the combinatorial film. The observed trend in the degree of preferred orientation was quite similar to that of crystallinity; where increasing crystallite size went hand in hand with a greater degree of preferred orientation in the (101) plane. The average crystallite size for each position across the combinatorial film was plotted against its corresponding degree of preferred orientation in the (101) plane (Figure 3.5.5(b)). An approximately linear correlation was observed with an acceptable degree of fit (r^2 = 0.76).

3.5.3.3. Nitrogen/ titanium concentration mapping and X-ray photoelectron spectroscopy

The overlapping emission of N K-lines and Ti L-lines from 90 grid positions, spaced evenly across the combinatorial film (Figure 3.5.2), were recorded using high resolution wavelength dispersive X-ray (WDX) analysis. Each contributing component then was separated in accordance with modelled Ti metal and BN standards through a deconvolution, as described in our section on nitrogen/ titanium concentration mapping (Section 2.5). With the contributing area of each emission known, by comparison with standards, the mass (%) of each element was determined (Equation 2.13). The N: Ti concentration (at. %) was then found using a simple conversion described in Equation 2.14. A 3-dimensional bar chart of all N: Ti concentrations determined across the combinatorial film are shown in Figure 3.5.6. The N: Ti (%) maximised in the top-right section of the film at position J1 (8.36 at. %).

Given the proximity of position J1 to the NH_3 (N source) gas inlet during the deposition (Figure 3.5.2), it was not surprising that the greatest concentration of nitrogen was incorporated at this point. Little variation in the N: Ti concentration was observed from left to right, however, going down the film from top to bottom, the concentration decreased in a relatively smooth fashion. This decreased to almost zero levels of N: Ti in the bottom section of the film (Rows 37 to 43). In fact, at two positions (B37 and D43) no presence of nitrogen was detected at all.

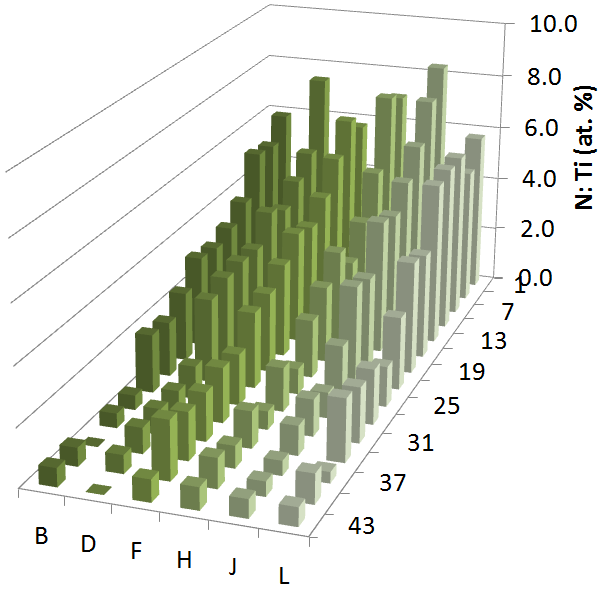

Figure 3.5.6: *3-dimensional bar chart of N: Ti concentration (at. %) that was determined by separating out the overlapping N K-line and Ti L-line emissions from wavelength dispersive X-ray analysis using our deconvolution method descried in Section 2.5.*

The oxidation state and environment of constituent elements for 5 locations distributed evenly across the combinatorial film were investigated by X-ray photoelectron spectroscopy (XPS) at positions D12, D39, G19 J3 and J33. Using an argon-ion gun, the surface of each sample was etched several nanometres deep and then analysed again. This cycle of etching and analysis was repeated four times. This revealed a compositional depth profile of each position. The technique confirmed the presence of titanium, oxygen and nitrogen in all samples at the surface and in the bulk. Deconvoluting peaks within the N (1s) binding energy range revealed three distinct nitrogen environments (Figure 3.5.7). Example spectra of the most heavily N_s-doped (J3) and N_i-doped (J33) positions analysed, including their depth profiles, are shown in Figure 3.5.7. At the surface of all samples analysed, a peak at 407.0 eV was observed. When the surface of the film was etched, this environment was not seen in the bulk and was therefore present only at the surface. This environment was attributed to the presence of surface-bound NO_3^-.[235] It was present in relatively equal concentrations across the samples analysed where NO_3^- : Ti ≈ 3.5 at. %. Such formation of NO_3^- species at the surface of the film is inherent with the synthetic preparation method, where nitrogen

exposed at the surface of the film is fully oxidised when the film is first exposed to air. All positions analysed, except for position J33 (Figure 3.5.7(b)), showed a peak at 395.6 eV relating to the presence of a highly reduced (N^{3-}) nitrogen species. This was attributed to the presence of N_s-doped (N^{3-}) species[118] as no formal presence of a separate cubic TiN[213] or pseudo-brookite $Ti_{3-\delta}O_4N$[112] phase was observed in either XRD patterns or Raman spectra. The percentage presence of N_s-doping was found to increase further into the sample though depth profiling.

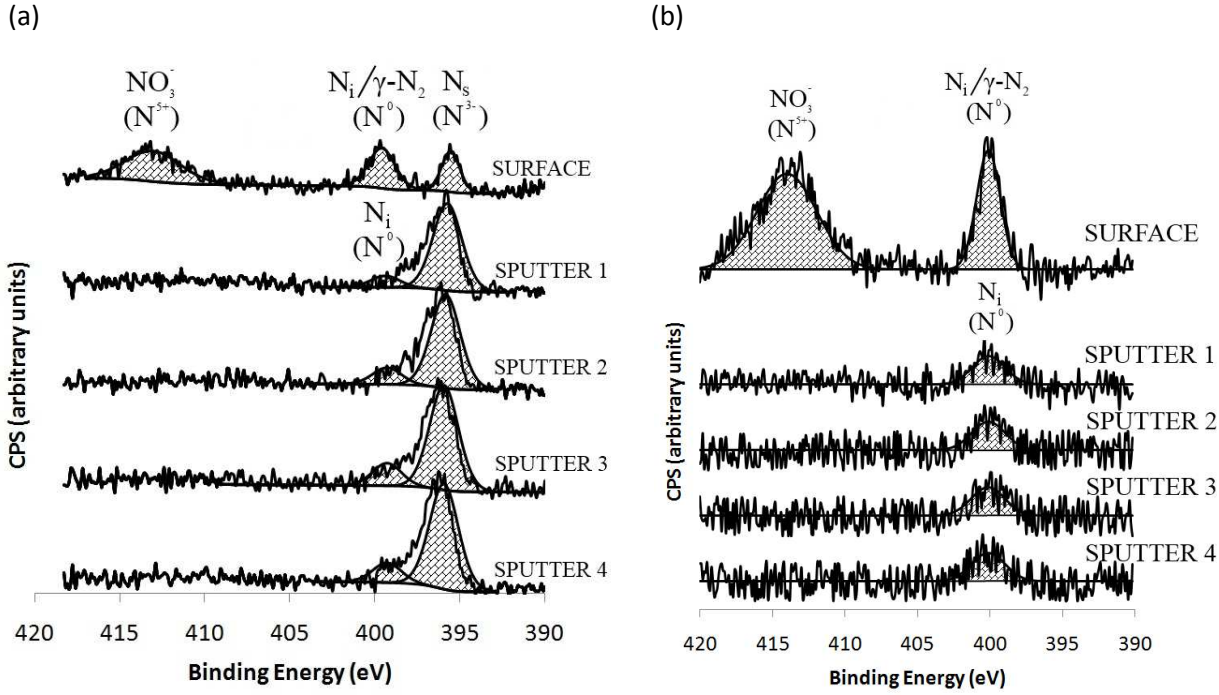

Figure 3.5.7: *The X-ray photoelectron spectrum in the N (1s) binding energy (390 – 420 eV) region of the surface and with each subsequent sputter cycle (Ar-ion gun, 30 s) of positions (a) J3 and (b) J33. Deconvoluting peak areas revealed three distinct nitrogen environments; substitutionally doped N_s (N^{3-}), surface-bound γ-N_2 (N^0) and surface-bound nitrate NO_3^- (N^{5+}).*

The last peak, observed at 399.7 eV, was observed in all samples. In the literature, this has been attributed to the presence of either surface-bound γ-N_2[199] or N_i-dopants.[198] Upon depth profiling, the presence of this environment diminished. As γ-N_2 can only be present at the surface of a material, the presence of this environment after etching confirmed the presence of N_i-doping in the material bulk. The fact that the environment decreased in area so much after sputtering was due to the heavy presence of γ-N_2 at the surface, similar to the surface-bound NO_3^- species observed, where such γ-N_2 species are common for thin-film samples that have been handled in air. The N: Ti concentrations (at. %) were determined by multiplying XPS environment peak areas with corresponding sensitivity factors.[157] The level of N_s and N_i doping for each position was taken as the average presence of each environment from sputter 1 to 4. The assumed error in each value was taken as the standard deviation of the presence of each species from sputter 1 to 4. These N_s and N_i doping levels (N: Ti at.

%) are listed alongside those acquired from wavelength dispersive X-ray (WDX) analysis of their next nearest neighbouring position in (Table 3.5.2) for comparison.

	XPS			WDX
	N_s	N_i	N_s+ N_i	(N_s+ N_i)
D12	4.0 ± 0.90	0.86 ± 0.15	4.9 ± 0.91	4.12 ± 0.50 (D13)
D39	0.59 ± 0.12	0.57 ± 0.21	1.2 ± 0.24	0.64 ± 0.50 (D40)
G19	2.7 ± 0.56	0.67 ± 0.23	3.4 ± 0.61	3.35 ± 0.50 (F19)
J3	8.4 ± 0.67	1.6 ± 0.43	10 ± 0.80	7.46 ± 0.50 (J4)
J33	0.0 ± 0.00	3.3 ± 1.15	3.3 ± 1.15	1.03 ± 0.50 (J34)

Table 3.5.2: *A table listing the levels of N_s and N_i doping (N: Ti at. %) found in the five positions analysed by XPS depth profiling alongside the doping levels determined by WDX analysis of their next nearest neighbouring position analysed (position stated in brackets) for comparison.*

As WDX analysis can only distinguish elemental composition and not environment, the N: Ti concentrations that were determined could only be listed as a total of the contribution of N_s and N_i doping detected in the material bulk. The error in deriving the N: Ti concentration level from the separation of overlapping N K-lines and Ti L-lines was assumed to be 0.5 at. % (Section 2.5). The error in the levels of N_s and N_i doping from XPS analysis were relatively low when considered as a percentage of the corresponding value (generally < 20 %). This demonstrated how the level of each nitrogen environment did not change much with sputter depth. Position J3 showed the highest level of N_s-doping of the samples analysed by XPS (N_s: Ti = 8.4 ± 0.67 %). Position J33 showed the lowest, with no N_s-doping present at all. In contrast, the highest level of N_i-doping was observed at J33 (N_i: Ti = 3.3 ± 1.15 %). The total level of N_s and N_i doping found for each position in XPS studies were summed. Position D39 showed the lowest total level of nitrogen doping of all 5 positions analysed. This was attributed to the fact that this position lay furthest from the gas inlet where the nitrogen source (NH_3) flowed into the reactor during the deposition. Looking at all positions analysed, wide ranging levels of nitrogen doping from $0.0 \leq N_s$: Ti (at. %) ≤ 8.4 to $0.57 \leq N_i$: Ti (at. %) ≤ 4.3 were present. The total level of nitrogen doping found in both XPS and WDX studies were compared by plotting the values from Table 3.5.2 in Figure 3.5.8. A strong linear correlation was observed between the two methods of deriving nitrogen content ($r^2 = 0.90$). However, those derived from XPS analysis tended to over predict the total nitrogen doping level compared with those derived by WDX analysis by ≈ 15 – 25 %. Although this may have been due to a culmination in the relative errors of each method, it may have also been due to some surface segregation effects, where a greater level of nitrogen doping may have been achieved nearer to the surface of the film that was probed more specifically by XPS.

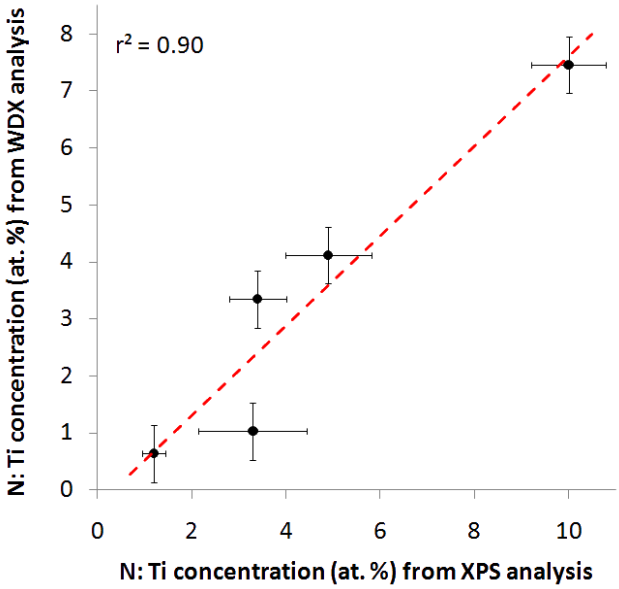

Figure 3.5.8: *A plot of the total N: Ti concentration (at. %) determined by XPS for the 5 positions analysed across the combinatorial film against those of the next nearest neighbouring positions determined by WDX analysis. A strong linear correlation was observed (r^2 = 0.90).*

3.5.3.4. Film-thickness mapping

The reflectance spectrum of each colour band due to interference was recorded from 300 – 2500 nm at the positions designated in Figure 3.5.9(a). As the position of a transmittance maximum occurs analogous to where a reflectance minimum occurs (Figure 2.3.2(a)), the Swanepoel method for determining the thickness of thin-films could be applied.[122] The method determines film-thickness with knowledge of the positions at which interference maxima and minima occur, combined with the spectral dependence of the refractive index of the material. However, the combinatorial thin-film under study contained a range of N_s and N_i dopant levels across the entire thin-film. Therefore, the analysis of colour bands at positions containing high levels of nitrogen doping could not be avoided, especially near the top-sections of the film where the greatest levels of nitrogen doping were achieved. The effect that high levels of mixed N_s and N_i doping would have upon the spectral dependence of the refractive index of the anatase TiO_2 host was not known to us as such specific information was not available in the literature. It was therefore assumed, as a starting point, that the spectral dependence of the refractive index for pure anatase TiO_2 be used to determine film-thickness using the Swanepoel method. A high degree of fit for all of our Swanepoel plots (Figure 2.3.2(b)) was still observed, where $r^2 > 0.98$ for all colour bands analysed (Figure 3.5.9(a)). This was a little surprising, especially for the top-most colour band analysed, centred at around position D1, that contained such high levels of nitrogen doping (N: Ti = 7.46 at. %). This result indicated that nitrogen doping of anatase TiO_2 little affects the permittivity of light through the material compared to un-doped anatase TiO_2, even though the band structure is modified. With the thickness at the centre of

each colour band known, the thickness at the colour boundaries and then the 528 designated grid positions (Figure 3.5.2) were calculated by approximating linear growth between the colour boundaries (Section 2.4). A contour map of film-thickness was constructed and is shown in Figure 3.5.9(b). The contour map quantified the variation in thickness observed by eye across the combinatorial film, showing maximum thickness at position E31 (722 nm) where the colour bands peaked. The thinnest point within the allotted grid positions was found to lie at position L1 (100 nm) and was more than 7 times thinner than the thickest point.

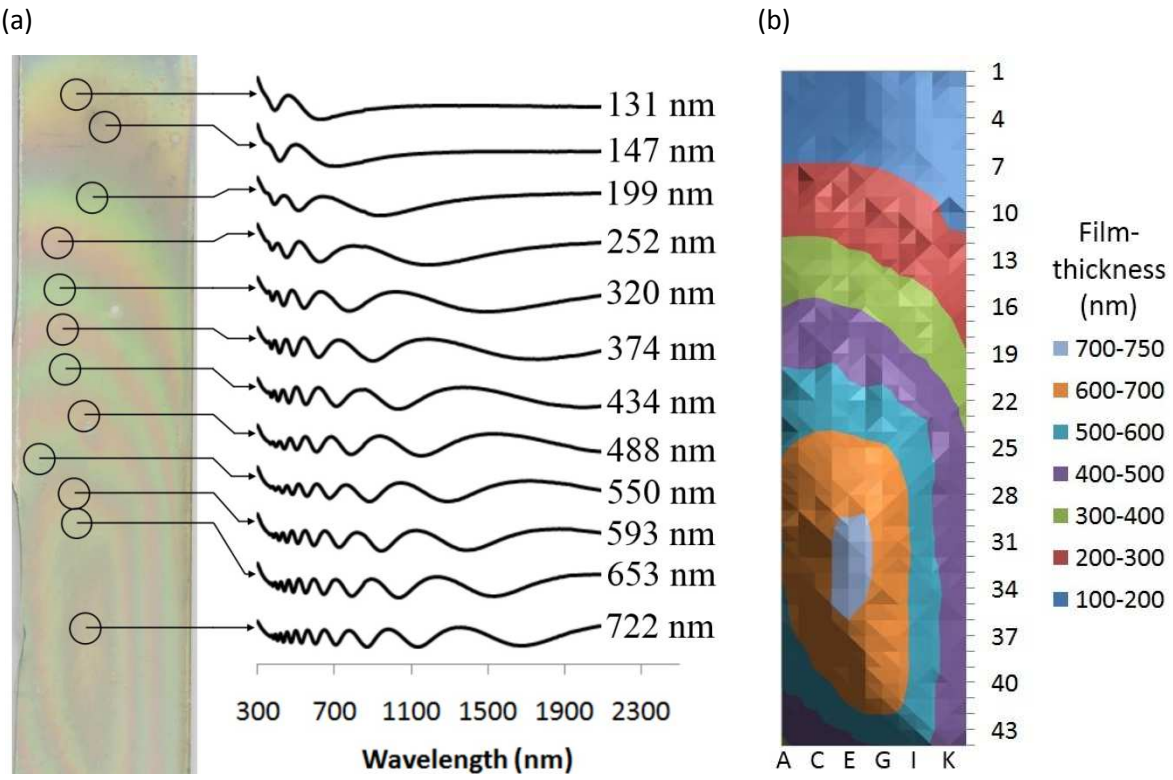

Figure 3.5.9: *(a) Stacked reflectance spectra at the centre of each of the 12 colour bands observed, with film-thicknesses determined by the Swanepoel method and (b) a film-thickness contour map of all 528 designated grid positions over the combinatorial film, calculated by approximating linear growth using our film-thickness mapping method described in Section 2.4.*

3.5.3.5. Atomic force microscopy mapping

Atomic force microscopy (AFM) was used to map the topography of the combinatorial film at 15 equally spaced locations along Columns B, F and J (Figure 3.5.2). The method was used in tapping mode, mapping the topography of a sample by moving a silicon cantilever with an atomically fine tip in rosters across the surface with a fixed tapping force (applied current in the piezo electric tip). By monitoring the retraction of the tip against the surface with a laser, the tip-surface height at each oscillation is measured. The topography of a 1 x 1 µm area was probed, in ≈ 2 nm steps, for each grid position analysed. Some topographical images for the positions analysed along Column F are shown in Figure 3.5.10(a).

(a)

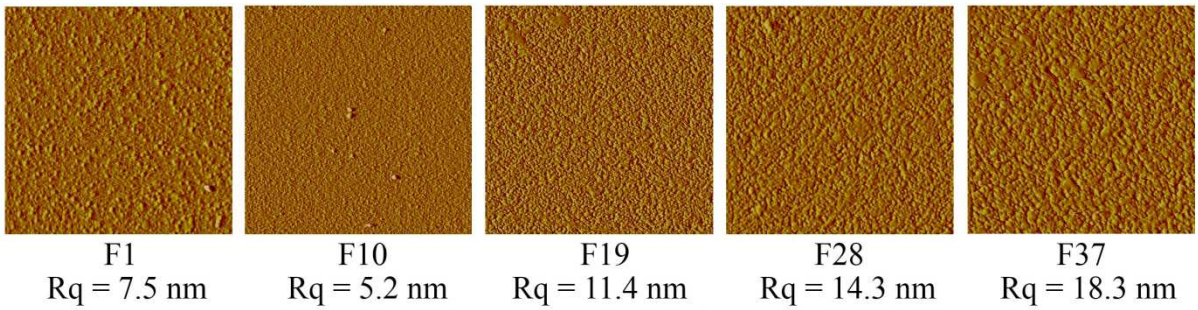

(b)

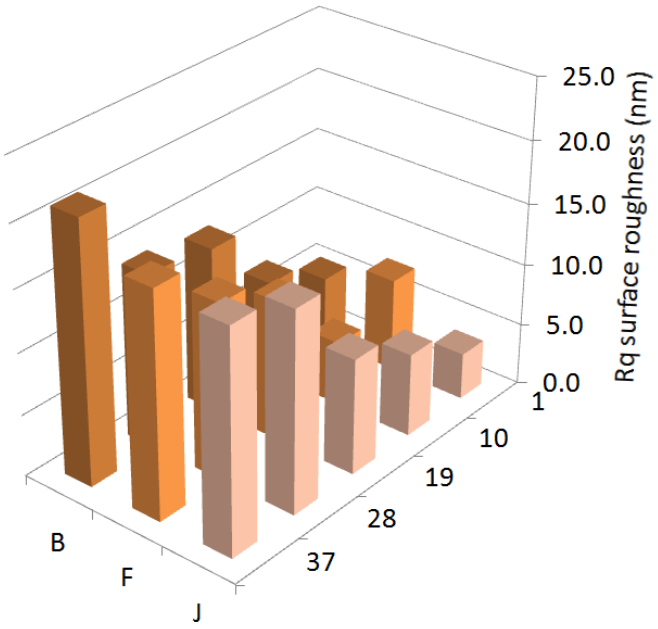

Figure 3.5.10: *(a) Topographical images of the film's surface for positions analysed along Column F through atomic force microscopy (AFM) and (b) A 3-dimenstional bar chart of the root mean square (Rq) surface roughness (nm) for all positions analysed across the combinatorial film by AFM.*

It can be observed, that the surface generally became rougher down the Column from position F1 to F37. These roughnesses could be quantified by the root mean squared (Rq) relationship shown below:

$$Rq = \sqrt{\frac{1}{n}\sum_{i=1}^{n} y_i^2}$$

(3.11)

where *n* is the number of heights measured and *y* is the height of a given position. The root mean squared was determined for all positions investigated by AFM and are displayed in a 3-dimensional bar chart in Figure 3.5.10(b). The general trend observed down Column F for increasing roughness was shared by the other Columns, B and J, that were investigated. Although only 15 positions were analysed, there was strong evidence to suggest that surface roughness increased going down the

combinatorial film. This tied in with our X-ray diffraction experiments, which showed how increasingly larger crystallites formed going down the film.

3.5.3.6. Reaction chemistry

A combinatorial anatase TiO_2 thin-film with a range of mixed levels of N_s and N_i-doping to pure N_i-doping ($0 \leq N_s$: Ti ≤ 8.4 %, $0.57 \leq N_i$: Ti ≤ 3.3 %) was formed by combinatorial APCVD from reaction of $TiCl_4$, ethyl acetate and NH_3 at 500 °C. The precursor temperature and carrier gas flow rate was adjusted to achieve the reagent mass flow rates specified in Table 3.5.1.[200] From our nitrogen/ titanium concentration mapping experiments (Section 3.4.3.5) the average nitrogen doping level was found to be 3.0 at. % ($\sigma = 2.1$). This corresponded to an average O: Ti ratio of 1.96. As the molar ratio of the oxygen source (ethyl acetate): titanium source ($TiCl_4$) was in a 3.5: 1 ratio, the titanium source was the limiting reagent in the formation of TiO_2. In mapping the nitrogen dopant level (Figure 3.5.6) and film-thickness (Figure 3.5.9(b)), and by also confirming that the film was of single anatase TiO_2 phase (Figure 3.5.3), the reaction rate of each precursor at 90 grid positions (over a 0.12.cm^2 area) could be derived (Figure 3.4.10). In calculating these reaction rates we made the assumption that the anatase TiO_2 combinatorial film consisted of unitary density (3.89 g.cm^{-3}).[201] The reaction rates could only be determined for positions in which both the film-thickness and nitrogen/ titanium concentration was known. Therefore, the reaction rate at only 90 positions of the 528 designated positions could be determined. Nevertheless, these positions were quite evenly distributed across combinatorial space and gave a good impression of the general trend in reaction rate.

The reaction rates of $TiCl_4$ and ethyl acetate showed a similar trend, peaking near the middle-bottom section of the film. Given the cold-walled reactor environment in which these reactions took place, the substrate was marginally hotter at the centre of the film than at the edges by ≈ 25 °C. Film growth was most rapid near the centre of the film, peaking at position E31 with a growth rate of 18.0 nm.s^{-1}; more than 1.5 times more rapid than the average growth rate of 11.7 nm.s^{-1}. As the reactions of $TiCl_4$ and ethyl acetate were most rapid where the film was hottest and not local to their point of entry, the formation of TiO_2 was certainly a reaction rate limited process.[108] However, the trend in reaction rate of NH_3 was very different to those of $TiCl_4$ and ethyl acetate, peaking near the middle-top section of the film at position D22 (N: Ti = 3.2 at. %). Little variation in the NH_3 reaction rate was observed across rows, however, going down the columns and away from the gas inlet in which the nitrogen precursor was introduced, the NH_3 reaction rate decreased in a relatively smooth fashion. This was quite adverse to our previous combinatorial study in which the exact same set of precursors was used (Section 3.4). In that combinatorial film, the NH_3 reaction rate maximised a lot more local

to the gas inlets in which the nitrogen precursor was introduced. In addition, the NH_3 reaction rate fell sharply from left to right, in complete contradiction with this study.

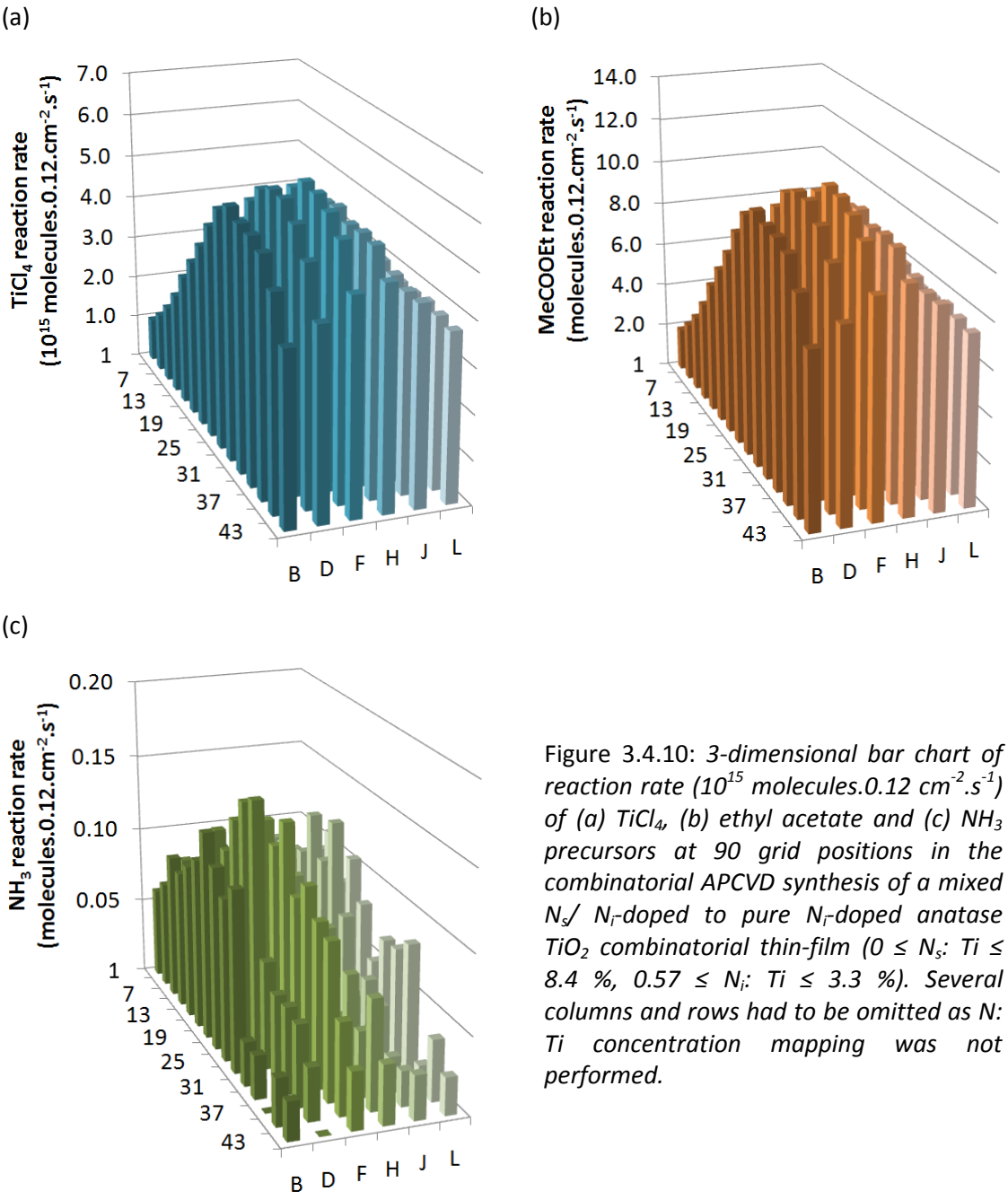

Figure 3.4.10: *3-dimensional bar chart of reaction rate (10^{15} molecules.0.12 $cm^{-2}.s^{-1}$) of (a) $TiCl_4$, (b) ethyl acetate and (c) NH_3 precursors at 90 grid positions in the combinatorial APCVD synthesis of a mixed N_s/ N_i-doped to pure N_i-doped anatase TiO_2 combinatorial thin-film ($0 \leq N_s$: Ti $\leq$ 8.4 %, 0.57 $\leq N_i$: Ti $\leq$ 3.3 %). Several columns and rows had to be omitted as N: Ti concentration mapping was not performed.*

If we first try to explain why the NH_3 reaction rate fell sharply across rows in the previous combinatorial study and did not change much across rows in this study, one might suggest that it was due to the different sizes of substrate used, where in this study a much more narrow substrate was used (≈ half the width of the substrate used in Section 3.4). This meant that the gas flows containing the nitrogen precursor had less space in which to laterally diffuse and react. This was disproved by the fact that the changes in NH_3 reaction rate were still comparatively too sharp when we looked at

just half of film-space in our previous study. This difference across rows was therefore attributed to two factors: (i) even though equal molar concentrations of NH_3 were introduced in each reaction, the NH_3 precursor entered the reactor 6 times more slowly in our previous study (Section 3.4) than in this study as an additional plain line of N_2 was combined with NH_3 and (ii) a high plain line flow of N_2 carrier gas was pushed right down the middle of the film in our previous study (5.0 $L.min^{-1}$) that most probably inhibited the NH_3 gas flow from laterally diffusing evenly across the substrate. In fact, point (i) can also be used to address why there was also a difference in where the NH_3 reaction rate maximised. As the NH_3 precursor was injected with a greater rate of flow in this combinatorial study, TiO_2 film growth was inhibited near the gas inlet. There is evidence of this if we look at the average thickness of Row 1 in each combinatorial study, where in this combinatorial study a more inhibited film growth rate of ≈ 3 $nm.s^{-1}$ was observed compared with our previous study of ≈ 5 $nm.s^{-1}$. Although the level of nitrogen doping was most great near the gas inlet for this combinatorial study, maximising at J1 (8.36 at. %), the reaction rate did not maximise in this region due to the inhibition of film growth by a fast plain line gas flow. The reaction rate maximised slightly further down the film, across Rows 16 to 22, where the gas flows were possibly less turbulent (Figure 3.4.10(c)). As the reaction of NH_3 was dictated by transportation issues rather than temperature, its reaction was indicated to be a mass-transport limited process, as implicated by our previous combinatorial study (Section 3.4.3.8).

The APCVD of $TiCl_4$, ethyl acetate and NH_3 (the same set of precursors used in our combinatorial study) was first demonstrated by Yates *et. al.*[221] In their reactions, the nitrogen and titanium sources were introduced in a range of concentrations ranging from N: Ti = 7.5: 1 to 9.2: 1 and formed solely N_s-doped TiO_2. In our first combinatorial study using the same set of precursors mentioned above (Section 3.4), the nitrogen and titanium sources were introduced in much lower ratio of 0.7: 1 yet still brought about the sole formation of N_s-doped TiO_2. In this combinatorial study, using the same set of precursors once again, the nitrogen and titanium sources were introduced in a slightly higher ratio of 2.2: 1 and brought about the formation of N_s and N_i doped mixtures. This might seem completely against the trend but one has to consider the fact that our NH_3 precursor was not introduced directly from the cylinder as in our previous combinatorial study (Section 3.4). In fact, the NH_3 precursor was first diluted to a 20 % mixture of NH_3: N_2 gas and this dilution is what we believe encouraged the formation of such N_s and N_i mixtures. Although the formation of N_s/ N_i-doped TiO_2 thin-films from a range of synthetic methods has often been suggested in the literature, it has little been confirmed by an X-ray photoelectron spectroscopy depth profile.[30,118,223,236]

The average level of nitrogen doping in this combinatorial study was N: Ti = 3.0 at. %. Although this was more than double what was observed in our previous combinatorial study (N: Ti = 1.35 at. % - Section 3.4), where the same set of precursors and molar concentrations were used, one could not make a direct comparison of the two studies as differently sized substrates were used. As the substrate used in this study was approximately half the width used in our previous study, the average N: Ti doping concentration was recalculated for the half more local to the nitrogen gas inlet. This yielded a comparatively more equal value of N: Ti = 2.5 at. %, which was unsurprising given the overall level of NH_3 introduced in both reactions was the same. When comparing the relative mass flows of each precursor (Table 3.5.1) against the average reaction rate, it was found that $TiCl_4$ reacted most efficiently. However, the reaction of NH_3 was ≈ 60 times less efficient than ethyl acetate and ≈ 100 times less efficient than $TiCl_4$. Similar reaction efficiencies were also observed in our previous combinatorial study (Section 3.4.3.8).

Our preferred orientation mapping experiments quantified the level of preferred orientation growth in the (101) plane of anatase TiO_2 (Figure 3.5.5(a)). It was shown that film-crystallinity had a strong (r^2 = 0.76) and positive linear relationship with the degree of preferred growth in this plane (Figure 3.5.5(b)). However, the basis for why each physical property arises is different in each case. For example, in APCVD reactions, film-crystallinity is generally dependent on substrate temperature effects, whereas the degree of preferred growth is dependent on substrate directing effects. In this combinatorial study, the reaction of $TiCl_4$ and ethyl acetate was a reaction rate limited process governed by substrate temperature. This meant that where the substrate was hottest, a thicker film would form, which should in turn be of higher crystallinity. In addition, as films grow thicker, substrate directional effects at the substrate-film interface become less pronounced and the degree of preferred orientation may change. This might lead one to believe that film-thickness mediated both the degree of film-crystallinity and preferred orientation. This was true to a certain extent where positive relationships between film-thickness and film-crystallinity (r^2 = 0.65) and film-thickness and preferred growth (r^2 = 0.81) were observed. An example of the relationship between film-thickness and preferred growth is shown in Figure 3.5.12. In addition to this, going down the combinatorial film the surface became rougher. This was related to the increase in film-crystallinity and movement away from the smoothness that comes with amorphous materials.[58]

By culminating reaction rate data, the overall combinatorial APCVD reaction for the formation of anatase TiO_2 with a range of mixed levels of N_s and N_i-doping to pure N_i-doping ($0 \leq N_s$: Ti ≤ 8.4 %, $0.57 \leq N_i$: Ti ≤ 3.3 %) could be written as follows:

$$TiCl_4 + MeCOOEt + NH_3 \rightarrow TiO_{2-x}(N_sN_i)_x + \text{by products } (7.4\ \%) \qquad (3.12)$$

where $0 \leq x \leq 0.084$ (<x> = 0.030, σ = 0.021), $0 \leq N_s \leq 0.084$ (<x> = 0.031, σ = 0.034) and $0.0057 \leq N_i \leq 0.033$ (<x> = 0.014, σ = 0.011). An average molar ratio of $TiCl_4$: MeCOOEt: NH_3 = 1.0: 3.5: 2.2 was introduced in this combinatorial reaction over a glass substrate held at 500 °C (± 25 °C). As the reaction chemistry of 10.8 cm^2 over a total of 90 cm^2 of combinatorial film-space was investigated (Figure 3.4.10), the overall reaction efficiency in terms of the limit reagent was determined (7.4 %). This was a similar efficiency to our previous combinatorial study of $TiCl_4$, ethyl acetate and NH_3 in Section 3.4 (9.0 %), which was unsurprising given almost equivalent molar concentrations of reagents were deposited at the same temperature.

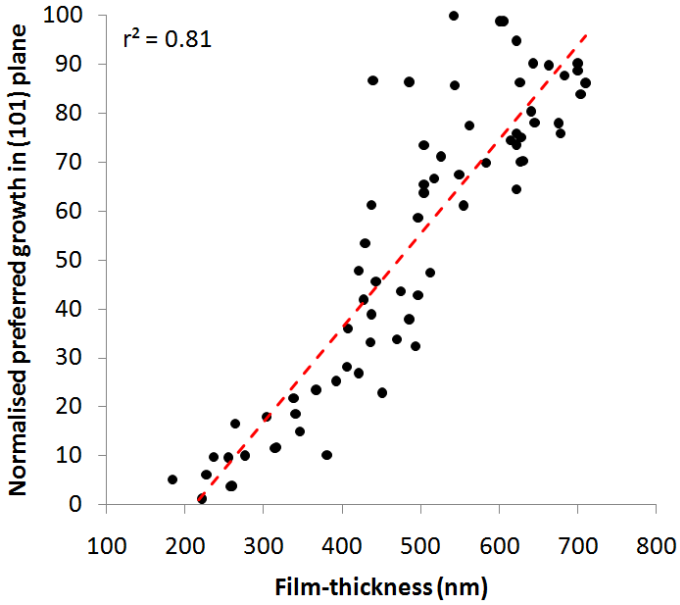

Figure 3.5.12: *A plot of film-thickness (nm) against corresponding normalised preferred growth in the (101) crystal plane of anatase TiO_2 for all positions across the combinatorial thin-film analysed by X-ray diffraction that were not amorphous.*

3.5.3.7. Bandgap determination

The bandgap at five unique locations, positions D12, D39, G19, J3 and J33 was determined through a Tauc plot.[195] This entails the plotting of $(Ahv)^{1/2}$ against energy (eV), where A is the absorbance of the film, h is Planck's constant and v is the frequency of light at the absorbing wavelength. The change in absorbance with wavelength was measured from 190 to 2500 nm, completely encapsulating the bandgap of TiO_2 (≈ 390 nm). For indirect bandgap semiconductor materials such as TiO_2,[237] such a plot is linear on approach to the absorption band edge and a simple extrapolation of these points to the energy axis yields the bandgap energy at the intersection. Two examples are shown together in Figure 3.5.13(a) for sample positions J3 and J33 revealing bandgaps of 2.45 and 3.19 eV respectively. The bandgaps for the remaining three positions were determined in the same way and are listed in the following section in Table 3.5.3. These values were the plotted against their corresponding N_s and

N_i doping levels, determined through X-ray photoelectron spectroscopy depth profiling. No meaningful correlation was observed between the level of N_i-doping and measured bandgap. On the other hand, a strong linear and negative correlation ($r^2 = 0.91$) was observed between the level of N_s-doping and measured bandgap (Figure 3.5.13(b)).

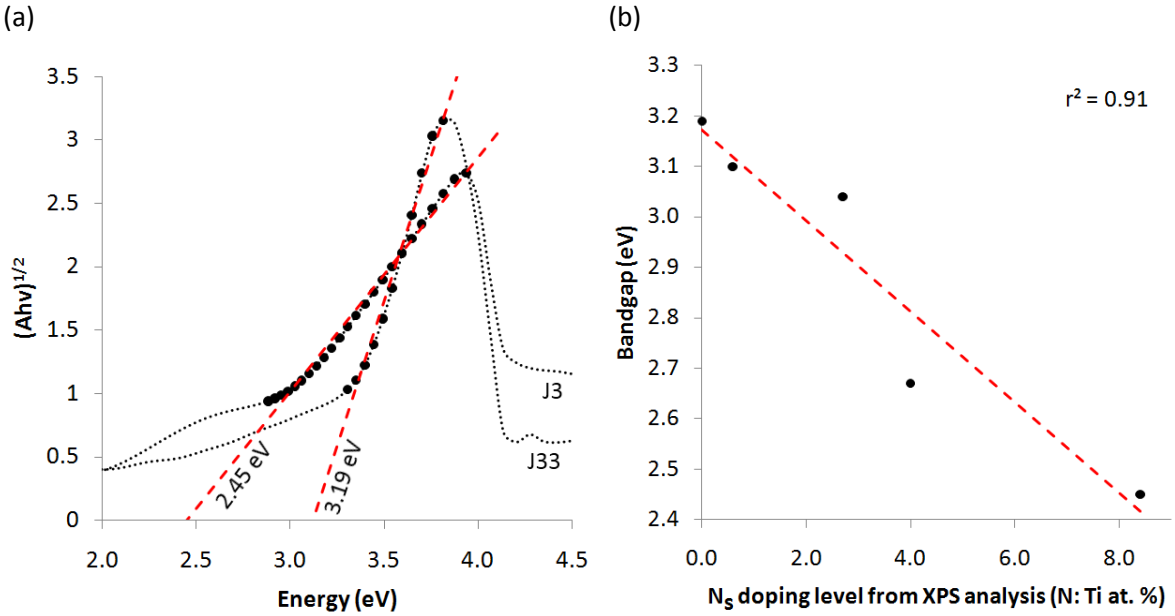

Figure 3.5.13: *(a) Tauc plot*[195] *of* $(Ahv)^{1/2}$ *against photon energy (eV) for the change in film absorbance with wavelength at positions J3 and J33 yielding bandgaps of 2.45 and 3.19 eV respectively and (b) a plot of Tauc plot derived bandgap versus corresponding* N_s*-doping level determined from X-ray photoelectron spectroscopy (XPS) analysis for the five locations; D12, D39, G19, J3 and J33.*

This was attributed to several factors. For instance, in Seraphin *et. al.*'s study of a series of solely N_i-doped TiO_2 powders made by a variety of methods,[238] no inter-band state, as predicted by computational modelling,[206,222] was seen in their Tauc plots. In fact, most of their materials did not show a significant difference in their bandgap energy to that of a P25 Degussa standard. Nevertheless, a slight tail in the band edge of each material was seen protruding into the visible, ranging from 400 – 500 nm, and could be attributed to the inter-band photo excitation. Such a tail was observed at position J33, where solely N_i-doping of TiO_2 was observed, as shown in Figure 3.5.14. The tail was rather broad and ranged in energy from 370 – 520 nm. The absorbance of the tail was also low, ranging from 0.15 – 0.25 absorbance units (roughly 30 – 40 % absorption of light respectively). From Tauc plots, a bandgap energy more similar to that of un-doped anatase TiO_2 was observed (3.19 eV). Although a red shifted absorption tail was seen, the low absorption of this feature was swamped by the overpowering absorption edge at ≈ 350 nm when determining the bandgap through a Tauc plot. For this reason we feel that a Tauc plot is not the best method for finding the inter-band state transition in N_i-doped TiO_2, where possibly photo-luminescence

spectra[239] or more complex Mott-Schottky experiments[240] might confirm the existence and energy level of any inter band state. Quite importantly however, the low absorbance of the tail in the band edge did tell us that the inter band state could only mediate the photo-excitation of a fraction of light and would have severe implications on any visible light/ solar photocatalysis.

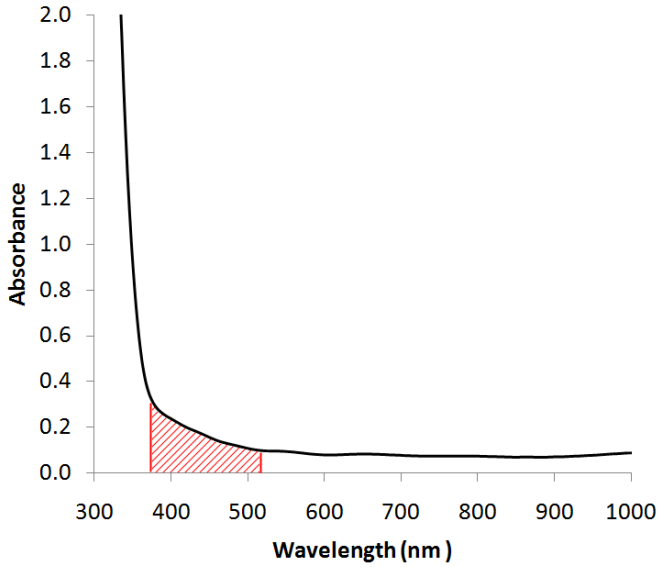

Figure 3.5.14: *The UV-visible absorption spectrum for sample position J33 with the tail region before the band edge marked in red (370 – 520 nm).*

There is little consensus in the literature as to the experimentally observed effect of N_i-doping TiO_2, where most studies have in fact reported a bandgap narrowing.[30,209] Although this is quite contrary to our result, it is also in opposition to theory, where computational studies have indicated that an inter-band state forms rather than a bandgap narrowing. However, it just may be, that due to the lower energy of oxygen vacancy (V_O) formation in N-doped TiO_2,[225] what is in fact being observed is a narrowing due to oxygen vacancies being present in the lattice that are known to form inter-band states just below the conduction band. However, in our combinatorial study, no bandgap narrowing was observed at the purely N_i-doped position (J33, N_i: Ti = 3.3 at. %). This indicated that little or no V_O was present and could be related to the synthetic method, where our oxygen source (ethyl acetate) was far in excess of our titanium source ($TiCl_4$).

In complete contrast, Tauc plots of positions across the combinatorial film where N_s-doping was observed showed significant red shifts in their bandgap energy compared with un-doped anatase TiO_2 (3.2 eV). It is not so surprising that the effects of N_s-doping where observed in Tauc plots, whereas the effect of N_i-doping was not. This is because N_s-doping of TiO_2 directly affects the band edge of the material, pushing it toward the visible, where for N_i-doped TiO_2, an entirely new inter band state is formed, which is possibly too dilute to be observed by such a method. The bandgap is narrowed through N_s-doping due to the mixing of N (2p) and O (2p) orbitals, which raise the energy

of the valence band toward the conduction band.[206,222] It seems, from the relationship shown above (Figure 3.5.13(b)), that increased N_s-doping quite steadily increases this bandgap narrowing.

3.5.3.8. Photocatalytic activity mapping

An even layer of a resazurin-based intelligent ink was spray-coated over the entire surface of the combinatorial film. The combinatorial film and ink overlayer were photographed between periods of UVA-irradiation (365 nm, 2 x 8 W) that was used to initiate and propagated photocatalysis until most of the ink overlayer had been bleached. A non-homogenous yet smooth transition from royal blue to pink to colourless was observed and represented the photo-reduction of the redox dye from resazurin to resorufin to its colourless intermediate respectively, as seen in Figure 3.5.15.

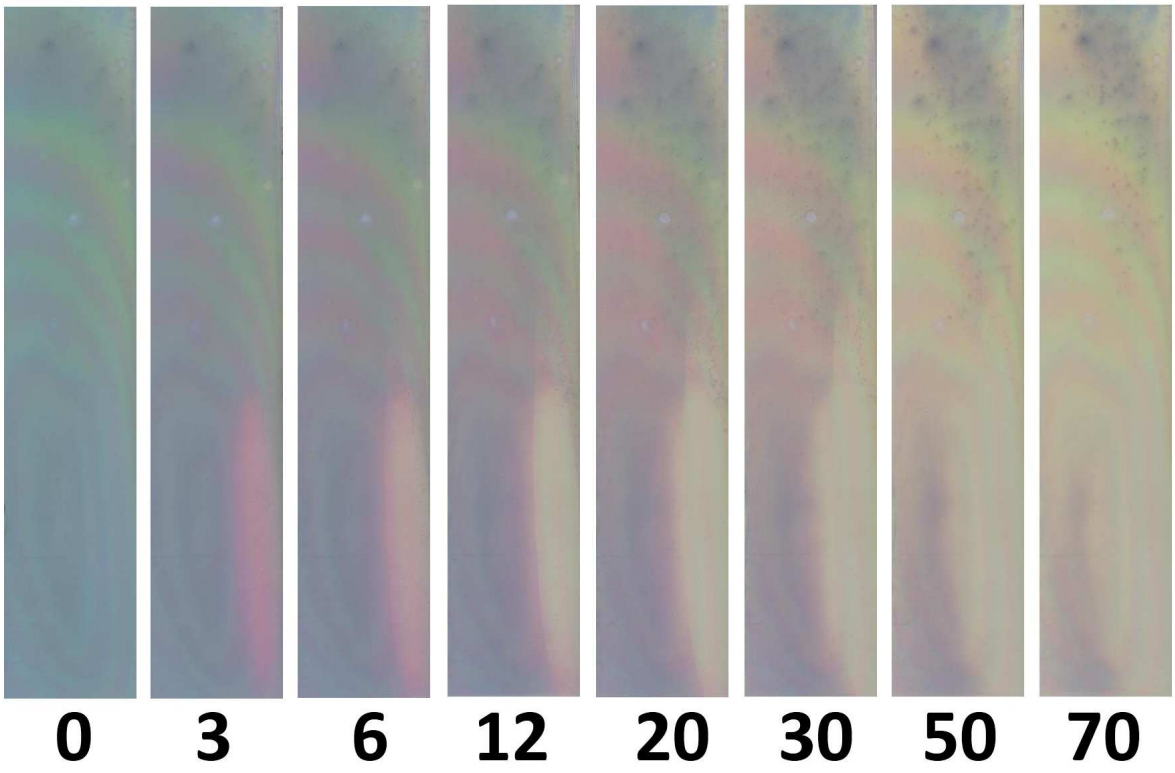

Figure 3.5.15: *A time-line of the photo-reduction reaction of a resazurin-based intelligent ink grid to a UVA (365 nm, 2 x 8W) light-source, where the numbers represent the total irradiation time (minutes). The even layer of a resazurin-based intelligent ink was spray-coated using an aerosol gun at an air-pressure feed of 3.5 bar over the entire surface of the combinatorial film.*

A small strip in the bottom-right section of the film was, by eye, the most photocatalytically active region of the combinatorial film, turning the dye pink after ≈ 3 mins and completely decolouring it after ≈ 12 mins exposure to UVA. The middle-top section of the film was the next most active region of the combinatorial film, bleaching the dye after ≈ 50 mins exposure. The bottom-left and top sections of the film were the least active regions. The bottom-left section showed marginally greater

activity than the top section in turning the dye pink after ≈ 50 mins exposure, whereas the top section had only caused the ink to slightly fade.

Both the red and green components of digital colour at each of the 528 designated grid positions (Figure 3.5.2) was extracted using the software we developed called RGB Extractor[(c)]. Most grid positions, except for those within the bottom-left and top sections of the film, showed an increase in the red component of digital colour until a point of plateau. These points represented the time of complete photo-reduction of resazurin to resorufin (Equation 2.20). All positions on the grid showed a minimisation in the green component of digital colour, where these points represented the time at which the maximum concentration of resorufin intermediate was formed (Equation 2.21(a)). The red components of digital colour were fit to a Boltzmann model (Table 2.2) and the time taken for each grid position to reach a plateau was determined. An example of this fitting for positions along Row 33 is shown in Figure 3.5.16(a).

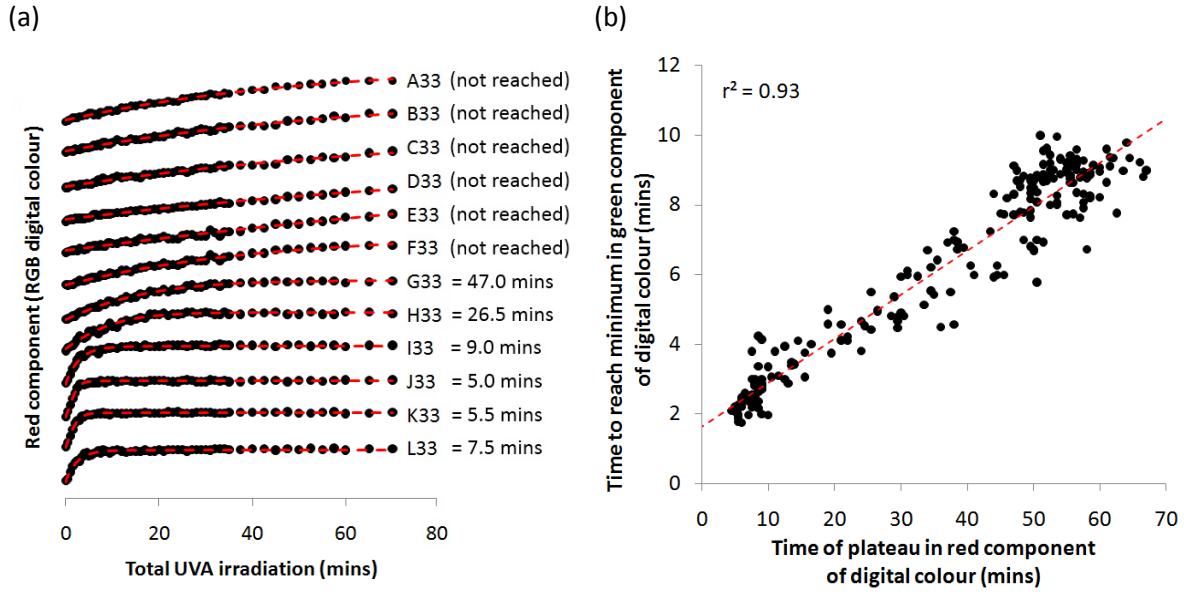

Figure 3.5.16: *(a) Stacked plot of red components of digital colour (arbitrary units) extracted from positions along Row 33 and fit to a Boltzmann model (<r^2> = 0.99, σ = 0.01) so that the time taken to reach a plateau could be accurately determined and (b) a plot of the all times to reach a plateau in the red component of digital colour against the corresponding time to reach a minimum in the green component of digital colour.*

Across Row 33, the time taken for the red component of digital colour to plateau generally increased from 7.5 mins at L33 to 47.0 mins at G33. From position F33 to A33 the red component of digital colour had not yet reached a plateau and signified how the photo-reduction of resazurin to resorufin had not completed. The longer it took for the red component to plateau, the longer it took for the resazurin to be completely photo-reduced to resorufin and the less active the photocatalyst was. The general trend for the decrease in photocatalytic activity from L33 to A33 quantified the trends in

photocatalysis seen by eye (Figure 3.5.15). The green components of digital colour were fit to a bi-phasic model (Table 2.2) and the time taken for each grid position to reach a minimum was also determined. The times to reach a plateau in the red component of digital colour were plotted against their corresponding time to reach a minimum in the green component (Figure 3.5.16(b)). As expected, a directly proportional relationship between the two properties was observed with a good degree of correlation (r^2 = 0.93). This was because the longer it took for the green component to reach a minimum, the longer it took for maximum concentration of the resorufin intermediate to form and the slower the conversion of resazurin to resorufin was. A relationship was extracted where:

$$t(G_{\text{minimum}}, RGB) \approx 0.126.\, t(R_{\text{plateau}}, RGB) \tag{3.13}$$

For this photoreduction reaction, this indicated that the time for a minimum in the green component of digital colour to occur was ≈ 8 times faster than the time for a plateau in the red component to occur and gave insight into the reaction kinetics where:

$$t([resorufin] \approx 0.126.\, t([resazurin] = 0) \tag{3.14}$$

Contour maps of the times taken to reach both a minimum in the green component (Figure 3.5.17(a)) and plateau in the red component of digital colour (Figure 3.5.17(b)) were drawn. The contour maps quantified the trends observed by eye with the quickest times, indicative of a more rapid photocatalyst, observed along a strip in the bottom-right section of the combinatorial film. The next quickest times were seen within in the top-middle section of the film followed by the bottom-left and then top sections across the combinatorial film. In the two slowest regions (the bottom-left and top) the full photo-reduction of resazurin did not occur within the time-frame of the experiment. Looking at these trends it is not too surprising that the bottom-right section of the film was more photocatalytically active than the top and middle sections of the film because of the comparatively higher crystallinity (Figure 3.5.4(a)), thickness (Figure Figure 3.5.9(b)) and surface roughness (Figure 3.5.10(b)) found in this region from physical characterisations. However, the bottom-left region of combinatorial film-space was more crystalline, thick and rough than any other region, yet showed mediocre levels of photocatalysis. This indicated that there was some relationship between the level of nitrogen doping that was incorporated into the film and the level of UVA photocatalysis. The nitrogen doping level, determined from our nitrogen/ titanium concentration experiments (Figure 3.5.6), was plotted for those positions analysed against their corresponding time taken to cause a minimisation in the green component of digital colour from our photocatalysis mapping experiments. No relationship was observed between these two properties, with a correlation coefficient of r^2 =

0.13. This plot represented the total level of nitrogen doping against the observed rate of UVA photocatalysis. This is because the N K-line and Ti L-line emissions detected in wavelength dispersive X-ray analysis (the basis of our nitrogen/ titanium concentration experiments) cannot distinguish between elements of different oxidation state and therefore represents a total bulk level of N_s and N_i doping. We therefore looked at rate of UVA photocatalysis for the five unique locations assessed by X-ray photoelectron spectroscopy (XPS) depth profiling, which was used to distinguish between the bulk levels of both N_s and N_i doping. A general trend was observed whereby increased levels of N_s-doping caused detriment to the overall level of UVA photocatalysis. This was a directly analogous trend to what we observed in our previous combinatorial study of solely N_s-doped TiO_2 in Section 3.4 (Figure 3.4.13(b)) and can be attributed to the increasing tendency for photo-generated electrons and holes to recombine with increasing levels of N_s-doping. Interestingly, the most active region of combinatorial film-space contained only N_i-doping (position J33 – Table 3.5.2).

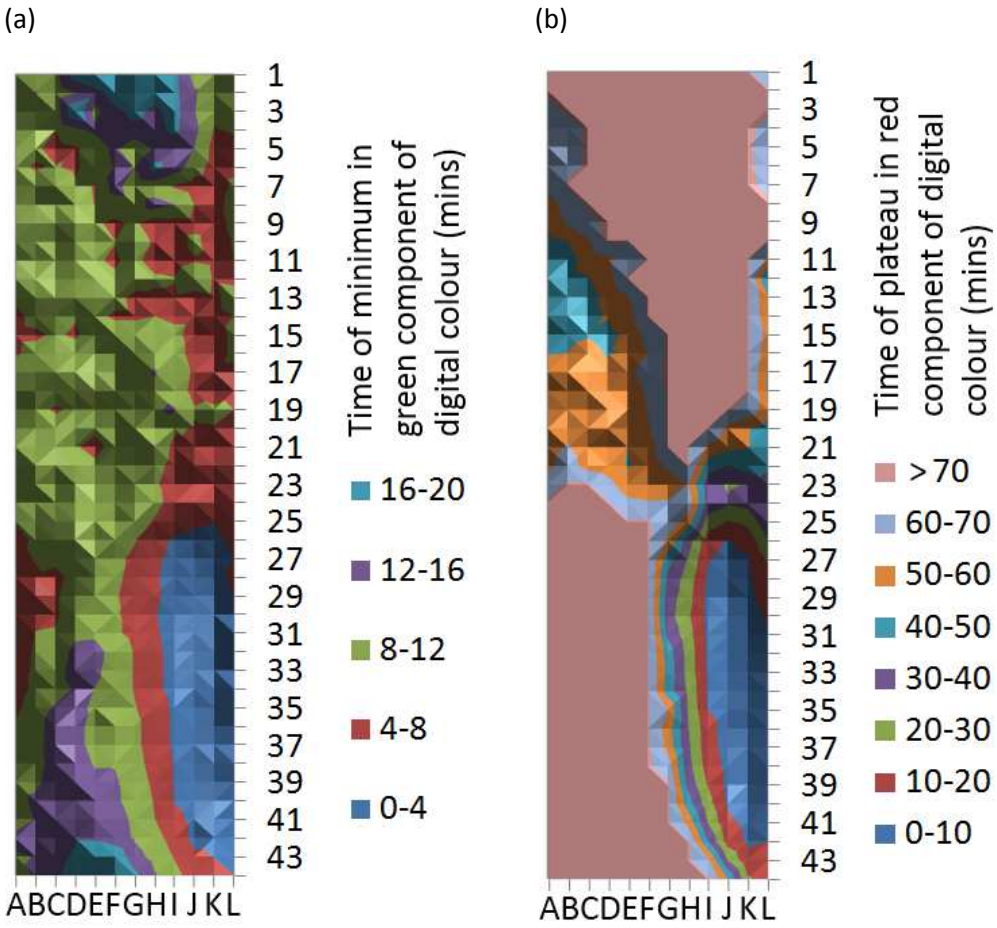

Figure 3.5.17: C*ontour maps of the time taken (minutes) for (a) the green component of digital colour to reach a minimum, thereby indicating the point at which the maximum concentration of the resorufin intermediate was formed and (b) the red component of digital colour to reach a plateau, thereby indicating the point at which the resazurin redox dye was fully photo-reduced to resazurin for all 528 allotted grid positions in the photocatalysis of an even layer of a resazurin-based intelligent ink to UVA light.*

The five positions analysed by XPS represented the four distinctly different regions of photocatalytic activity observed across the combinatorial film:

(i) Rapid acting, bottom-right region (position J33)
(ii) Medium acting, middle top region (positions D12 and G19)
(iii) Mediocre acting, bottom-left region (position D39)
(iv) Slow acting, top section (position J3)

The photocatalytic activity at these five positions probed by X-ray photoelectron spectroscopy depth profiling were investigated by a more traditional testing method, the photo-oxidation of methylene blue dye in solution, in order to confirm if the observed trends in photocatalysis (Figure 3.5.17) were real. The observed decreases in the absorbance maximum of methylene blue dye (≈ 660 nm) could be related to the decrease in dye concentration and converted into a photocatalytic rate (methylene blue molecules photocatalytically oxidised $cm^{-2}.s^{-1}$). These rates are listed in Table 3.5.3 alongside results from photocatalytic activity mapping experiments.

	XPS		Tauc plot	Photocatalysis		
				UVA		Visible light
	N_s	N_i	Bandgap (eV)	Resazurin G_{min}/ $R_{plateau}$ (mins)	MB (10^{10} molecules $cm^{-2}s^{-1}$)	Stearic acid (10^{10} molecules $cm^{-2}s^{-1}$)
D12	4.0 ± 0.90	0.86 ± 0.15	2.67	8.9/ 54	7.0	7.8
D39	0.59 ± 0.12	0.57 ± 0.21	3.10	14.8/ -	4.2	6.1
G19	2.7 ± 0.56	0.67 ± 0.23	3.04	10.1/ -	7.6	8.0
J3	8.4 ± 0.67	1.6 ± 0.43	2.45	12.2/ -	3.1	5.4
J33	0.0 ± 0.00	3.3 ± 1.15	3.19	2.2/ 5.7	12	8.9

Table 3.5.3: *Table listing the level of N_s and N_i doping (N: Ti at. %) determined from X-ray photoelectron spectroscopy (XPS) depth profiling for positions D12, D39, G19, J3 and J33 against their Tauc plot derived bandgap energy (eV) and relative levels of photocatalytic activity for the photo-reduction of a resazurin-based intelligent ink (UVA light source), the photo-oxidation of methylene blue (MB) solution (UVA light source) and the photo-oxidation of a stearic acid overlayer (visible light source).*

As the plateau in the red component of digital colour was not reached for all five positions, the minimum in the green component of digital colour was compared with the rate of photo-oxidation of methylene blue (MB) in solution. A strong (r^2 = 0.88) and negative linear correlation was observed between the two measures of UVA photocatalysis. This validated the trends observed in our photocatalytic activity mapping experiment. As the relationship between these two properties was linear, the proportion constant could be determined:

$$methylene\ blue\ (10^{10} molecules.cm^{-2}.s^{-1}) \approx 0.70.t(G_{\text{minimum}}, RGB) \quad (3.15)$$

This showed us that the range of photo-reduction rates for the five positions analysed was more broad than that of the photo-oxidation of methylene blue and might be attributed to any number of factors such as differences in mechanistic pathway to achieve photocatalysis, differences in media (water/ air) etc.

The degree of visible light photocatalysis was then tested for these five positions (D12, D39, G19, J3 and J33) to the photo-oxidation of a stearic acid overlayer. A filter was used to block any UV light that might have been generated by the light source or surroundings. An example is shown for this photo-oxidation reaction at position J33 in Figure 3.5.18. Figure 3.5.18(a) shows how the absorbance of the C-H symmetric (2920 cm^{-1}) and anti-symmetric (2850 cm^{-1}) stretches of the stearic acid molecules decreased due to their photo-oxidative conversion to CO_2 and H_2O (Equation 2.15). Figure 3.5.18(b) shows the change in integrated absorbance area (cm^{-1}) with irradiation time (hours), which can be converted into the number of stearic acid molecules present using a simple conversion factor (9.7 x 10^{15} molecules ≡ 1 cm^{-1}).[161] The rate of stearic acid photo-oxidation could thus be determined (molecules $cm^{-2}s^{-1}$). The rates for the five positions tested are listed in Table 3.5.3.

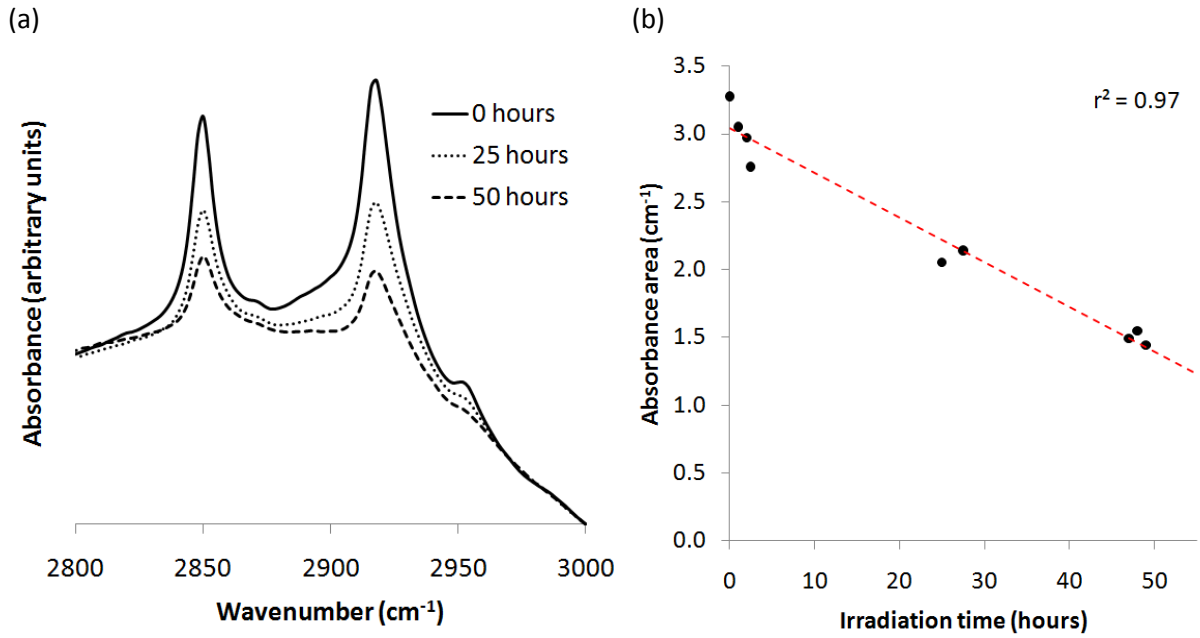

Figure 3.5.18: *(a) The change in absorbance of the C-H symmetric (2920 cm^{-1}) and anti-symmetric (2850 cm^{-1}) stretches in a stearic acid overlayer at 0, 25 and 50 total hours of white light irradiation during its photo-oxidation at position J33 and (b) a plot of the integrated absorbance (cm^{-1}) of these C-H stretches against irradiation time (hours) that show a linear decrease in concentration due to the zero-order kinetics of this photo-oxidation reaction.*

The most photocatalytically active position to the photo-oxidation of stearic acid using white light was J33. This position had consistently shown the highest rates of UVA photocatalysis of resazurin

intelligent ink and methylene blue solution across the five positions analysed as well. Intriguingly, this position contained solely N_i-dopants (N_i: Ti = 3.3 at. %). On the other hand, the lowest visible light photocatalysis was seen at position J3, which was also the most heavily N_s-doped of the five positions tested. This was quite contrary to the derived bandgap energy, where the most dramatic red-shift occurred at this location (2.45 eV). Given position J3 was not as crystalline, surface rough or thick as the other positions tested, it would be unfair to wholly account for the lower photocatalytic activities observed from N_s-doping levels alone. Of the five positions tested, only positions J33 and D39 showed comparatively equal film-crystallinity, surface roughness and film-thickness. However, differing levels of N_s and N_i doping were incorporated (D39, N_s: Ti = 0.59, N_i: Ti = 0.57; J33, N_s: Ti = 0, N_i: Ti = 3.3 at. %). In comparing these two positions, J33 showed ≈ 1.5 times the rate of visible light photocatalysis than D39. This result concurred with the general observation, that N_s-doped TiO_2 produced a less active visible light photocatalyst than that of purely N_i-doped TiO_2.[30] The stearic acid photo-oxidation of N_i and N_s-doped TiO_2 thin-films under a visible light source, identical to the one used in this combinatorial investigation, was reported by Dunnill *et. al.*[30] However, it was not possible to directly compare the rates of stearic acid photo-oxidation in this study with theirs, as they had normalised their rates to a starting concentration. Nevertheless, they also found that solely N_i-doping TiO_2 produced a more active visible light photocatalyst than those that were N_s-doped. In a recent study of a range of Ag_2O, Au and WO_3 composite TiO_2 thin-films, the photo-oxidation of a stearic acid overlayer was also investigated using the same visible light source.[22] The most active material consisted of a Au/Ag_2O composite with TiO_2 and showed a stearic acid photo-oxidation rate of 3.57 x 10^{10} molecules $cm^{-2}s^{-1}$. This rate was nearly 1.5 times lower than the lowest rate of visible light photocatalysis observed from our set of five nitrogen doped TiO_2 positions investigated (Table 3.5.3). A TiO_2 thin-film formed by a sol-gel process was modified at the surface by loading Ag nanoparticles using a photo-assisted deposition and also tested under the same visible light source to the photo-oxidation of a stearic acid overlayer.[20] A much lower rate of visible light photocatalysis (1.74 x 10^{10} molecules $cm^{-2}s^{-1}$) compared with those positions tested within our combinatorial study was seen. All comparisons give credit to the enhanced visible light effect of nitrogen-doped TiO_2 thin-films over other TiO_2 based materials.

The corresponding rates of photocatalysis for the two photo-oxidation reactions, methylene blue solution (UVA light source) and stearic acid (white light source), studied at the five positions across the combinatorial film in this section were plotted (Figure 3.5.19). A positive and linear correlation with a strong degree of fit was observed (r^2 = 0.91). Such a strong degree of linear correlation led us to question why there was a relationship between the level of UVA and visible light photocatalysis. The light source used in the UVA photocatalysis experiments completely

encapsulated the observed bandgap of all positions tested, where a more red-shifted material received no increase in the number of potential photons it might absorb to produce a photo-excitation. Therefore, the trend in photocatalytic rates from this experiment represented, in part, the stability of the photo-generated electrons and holes in the material, where a more heavily N_s-doped material caused detriment to UVA photocatalysis.

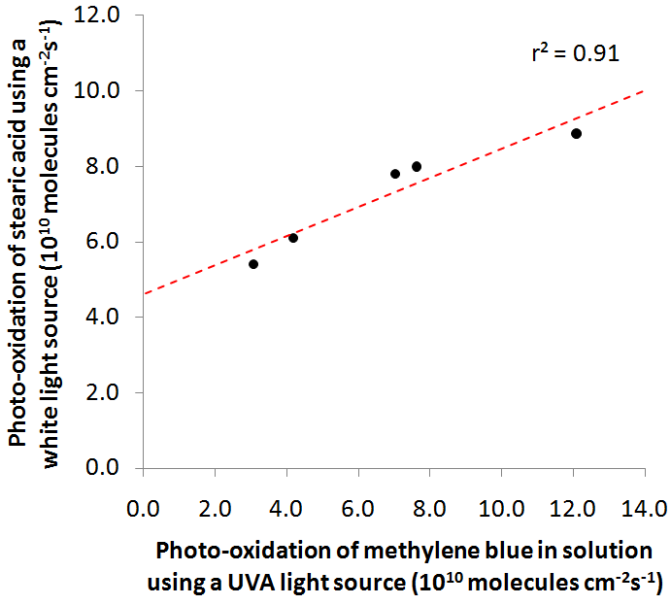

Figure 3.5.19: *A plot of the corresponding rates of photocatalysis for the photo-oxidation of methylene blue solution under a UVA light source against the photo-oxidation of a stearic acid overlayer under a white light source were plotted for the five positions investigated across the combinatorial film (D12, D39, G19, J3 and J33). A positive and linear correlation with a strong degree of fit was observed (r^2 = 0.91).*

The fact that this trend in UVA photocatalysis was directly related to the trend in visible light photocatalysis indicated that the rate of visible light photocatalysis was not entirely dependant on the material's ability to generate a photo-excitation, but rather its capacity to keep photo-generated electrons and holes from recombining. This was not the sole reason for the observed trend in visible light photocatalysis, as the range of visible light photocatalytic rates was heavily narrowed compared with the range of UVA light photocatalytic rates:

$$visible\ light\ photocatalysis \approx 0.39 \times UVA\ light\ photocatalysis \tag{3.15}$$

Other factors such as the number of photo-excitations that were occurring at each position tested could certainly have caused the range of visible light photocatalytic rates to narrow, as the positions with the lowest levels of UVA photocatalysis had the advantage of lower bandgap energy.

From this combinatorial investigation of N_s/ N_i-doped anatase TiO_2 phase-space two key observations came to light:

(i) A greater narrowing of the bandgap energy does not necessarily mediate more solar light activity.

(ii) Solely N_i-doping of anatase TiO_2 demonstrated marginally better visible light photocatalysis than samples that contained some level of N_s-doping.

Although no alteration in the bandgap energy was seen at position J33 (3.19 eV), it was deduced that the inter-band state formed by N_i-doping of anatase TiO_2 might not be directly observable by UV–visible spectroscopic methods and would explain why position J33 showed any visible light photocatalysis at all. With the above two points being considered, we believe that the major quality of N_i-doped over N_s-doped anatase TiO_2 for producing more efficient visible light photocatalysts lies in the greater stability of photo-generated electrons and holes.

3.5.4. Conclusions

A combinatorial anatase TiO_2 thin-film with a range of mixed levels of N_s and N_i-doping to pure N_i-doping ($0 \leq N_s$: Ti ≤ 8.4 %, $0.57 \leq N_i$: Ti ≤ 3.3 %) was formed by combinatorial APCVD from reaction of $TiCl_4$, ethyl acetate and NH_3 at 500 °C on glass. By introducing the precursors at different points inside the reactor, a N: O source concentration gradient was imposed, creating a range of deposition conditions in a single experiment. This induced the formation of a graded range of N_s and N_i doping levels. The preferred orientation, phase, thickness, nitrogen/ titanium concentration and photocatalytic activity at up to 528 allotted grid positions across the combinatorial film were rapidly deduced using our high-throughput characterisation methods. Four key regions of photocatalysis were identified and studied in greater detail to find the level of N_s and N_i doping, bandgap energy and determine the level of UVA and visible light photocatalysis more accurately. By correlating the physical properties of the film against the rates of photocatalysis it was identified that: (i) a greater narrowing of the bandgap energy does not necessarily mediate more visible light activity and (ii) solely N_i-doping of anatase TiO_2 demonstrated marginally better visible light photocatalysis than samples that contained some level of N_s-doping over the dopant ranges investigated. The mode for comparatively worsened UVA photocatalysis of N_s-doped anatase TiO_2 was attributed to the lower energy pathway these dopant centres provide for the recombination of photo-generated electrons and holes. The mode for improved visible light photocatalysis of N_i-doped versus N_s-doped anatase TiO_2 lies in the material's capacity to keep photo-generated electrons and holes separated.

In the following section we will summarise the major relationships that were established through our combinatorial investigation of nitrogen doped TiO_2. We will also culminate our results from

Sections 3.4 and 3.5 in trying to predict what level of N_s-doping in anatase TiO_2 would yield a more active solar photocatalyst.

3.6. Summary of N-doped TiO_2 systems explored

3.6.1. Functional-physical property relationships

Combinatorial APCVD was used to produce three unique titania based thin-film systems on glass substrates with graded levels and a changing nature of incorporated nitrogen. By introducing the precursors at different points inside the reactor, a N: O source concentration gradient was imposed, creating a range of deposition conditions in a single experiment. The three systems produced were:

(i) A dual-phased pseudo-brookite $Ti_{3-\delta}O_4N$ and N_i-doped anatase TiO_2 composite, containing graded levels of phases from pure pseudo-brookite $Ti_{3-\delta}O_4N$ at one end to pure N_i-doped anatase TiO_2 at the other – produced from the reaction of $TiCl_4$, ethyl acetate and t-butylamine precursors at 630 °C.

(ii) A dual-phased anatase TiO_2 and rutile TiO_2 composite ($0 \leq$ anatase $TiO_2 \leq 100$ %, $0 \leq$ rutile $TiO_2 \leq 41$ %) with graded levels of substitutional nitrogen doping ($0 \leq N_s$: Ti ≤ 11 %) – produced from the reaction of $TiCl_4$, ethyl acetate and NH_3 precursors at 500 °C.

(iii) A single-phased anatase TiO_2 system with a range of mixed levels of substitutional (N_s) and interstitial nitrogen (N_i) doping ($0 \leq N_s$: Ti ≤ 8.4 %, $0.57 \leq N_i$: Ti ≤ 3.3 %) – produced from the reaction of $TiCl_4$, ethyl acetate and NH_3 precursors at 500 °C.

The first system we investigated established a new route to the recently discovered pseudo-brookite $Ti_{3-\delta}O_4N$ phase. It was also the first case in which a composite between the pseudo-brookite $Ti_{3-\delta}O_4N$ phase and anatase TiO_2 was formed. In developing an arsenal of high-throughput characterisation methods, which are described in further detail in Chapter 2, the phase composition, film-crystallinity, preferred orientation, film-thickness, nitrogen concentration and photocatalytic activity for a large number of positions across each combinatorial film could be rapidly deduced. By correlating the physical properties of these combinatorial films against the measured rates of photocatalysis several relationships were discovered. These relationships indicated that:

(i) Pure pseudo-brookite $Ti_{3-\delta}O_4N$ was a more active UVA light photocatalyst than N_i-doped anatase TiO_2 with a first-order relationship (Figure 3.3.7). No evidence for a synergistic enhancement was observed.

(ii) Increased N_s-doping within anatase TiO_2 causes detriment to UVA light photocatalysis where the rate is slowed by approximately a factor of:

$$1 + 0.367 \times N_s \quad (3.16)$$

where N_s is the N_s: Ti at. % doping level (Figure 3.4.12(b)).

(iii) Increased rutile TiO_2 phase component in anatase TiO_2: rutile TiO_2 composites causes detriment to UVA light photocatalysis where the rate is slowed by approximately a factor of:

$$1 + 0.077 \times R \quad (3.17)$$

where R is the percentage rutile TiO_2 phase contribution in the composite (Figure 3.4.13(a)). No evidence for a synergistic enhancement was observed and gave little credit to the much debated synergistic effect of anatase TiO_2: rutile TiO_2 composites.

(iv) Solely N_i-doping of anatase TiO_2 demonstrated marginally better visible light photocatalysis than samples that contained some level of N_s-doping

(v) A linear relationship between the level of N_s-doping and red-shift of the bandgap exists whereby:

$$bandgap\ (eV) = 3.20 - 0.095 \times N_s \quad (3.18)$$

where N_s is the N_s: Ti at. % doping level (Figure 3.5.13(b)).

3.6.2. Predicted solar photocatalysis

The main focus of nitrogen doped TiO_2 has been the search for optimal visible light photocatalysis. Such materials, due to their red-shifted bandgap, have the potential to be used as self-cleaning surfaces indoors and outdoors. There has especially been a drive for applying these materials as self-cleaning surfaces in hospital environments to try and stop the transfer of nosocomial diseases such as *methicillin resistant staphylococcus aureus*, known more widely in the media as MRSA.[11]

Given such a variety of lamps are used indoors, it would be difficult for us to try and model what the optimum nitrogen-doping level might be. However, modelling what the optimum nitrogen dopant level might be for outdoor applications is simpler, as the pattern for the solar spectrum is relatively constant and merely changes in intensity with season and weather. From our combinatorial investigation of nitrogen doped TiO_2, the relationship between the level of N_s doping and the effect on bandgap narrowing was established (Equation 3.18). However, neither the energy level of the inter-band state in solely N_i-doped anatase TiO_2 could be derived (Section 3.5.3.7, position J33)) nor the fraction of photons that this inter-band state can accommodate. We could therefore only model the solar photocatalysis for N_s-doped anatase TiO_2.

A typically solar spectrum, acquired at sea level, is shown in Figure 3.6.1. The predicted fraction of light that is absorbed by anatase TiO_2 (3.2 eV), rutile TiO_2 (3.0 eV) and our N_s-doped TiO_2 sample (2.45 eV) from Section 3.5 (position J3, N_s: Ti = 8.4 at. %) is shaded beneath each portion of the solar spectrum.

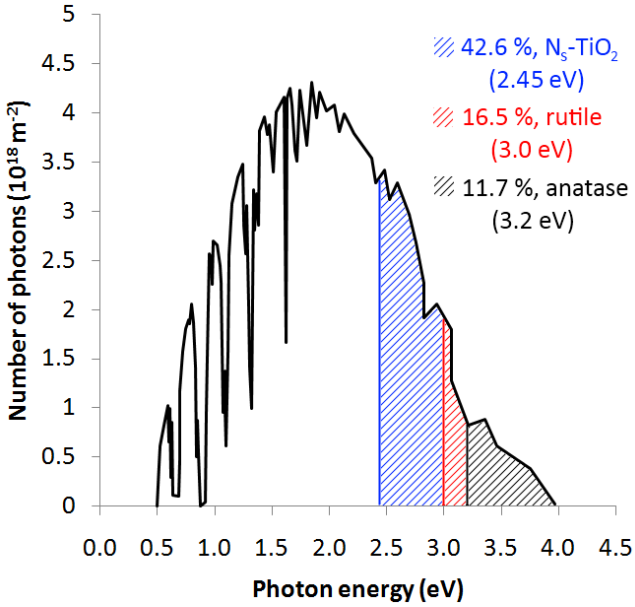

Figure 3.6.1: *A solar spectrum acquired at sea level plotted for photon energy (eV) against number of photons at this energy (10^{18} m^{-2}). The fraction of light that is absorbed by anatase TiO_2 (black), rutile TiO_2 (red) and our N_s-doped TiO_2 sample (blue) from Section 3.5 (Position J3, N_s: Ti = 8.4 at. %) is predicted.*

To try and model the optimum level of N_s-doping anatase TiO_2 for solar applications we will use two fundamental relationships we derived from experimentally studying a range of states by our combinatorial approach. The first relationship, shown in Equation 3.16, tells us the relative detriment to the stability of photo-generated electrons and holes with increased N_s-doping in anatase TiO_2. The second relationship, shown in Equation 3.18, predicted the bandgap energy narrowing with increased N_s-doping. The second relationship was first verified by plotting the bandgap energies determined from literature studies of N_s-doped TiO_2 alongside our own (Figure 3.6.2). Given the number of studies of N_s-doped TiO_2 in the literature it is surprising how few studies quote both the nitrogen doping level and bandgap. However, a number of bandgap energies for a variety of N_s: Ti doping levels in anatase TiO_2 thin-films were reported by Wu *et. al.*[241] By varying the nitrogen partial pressure for each ion-sputter reaction, a variety of N_s doping levels were achieved. Jiang *et. al.* reported their bandgap of 2.60 eV with a N_s: Ti doping level of 3.21 at. % in their synthesis of N_s-doped anatase TiO_2 thin-films from a micro-arc oxidation process.[242] Zhao *et. al.* also reported their bandgap energy of 2.50 eV with a N_s: Ti doping level of 5.67 at. % in their pulsed-laser deposition of N_s-doped anatase TiO_2 films.[194] Similarly to our studies, the bandgap energies were all determined

from a Tauc plot. Quite a good agreement was found between our results and theirs with a total linear correlation factor of r^2 = 0.76. When their results were incorporated with our own, a new relationship between N_s dopant level and bandgap energy was formed:

$$bandgap\ (eV) = 3.2 - 0.097 \times N_s \quad (3.19)$$

where N_s is the N_s: Ti at. % doping level. This did not differ too much from the original relationship described in Equation 3.18, deviating by a factor of just ≈ 0.02.

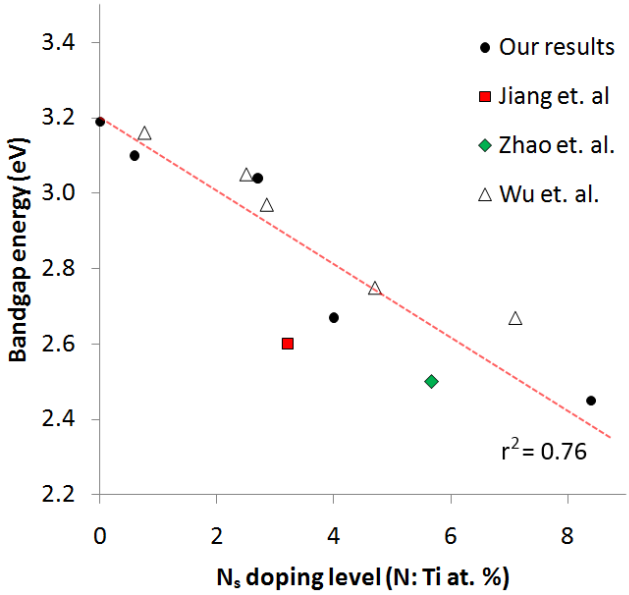

Figure 3.6.2: A plot of bandgap energy (eV) against N_s doping level in anatase TiO_2 thin-films from a series of studies by Jiang et. al.,[242] Zhao et. al.,[194] Wu et. al.[241] and our own. A linear correlation was observed with good correlation (r^2 = 0.76).

Culminating these experimental relationships we can now predict:

(i) the fraction of light that will theoretically be absorbed by an N_s-doped anatase TiO_2 thin-film photocatalyst that leads to a photo-excitation (Equation 3.19) and

(ii) the fraction of photo-generated electrons and holes that will recombined before photocatalysis can occur (Equation 3.16).

This is plotted in Figure 3.6.3(a) for a range of N_s doping levels from 0 to 8.4 at. %. As the N_s-doping level increases, the percentage of solar photons that can be absorbed increases exponentially from ≈ 7 % in un-doped anatase TiO_2 to 38 % in N_s-doped anatase TiO_2 when N_s: Ti = 8.4 at. %. On the other hand, the relative stability of these photo-generated electrons decreases quite sharply with a 2nd order exponential type relationship from 1.0 in un-doped anatase TiO_2 to ≈ 0.24 % in N_s-doped anatase TiO_2 when N_s: Ti = 8.4 at. %. By multiplying these relative photo-generated electron hole stabilities with the fraction of light that can be absorbed we acquire a relationship that tells us the

predicted relative rate of solar photocatalysis. This was normalised to un-doped anatase TiO_2 and plotted in Figure 3.6.3(b). As we can see, from a N_s doping level of N_s: Ti = 0 at. % to ≈ 5 at. %, a decrease in the relative rate of solar photocatalysis is predicted. This was attributed to the small increase in the fraction of solar photons absorbed relative to the decrease in stability of the electrons and holes that would be photo-generated. However, from N_s: Ti > 5 at. % to 8.4 at. %, an increase in the relative rate of solar photocatalysis is predicted. This was attributed to the sharp increase in the number of photons in the solar spectrum from ≈ 2.7 eV toward the visible. Nevertheless, the predicted increase in solar photocatalysis was marginal and increased by roughly just 30 % compared with an un-doped TiO_2 sample at best. To make matters worse, the principles by which this relative rate of solar photocatalysis was predicted were not statistically concrete, showing degrees of correlation that were just about passable (r^2 = 0.76 to 0.78). With all effects being considered, the error in our predictions may actually outweigh the marginal predicted benefit to solar photocatalysis of more heavily N_s-doped anatase TiO_2 (N_s: Ti > 5 at. % to 8.4 at. %).

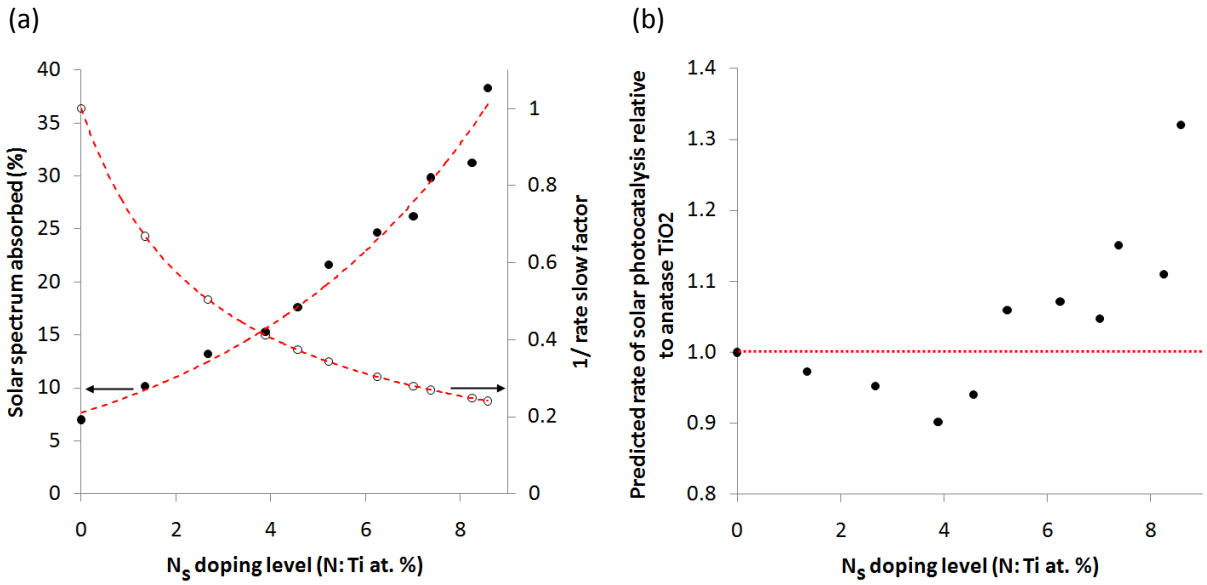

Figure 3.6.3: *(a) A plot of the predicted fraction of solar photons that will be absorbed (%) that leads to a photo-excitation and the relative stability of these electrons and holes against the N_s doping level in anatase TiO_2 (N: Ti at. %) and (b) a plot of the predicted rate of solar photocatalysis against N_s-doping level in anatase TiO_2 (N: Ti at. %) normalised to un-doped anatase TiO_2.*

In the literature, the majority of N_s-doped TiO_2 studies of did not encompass the investigation of such high levels of N_s-doping, which we predicted would invoke a marginally significant increase in solar photocatalysis. In addition, most studies have focussed on testing the photocatalysis of N_s-doped TiO_2 thin-films solely against visible light. If we look at the average effect of our predictions over the entire region of N_s-doping investigated, there is no increase in solar activity. For this reason we feel that it would be of greater benefit for those in the field to focus on the indoor application of N_s-doped TiO_2 to visible lighting conditions, where fewer UV photons are available. Although the

relative rate of solar photocatalysis could not be modelled for N_i-doped anatase TiO_2, our combinatorial studies did indicate that N_i sites did not act as centres for the recombination of electrons and holes, whereas N_s sites did. In effect, this would indicate that any level of N_i-doping of anatase TiO_2 would produce a more active solar photocatalyst than that of un-doped anatase TiO_2. However, the degree of activity increase would depend much upon the energy level of the inter-band state that is formed in N_i-doped TiO_2 as well as the fraction of photons that this state can absorb.

In the following chapter we will use combinatorial APCVD to investigate solid solutions of Nb-doped (Section 4.3) and W-doped anatase TiO_2 (Section 4.4). Although the resistivities of these materials have been studied, their photocatalytic activities are, to our knowledge, yet to be reported. We will use our high-throughput screening methods to try and understand the links between the physical and functional properties of these materials as well as the link, if any, between resistivity and photocatalysis. First we will start with a general introduction on the effects of metal-ion doping anatase TiO_2 (Section 4.1) and follow this with a general experimental section describing how both our Nb-doped and W-doped anatase TiO_2 combinatorial films were analysed (Section 4.2).

4. Metal-ion doped anatase TiO_2

4.1. Introduction

Studies focused on the photocatalysis of metal-ion doped TiO_2 can be traced back to the late-80's,[243] where the effect of doping Cr^{3+} ions for Ti^{4+} centres was assessed. Since then, the photocatalytic effects of doping TiO_2 with almost all transition metals[31-38] as well as many of the lanthanides[244,245] have also been investigated.

Although metal ion dopants, if sufficiently small, can lie in interstitial sites,[246] they primarily substitute Ti^{4+} centres and form solid solutions. Two main effects arise from solid solution formation:

(i) a change in the bulk density of states and
(ii) a modification of the surface properties

Several outcomes arise from a change in the material's density of states; such as a raising/ lowering of the Fermi level, formation of new inter-band states or the injection/ removal of electrons from the system.[247] The properties at the surface of the material change with the nature of the dopant, the concentration of dopant, the length of the induced space charge layer as well as photo-corrosion processes due to increased chemical instability.[248,249] These changes in surface and bulk properties of metal-ion doped TiO_2 materials can significantly alter the function of photo-induced surface hydrophilicity.[250,251] However, the effect they have on photocatalysis has been studied more intensely, where surface modifications alter the attraction of organic media and stability of migrated electrons and holes and electronic modifications alter the capacity for photo-excitation as well as their movement and stability. For instance, in Fe^{3+} or Cr^{3+} doped TiO_2, inter-band states form between the valence and conduction band of TiO_2 (Scheme 1.1.3 (c)).[246] This coincided with shifts in the absorbance shoulder into the visible and gave such materials the capacity for visible light photocatalysis.[252,253] In addition, when incorporating cations of lower oxidation state than the TiO_2 host (Ti^{4+}), such as Fe^{3+} or Cr^{3+}, neutrality requires the simultaneous formation of oxygen vacancies (V_O). Computational studies have shown these oxygen vacancies to produce inter-band states near the conduction band of TiO_2[206] and some attribute the visible light photocatalysis in such materials to this phenomenon (Scheme 1.1.3 (d)).[222] When cations of higher oxidation state than the TiO_2 host are incorporated, such as V^{5+}, neutrality requires the simultaneous formation of cation vacancies.[246] These cation vacancies are good photo-generated hole acceptors and have the capacity to drive photo-reduction processes at the surface through scavenging holes.[254]

Although there are a large number of examples in the literature that demonstrate how metal-ion doping TiO_2 improves the visible light absorption properties of the material, it should be pointed out that increased visible light absorption does not solely necessitate increased photocatalysis.[34] For instance, metal-ion dopants greatly affect the lifetime of photo-generated electrons and holes.[255] Whereas some studies have shown that metal-ion dopants can selectively trap one charge carrier and allow the other to reach the surface and take part in the desired redox reaction,[256] most studies have indicated metal-ion dopants to act as recombination centres for photo-generated electrons and holes.[243] This is certainly similar to the case of N_s-doping in TiO_2, where a balance between increased visible light absorption and detriment to the photocatalytic efficiency is observed (Section 3.5). Such a decrease in the photocatalytic activity of metal-ion doped TiO_2 is frequently reported in the literature, particularly at higher doping levels.[257]

Another feature of metal-ion doping TiO_2 is the change in conductivity. The more substantial increases in conductivity occur when TiO_2 is doped with a cation of either higher or lower oxidation state than the host. In the case of doping with a higher oxidation state metal-ion, such as Nb^{5+},[258] electrons are injected into the system to achieve electro-neutrality. As the valence band of TiO_2 is already full, these electrons fall into the conduction band of the material and are called charge carriers (*n*). This type of conduction increase is denoted n-type (negative type). In the case of doping with a lower oxidation state metal-ion, such as Fe^{3+} in low concentration,[259] electrons are removed from the system to achieve electro-neutrality. The electrons are removed from the filled valence band of TiO_2 leaving holes. These holes accommodate the hopping of electrons through the system, increasing conductivity. This type of conduction is called p-type (positive type).

Although substantial efforts have been made to try and enhance the photocatalytic activity of TiO_2 thin-films by metal-ion doping, there has also been a considerable interest of late into investigating the effects on film conductivity for optoelectronic applications.[260] The benefits of doping anatase TiO_2 thin-films for use as transparent conducting oxides (TCO) or as protective layers over TCOs are clear given their long-term stability in high humidity conditions as well as their resistance to acid degradation compared with traditional tin or zinc oxide based TCOs. The film conductivity of both niobium[261,262] and tungsten[149] doped TiO_2 thin-film solid solutions have been investigated. However, to our knowledge, the photocatalysis of such materials is yet to be studied. In addition, neither niobium nor tungsten doped TiO_2 thin-films have been synthesised through CVD. Using our combinatorial APCVD process, we will synthesise anatase TiO_2 thin-films with graded concentrations of niobium (Section 4.3) and tungsten doping (Section 4.4). The combinatorial films formed will then be characterised using our array of screening methods. Any variation in the

functional properties of each system with be rationalised and the optimum conditions for improved functionality suggested.

4.2. Experimental methods

All chemicals were purchased from Sigma-Aldrich Chemical Co; dichloroindophenol 98.0%, resazurin 92%, hydroxyethyl cellulose (HEC) [average $M_v \approx 90{,}000$], glycerol 99.5%, stearic acid 99%, isopropanol 99.98%, acetone 99%, ethyl acetate (MeCOOEt) 99%, titanium chloride ($TiCl_4$) 99.9%, niobium pentachloride ($NbCl_5$) 99.9%, tungsten hexachloride (WCl_6) 99.9%. Di-nitrogen gas cylinders were supplied by BOC. The glass blank, consisting of a piece of standard 3.2 mm thick float glass coated with a 50 nm SiO_2 barrier layer was supplied by the Pilkington NSG Group.

4.2.1. Physical characterisation

Phase mapping was conducted using a Renishaw 1000 Raman spectrometer using a red (633 nm) laser. Samples were analysed over the 100 - 1200 cm^{-1} energy range. X-ray diffraction mapping was carried out using a micro-focus Bruker GADDS powder X-ray diffractometer, with a monochromated Cu Ka1 (1.5406 Å) source and a CCD area X-ray detector, capable of 0.01° resolution in 2θ with an automated X–Y movable stage. The degree of preferred orientation was assessed using our preferred orientation mapping method described in Section 2.3. The wavelength where a transmittance maximum occurs is analogous to where a reflectance minimum occurs (Figure 2.3.2(a)), therefore reflectance spectra recorded over the 300 - 2500 nm range on a Helios double beam instrument (standardised relative to a rhodium mirror) allowed the thickness to be determined at any allotted grid position in accordance with our thickness-mapping method described in Section 2.4. The Nb: Ti % composition was investigated by wavelength dispersive X-ray (WDX) analysis on a Jeol Superprobe JXA-8600. The average Nb: Ti atom % composition over five area scans (200 μm^2) was derived from Ti K_α-Line (4508 eV) and Nb Lα-Line (2164 eV) emission intensities that were adjusted to pre-calibrated standards. The W: Ti atom % composition was derived from Ti K_α-Line (4508 eV) and W Lα-Line (8376 eV) emission intensities that were adjusted to pre-calibrated standards using a Philips ESEM. X-ray photoelectron spectroscopy (XPS) was performed at Cardiff University using a Kratos Axis Ultra - DLD photoelectron spectrometer with monochromatic Al-K_α radiation. Survey scans of the binding energy were collected over the 0 – 1100 eV range at a pass energy of 160 eV. Higher resolution scans encompassing the principal peaks of Ti (2p), O (1s), C (1s), Si (2p) and either Nb (3d) or W (3d and 4f) were collected at a pass energy of 40 eV. For compositional depth profiling, an Ar-ion gun was used to etch away the surface layers of samples for a sputtering time of 30s per etch. The peaks of each

contributing oxidation state were modelled using CasaXPS. The peak positions were adjusted to adventitious graphite present at the surface (284.5 eV) and peak areas were converted using appropriate sensitivity factors[157] to determine the concentration of each state. The surface topography was investigated by atomic force microscopy (AFM) using a Veeco Dimension 3100 in air with a contact operating mode and a silicon tipped cantilever for either 1 x 1 µm or 100 x 100 µm sample areas.

4.2.2. Functional property characterisation

4.2.2.1. Bandgap determination

Transmittance spectra were recorded over the 300 - 2500 nm range on a Helios double beam instrument to determine bandgap energies through Tauc plots.[195]

4.2.2.2. Water droplet contact angles

Water droplet contact angles were measured using a First Ten Angstroms 1000 set-up with a side mounted rapid-fire camera. An 8.6 µl droplet was measured using a 27 gauge needle and cast from directly above the surface at a fixed height. The contact angles were determined by FTA Software[263] when the water droplet had stopped spreading. Water droplets were cast and measured at set times between UVC irradiations (254 nm: Vilber Lourmat 2 x 8W VL-208G-BDH/VWR Ltd) irradiation.

4.2.2.3. Resistivity mapping

A fixed-width in-line spring-mounted four-point electrode was set-up in house for measuring sheet resistance by the Van der Pauw method.[264] A constant voltage was applied through grid-positions along the material using a Maplin N93CX switching mode power supply. Voltages and currents were measured using a Caltek CM2700 and a Sinometer M-830B meter diode respectively. The sheet resistance was thus determined using the Van der Pauw equation:

$$sheet\ resistance\ (\Omega/\square)\ = 4.53 \times \frac{Volatge\ (V)}{Current\ (A)} \tag{4.1}$$

As the film thickness at each position was determined using our film-thickness mapping method (Section 2.4), the resistivity could be determined by:

$$resistivity\ (\Omega \mathrm{m}) = sheet\ resistance\ (\Omega/\square) \times thickness(m) \tag{4.2}$$

4.2.2.4. Photocatalytic rate mapping

Intelligent ink was used to map the photocatalytic activity for a large number of positions simultaneously across the combinatorial thin-film. The method by which the relative times for photocatalysis to occur is described in Section 2.6. The combinatorial film was first washed with distilled water, rinsed with isopropanol and then placed under UVC irradiation (254 nm, 2 x 8W - Vilber Lourmat VL-208G) for 1 hr to ensure the surface was free from contaminants. An even layer was applied onto wall-mounted combinatorial films using an aerosol-spray gun (SIP Emerald Spray Gun/Halfords Plc) at an air-pressure feed of 3.5 bar. Blank microscope slides (VWR ISO 8037/1, 76 x 26 mm) were coated simultaneously in order to assess the thickness of the coating by UV-visible spectroscopy (PerkinElmer Lambda 25 UV/VIS spectrometer) over the 300 – 800 nm range. The ink consisted of resazurin (4 mg) redox dye in an aqueous solution (3 ml) with glycerol (0.3 g) and hydroxyl-ethyl cellulose (0.05 g). The photocatalysis reaction was conducted using UVA irradiation (365 nm, 2 x 8W - Vilber Lourmat VL-208BL) and monitored solely by digital photography (Epson Perfection 1200 Photo Scanner) at intervals. For each digital image acquired, the red-green-blue components of digital colour were extracted at each position on the grid, specified in each study. The time it took for the red component of digital colour to plateau for each location analysed was determined by fitting the colour data to a Boltzmann model. This time represented the complete photo-reduction of the resazurin redox dye (Equation 2.20). Different to previous photocatalysis mapping experiments (Chapter 3), the thickness of the intelligent ink layer was known. This allowed us to determine the photocatalytic rate of resazurin photo-reduction for each position analysed. A few assumptions were made in order for us to do so. Firstly, we assumed that the concentration of resazurin in the intelligent ink remained constant before and after loading using the aerosol spray. Secondly, we assumed that the rate of resazurin photo-reduction was approximately constant throughout the entire photo-reduction reaction. This was observed by Mills *et. al.* in his original studies of intelligent inks, where a relatively constant rate of removal of the redox dye was observed, irrespective of the initial concentration of the redox dye or thickness of the ink layer loaded.[172,174] The rate of resazurin photo-reduction could thus be determined by:

$$molecules\ photoreduced\ (cm^{-2}s^{-1}) = \frac{initial\ resazurin\ molecules\ (cm^{-2})}{t(R_{\mathrm{plateau}}, RGB)} \tag{4.3}$$

as the time taken to reach the plateau in the red component of digital colour represents the time at which all resazurin present at the point analysed has been photo-reduced (Equation 2.20). Where the photon flux of the UVA lamp was determined using a photo counting device (UVX radiometer, 365 nm sensor attached), the formal quantum efficiency of the photo-reduction reaction could be

determined (Equation 1.2). If the fraction of photons absorbed by the semiconductor film layer from this lamp was also known, then the formal quantum yield could also be determined (Equation 1.2).

4.2.2.5. Photocatalysis of stearic acid

The photocatalytic oxidation of a stearic acid overlayer was investigated using Fourier transform infrared (FTIR) spectroscopy over the 2980-2800 cm^{-1} range on a Perkin Elmer RX-I instrument. Samples were affixed to measurement cells centred on the test position; exposing a 1 cm^2 area. The films were washed with propan-2-ol and then placed under UVC irradiation for 1 hr to ensure the surface was free from contaminants. Samples were coated with a waxy stearic acid over-layer (0.02 M solution in methanol) by depositing a few solution droplets onto the film's surface. After spinning the samples at 1000 rpm for 10 s, the samples were oven dried for 1 hr at 50 °C to ensure the complete evaporation of the methanol solvent. The photocatalytic oxidation of the stearic acid overlayer was initiated and propagated using a UVC light source. The decrease in absorbance of C-H symmetric/anti-symmetric stretches in the infra-red region investigated signified the photocatalytic oxidation of the stearic acid overlayer. The absorbance area could be related to the concentration of the stearic acid overlayer by a conversion factor (9.7 x 10^{15} molecules ≡ 1 cm^{-1}).[161] The change in absorbance area, and thus a decrease in the number of stearic acid molecules, was followed as a function of time for 25 hrs of UVC irradiation. Where the photon flux of the UVC lamp was determined using a photo counting device (UVX radiometer, 254 nm sensor attached), the formal quantum efficiency of the photo-oxidation reaction could be determined (Equation 1.2).

4.3. Nb-doped anatase TiO_2

4.3.1. Introduction

Doping anatase TiO_2 with niobium has become a potential alternative transparent conducting oxide (TCO) material to the more commonly used indium doped tin oxide material since comparable resistivities (ρ) as low as 2.3 x 10^{-6} Ωm were achieved on strontium titanate substrates by Furubayashi *et. al* in 2005.[258] Subsequent investigations found a relationship between the oxygen concentration during film growth and the resulting film conductivity.[261,265,266] Computational calculations showed how oxygen vacancy formation was encouraged in a reducing growth environment, which increased the mobility (μ) of charge carriers and conductivity in the resulting film; a phenomenon similarly observed in indium doped tin oxide.[265] This was also determined through experimentation, where changing the oxygen concentration during film growth affected the

resultant conductivity of the film formed, especially when coupled with Nb dopant levels above 1 at. %.[261] Other factors that contributed to the electrical conductivity, such as the grain size[267] and surface morphology[268] were also investigated, where an increased grain size and a smoother surface increased film conductivity. The mode of conductivity in Nb-doped TiO_2 was experimentally found to be n-type.[261] This was unsurprising given Nb-doping within anatase TiO_2 was found to insert primarily in the Nb^{5+} state,[266] where electro-neutrality required the injection of charge carriers into the conduction band. Nb-doped TiO_2 thin-films grown on more insulting barrier glass coated substrates showed a greater impedance to film conductivity, with resistivities ranging from 1.3×10^{-3} to 9×10^{-3} Ωm.[150,262] Post treatment annealing of these films in air caused a further reduction in conductivity by a factor of ≈ 2.[150] This verified computational predictions that suggested the presence of oxygen vacancies were vital to the movement of charge carriers within niobium doped anatase TiO_2.[265] Computational studies also found how Nb-doping increased the stability of oxygen vacancies relative to un-doped TiO_2.[265] Relatively high levels of Nb-doping (≈ 10 at. %) caused an increase in the bandgap energy from 3.18 eV in un-doped anatase TiO_2 to *ca.* 3.35 eV.[269] It was found that doping anatase TiO_2 with Nb levels greater than ≈ 5 at. % caused the Fermi energy level to lie in the conduction band. This was caused by the introduction of excessive electron donors into the system, explained by the Moss-Burstein effect.[270,271] High levels of Nb incorporation in TiO_2 have been achieved (≈ 40 at. %) and was attributed to the similar sized ionic radii of Nb^{5+} (0.78Å) and Ti^{4+} (0.75Å).[272]

Nb-doped anatase TiO_2 systems may also have applications as gas sensors, where significantly better response times to detecting the presence of di-oxygen gas have been observed in comparison to its pure anatase TiO_2 counterpart.[262,273] However, to our knowledge, the photocatalysis of Nb-doped TiO_2 thin-films is yet to be reported.

The Nb-doped anatase TiO_2 thin-films reported in the literature thus far have been formed primarily by PVD or pulsed laser depositions (PLD). Although individual thin-films of Nb_2O_5[274,275] and anatase TiO_2[18] have been grown by APCVD, a Nb-doped anatase TiO_2 solid solution is yet to be synthesised by this method. The advantage of producing films by CVD over PVD are clear, where films of superior adhesion, durability and conformity can be produced at a lower cost.[276]

In this section we describe the combinatorial APCVD synthesis of anatase thin-films with graded niobium dopant content from $0.0004 \leq x \leq 0.0194$ in $Nb_xTi_{1-x}O_2$. This was formed using a triple source of precursors, with $TiCl_4$ as the titanium source, $NbCl_5$ as the niobium source and ethyl acetate as the oxygen source. This was the first demonstration in forming Nb-doped TiO_2 by a CVD process. It was also the first time in which combinatorial APCVD was used to cation dope a metal oxide. The

properties of up to 400 unique positions were investigated across each combinatorial film. Phase mapping confirmed the solitary presence of the anatase TiO_2 phase throughout the combinatorial film. The variation in film-thickness was quantified by our mapping method (Section 2.4). Atomic force microscopy (AFM) was used to map the degree of surface roughness and topography. The resistivity and photocatalytic activity at all 200 unique positions were mapped in accordance with the methods outlined in Sections 4.2.2.3 and 4.2.2.4 respectively. The bandgap at designated positions along a single strip of each combinatorial film was also determined (Section 4.2.2.1). A strong inter-relationship between each of these three functional properties was observed, correlating in 3-dimensions. Further experimentation indicated that these properties were primarily dependent on the number of oxygen vacancies present within the material as opposed to some optimum niobium doping level.

4.3.2. Experimental combinatorial film synthesis

Two anatase TiO_2 thin-films with graded substitutional Nb-dopant content were formed by combinatorial APCVD. The first combinatorial film was denoted $NbTiO_2$-A ($0.0004 \leq x \leq 0.0011$ in $Nb_xTi_{1-x}O_2$) and the second combinatorial film was denoted $NbTiO_2$-B ($0.0017 \leq x \leq 0.0194$ in $Nb_xTi_{1-x}O_2$). Each film was deposited on float glass (225 × 90 × 3.2 mm; length × breadth × thickness) that contained an ≈ 50 nm thick barrier layer of SiO_2 at the substrate's surface to inhibit the diffusion of ions from the glass (i.e. Na, Mg, Ca) into the film. A schematic of the apparatus used to deposited each film is shown in Figure 4.3.1. Each combinatorial film was synthesised from volatised precursors stored and carried from bubblers, where bubbler 1 contained $NbCl_5$ (niobium source), bubbler 2 contained $TiCl_4$ (titanium source) and bubbler 3 contained ethyl acetate (oxygen source). The volatility of each precursor was altered by adjusting the temperature at each bubbler. The vapours were transported from each of their respective bubblers by an inert N_2 gas. The $NbCl_5$ vapours were carried to mixing chamber A, where they were then combined with a plain line flow of inert N_2 gas and carried into the cold-walled reactor (500 °C). The $TiCl_4$ and ethyl acetate vapours were carried to mixing chamber B, where they were then combined with a plain line flow of inert N_2 gas and carried into the reactor. The separate entries of the niobium and titanium sources created a horizontal gradient in the niobium: titanium source concentration across the substrate and a range of deposition conditions in a single experiment. The use of two metallic source precursors provided us with a large number of experimental parameters. For simplicity, the temperature of just one bubbler, containing the niobium source, was varied in both experiments. The parameters used to achieve the two combinatorial films analysed in this study, $NbTiO_2$-A and $NbTiO_2$-B, are displayed in Table 4.3.1.

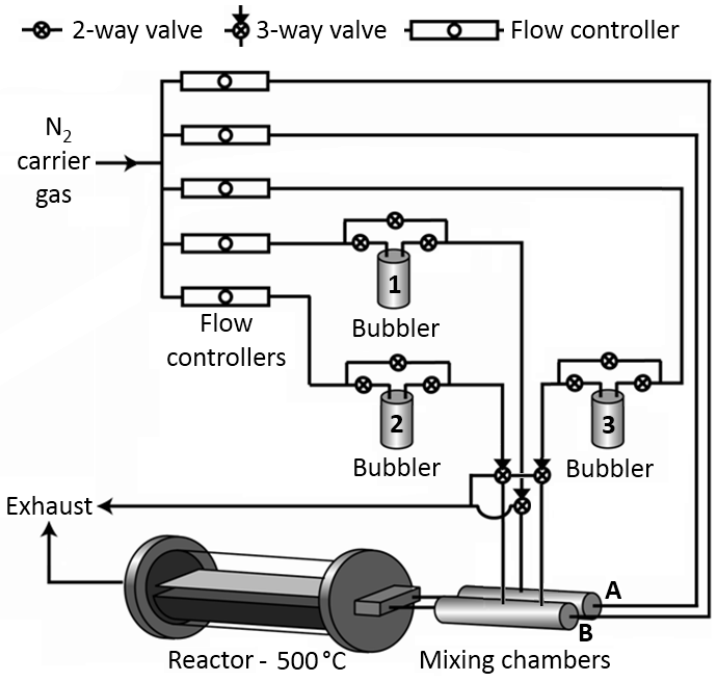

Figure 4.3.1: *Schematic of the combinatorial APCVD apparatus. The combinatorial films were synthesised from volatised precursors carried from bubblers, where bubbler 1 contained $NbCl_5$, bubbler 2 contained $TiCl_4$ and bubbler 3 contained ethyl acetate. Of particular importance are the two separate entry points of the precursors into the reactor, where $NbCl_5$ entered the reaction from mixing chamber A and $TiCl_4$ and ethyl acetate entered the reactor from mixing chamber B. This created a gradient in the niobium source concentration across the substrate and a range of deposition conditions in a single experiment.*

	Mixing Chambers		Bubblers					
			$NbTiO_2$-A			$NbTiO_2$-B		
			1	2	3	1	2	3
	A	B	$NbCl_5$	$TiCl_4$	Ethyl acetate	$NbCl_5$	$TiCl_4$	Ethyl acetate
Temperature (°C)	200	140	142	70.4	38.8	179	69.9	34.6
Flow rate (L min^{-1})	5.1	2.3	2.0	1.0	0.7	2.0	1.0	0.7
Vapour pressure (mm Hg)	-	-	8.3	98	180	65	96	150
Mass flow rate (10^{-3} mol min^{-1})	-	-	0.91	6.1	9.0	7.7	5.9	7.0
Molar ratios (to Ti source)	-	-	0.15	1.0	1.5	1.3	1.0	1.2

Table 4.3.1: Temperatures (°C) of components and N_2 carrier gas flow rates (L min^{-1}) in the combinatorial APCVD syntheses of two anatase TiO_2 thin-films with graded Nb-doping levels. The parameters for synthesising each combinatorial film, denoted $NbTiO_2$-A ($0.0004 \leq x \leq 0.0011$ in $Nb_xTi_{1-x}O_2$) and $NbTiO_2$-B ($0.0017 \leq x \leq 0.0194$ in $Nb_xTi_{1-x}O_2$), are shown. The carbon block inside the reactor was maintained at 500 °C during each 60 s deposition. Mass flow rates (mol min^{-1}) were derived from vapour pressure (mm Hg) curves to yield the molar ratio of each precursor relative to $TiCl_4$.

A reference system that shows the exact locations of the positions analysed by each characterisation method for both combinatorial films studied is shown in Figure 4.3.2. The methods of characterisation applied at each of the allotted grid positions are shown in the central key. Further details of the experimentation and apparatus can be found in the experimental methods, Section 4.2.

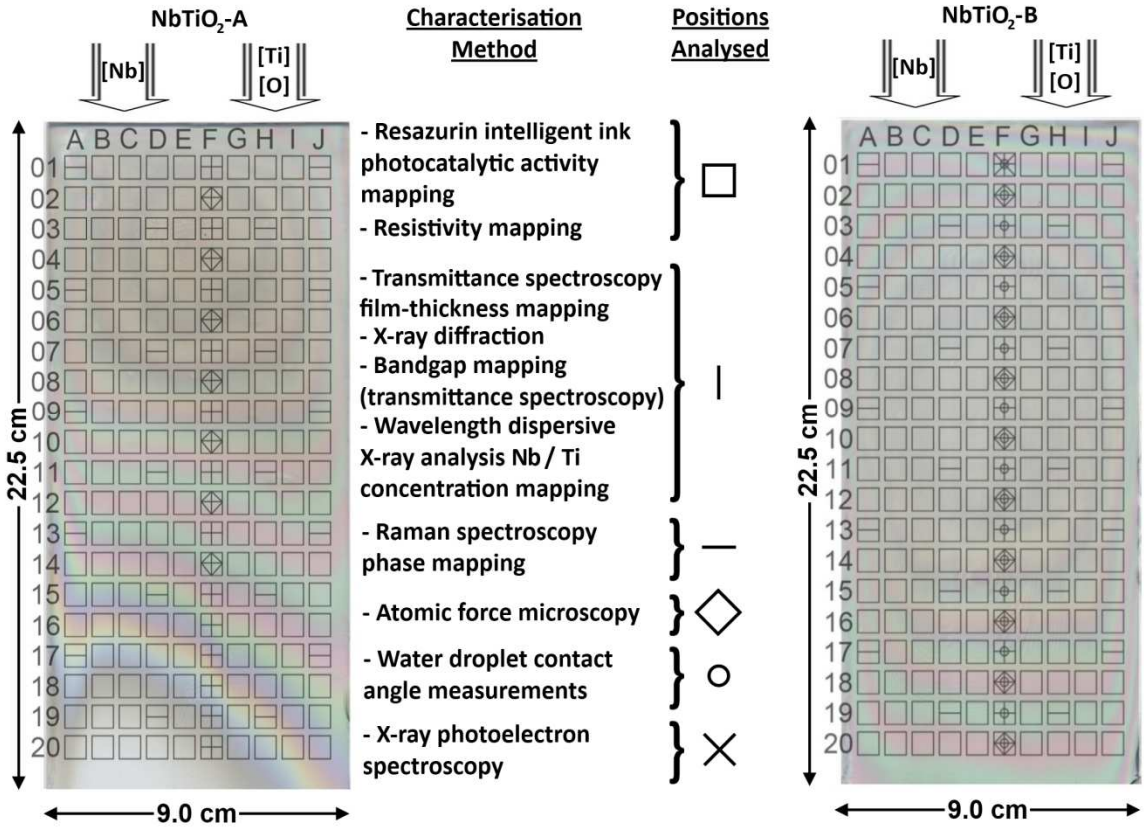

Figure 4.3.2: *Picture of each combinatorial thin-film and super-imposed grid reference system used throughout this section. The type of characterisation used at each allotted grid position is described in the central key. Up to 200 unique grid positions were analysed over each combinatorial system (10 x 20; horizontal x vertical). The positions of the gas inlets relative to the glass substrate at the time of deposition within the reactor are shown; with Row 1 lying closest to the gas inlets and Row 20 lying closest to the exhaust. The centres of neighbouring grid positions are spaced 0.75 cm apart in rows and in columns.*

4.3.3. Results

In order to rationalise the functional properties across both combinatorial films in this study, the positions down a central strip of each film (Column F) were probed in more detail. The results from characterising each combinatorial film were amalgamated into a large table for comparison (Table 4.3.2(a); $NbTiO_2$-A and Table 4.3.2(b); $NbTiO_2$-B).

(a)

$NbTiO_2$-A	Physical properties					Functional properties				
Grid position	XRD		WDX	AFM	Transmittance (%)		Four-point probe resistance			UVA photocatalysis mapping
	Crystallite size (nm ± ≈ 1 %)	Unit cell volume (Å ± ≈ 0.1 %)	Nb: Ti (at. % ± ≈ 10%)	Surface area (μm^2 ± ≈ 1 %)	Film-thickness (nm ± ≈ 1 %)	Band Gap (eV ± ≈ 1 %)	Rs (10^{-4} Ω/□ ± ≈ 1 %)	Log_{10}(Rs (Ω/□))	Resistivity (Ωm)	10^{12} molecules photo-reduced $cm^{-2}s^{-1}$ ± ≈ 10 %)
F1	20.4	136.4	0.11	1.20	836	3.23	2.64	4.42	0.022	3.38
F2	19.7	136.5	0.09	1.08	850	3.23	3.31	4.52	0.028	3.04
F3	19.9	136.7	0.09	1.21	841	3.24	4.27	4.63	0.036	2.82
F4	19.2	136.3	0.07	1.05	823	3.24	5.40	4.73	0.044	2.35
F5	19.7	136.4	0.07	1.22	783	3.26	7.42	4.87	0.058	2.35
F6	18.9	136.7	0.07	1.04	743	3.26	11.3	5.05	0.084	2.09
F7	19.0	136.1	0.06	1.29	664	3.27	17.0	5.23	0.113	1.94
F8	18.0	136.1	0.06	1.06	574	3.28	20.2	5.30	0.116	1.77
F9	20.4	136.4	0.06	1.04	523	3.29	28.2	5.45	0.148	1.66
F10	19.4	136.6	0.05	1.05	436	3.31	39.9	5.60	0.174	1.50
F11	18.0	136.1	0.04	1.04	383	3.32	40.6	5.61	0.155	1.39

Table 4.3.2: *List of physical and functional property data acquired from X-ray diffraction (XRD), wavelength dispersive X-ray analysis (WDX), transmittance spectroscopy, atomic force microscopy (AFM), four-point probe sheet resistance, intelligent ink photocatalysis mapping (UVA light) and water droplet contact angle measurements (UVC light) for positions along Columns F in (a) $NbTiO_2$-A and (b) $NbTiO_2$-A.*

(b)

$NbTiO_2$-B	Physical properties						Functional properties					
Grid position	XRD		WDX	AFM	Transmittance (%)		Four-point probe resistance			UVA photocatalysis mapping	Water droplet contact angle (° ± ≈ 10 %))	
	Crystallite size (nm ± ≈ 1 %)	Unit cell volume (Å ± ≈ 0.1 %)	Nb: Ti (at. % ± ≈ 10%)	Surface area (μm^2 ± ≈ 1 %)	Film-thickness (nm ± ≈ 1 %)	Band Gap (eV ± ≈ 1 %)	Rs (10^{-4} Ω/□ ± ≈ 1 %)	Log_{10}(Rs (Ω/□))	Resistivity (Ωm)	10^{12} molecules photo-reduced $cm^{-2}s^{-1}$ ± ≈ 10 %)	Before UVC	After UVC
F1	16.4	136.4	1.94	1.21	286	3.35	43.2	5.64	0.124	1.76	49	1.9
F2	18.0	136.7	1.73	1.04	383	3.33	28.0	5.45	0.107	1.84	52	4.1
F3	18.0	136.1	1.29	1.17	522	3.28	19.0	5.28	0.099	1.92	46	3.3
F4	18.4	136.4	1.02	1.01	595	3.27	14.0	5.15	0.083	2.00	46	3.1
F5	17.0	136.5	0.95	1.16	682	3.26	9.81	4.99	0.067	2.10	52	1.9
F6	17.8	136.7	0.83	1.07	735	3.25	7.74	4.89	0.057	2.23	44	2.8
F7	19.0	136.4	0.76	1.01	758	3.25	6.54	4.82	0.050	2.69	43	1.7
F8	17.9	136.7	0.73	1.21	794	3.24	5.70	4.76	0.045	3.18	56	2.5
F9	17.4	136.1	0.68	1.01	788	3.24	5.65	4.75	0.045	3.31	51	1.5
F10	19.2	136.7	0.64	1.15	781	3.24	5.86	4.77	0.046	3.25	63	3.8
F11	18.3	136.3	0.58	1.01	781	3.23	5.10	4.71	0.040	3.27	40	3.3
F12	18.7	136.4	0.54	1.14	772	3.23	4.44	4.65	0.034	3.27	39	4.8
F13	18.6	136.7	0.44	1.01	750	3.23	4.09	4.61	0.031	3.06	39	3.2
F14	19.1	136.4	0.42	1.01	723	3.24	5.40	4.73	0.039	2.67	38	3.5
F15	18.7	136.7	0.45	1.18	604	3.26	6.64	4.82	0.040	2.25	37	2.1
F16	18.4	136.1	0.42	1.03	577	3.26	8.28	4.92	0.048	2.09	35	2.5
F17	18.5	136.4	0.26	1.04	521	3.28	1.11	5.05	0.058	2.02	38	1.5
F18	19.2	136.5	0.24	1.06	473	3.28	1.47	5.17	0.070	1.94	40	1.5
F19	17.6	136.7	0.19	1.03	415	3.29	2.37	5.37	0.098	1.92	39	2.4
F20	17.8	136.6	0.17	1.01	379	3.30	4.08	5.61	0.155	1.84	43	3.1

4.3.3.1. Appearance

Two combinatorial anatase TiO_2 thin-films with a gradient in the Nb dopant concentration ($0.0004 \leq x \leq 0.0011$ and $0.0017 \leq x \leq 0.0194$ in $Nb_xTi_{1-x}O_2$) were grown by a combinatorial APCVD reaction of $TiCl_4$ and $NbCl_5$ metal sources with an ethyl acetate oxygen source at 500 °C. Interference fringes, characteristic of thin-films with high refractive indices were observed (Figure 4.3.2). This showed how film-thickness varied across the combinatorial film. The contours of the fringes peaked in the top-middle section of $NbTiO_2$-A (positions E4/ F4) and the middle section of $NbTiO_2$-B (positions E10: F11), indicating where the films were most thick. The films showed a dark-blue tinge in reflectance, characteristic of Nb doping in TiO_2 thin-films.[269] In $NbTiO_2$-B, good film coverage was observed, where the entire glass substrate was coated; however a semi-circular portion of the glass substrate near the bottom-end of $NbTiO_2$-A remained uncoated. A stronger coloration was seen in $NbTiO_2$-B and was attributed to the greater level of Nb doping. On closer inspection, the dark-blue tinge was found to be most prominent at the thickest sections in both films. This indicated that the Nb-doping level was graded, which was later confirmed by niobium/ titanium concentration mapping through wavelength dispersive X-ray analysis. Both films were highly adhesive to their glass substrate and impervious to prolonged immersion in common solvents (water, acetone and isopropanol). Both films passed the Scotch$^{(R)}$ tape test, impervious to scratching with a stainless steel stylus but could be scratched with a diamond tip. From the accumulated thicknesses determined by our film-thickness mapping method the average growth rates were similarly 10.3 and 10.7 $nm.s^{-1}$ for $NbTiO_2$- A and $NbTiO_2$- B respectively.

4.3.3.2. Niobium/ titanium concentration mapping

Wavelength dispersive X-ray (WDX) analysis quantified the levels of Nb substitution down the central strip (Column F) in both combinatorial films. Substantial differences in the level of Nb was observed between films, with $0.04 \leq$ Nb: Ti (at. %) ≤ 0.11 in $NbTiO_2$-A and $0.17 \leq$ Nb: Ti (at. %) ≤ 1.94 in $NbTiO_2$-B. The Nb: Ti (at. %) concentrations were determined from an average of five readings taken local to each grid position over 100 μm^2 excitation areas. The Nb-doping level was taken as the average of the five readings, with the standard deviation taken as the error. These values are plotted in Figure 4.3.3 for both $NbTiO_2$-A and $NbTiO_2$-B. The levels of Nb incorporated across both combinatorial films differed by an order of magnitude. This was unsurprising given almost 10 times more $NbCl_5$ was introduced in the formation of $NbTiO_2$-B (Table 4.3.1). The Nb-doping level was greatest at the top of each strip analysed (position F1). In $NbTiO_2$-A, the Nb-doping level decreased almost linearly (r^2 = 0.93) to position F14, where no further detectable levels of Nb were observed. However, in $NbTiO_2$-B, the doping level fell exponentially (r^2 = 0.96). The Nb-doping levels in $NbTiO_2$-A were so low that they

neared the detection limits of the WDX apparatus. Therefore, significantly greater associated errors were observed in $NbTiO_2$-A (Figure 4.3.3(a)) compared with those in $NbTiO_2$-B (Figure 4.3.3(b)). This was shown by the fact that the average percentage error across the positions analysed in $NbTiO_2$-A (25 %) was 15 % greater than those in $NbTiO_2$-B (10 %).

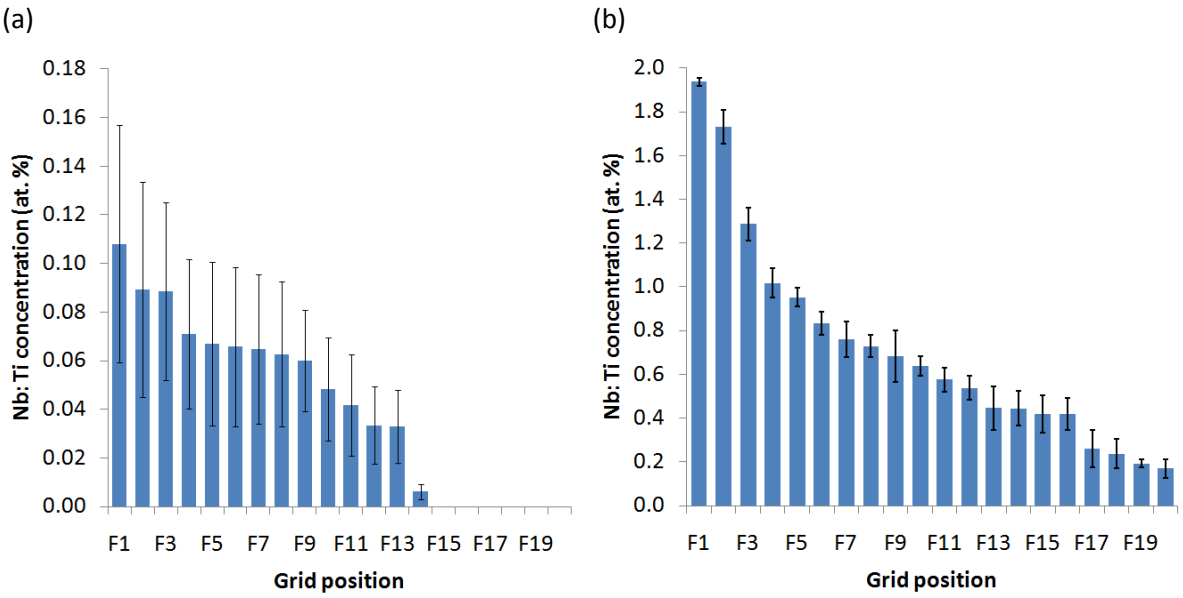

Figure 4.3.3: *Charts displaying the Nb: Ti concentration (at. %) and error in both (a) NbTiO2-A and (b) NbTiO2-B for each position analysed by wavelength dispersive X-ray analysis along Column F.*

4.3.3.3. Preferred orientation and phase mapping

The X-ray diffraction pattern of each position along Column F where underlying film growth was observed were analysed in both $NbTiO_2$-A and $NbTiO_2$-B. All diffraction patterns solely featured the anatase TiO_2 phase ($I4_1/amdz$, a = 3.785 Å, c = 9.512 Å).[146] Not only did Raman spectroscopy confirm the presence of this solitary anatase TiO_2 phase at analogous positions along Column F, but also for positions scattered across both films (Figure 4.3.2). This indicated that both combinatorial films were entirely composed of anatase TiO_2. Some example XRD and Raman patterns are shown in Figure 4.3.4 for the even numbered positions along Column F in $NbTiO_2$-B. Peaks of greater intensity were observed where the underlying film was thicker. Upon comparing XRD patterns, no discernible shifts in any of the peaks were observed. This was confirmed by fitting patterns to a Le Bail refined model. No significant change in the unit cell lattice parameters was observed, where the average unit cell volume across both combinatorial films was 136.6 ± 0.31 $Å^3$ and was very similar to that of pure anatase TiO_2 (136.2 $Å^3$). This result showed how Nb substituted for Ti sites with little disruption to the lattice over the dopant regime investigated (0.04 ≤ Nb: Ti at. % ≤ 1.94). The relative heights of each diffraction pattern were almost identical and demonstrated how the effect of preferred orientation was consistent across both combinatorial films (Figure 4.3.4(a)). The degree of preferred

orientation relative to a single crystal was thus investigated for a single representative position (F11, $NbTiO_2$-B).

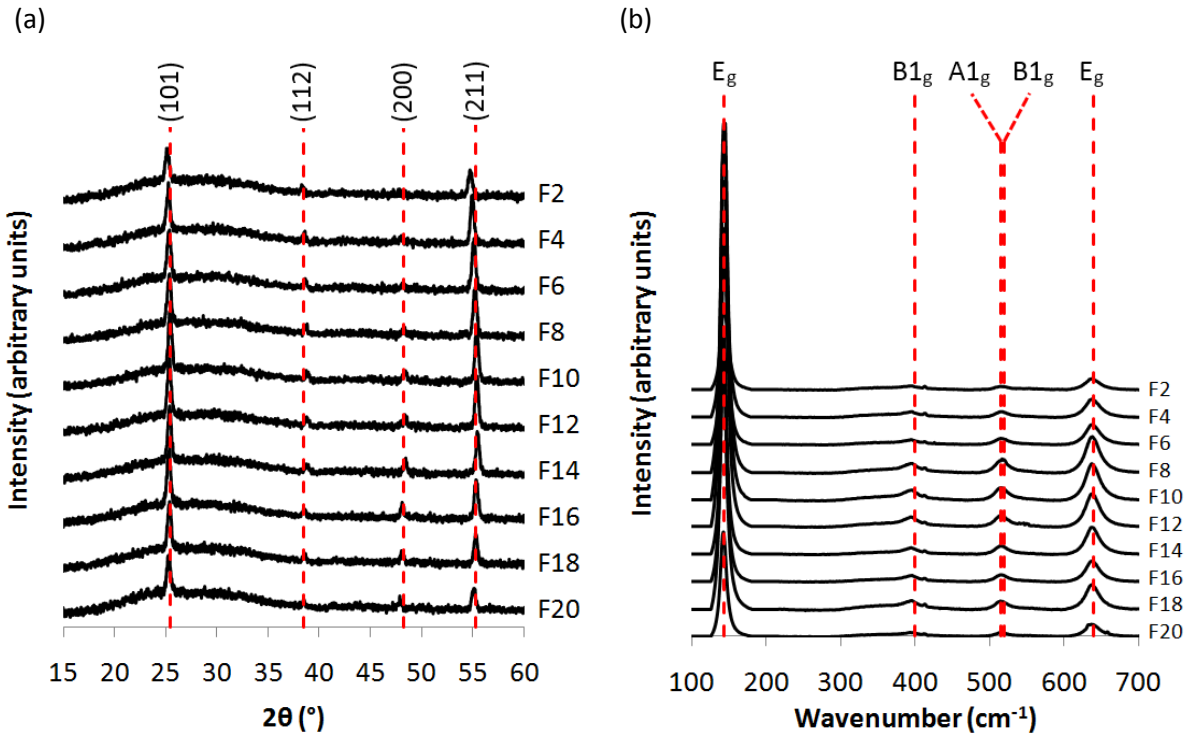

Figure 4.3.4: *Labelled (a) X-ray diffraction and (b) Raman patterns of the even numbered positions analysed along Column F in $NbTiO_2$-B.*

The diffraction pattern was plotted alongside that of a single crystal (Figure 4.3.5(a)). The patterns were both normalised relative to the height of the most prominent (101) peak. As we can see, the (103), (004) and (105) diffraction peaks were not present. This demonstrated how the preferred orientation of the crystallites had little or no preference to grow in these planes. However, if we look at the (211) plane, a strong increase in intensity relative to the single crystal is observed.

In order to quantify these differences, the percentage contribution of the intensity of each diffraction plane was determined (Equation 2.3). The percentage difference compared to that of the single crystal could then be determined (Equation 2.4), as shown in Figure (4.3.5(b)). This quantified the changes observed by eye, where the (103), (004) and (105) peaks were all highly negative. In addition, the greatest degree of preferred growth was observed in the (211) plane, with nearly a five time increase in intensity relative to a single crystal. This was followed by growth in the (112) plane that almost doubled in intensity relative to a single crystal. Such a result was unsurprising given the similar directions in which the (211) and (112) planes point.

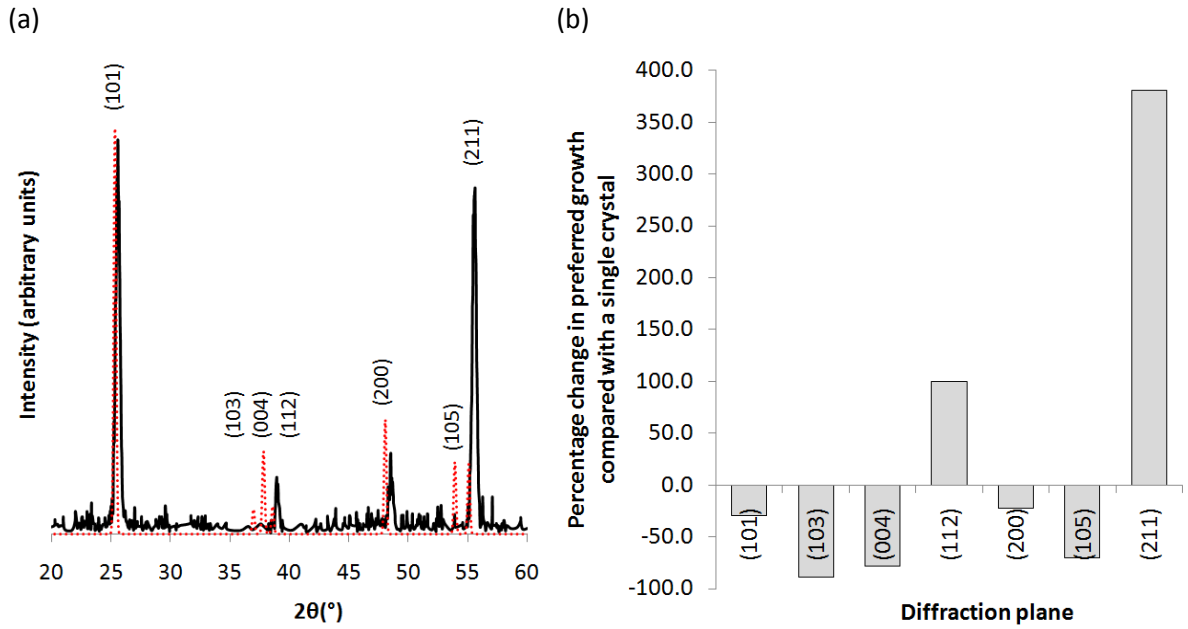

Figure 4.3.5: *(a) The X-ray diffraction pattern at position F11 in $NbTiO_2$-B of unitary anatase TiO_2 phase plotted alongside that of a single crystal (red dotted lines) normalised to the height of the (101) plane and (b) the percentage change in preferred growth of each diffraction plane relative to the single crystal.*

The Scherrer equation[132] (Equation 3.9) was applied to the most prominent (101) diffraction peak to calculate the average crystallite size at each position analysed by XRD. Little variance in the average crystallite size across both combinatorial films was observed. The average and standard deviation error in the crystallite size across both combinatorial film sets were similarly 19.0 ± 1.1 nm for $NbTiO_2$-A and 18.2 ± 0.73 nm for $NbTiO_2$-B.

4.3.3.4. Film-thickness mapping

The transmittance at each grid position in Column F where underlying film growth was observed was analysed in both $NbTiO_2$-A and $NbTiO_2$-B. A high average transmittance of light in the visible region of the spectrum (450 – 1000 nm) of ≈ 70 ± 2 % was seen across both combinatorial films, irrespective of changes in film-thickness. Wave-like transmittance patterns were observed, characteristic of thin-layer high refractive index materials. Example transmittance patterns of the positions analysed along Column F in $NbTiO_2$-A are shown in Figure 4.3.6(a). The number of waves increased from where the film was observed to be thinnest by eye (position F16) to where the film was observed to be thickest (position F2). This was as expected as a thicker film can accommodate a wider number of interfering wavelengths. With knowledge of the dependence of the material's refractive index with frequency as well as the positions where maximum and minimum interference occur, the Swanepoel method[122] can be was used to determine film-thickness. Given quite low levels of niobium doping were contained within both films, never reaching greater than 2 at. %, it was assumed that the spectral

dependence of the refractive index would not significantly change in comparison with the pure material. A high degree of fit (r^2 > 0.99) was observed in all Swanepoel plots (Figure 2.3.2(b)), validating this assumption. The film-thicknesses and their associated errors for the positions analysed along Column F in $NbTiO_2$-A are shown in Figure 4.3.6(b). The film-thickness maximised at position F2 (850 nm) and decreased steadily from this point to position F16 (90 nm). No film growth was observed from position F17 to F20. Contrastingly, in $NbTiO_2$-B, the film-thickness increased steadily from position F1 (286 nm) to where it maximised at position F8 (794 nm) and then fell steadily back down to position F20 (379 nm). The average film-thicknesses along Column F were 535 nm in $NbTiO_2$-A and 620 nm and $NbTiO_2$-B.

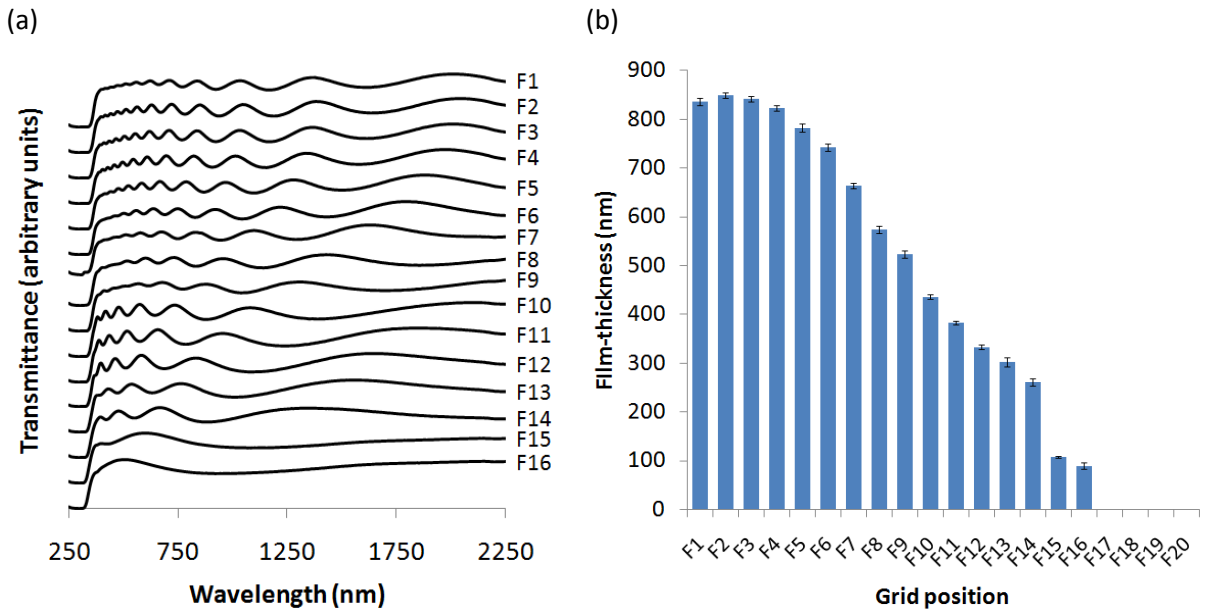

Figure 4.3.6: *(a) A stacked plot of the transmittance patterns (arbitrary units) acquired along Column F in $NbTiO_2$-A over the 250 to 2250 nm range and (b) a bar chart of the film-thicknesses and associated errors derived from each of these transmittance patterns using the Swanepoel method.*[122]

4.3.3.5. Surface topography mapping

The topography along all positions in Column F, where an underlying film was present, in both combinatorial films, was mapped using atomic force microscopy (AFM). Areas 1 x 1 µm in size were scanned. The images acquired from the even positions along Column F in $NbTiO_2$-B are shown in Figure 4.3.7 alongside images taken from a 50x zoom optical camera. Changes in film colour seen in the digital images were predominantly due to interference effects. A similarly smooth surface topography was observed across all positions analysed. Crystallite sizes were roughly 20 nm in diameter. This was similar to the average crystallite sizes predicted by applying the Scherrer equation to the most prominent (101) peak in XRD patterns. The surface areas were determined from height data. Little change in the surface areas were observed across both combinatorial films. The average

surface areas were 1.10 ± 0.10 μm^2 in $NbTiO_2$-A and 1.04 ± 0.08 μm^2 in $NbTiO_2$-B. The average surface areas deviated little from the projected test area (1.00 μm^2) and demonstrated the high smoothness across both films.

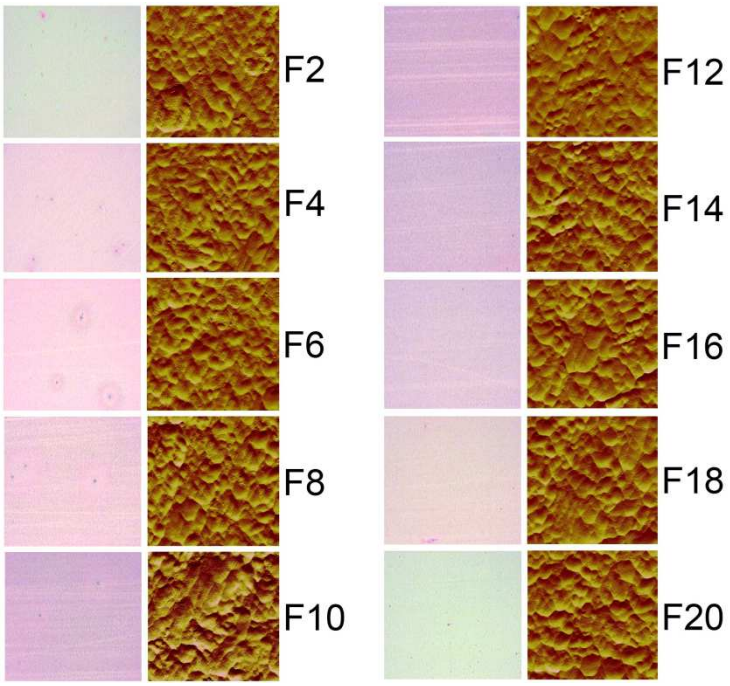

Figure 4.3.7: *Atomic force microscopy (AFM) images of the even numbered positions along Column F in $NbTiO_2$-B shown alongside top-down digital images acquired from a 50x optical camera. The widths of the optical camera and AFM images are 100 µm and 1 µm respectively.*

4.3.3.6. Reaction chemistry

Two combinatorial anatase TiO_2 thin-films with a gradient in the Nb dopant concentration ($0.0004 \leq x \leq 0.0011$ and $0.0017 \leq x \leq 0.0194$ in $Nb_xTi_{1-x}O_2$) were grown by a combinatorial APCVD reaction of $TiCl_4$ and $NbCl_5$ metal sources with an ethyl acetate oxygen source at 500 °C. This was the first time in which solid solutions of Nb-doped anatase TiO_2 had been synthesised by CVD, let alone with compositional gradients. It was also the first time that combinatorial APCVD had been used to dope cations into a metal oxide. $TiCl_4$ was chosen because of its high volatility, relative inexpensiveness and zero carbon content. This reagent has been used as the titanium source on numerous occasions for the APCVD synthesis of TiO_2; forming robust, well-adhered, transparent and crystalline thin-films.[110,277] Ethyl acetate was selected as our oxygen source. Although one might predict the cleaner reaction of H_2O with $TiCl_4$, given their combined zero carbon content, well adherent thin-films do not form. The greater propensity for the reaction to occur in the gas phase rather than at the substrate surface leads to the formation of powdery and hazy films with low adherence. Ethyl acetate was chosen as it reacts with $TiCl_4$ in a way that forms robust and strongly adhered transparent thin-films. When used in the correct ratio, little or no carbon contamination occurs. It was previously shown

that solid $NbCl_5$ and liquid ethyl acetate precursors could be used to synthesise thin-films of Nb_2O_5 by APCVD onto glass.[275] As both $TiCl_4$ and $NbCl_5$ metal source precursors have been combined with ethyl acetate to form thin-films of each respective metal oxide, we therefore combined all three precursors in forming our combinatorial Nb-doped TiO_2 thin-films. The precursor temperatures and carrier gas flow rates were adjusted to achieve the reagent mass flow rates specified in Table 4.3.1.[200] In the formation of $NbTiO_2$-A and $NbTiO_2$-B, the average niobium dopant levels determined from our niobium/ titanium concentration mapping experiments (Section 4.3.3.2) were 0.06 (σ = 0.03) and 0.71 (σ = 0.48) at. %. X-ray photoelectron spectroscopy measurements showed how the niobium dopant existed primarily in the Nb^{5+} state. Therefore, in both cases, the average oxygen: metal ratio incorporated was 2.00. As the molar ratio of the oxygen source (ethyl acetate): metal sources ($TiCl_4$ & $NbCl_5$) were 1.30 and 0.52 in the formation of $NbTiO_2$-A and B respectively, in both cases ethyl acetate was the limiting reagent in the formation of $Nb_xTi_{1-x}O_2$. By mapping the niobium dopant level and film-thickness along Column F in both combinatorial films, as well as confirming that both films were of unitary anatase TiO_2 phase, the reaction rate of each precursor at each grid position (over a 0.56 cm^2 area) could be derived (Figure 4.3.8). In calculating these reaction rates we made the assumption that the anatase TiO_2 combinatorial film consisted of unitary density (3.89 $g.cm^{-3}$).[201]

The major disparity between the two combinatorial depositions was the level of $NbCl_5$ introduced. In the formation of $NbTiO_2$-A, 0.91 x 10^{-3} $mol.min^{-1}$ was introduced whereas in the formation of $NbTiO_2$-B, 7.7 x 10^{-3} $mol.min^{-1}$ was introduced; a factor increase of ≈ 8.5. When looking at the reaction rate of the $NbCl_5$ precursor (Figure 4.3.8(c)), it is clear that the level of Nb inserted depended on the level of $NbCl_5$ introduced. In fact, an approximately linear dependence on the level of Nb inserted and the level of $NbCl_5$ introduced was observed. In both reactions, the reaction rate of $NbCl_5$ was highest at positions most local to where the precursor was introduced. This indicated that the reaction of $NbCl_5$ was a mass-transfer limited process in both depositions. However, when looking at the reaction rates of both $TiCl_4$ and ethyl acetate, contrasting differences between each combinatorial synthesis were observed. This was quite unexpected given the similarity of the mass flow rates of $TiCl_4$ and ethyl acetate introduced in each deposition (Table 4.3.1). Both films were produced in a cold-walled reactor, where the temperature was marginally hotter at the centre of the heating block than at the edges (by ≈ 25 °C). The glass substrate in which the films were deposited onto would therefore have been hottest at its centre. In the formation of $NbTiO_2$-A, the reaction rate of $TiCl_4$ and ethyl acetate maximised at positions on the film most local to where the precursor was introduced. However, in the formation of $NbTiO_2$-B, the reaction rate of $TiCl_4$ and ethyl acetate maximised near the centre of the film. This indicated that the formation of TiO_2 in $NbTiO_2$-B was a

reaction rate limited process whereas in $NbTiO_2$-A it was a mass-transfer limited process.[108] Given that the concentration of the oxygen source, ethyl acetate, was approximately equal in both depositions, it was deduced that the reaction pathway in the formation of TiO_2 was dependent on the total concentration of the metal sources, where a higher metal source ratio encourage a surface reaction rate limited over a mass-transfer limited process. Although approximately equal concentrations of $NbCl_5$ and $TiCl_4$ metal sources were present in the formation of $NbTiO_2$-B, merely 0.71 at. % Nb doping occurred on average along Column F. This demonstrated the comparatively rapid reaction kinetics of the $TiCl_4$ compared with $NbCl_5$ under the experimental conditions imposed, with $TiCl_4$ reacting approximately 180 times more efficiently.

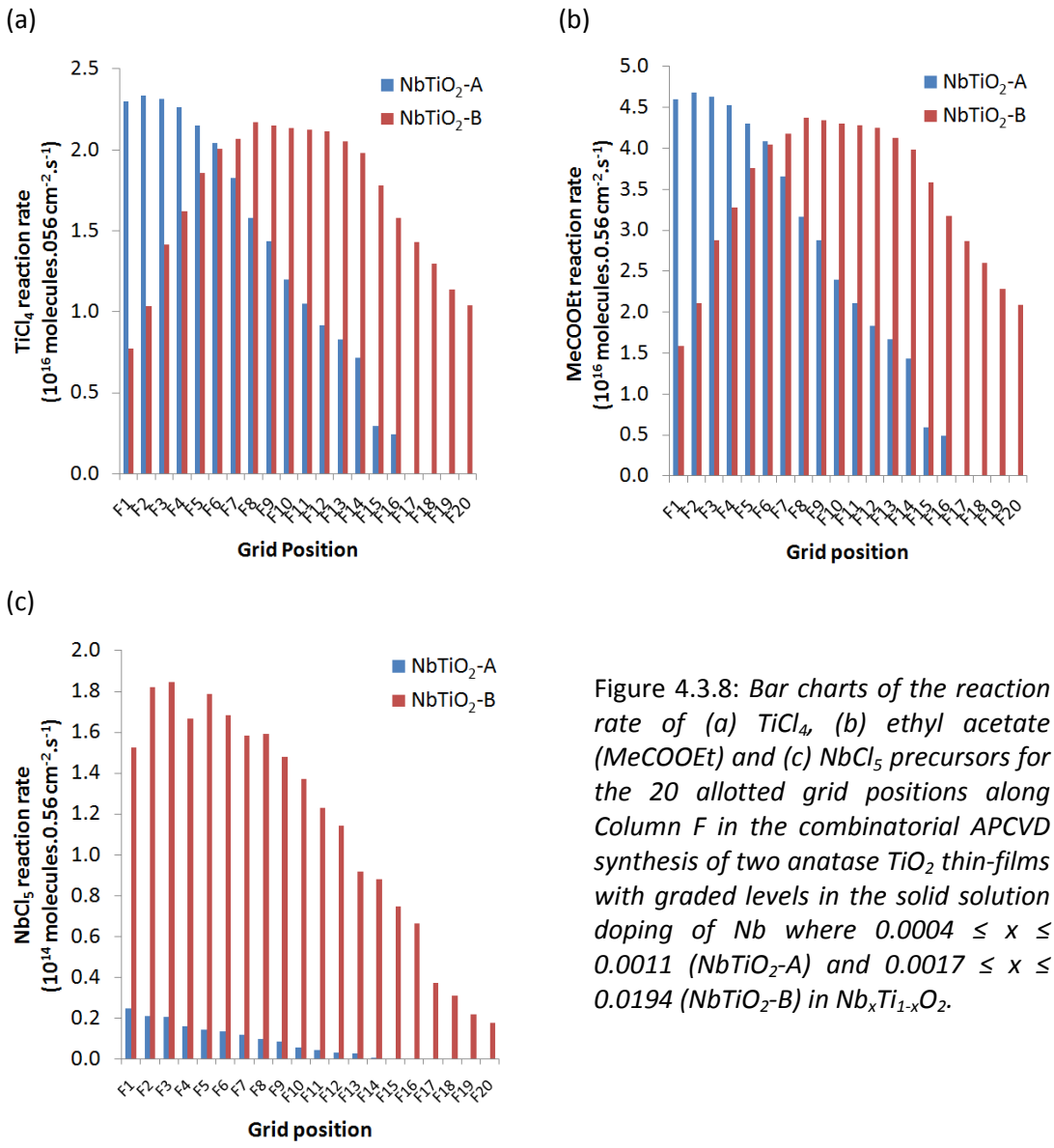

Figure 4.3.8: *Bar charts of the reaction rate of (a) $TiCl_4$, (b) ethyl acetate (MeCOOEt) and (c) $NbCl_5$ precursors for the 20 allotted grid positions along Column F in the combinatorial APCVD synthesis of two anatase TiO_2 thin-films with graded levels in the solid solution doping of Nb where $0.0004 \leq x \leq 0.0011$ ($NbTiO_2$-A) and $0.0017 \leq x \leq 0.0194$ ($NbTiO_2$-B) in $Nb_xTi_{1-x}O_2$.*

XRD and Raman spectroscopy confirmed the solitary presence of the anatase TiO_2 phase across both combinatorial films. As the depositions were conducted at 500 °C, it was unsurprising that

unitary anatase TiO_2 phase formation occurred as the growth of the thermodynamic rutile TiO_2 phase on glass typically requires more elevated temperatures (> 600 °C).[110] In fitting XRD patterns to a Le Bail refined model, no significant variations in the unit cell lattice parameters *a* and *c* were observed. This indicated that up to ≈ 2 Nb: Ti at. % doping in $Nb_xTi_{1-x}O_2$ solid-solutions does not significantly affect the TiO_2 lattice when substituting for Ti. This was also unsurprising given the similarity in octahedral radii of Nb^{5+} (0.64 Å) and Ti^{4+} (0.60 Å) in addition to the high solubility limit of niobium substitution within anatase TiO_2.[272] Although greater levels of Nb were incorporated local to the point of entry of the Nb source during the deposition, the crystallinity, surface roughness and topographies were largely invariant across both films and seemingly unaffected by the difference in doping level.

4.3.3.7. Bandgap mapping

The bandgap was determined for all positions along Column F in both combinatorial films through extrapolating Tauc plots of transmittance data.[195] Example Tauc plots for positions F1 and F11 in $NbTiO_2$-A are shown in Figure 4.3.9(a). The straight portions of each plot are extrapolated to the energy axis, where this energy represents the indirect bandgap of the material. Across Column F in $NbTiO_2$-A the bandgap energy increased quite steadily from position F1 (3.23 eV) to position F11 (3.32 eV). However, in $NbTiO_2$-B the bandgap energy increased steadily from position F1 (3.35 eV) to position F12 (3.23 eV) and then decreased steadily to position F20 (3.30 eV). This seemingly correlated with underlying film-thickness. By plotting the derived bandgap energies against their corresponding film-thickness (Figure 4.3.9(b)), a negative linear correlation was observed with good fit ($r^2 = 0.88$).

The bandgap of a bulk semiconductor material is primarily dependent on two factors:

(i) the elements that it is composed and how their orbitals mix.
(ii) the number of defects and degree of crystallinity.

The niobium impurities were being introduced into the TiO_2 lattice would have certainly affected factor (i). However, no sensible relationship between the level of niobium doping and resulting bandgap energy was observed. Given the maximum level of Nb doping in this system was less than 2 at. %, it was quite probable that factor (ii) may have played a larger role in the resulting bandgap energy. In one of our previous combinatorial studies we observed a relationship whereby increased film-thickness corresponded to an increased film-crystallinity (Section 3.5.3.2). However, no relationship between film-thickness and film-crystallinity was observed in this study and was attributed to the fact that film-crystallinity was approximately constant across both combinatorial

films. The change in bandgap energy was therefore attributed to the potential increase in defects from a more rapidly growing film. Computational studies on the formation of Nb-doped TiO_2 indicated how oxygen vacancies were most liable to form in a reducing growth environment. Another study showed how these oxygen vacancies produce inter-band states just below the conduction band of TiO_2, lowering the bandgap energy.[206,222] We therefore suggest that the more rapid film growth in the top sections of $NbTiO_2$-A and mid-sections of $NbTiO_2$, combined with Nb insertion, produced more oxygen vacancy defects throughout the material, resulting in a lower bandgap energy due to the inter-band states that formed.

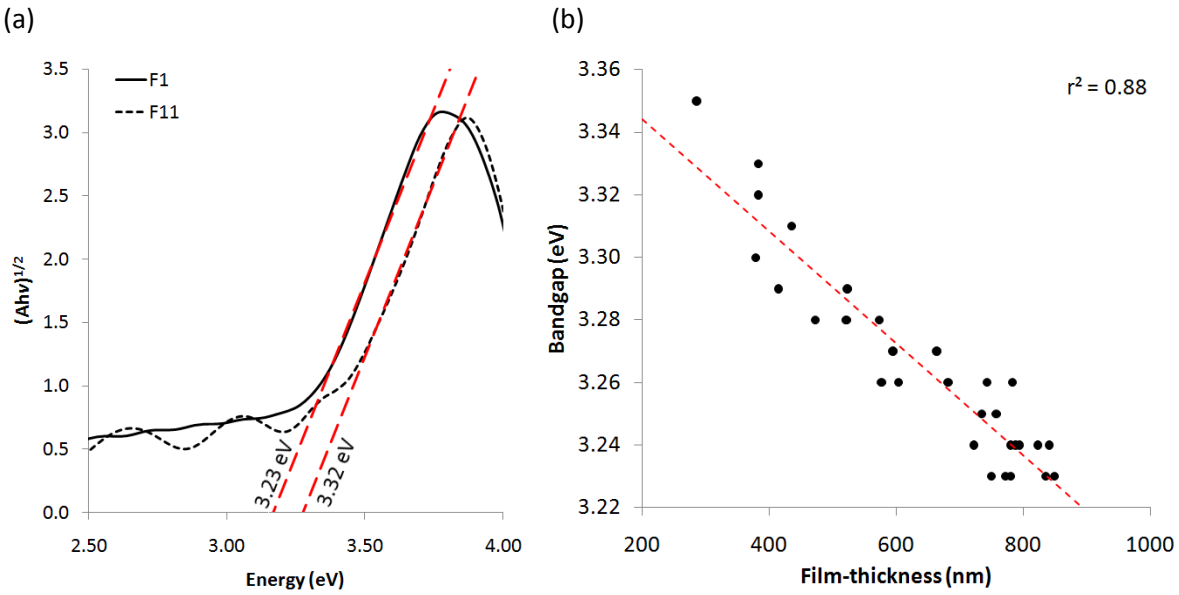

Figure 4.3.9: *(a) a Tauc plot of $(Ahv)^{1/2}$ against photon energy (eV) from transmittance spectroscopy over the 200 to 2500 nm range for positions F1 and F11 in $NbTiO_2$-A and (b) a plot of the Tauc plot derived bandgap energies (eV) against corresponding film-thickness (nm) determined by the Swanepoel method amalgamated from all positions analysed across Column F in both $NbTiO_2$-A and B. A negative linear correlation with a good degree of fit was observed (r^2 = 0.88).*

4.3.3.8. Resistivity mapping

The electrical sheet resistance (Ω/□) was determined by applying the van der Pauw method[264] to electrical voltage and current measurements made between a four-point probe for all 200 grid positions on both combinatorial films (Equation 4.1). In $NbTiO_2$-A, a minimum in the sheet resistance of 2.4 x 10^4 Ω/□ was observed at position E1. The sheet resistance increased quite sharply from this point on moving further down the film. Within the bottom-half of the film (Rows 10 to 20) resistances were so high they were beyond the detection limits of the apparatus. In $NbTiO_2$-B, the sheet resistance varied by almost two orders of magnitude, showing a minimum of 3.8 x 10^4 Ω/□ at position E12 to a maximum of 1.0 x 10^6 Ω/□ at position J1. The natural logarithm of the sheet resistances were plotted in 3-dimensions for both combinatorial films (Figure 4.3.10).

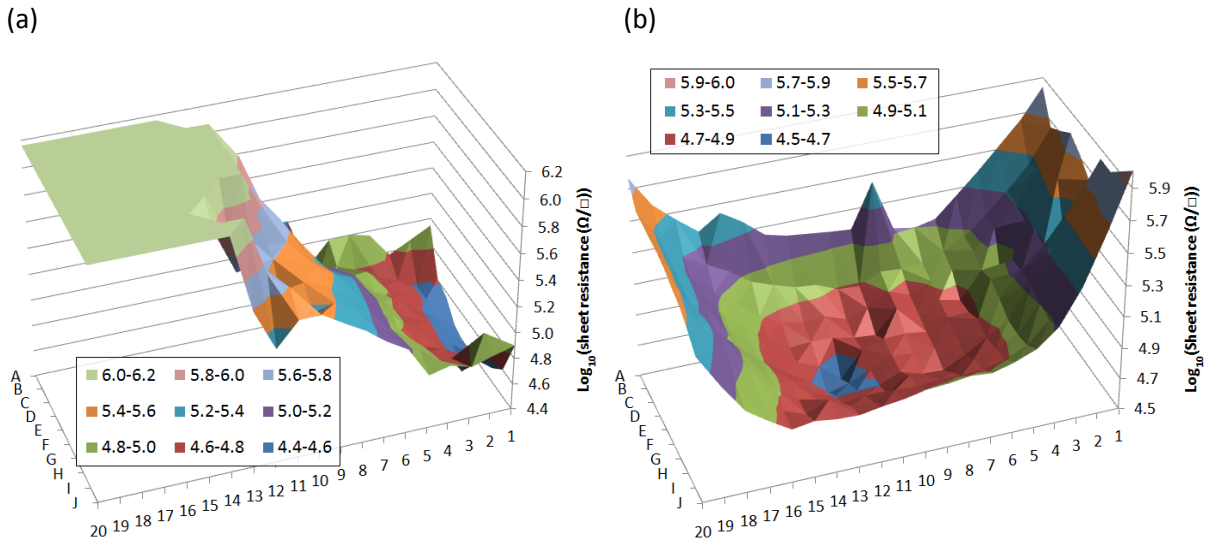

Figure 4.3.10: *The log_{10}(sheet resistivity (Ω/□)) determined by the Van der Pauw method*[264] *for all 200 grid positions on (a)$NbTiO_2$-A and (b) $NbTiO_2$-B.*

For both combinatorial films, a trend was observed whereby increased underlying film-thickness yielded a less electrically resistive material. However, the conductivity of a thin-film material is dependent on film-thickness, as this determines the number of pathways in which charge carriers can flow. Film-thickness can therefore be accounted for by converting sheet resistance into resistivity (Equation 4.2). This was done for all positions along Column F in both sets of combinatorial films. In $NbTiO_2$-A, the resistivity increased almost linearly from 0.022 Ωm at position F1 to 0.155 Ωm at position F11. In $NbTiO_2$-B, the resistivity decreased steadily from 1.76 Ωm at position F1 to 0.031 Ωm at position F13 and then increased slightly more sharply to 0.155 Ωm at F20. The least resistant material in our study was observed at position F1 in $NbTiO_2$-A, even though it contained considerably lower levels of Nb-doping than any position along Column F in $NbTiO_2$-B. From looking at the trends it was clear that the Nb-doping level was not directly linked with film-conductivity. In a recent study it was shown that the conductivities of Nb-doped TiO_2 thin-films were primarily dependent on the mobility of the charge carriers (μ), not the number of charge carriers (n).[266] By varying the partial pressure of oxygen during the PLD growth of these films they were also able to establish that the mobility of these charge carriers were linked with the number of oxygen vacancies in the system. We again suggest that the more rapid growth observed in the top sections of $NbTiO_2$-A and mid-sections of $NbTiO_2$ encouraged the formation of oxygen vacancies which in turn increased electron mobility and lowered film-resistivity.

The resistivity of Nb-doped anatase TiO_2 thin-films on glass have previously been reported ($1.3 – 9.0 \times 10^{-3}$ Ωm),[150,278] showing significantly lower resistivities than those observed in this study. However, these films were deposited under high vacuum (low ρO_2) using a magnetron sputtering process that may have better encouraged interstitial oxygen formation. In order to verify if the level

of oxygen vacancies within our Nb-doped TiO_2 thin-films was indeed the primary cause for a reduction in resistivity, an off-cut at position F11 in $NbTiO_2$-B was heated under reduced pressure (1 x 10^{-2} mbar) for several hours to induce oxygen vacancy formation. We chose to heat this sample at 50 °C lower than the synthesis temperature to limit the increase in film-crystallinity from annealing. After the sample had cooled to room temperature under vacuum, the sheet resistance was measured again and the resistivity re-calculated. A decrease in film-resistivity from 4.39 x 10^{-2} to 1.79 x 10^{-2} Ωm was observed. A similar effect was also observed by Zhao *et. al.* when they annealed thin-films of Nb-doped TiO_2 under a reducing environment, producing more conductive thin-films.[266] It was also suggested by Zhao *et. al.* that the improvements in film-conductivity were due to the formation of oxygen vacancies, a phenomenon similarly observed in indium doped tin oxides.[265]

4.3.3.9. Photocatalytic activity mapping

Our photocatalytic activity mapping method (Section 2.6) was used to rapidly assess photocatalysis across both combinatorial films. Films were both wall-mounted and aerosol-spray coated with a resazurin-based intelligent ink. At the same time, blank pieces of glass were coated alongside the combinatorial films so that the thickness of the intelligent ink layer could be determined through spectroscopy. By assuming that:

(i) the thickness of the intelligent ink layer deposited onto the blank pieces of glass were equivalent to that deposited onto our films,
(ii) the thickness of the intelligent ink layer was uniform and
(iii) the concentration of resazurin in the ink did not change before and after spraying

the number of resazurin molecules that were photo-reduced could be determined. The photocatalysis reaction was initiated and propagated using UVA light (365 nm, 1.75 $mW.cm^{-2}$). The colour changes that ensued were monitored by digital photography. Non-homogenous yet smooth transitions from royal blue (resazurin) to pink (resorufin) to colourless (intermediate) were observed. In both $NbTiO_2$-A and $NbTiO_2$-B, the most rapid changes correlated with where the underlying semiconductor-film was thickest. An example of this is shown in Figure 4.3.11 for $NbTiO_2$-B. From looking at this series of chronological images it is quite clear that the photo-reduction reaction is most rapid at the centre of the film, reducing the ink and causing it to become pink after just 2 mins of irradiation. After 5 mins irradiation, the rest of the film had also turned pink whereas the centre had now been fully reduced to the colourless intermediate. After 20 mins, the entire ink layer had been photo-reduced to the colourless intermediate. The entire photo-reduction reaction was far

more rapid than any of our previous studies (Chapter 3) indicating that Nb-doped TiO_2 may be a significantly more active UVA photocatalyst.

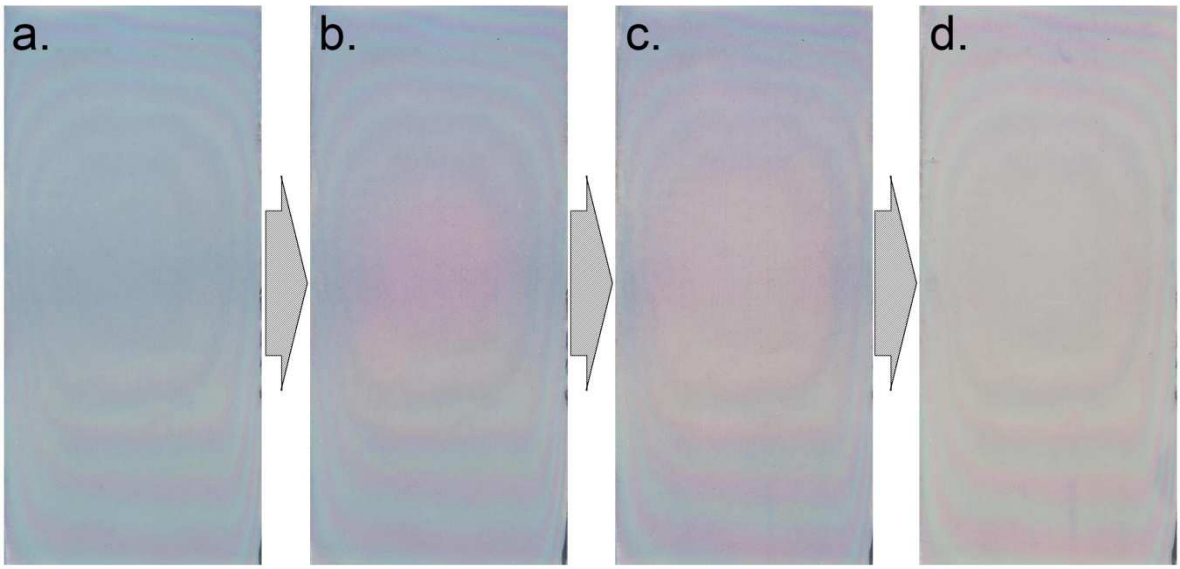

Figure 4.3.11: *Digital images showing the photo-reduction reaction of an aerosol-spray coated resazurin-based intelligent ink layer to UVA light (1.75 mW.cm^{-2}) at (a) 0 (b) 2 (c) 5 and (d) 20 mins on film $NbTiO_2$-B.*

The red-green-blue components of digital colour were extracted for all 200 allotted grid positions across both combinatorial films for every digital image acquired during the photo-reduction reaction using our in-built software (RGB Extractor$^{(C)}$). For all positions, the red component of digital colour increased to a point of plateau. The time at which each plateau was reached, indicating the point of full photo-reduction of the resazurin redox dye (Equation 2.20), were plotted and fit to a Boltzmann refined model. As the thickness and concentration of the original ink layer was known, the photo-reduction rate (molecules photo-reduced cm^{-2}s^{-1}) at each grid position could be determined (Equation 4.3). The varying rates of UVA photocatalysis were then plotted in 3-dimensions for both combinatorial films (Figure 4.3.12). The highest rates of photocatalysis were observed where the underlying film was thickest, quantifying the observations seen by eye. In $NbTiO_2$-A, the most active UVA photocatalyst was observed at position F2 with a rate of 3.4 x 10^{12} molecules destroyed cm^{-2}s^{-1}. In $NbTiO_2$-B, the most active UVA photocatalyst was observed at position G9 with an equivalent rate of 3.4 x 10^{12} molecules destroyed cm^{-2}s^{-1}. On comparing film-thickness with photocatalytic activity along Column F in both combinatorial films an exponential relationship was observed with a reasonable degree of fit (r^2 = 0.70). It is well known that the thickness of a TiO_2 thin-film and rate of photocatalysis are inter-related, where a thicker film can absorb more photons than a thinner film and thereby accommodate the photo-excitation of more electrons and holes that mediate photocatalysis. However, in all previous studies, no strong relationship between film-thickness and

the rate of photocatalysis was observed, where other factors such a phase composition or impurity dopant level played stronger roles.

(a)

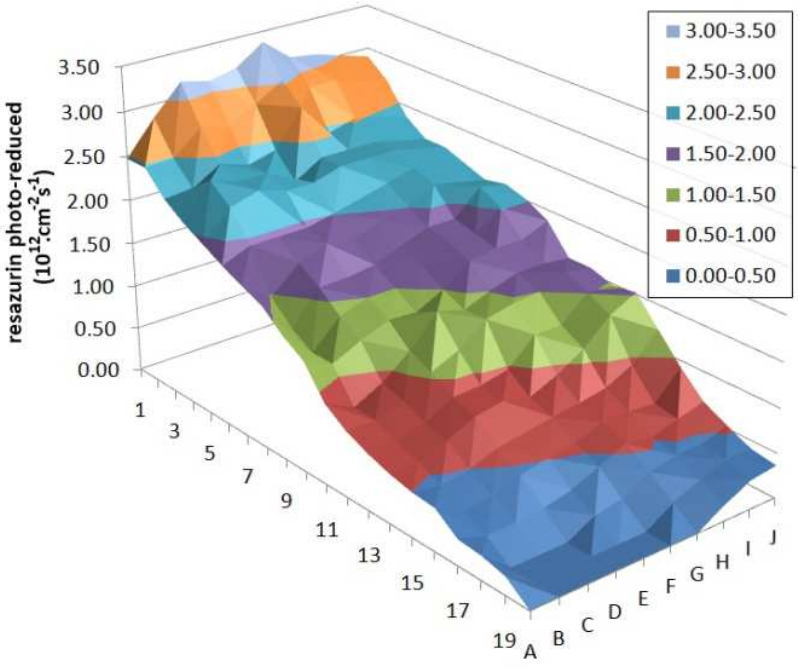

(b)

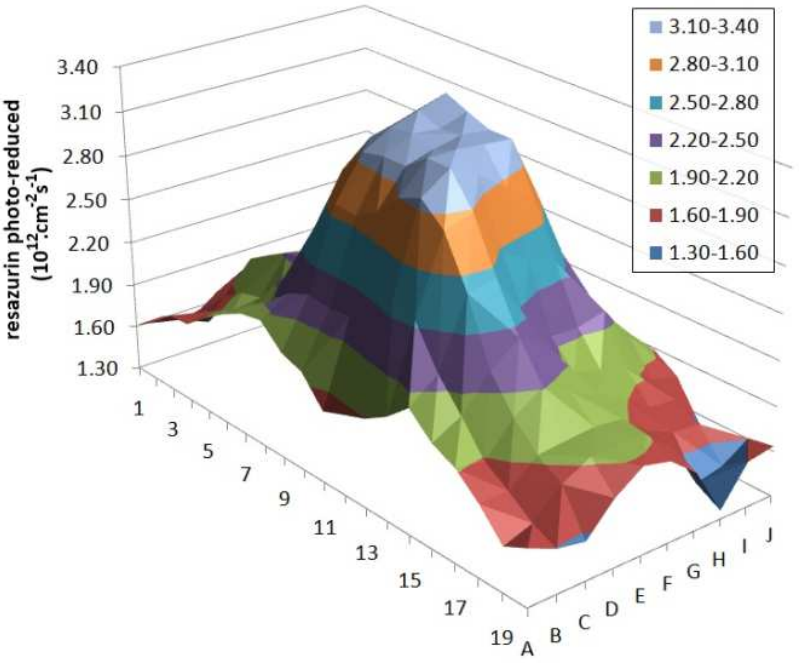

Figure 4.3.12: *3-dimensional plots of the photo-reduction rate of resazurin (molecules photo-reduced $cm^{-2}s^{-1}$) for the 200 allotted grid positions on (a) $NbTiO_2$-A and (b) $NbTiO_2$-B.*

By looking at the trends in photocatalysis, there was certainly no strong relationship with the level of Nb-doping. However, we postulated earlier that more rapid film growth might encourage a greater

level of oxygen vacancy formation in such Nb-doped TiO_2 thin-films. This in turn produced materials with lower bandgaps (Section 4.3.3.7). However, the largest bandgap observed of all materials tested (3.35 eV, position F1, $NbTiO_2$-B) was still below the output energy of the UVA lamp used (3.40 eV). This meant that the lowering of the bandgap energy should not have aided the capacity of any of the materials tested to generate a photo-excitation. Nevertheless, resistivity measurements indicated how charge carrier mobility was more efficient when more oxygen vacancies were present. Therefore, the enhancement in photocatalysis may have been due to the greater mobility of photo-excited electrons and holes to the surface where photocatalytic processes take place. The idea that greater oxygen vacancy formation produces a more active photocatalyst is not a novel concept where it was previously postulated to play a key role in enhancing the photocatalysis of nitrogen doped anatase TiO_2.[194,279] Taking everything into consideration, we could attribute the observed enhancement in photocatalysis at the thicker sections of the combinatorial films tested to either/ or:

(i) a greater UVA photon absorption level due to increased material thickness
(ii) increased charge carrier mobility and lower levels of electron-hole recombination due to the increased presence of oxygen vacancies

Neither point (i) or (ii) could be disproved from the results of this study; however, some additional investigations of our own have indicated that point (ii) is the more viable explanation. By investigating the photocatalysis of an un-doped anatase TiO_2 thin-film system with graded thickness, we observed that above ≈ 200 nm in thickness, the activity plateaued. This showed us that increased film-thickness above ≈ 200 nm to ≈ 800 nm did not lead to improvements in the photocatalytic activity of the material. The result was a little surprising given the thicker sections of the film were absorbing a greater fraction of photons from the UVA light source used (365 nm, 1.75 $mW.cm^{-2}$). This hinted that the average distance in which the photo-excited electrons and holes could travel before recombination was likely was ≈ 200 nm. The combinatorial films tested in this study were at least 86 nm thicker than this observed 200 nm cut off. This phenomenon was further supported by recent investigations by Kundu *et. al.* who found that Pt-TiO_2 photo-diodes were most active when the TiO_2 layer was ≈ 200 nm thick.[280] This effect was attributed to the distance in which the photo-generated electrons could travel through the material, where 200 nm was the optimum balance between how far the electrons could travel to the Pt layer and the level of UVA light absorbed.

4.3.3.10. Photo-induced wettability mapping

The degree of photo-induced wettability was measured by casting an 8.6 µl water droplet at positions along Column F in $NbTiO_2$-B before and after 1hr of UVC (254 nm, 6.35 $mW.cm^{-2}$)

irradiation. A transition from hydrophobicity to super-hydrophilicity was observed at all positions. Example images showing the effect of pre and post UVC treatment on the wettability of the surface at position F10 are shown in Figure 4.3.13. The level of photo-induced wettability was relatively consistent for all samples tested (Table 4.3.2(b)). This indicated that neither film-thickness nor the level of Nb-insertion affected the degree of photo-induced surface wetting, confirming the reports of previous studies on Nb-doped anatase TiO_2.[281] In addition, the degree of photo-induced surface wetting did not correlate with the varying trends in electrical film-conductivity, film-thickness or photocatalytic activity and thus highlighted the difference in the unique mechanism by which this phenomenon operates over photocatalysis.[2]

Figure 4.3.13: *High-speed digital camera images taken perpendicular to the surface of the thin-film at position F10 in $NbTiO_2$-B of (a) an 8.6 µl water droplet that was cast after (b) pre-UVC and (c) post-UVC treatment.*

4.3.4. Functional property correlations

In compiling functional property data from both sets of combinatorial films a strong inter-relationship between film-resistivity, bandgap energy and UVA photocatalysis was observed. Strong first-order exponential decay relationships between the rate of UVA photocatalysis and the film-resistivity (r^2 = 0.84) and bandgap energy (r^2 = 0.91) were observed. In addition, a strong linear correlation between the bandgap energy and film-resistivity was also present (r^2 = 0.89). These inter-relating properties are shown in a 3-dimensional graph (Figure 4.3.14). It was established that film-thickness most strongly dictated the degree of each of the three functional properties and not the level of Nb-doping. A closer look at our results indicated that the increased number of oxygen vacancies that formed in increasingly thicker films was the principle cause for varying these functional properties, where the rate of film growth determined the degree of oxygen vacancy formation. Each of the three functional properties examined were linked with oxygen vacancy formation in the following way:

(i) Bandgap energy: increased oxygen vacancy formation increased the number of inter-band states located close to the conduction band of TiO_2 and reduced the bandgap energy.

(ii) Sheet-resistivity: increased oxygen vacancy formation increased the mobility of charge carriers and decreased sheet-resistance.

(iii) UVA photocatalysis: increased oxygen vacancy formation increased the mobility of photo-generated electrons and holes and reduced the likelihood of recombination.

It should be noted for point (ii) that some presence of Nb-doping was essential to introduce the charge carriers into the system. It was just that the mobility of these charge carriers was more fundamental to the overall sheet-resistivity for the doping regime investigated (0.04 ≤ Nb: Ti at. % ≤ 1.94). As the sheet-resistance was found to inter-relate with both UVA photocatalysis and the bandgap energy it should be reasonable to assume that some presence of Nb-doping was required to necessitate the relationship they all shared with the level of oxygen vacancy formation as well.

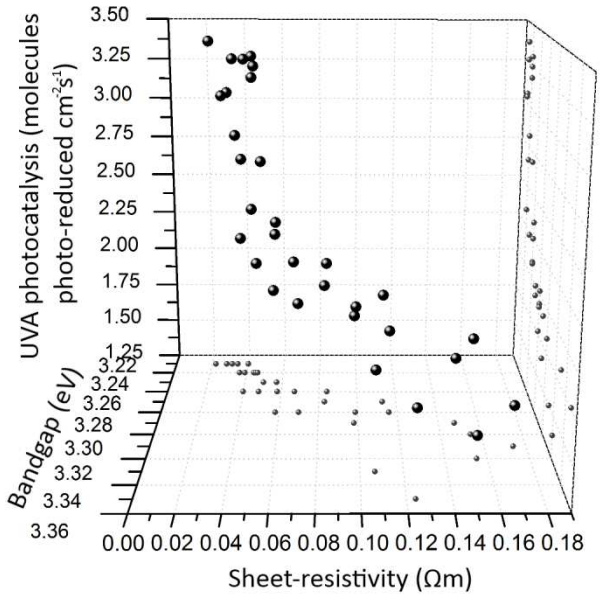

Figure 4.3.14: *3-dimensional plot of the bandgap energy (eV), sheet-resistivity (Ωm) and UVA photocatalysis (molecules photo-reduced $cm^{-2}s^{-1}$) of all positions analysed along Column F in both $NbTiO_2$-A and B. First-order exponential decay relationships between the level of UVA photocatalysis and film-resistivity (r^2 = 0.84) and bandgap energy (r^2 = 0.91) were observed. A negative linear correlation between the sheet-resistivity and bandgap was also observed (r^2 = 0.89).*

4.3.5. Conclusions

Two combinatorial thin-film solid solutions of anatase TiO_2 with graded levels of Nb-doping (0.04 ≤ Nb: Ti at. % ≤ 1.94) were synthesised by combinatorial APCVD using $TiCl_4$ (Ti source), $NbCl_5$ (Nb source) and ethyl acetate (O source) precursors. This is the first time in which Nb-doped TiO_2 was produced by a CVD process and also the first instance in which a metal oxide was doped with a cation using combinatorial APCVD. In applying high-throughput screening methods the physical and functional properties in both films were rapidly characterised.

A strong inter-relationship between the bandgap energy, UVA photocatalysis and sheet-resistivity was observed upon amalgamating information from both combinatorial films. The main root cause for the variation in these three properties was linked to the level of oxygen vacancies formed, where the thickest areas in both combinatorial films grew most rapidly and encouraged the formation of a greater level of oxygen vacancy defects. Our results indicated that a more photocatalytically active and electrically conductive Nb-doped anatase TiO_2 material is produced in: (a) low oxygen/ highly reducing environments or (b) with high reagent mass flow rates that induce rapid film growth. In contrast, a high degree of photo-induced surface wetting for the full range of Nb-doped TiO_2 environments investigated ($0.17 \leq$ Nb: Ti at. $\% \leq 1.94$) was independent of these growth conditions, highlighting the difference in mechanism. The combined conductivity and photocatalytic properties of the Nb-doped anatase TiO_2 solid-solutions presented make this material a promising candidate in a range of optoelectronic and self-cleaning applications.

In the following section we will use combinatorial APCVD to investigate solid solutions of W-doped anatase TiO_2. Although the effect of W-doping on the resistivity of this material has been studied, to our knowledge, its effect on photocatalysis and photo-induced surface wetting has not been reported. We will use our high-throughput screening methods to try and understand the links between the physical and functional properties of this material.

4.4. W-doped anatase TiO_2

4.4.1. Introduction

The use of tungsten as an impurity dopant in anatase TiO_2 has been shown to increase the conductivity,[149,282] gas-sensing,[283] electrochromic,[284] photo-induced surface wetting[285] and photocatalytic properties[23,286,287] of the material. The addition of tungsten has been shown to form either solid-solutions[149,282] within the anatase TiO_2 matrix or WO_3: TiO_2 composites.[23,284,286,287] However, in some cases, it was not even specified as to whether a solid-solution or composite had formed.[283,285] Nevertheless, a trend was observed, whereby sol-gel syntheses yielded composites[23,284,286,287] and PVD yielded solid-solutions.[149,282] The conductivity of films that formed solid solutions was shown to substantially increase.[149,282] This was attributed to the n-type behaviour of W-dopants and the introduction of charge carriers. In fact, computational studies suggested that each W dopant could introduce 2 electrons into the system[149] where:

$$W^{6+} \rightarrow W^{4+} + 2e^{-} \quad (4.4)$$

Nevertheless, photoemission spectroscopy studies indicated that the valence state of the W impurities was located near the top of the O (2p) valence state of TiO_2, which would have theoretically hindered the direct addition of free electrons from W into the conduction band of TiO_2 as the lower energy valence state of W would first be filled.[282] This corroborated with Hall effect measurements, where low charge carrier densities (*n*) were observed in these films. Resistivities of 1.5×10^{-4} Ωm were observed by Chen *et. al.* in their $Ti_{0.94}W_{0.06}O_2$ thin-films formed by magnetron co-sputtering on glass substrates.[149] Significantly lower resistivities of 2.0×10^{-5} Ωm were observed by Takeuchi *et. al.* in their $Ti_{0.95}W_{0.05}O_2$ films formed on glass by PLD, even though similar concentrations of W-doping were incorporated.[282] Nevertheless, Takeuchi *et. al* repeated their synthesis until the optimum growth conditions for maximum film-conductivity was achieved. The resistivities were compared with that of a Nb-doped anatase TiO_2 counterpart, with almost equivalent levels of impurity doping. The resistance was almost 10 times higher in the W-doped film and was accredited to the trapping of free electrons in the valence band of the W impurity.

All photocatalysis studies on the effect of introducing tungsten into anatase TiO_2 thin-films have involved the formation of WO_3: TiO_2 composites.[23,286,287] In all studies, the photocatalytic activities of these composites were shown to increase relative to their pure anatase TiO_2 counterpart. The mode of improvement under UVC and UVA light was attributed to charge transfer stabilisation of photo-generated electrons and holes, where the electrons could migrate from the conduction band of TiO_2 into the conduction band at WO_3 sites and the holes could migrate from the valence band of WO_3

sites into the valence band of TiO_2.[23] It was purported that this increased the separation of electrons and holes, hindering recombination and improving the efficiency of photocatalysis. The mode of improvement under visible light was attributed to the lower bandgap energy of WO_3 sites (2.8 eV) that increased the capacity for visible light capture. From testing a range of compositions, Rampaul *et. al.* found an optimum composite level of 2 % WO_3 for improved UV photocatalysis.[23] Quite similarly, an optimum composite level of 3 % WO_3 was found by Li *et. al.* for improved visible light photocatalysis.[287] However, to our knowledge, the effect of W-doped TiO_2 solid solutions on photocatalysis is yet to be studied.

The photo-induced surface wetting of WO_3: TiO_2 composites under UVC light were also investigated by Rampaul *et. al.*, where a slightly more pronounced degree of wetting corresponded with a 2 % WO_3 composite doping level.[23] This function was also investigated by Lee *et. al.* for W and Al doped TiO_2 thin-films formed by a sol-gel process under UVA light.[285] It was not specified by Lee *et. al.* whether a solid solution or phase composite had formed. However, a photo-luminescence band at 435 nm (≈ 2.8 eV) in their W-doped TiO_2 sample indicated that WO_3 was present. Again, to our knowledge, the effect of solid solution W-doping TiO_2 on the degree of photo-induced surface wetting is yet to be studied.

In this section we describe the combinatorial APCVD synthesis of an anatase TiO_2 thin-film with graded tungsten dopant content from $0.0038 \leq x \leq 0.138$ in $W_xTi_{1-x}O_2$. This was formed using a triple source of precursors, with $TiCl_4$ as the titanium source, WCl_6 as the tungsten source and ethyl acetate as the oxygen source. The properties of up to 200 equally spaced positions were investigated across the combinatorial film. Phase mapping confirmed the solitary presence of the anatase TiO_2 phase throughout the combinatorial film. The film-thickness, resistivity and photocatalytic activity of all 200 unique positions were mapped in accordance with the methods outlined in Sections 2.4, 4.2.2.3 and 4.2.2.4 respectively. Tungsten/ titanium concentration mapping of all 200 grid positions demonstrated how the tungsten doping level varied primarily in the lateral plane, which encouraged us to focus on the properties across a single horizontal strip of film in greater detail. In doing do, a strong inter-relationship between the unit cell volume, level of tungsten doping and shift of the primary Raman active E_g vibrational mode of TiO_2 was revealed. It was also found that the photocatalytic activity and resistivity properties were most highly dependent on film-crystallinity; whereas the property of photo-induced wetting was most highly dependent on changes in preferred orientation growth in the 211 plane. Given the primary crystal plane for the photo-induced wetting process in anatase is yet to be identified in the literature, these unique findings highlight the importance of the 211 plane.

4.4.2. Experimental combinatorial film synthesis

A combinatorial thin-film comprised solely of the anatase TiO_2 phase with graded levels of solid solution tungsten doping (0.38 ≤ W: Ti at. % ≤ 13.8) was synthesized by combinatorial APCVD. The film was deposited onto float glass (225 × 90 × 3.2 mm; length × breadth × thickness) inside a cold-walled reactor heated on its underside through a graphite block. The float glass contained an ≈ 50 nm thick barrier layer of SiO_2 at the surface, which inhibited the diffusion of ions from the glass (i.e. Na, Mg, Ca) into the deposited film. A schematic of the apparatus used is shown in Figure 4.4.1.

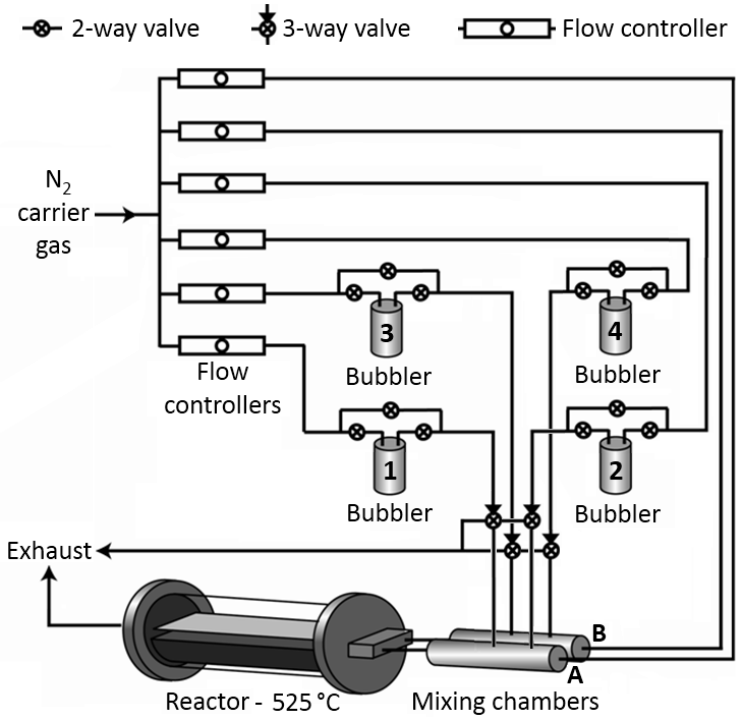

Figure 4.4.1: *Schematic of the combinatorial APCVD apparatus. The combinatorial film was synthesised from volatised precursors carried from bubblers, where bubbler 1 contained WCl_6, bubbler 3 contained $TiCl_4$ and bubblers 2 and 4 contained ethyl acetate. Of particular importance are the two separate entry points of the metal sources into the reactor, invoking a horizontal gradient in the W: Ti source ratio present inside the reactor.*

The combinatorial film was synthesised from volatised precursors stored and carried from bubblers, where bubbler 1 contained WCl_6 (tungsten source), bubbler 3 contained $TiCl_4$ (titanium source) and bubblers 3 and 4 contained ethyl acetate (oxygen source). The volatility of each precursor was altered by adjusting the temperature at each bubbler. The vapours were transported from each of their respective bubblers by an inert N_2 gas. Vapours of WCl_6 and ethyl acetate were carried to mixing chamber A, where they were then combined with a plain line flow of inert N_2 gas and carried into the cold-walled reactor (525 °C). Vapours of $TiCl_4$ and ethyl acetate were carried to mixing chamber B, where they were then combined with a plain line flow of inert N_2 gas and carried into the reactor. The separate entries of the tungsten and titanium sources created a horizontal gradient in

the tungsten: titanium source concentration across the substrate. This induced a range of deposition conditions in a single experiment. The parameters used to deposit the combinatorial film in this study are shown in Table 4.4.1. A reference system that shows the exact locations of the positions analysed by each characterisation method across this combinatorial film is shown in Figure 4.4.2. The methods of characterisation that were applied to each grid position in this combinatorial system are shown beside the image. Further details of the experimentation and apparatus can be found in the experimental methods, Section 4.2.

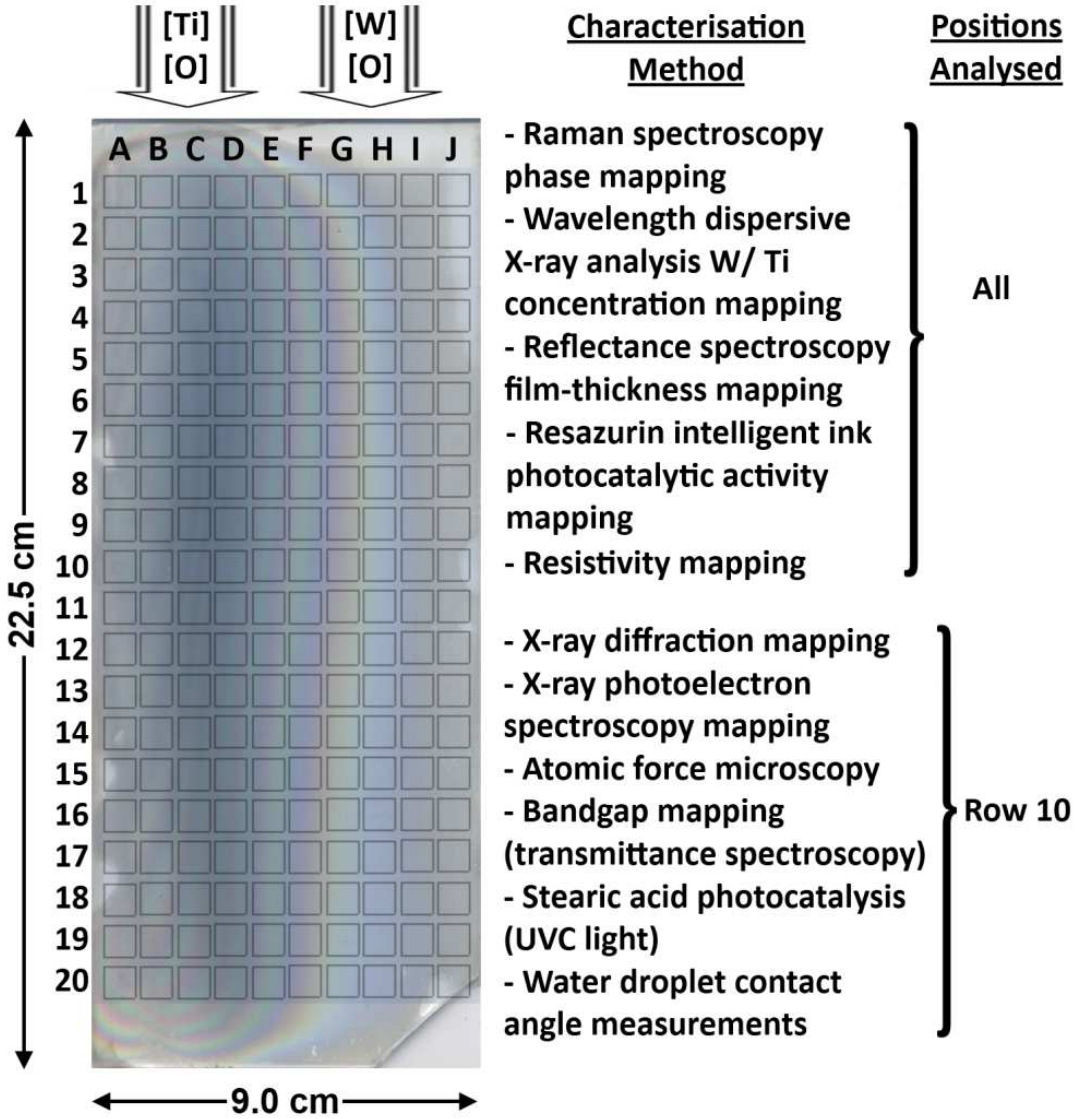

Figure 4.4.2: *Picture of the combinatorial thin-film and super-imposed grid reference system used throughout this section. Up to 200 unique grid positions were analysed over each combinatorial system (10 x 20; horizontal x vertical). The type of characterisation and the positions in which it was applied to is stated next to the image. The positions of the gas inlets relative to the glass substrate at the time of deposition within the reactor are shown; with Row 1 lying closest to the gas inlets and Row 20 lying closest to the exhaust. The centres of neighbouring grid positions are spaced 0.75 cm apart in rows and in columns.*

	Mixing chambers		Bubblers			
			1	2	3	4
	A	B	WCl_6	MeCOOEt	$TiCl_4$	MeCOOEt
Temperature (°C)	254	246	281	45.0	66.0	37.0
Flow rate (L /min)	1.0	4.0	4.0	0.20	1.2	0.25
Vapour pressure (mm Hg)	-	-	191	233	83	166
Mass flow rate (10^{-3} mol min^{-1})	-	-	55	3.6	6.0	2.9
Molar ratios	-	-	9.2	0.6	1.0	0.5

Table 4.4.1: *Temperatures (°C) of components and N_2 carrier gas flow rates (L min^{-1}) in the combinatorial APCVD syntheses of an anatase TiO_2 thin-film with graded levels of W-doped (0.38 ≤ W: Ti at. % ≤ 13.8) solid solutions. The carbon block inside the reactor was maintained at 525 °C during the 60 s deposition. Mass flow rates (mol min^{-1}) were derived from vapour pressure (mm Hg) curves to yield the molar ratio of each precursor relative to $TiCl_4$.*

4.4.3. Results

4.4.3.1. Appearance

An anatase titanium dioxide thin-film with a gradient in the tungsten solid solution dopant level was formed from the combinatorial APCVD reaction of $TiCl_4$ and WCl_6 metal sources with an ethyl acetate oxygen source at 525 °C. The entire glass substrate was coated. Colour bands due to variations in the thickness of the coating were observed; characteristic of thin-films with high refractive indices such as anatase TiO_2 (Figure 4.4.2). The colour contours alternated chiefly from green to purple and maximized toward the middle-left section where the film was thickest. A blue tinge, observed best off-angle, was also seen and was characteristic of tungsten doped solid solutions. The film was adhesive (passed the Scotch® tape test) and impervious to prolonged immersion in a variety of common solvents. The film was also impervious to scratching with a stainless steel stylus but could be scratched with a diamond tip. From thicknesses measurements based on optical interference the average film growth rate was 6.4 nm s^{-1} (standard deviation = 5.2 nm.s^{-1}).

4.4.3.2. Tungsten/ titanium concentration mapping

The level of tungsten for all 200 allotted grid positions across the combinatorial film was determined through wavelength dispersive X-ray (WDX) analysis of the Ti K_α-line and W L_α-line emissions relative to pre-calibrated standards. A 3-dimensional bar chart of the W: Ti ratio (at. %) is shown in Figure 4.4.3. A substantial variation in the tungsten dopant level was observed, ranging from 0.38 to 13.8

W: Ti at. %. Interestingly, an almost linear increase in dopant level was seen in rows upon movement from A to J. However, very little change in dopant level was observed in columns. During the deposition, position J1 was closest to the inlet in which the tungsten source was introduced and explained why the greatest levels of tungsten doping were seen in this region.

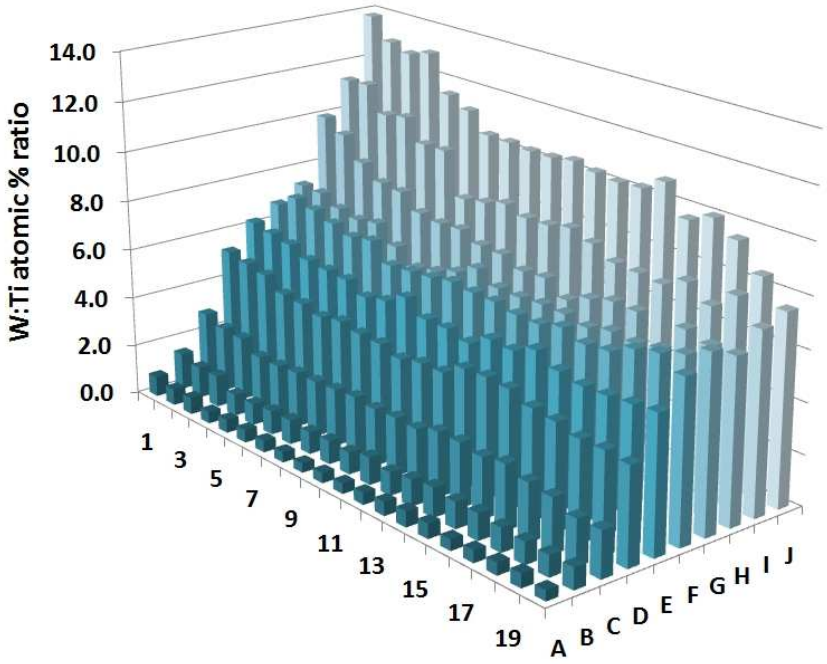

Figure 4.4.3: *3-dimensional bar chart of the W: Ti ratio (at. %) at each of the 200 allotted grid positions analysed over the combinatorial film. The values were determined from wavelength dispersive X-ray analysis of the Ti K_α and W L_α emission lines relative to pre-calibrated standards.*

4.4.3.3. X-ray photoelectron spectroscopy mapping

Wavelength dispersive X-ray analysis of all 200 grid positions demonstrated how the most significant changes in tungsten doping levels were across rows and encouraged us to focus on the properties across a single horizontal strip of film in greater detail. Row 10, the middle strip of the combinatorial film, was chosen. Each position along Row 10 was investigated by X-ray photoelectron spectroscopy (XPS). The most intense peaks in the XPS spectrum of tungsten are due to electronic excitations from the W 4f orbital. However, the binding energies of these excitations unfortunately fall in the same region as Ti 3d excitations.[149] For this reason, both the W 4f and the less intense W 4d regions were analyzed in order to discern the true nature of the dopant ion as well as the composition at the surface.

The binding energies of the prominent Ti 2p excitation varied very little across the row, ranging from 458.2 – 458.5 eV in the $2p_{3/2}$ peak. This binding energy was attributed to the solitary presence of Ti^{4+} across the group.[288] At position A10, XPS peaks attributed to the presence of

tungsten were of low intensity, corroborating with observations from WDX analysis (W: Ti = 0.42 at. %). Nevertheless, this allowed the location and nature of the Ti 3d peak to be elucidated. The contribution of W 4f in more heavily doped environments could then be separated more reliably from Ti 3d. The areas of both W 4f and W 4d peaks were used to determine the level and nature of tungsten doping, as shown in Figure 4.4.4.

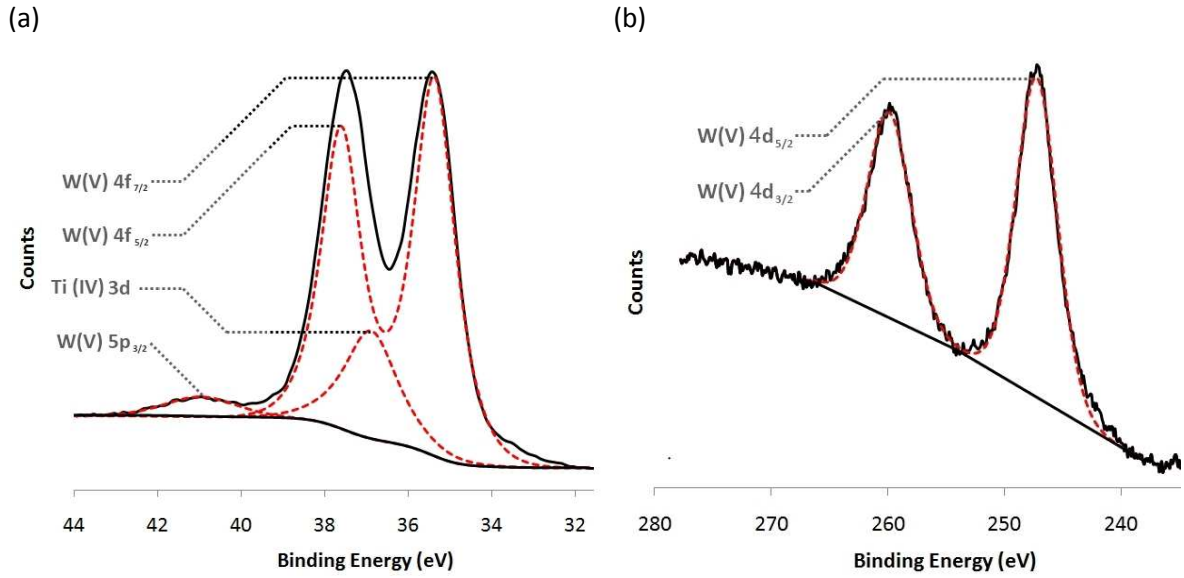

Figure 4.4.4: *X-ray photoelectron spectral profiles at grid position J10 in (a) the W 4f/ Ti 3d and (b) the W 4d binding energy regions, with labelled deconvoluted portions shown in red.*

The binding energy of the deconvoluted W 4f and W 4d excitations did not vary significantly across the group, ranging from 35.2 – 35.7 eV in W $4f_{7/2}$ peaks and 246.6 – 247.6 eV in W $4d_{5/2}$ peaks. This indicated that tungsten was primarily present in a single oxidation environment. There is little consistency in the literature as to the precise binding energies of W^{4+}, W^{5+} & W^{6+} states.[149,287,289-294] However, if we calculate the average binding energy attributed to these tungsten $4f_{7/2}$ states from this literature we find: W^{4+} = 33.1 eV, W^{5+} = 35.0 eV and W^{6+} = 36.4 eV. The average $4f_{7/2}$ binding energy seen across our combinatorial film was 35.4 eV. This indicated that the tungsten dopant in this system was predominantly in the W^{5+} state, where some un-resolvable levels might have existed as W^{6+}. The W: Ti ratio (at. %) was determined for each position by multiplying peak areas by their respective sensitivity factor. The average ratio of the W 4f and W 4d environments was taken, with the difference between the two values as the error.

The X-rays generated and focussed on samples in both WDX and XPS analysis penetrate several microns deep into a sample. In WDX analysis, the resulting photo-excitations can escape from this depth, revealing information about the bulk. However, in XPS analysis, the excited electrons that are released can only escape from the first few nanometres of the material (typically 1 - 10 nm deep), revealing information about the near-surface. Upon comparing the tungsten doping levels from WDX

and XPS analysis shown in Figure 4.4.5, one can relate this to the bulk and surface tungsten doping levels respectively. Although the average bulk and surface levels of tungsten doping were approximately equal across the group, where the W: Ti ratio = 5.1 at. % from WDX analysis and 6.4 at. % from XPS analysis, there was no proportional relationship between the level of bulk and surface doping. In fact, tungsten doping levels increased exponentially at the surface and more linearly in the bulk on going from position A10 to J10. This was attributed to surface segregation effects.

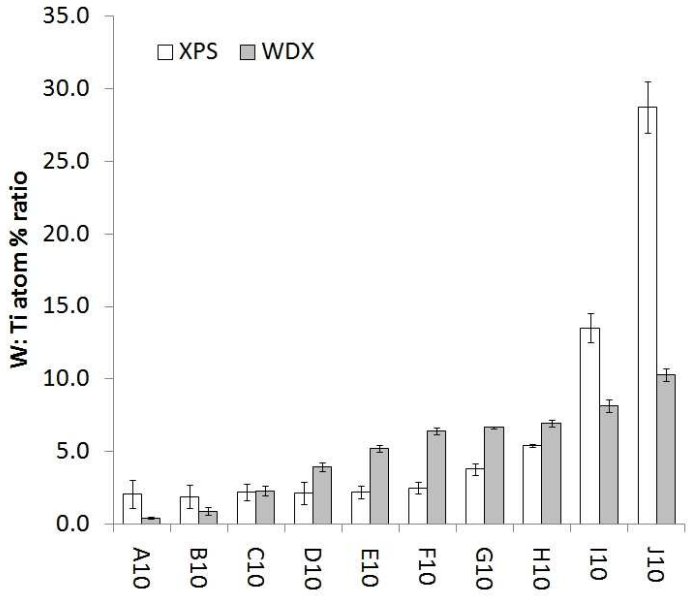

Figure 4.4.5: *Bar chart of the W: Ti ratio (at. %) determined by both X-ray photoelectron spectroscopy (XPS) and wavelength dispersive X-ray (WDX) analysis of positions across Row 10.*

4.4.3.4. Raman and X-ray diffraction mapping

All Raman patterns acquired over the 200 allotted grid positions showed peaks consistent with that of anatase TiO_2 tetragonal symmetry.[295] However, some noticeable differences were observed. For instance, the width of Raman peaks increased quite systematically across the film, where the widest peaks were seen in regions of high tungsten doping. In addition to this, an increasing blue-shift in the principle E_g (144 cm^{-1}) vibrational mode[295] was also observed with increased tungsten doping. The widths of Raman peaks are directly related to film-crystallinity, where increasingly wider peaks correspond with an increasingly amorphous film.[233] This phenomenon was observed in our combinatorial investigation of nitrogen doped anatase TiO_2, where by comparing the widths of the principle E_g (144 cm^{-1}) vibrational modes with the average crystallite size, a negative linear correlation was observed (Figure 3.5.4(b)). Literature studies have also shown how increased levels of solid solution doping can restrict phonons, increasing the energy that is required for a vibrational excitation to occur and causing a blue-shift in the detected peaks.[296,297]

The positions across Row 10 were investigated in greater detail to assess the scale of the blue-shift in the principle E_g mode of anatase TiO_2. The resulting spectra are stacked in Figure 4.4.6. A systematic decrease in peak intensity coupled with an increasing blue-shift in the principle E_g mode was seen on moving from position A10 to J10. The spectra were each individually fit to a Gaussian model, allowing precise values for the peak centres and degree of blue-shift to be determined. A consistent increase in the excitation energy of the principle E_g mode was observed with increasing tungsten content. A strongly correlating positive linear relationship between the level of tungsten doping and degree of blue-shift in the principle E_g mode was observed ($r^2 = 0.90$), where a low doping level of W: Ti = 0.42 at.% at position A10 caused a marginal shift to 144.9 cm^{-1} and a high doping level of W: Ti = 10.3 at. % at position J10 caused more a substantial shift to 159.8 cm^{-1}. This effect was previously reported by Kim *et. al.* from analysis of a series of tungsten doped nano-crystals where a regular shift in the E_g band from 144.3 – 149.3 cm^{-1} over 0 – 20 atom % W: Ti was observed.[297]

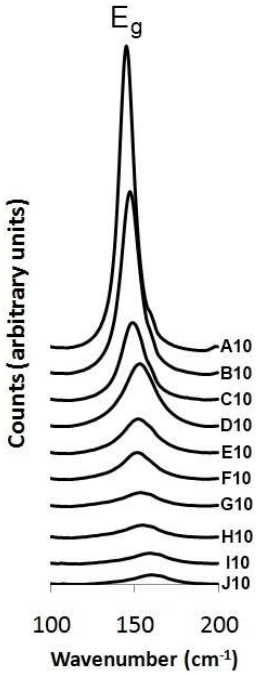

Figure 4.4.6: *Stacked plot of Raman spectra focussed over the region of the principle E_g vibrational mode of anatase TiO_2 (144 cm^{-1}) for sample positions across row 10.*

X-ray diffraction was employed to quantify the level of lattice strain suggested from the blue-shifts in Raman patterns. The positions along row 10 were studied for a direct comparison. A stack of the diffraction patterns are displayed in Figure 4.4.7(a). The patterns confirmed the presence of anatase ($I4_1/amdz$, a = 3.785 Å, c = 9.512 Å) with no evidence of a separate TiO_2 phase. In addition, no evidence of a separate tungsten oxide phase was seen and further clarified the case for solid solution formation. Given the high solubility of solid solutions of tungsten in anatase TiO_2, where tungsten doping levels as high a 30 at. % have been achieved,[283] it was no surprise that a tungsten

doping level of ≤ 13.8 at. % could be achieved in this study. A drop in the intensity of X-ray patterns from A10 to J10 was also observed and was attributed to both a decreasingly thick and crystalline film. The film-crystallinity was quantified by applying the Scherrer equation to the prominent (101) diffraction peak of anatase TiO_2, shown more clearly in Figure 4.4.7(b), to determined the average crystallite size. A decrease in average crystallite size from 19.9 nm at position A10 to 14.2 nm at position J10 was observed.

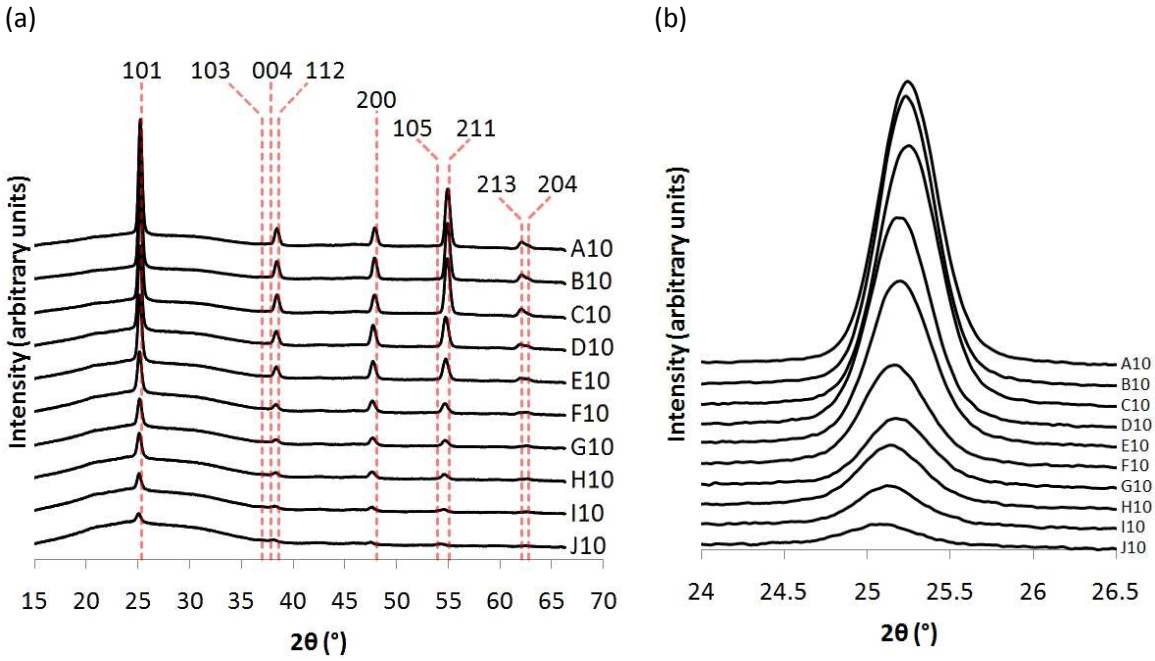

Figure 4.4.7: *(a) Stacked X-ray diffraction patterns of the positions analysed across row 10 and (b) a closer view of the prominent (101) peaks.*

A closer look at Figure 4.4.7(b) revealed a systematic leftward shift in centre of the (101) diffraction peak. In fitting the full X-ray diffraction pattern of each position to a Le Bail refined model,[298] a lattice expansion was evident, with the unit cell volume increasing across the row from 136.9 $Å^3$ at position A10 to 139.2 $Å^3$ at position J10. The most significant increases were seen in the *a*/*b* lattice parameters. A strong positive linear correlation between the level of tungsten doping and unit cell volume increase was observed (r^2 = 0.97). It therefore became evident that the three physical properties: (i) tungsten doping concentration (ii) blue-shift of the principle Raman active E_g mode and (iii) lattice expansion were inter-related; as shown in Figure 4.4.8.

The inter-relationship comprehensively quantified what one would expect from doping an anatase TiO_2 lattice with a larger cation as a solid solution. As increasing levels of tungsten were inserted within the TiO_2 matrix, the strain on the unit cell increased and pushed the surrounding atoms further apart. This in turn constricted phonons and increases the energy required to cause the

principle Raman E_g excitation. It is also worthy of note that the most significant increases in unit cell occurred across the *a*/*b* lattice plane, the direction in which the E_g vibrational mode operates.[295]

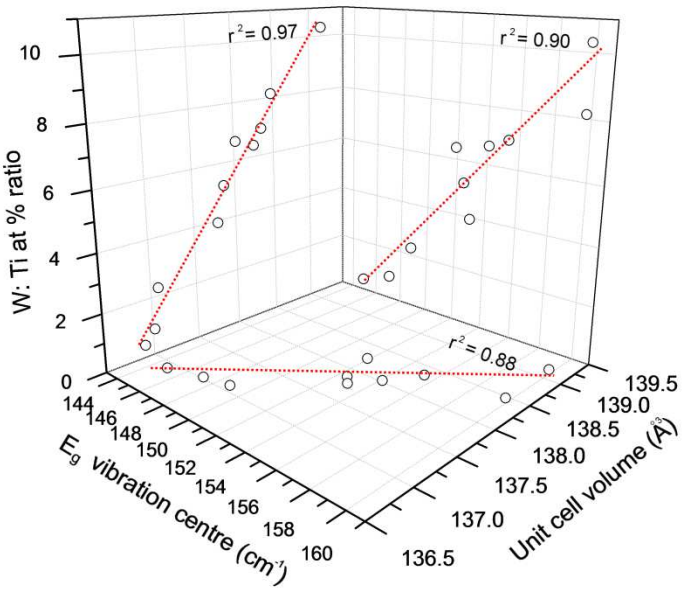

Figure 4.4.8: *A 3-dimensional plot of the strong inter-relationships between the blue-shift of the principle Raman active E_g mode (cm^{-1}), unit cell expansion ($Å^3$) and tungsten doping level (W: Ti ratio at. %) for the positions analysed across Row 10.*

This physical inter-relationship is quite useful if one wants to quickly estimate the W: Ti doping level in W-doped anatase TiO_2 materials by either Raman spectroscopy or X-ray diffraction. The more rapid estimate would come from finding the exact location of the principle E_g vibrational mode (cm^{-1}) through Raman spectroscopy:

$$W{:}Ti\ doping\ level\ (at.\%) = 0.624 \times E_g - 89.9 \quad (4.4)$$

Nevertheless, as the degree of correlation observed in determining this relationship from our studies (r^2 = 0.90) was lower than the degree of correlation observed between the unit cell volume and level of tungsten doping (r^2 = 0.97), there would be greater accuracy in predicting the level of tungsten doping from X-ray diffraction experiments:

$$W{:}Ti\ doping\ level\ (at.\%) = 4.347 \times V - 594.3 \quad (4.5)$$

where *V* is the unit cell volume in $Å^3$.

By equating the average lattice expansion against the average level of tungsten doping, the average ionic radius of the W^{5+} dopant was 0.61 Å and 0.55 Å for Ti^{4+}. As there is no direct study, to our knowledge, on the lattice expansion of W-doped TiO_2 solid solutions, the derived ionic radii could only be compared with average values. The ionic radius determined for W^{5+} compared well with the

literature (0.62 Å),[299] however, the ionic radius of Ti^{4+} was slightly lower than what is normally observed in other Ti^{4+} compounds (0.60 Å).[300]

Some preferred orientation effects were also observed across Row 10 (Figure 4.4.7(a)). In order to quantify these differences, we first determined the percentage intensity contribution of each diffraction plane (Equation 2.3) and then the percentage difference compared to that of the single crystal (Equation 2.4). The results for several of the major diffraction peaks are shown in Figure 4.4.9. For the (101) diffraction peak, very little difference in comparison to a single crystal was observed with the exception of position J10, where a -22.1 % difference was seen. For the (112) diffraction peak, all positions grew in intensity relative to a single crystal by roughly equal amounts, ranging from 33.4 to 57.0 %. In regards to the (200) diffraction, a rough trend whereby the degree of preferred orientation seems to maximise toward the centre of the row and minimise at the ends was observed. However, for the (211) diffraction peak, a very clear trend was observed, whereby the degree of preferred orientation decreased steadily from a 57.1 % increase at position A10 to a 13.0 % increase at position J10.

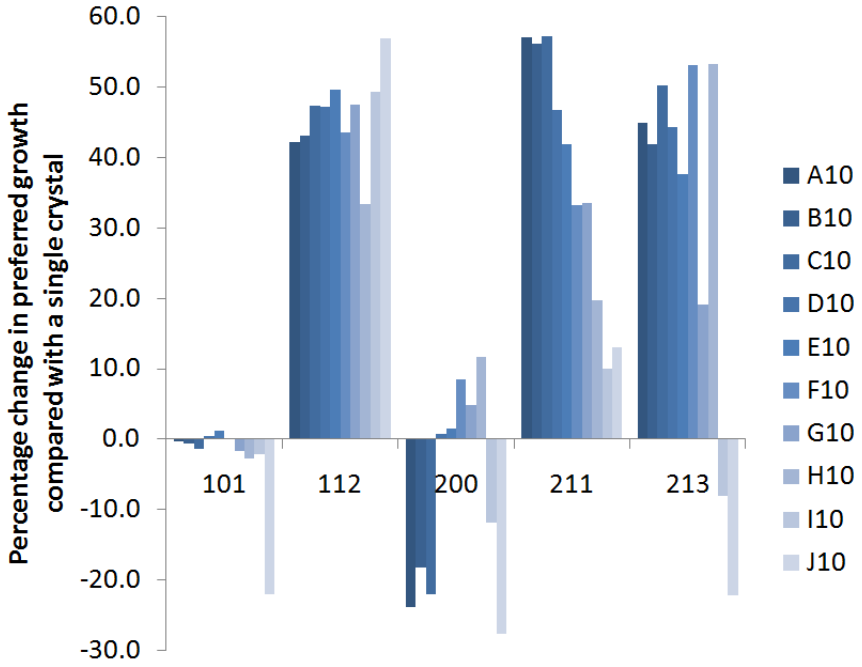

Figure 4.4.9: *The percentage change in preferred growth of the (101), (112), (200), (211) and (213) diffraction planes relative to a single crystal standard of anatase TiO_2 for all positions analysed by X-ray diffraction across Row 10. The error in each value is ≈ ± 1 %*

4.4.3.5. Film-thickness mapping

The reflectance spectrum of each colour band due to interference was recorded from 300 – 2500 nm at the positions designated in Figure 4.4.10(a). As the position of a transmittance maximum is analogous to where a reflectance minimum occurs (Figure 2.3.2(a)), the Swanepoel method for

determining the thickness of thin-films could be applied. The method determines film-thickness with knowledge of the positions at which interference maxima and minima occur combined with the dependence of the refractive index with frequency for the material in question.

(a) (b)

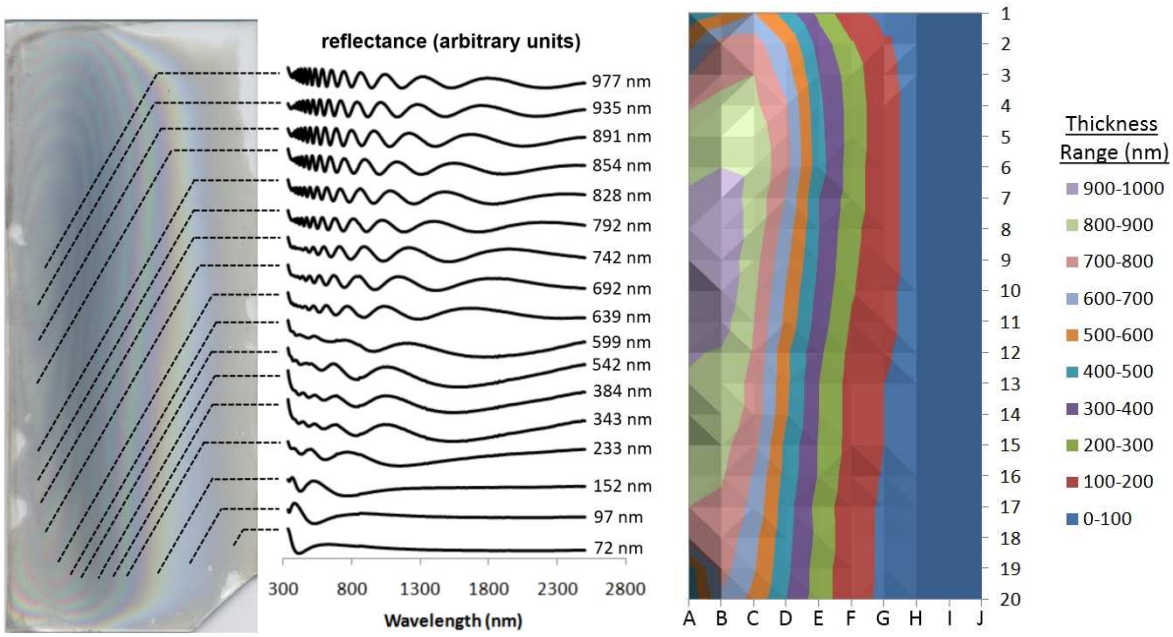

Figure 4.4.10: *(a) A map displaying the positions at which each interference colour band was analyzed by reflectance spectroscopy alongside its corresponding reflectance wave-pattern and Swanepoel derived film-thickness and (b) a colour contour map of film-thickness for the 200 allotted grid positions across the combinatorial film determined by approximating linear growth between interference fringes.*

The combinatorial thin-film under investigation contained a range of tungsten dopant impurities as a solid solution within the anatase TiO_2 framework. The effect of this solid-solution doping on the refractive index of anatase TiO_2 thin-films is, to our knowledge, un-reported. We therefore made the assumption that low levels of tungsten doping would not significantly affect the refractive index of anatase TiO_2 and determined the thickness of each interference colour band where the tungsten doping level was minimal (left side of the film, W: Ti ≈ 0.5 at. %). However, this was not possible for the thinnest sections of the film that lay in the regions where the highest levels of tungsten doping were achieved (right side of the film, W: Ti ≈ 10 at. %). Irrespective of this, a high degree of fit (r^2 > 0.99) was observed in all of our Swanepoel plots (Figure 2.3.2(b)). With the thickness at the centre of each colour band known, the thickness at the colour boundaries and the grid positions on the combinatorial film that were stationed between them were calculated by approximating linear growth (Section 2.4). A contour map of film-thickness was constructed, as shown in Figure 4.4.10(b), quantifying the variation in film-thickness seen by eye. Film-thicknesses could not be determined for grid positions stationed in Columns I and J as the film was too thin to show any interference bands

over the region (200 – 2500 nm) analysed. However, observed thicknesses ranged from as low as 70 nm (position H10) to as high as 810 nm (position B10).

4.4.3.6. Surface topography mapping

The surface roughness of a material can play an integral part in both photocatalytic and light scattering functions. For instance, the efficiency of silicon based solar panels can increase if light is more readily trapped and scattered by films with rougher surfaces.[301] Alternatively, the rate of photocatalysis is dictated by the number of surface sites available for reactions to occur.[9] One such method for deducing the surface roughness is through Braun-Emmett-Teller gas isotherm experiments. This method deduces the number of available surface sites by absorbing, weighing and desorbing inert gases.[302] However, the surface area of typical thin-films produced by CVD are notoriously difficult to measure by this method, as their specific surface areas normally fall below the detection limits of the apparatus (typically less than 0.2 m^2g^{-1}). Atomic force microscopy was therefore employed to map the surface topography and roughness of films across Row 10. Topographical images are shown in Figure 4.4.11. At position A10, long "worm-like" grains were observed. Moving across the row, from position A10 along to J10, the surface structure gradually changed, becoming grainier in nature. This coincided with a systematic decrease in surface roughness, where the root mean squared roughness (Equation 3.11) decreased from 11.1 nm at position A10 to 2.52 nm at position J10.

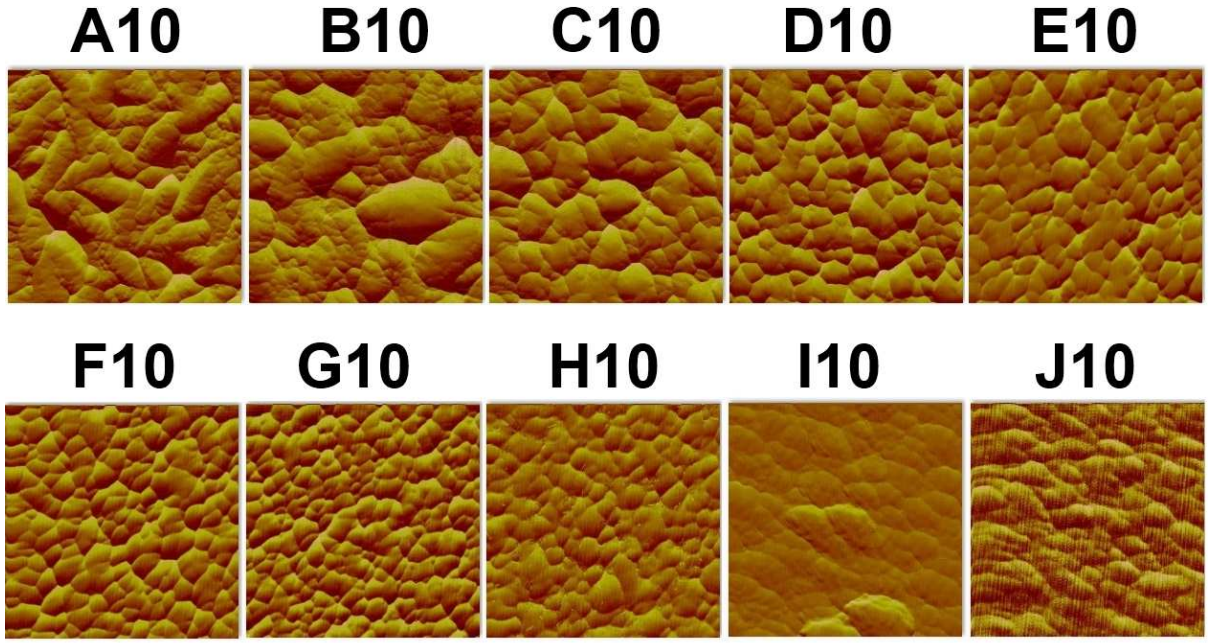

Figure 4.4.11: *Atomic force microscopy images displaying the surface topography of 1 μm x 1 μm (horizontal x vertical) squares for all positions across Row 10.*

4.4.3.7. Reaction chemistry

A combinatorial thin-film comprised solely of the anatase TiO_2 phase with varying levels of solid solution tungsten doping (0.38 ≤ W: Ti at. % ≤ 13.8) was formed by the combinatorial APCVD reaction of $TiCl_4$, WCl_6 and ethyl acetate at 525 °C. The precursor temperatures and carrier gas flow rates were adjusted to achieve the reagent mass flow rates specified in Table 4.4.1. From our tungsten/ titanium concentration mapping experiments (Section 4.4.3.2) the average tungsten doping level was found to be 5.3 at. % (σ = 3.2). X-ray photoelectron spectroscopy showed how the tungsten dopant existed primarily in the W^{5+} state. If we assume that the film was fully oxygenated, then the average oxygen: metal ratio incorporated was 2.03. As the molar ratio of the oxygen source (ethyl acetate): metal sources ($TiCl_4$ & WCl_6) was 0.098, ethyl acetate was the limiting reagent in the formation of $W_xTi_{1-x}O_2$. In addition, as the molar ratio of ethyl acetate: $TiCl_4$ was 0.9, ethyl acetate was also the limiting reagent in the formation of the TiO_2 matrix. In mapping the tungsten dopant level (Figure 4.4.3) and film-thickness (Figure 4.4.10(b)), and by also confirming that the film was of single anatase TiO_2 phase through Raman phase mapping, the reaction rate of each precursor at 180 grid positions (over a 0.56.cm^2 area) could be derived. In calculating these reaction rates we made the assumption that the anatase TiO_2 combinatorial film consisted of unitary density (3.89 $g.cm^{-3}$). The reaction rates could only be determined for positions in which both the film-thickness and tungsten/ titanium concentration was known. Therefore Columns I and J were omitted as the film was too thin to be determined by our methods.

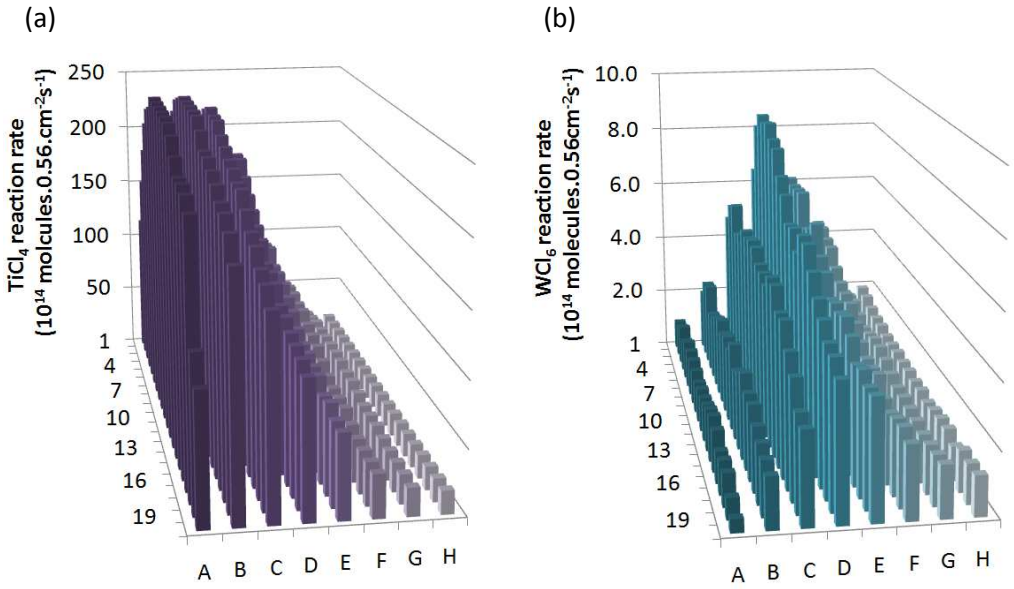

Figure 4.4.11: *3-dimensional bar chart of reaction rate (10^{14} molecules.0.56 $cm^{-2}.s^{-1}$) of (a) $TiCl_4$ and (b) WCl_6 precursors at 180 grid positions in the combinatorial APCVD synthesis of a tungsten doped solid solution within anatase TiO_2 (0.38 ≤ W: Ti at. % ≤ 13.8). Columns I and J were omitted as the film was too thin to be determined by our methods.*

As the ethyl acetate oxygen source entered the reactor from both inlets in approximately equivalent molar ratio and given the metal sources were in excess (Table 4.4.1), the relative reaction rates of $TiCl_4$ and WCl_6 were compared (Figure 4.4.11). Strong carrier gas flow rates were used for the combinatorial deposition. A total of 5.20 L min^{-1} entered the reactor from mixing chamber A carrying the WCl_6 source and on the opposite side, a total of 5.45 L min^{-1} entered from mixing chamber B carrying the $TiCl_4$ source. Given the small volume inside the reactor (≈ 0.25 L), these gas flows would have passed through the reactor in as little as one second. Given their speed and laminar flow, it was surprising that titanium deposition occurred at position J1 and *vice-versa* for tungsten at position A1. This demonstrated the mobility of these carrier gas flows to mix and diffuse laterally across the substrate. Although both WDX and XPS showed the tungsten doping level to be greatest on the right side of the film (column J), films were significantly thinner in these high dopant regions. From calculating the reaction rate of the WCl_6 tungsten source it was evident that insertion occurred most rapidly along the middle strip of the combinatorial film, along column D (Figure 4.4.11(b)). This coincided with the region of most intense blue tinge (Figure 4.4.2).

From mapping film-thickness, anatase TiO_2 film growth was observed to be most rapid in the middle left section of the film. A large disparity in film-thickness was observed across the combinatorial film. For example, at least factor of 10 difference in thickness was observed upon moving from position A10 (940 nm) to J10 (< 70 nm). This was attributed to the lateral diffusion barrier in the movement of the $TiCl_4$ source. There was also a disparity in thickness along the columns, where film formation was most rapid in the middle rows. This phenomenon is observed quite frequently in the APCVD of thin-films within a cold-walled reactor, where the substrate is marginally hotter at the centre of the reactor than at the edges.[110] Film growth was most rapid toward the centre of the film, peaking at position B10 with a growth rate of 16.3 $nm.s^{-1}$. This was more than 2.5 times more rapid than the average growth rate of 6.4 $nm.s^{-1}$. As the most rapid formation of TiO_2 occurred where the underlying substrate was hottest, the reaction of $TiCl_4$ was a reaction rate limited process. However, the reaction rate of the WCl_6 source was most rapid local its point of entry, maximising at position D3 (8.8×10^{14} molecules.0.56 $cm^{-2}s^{-1}$) and decreasing sharply in the lateral plane and more smoothly in the vertical plane from this point of maximum. This indicated that the reaction of WCl_6 was a mass-transport limited process.

During this deposition, the mass flow of WCl_6 was almost ten times larger than that of $TiCl_4$ (Table 4.4.1). Quite the contrary to this, anatase TiO_2 formed the main structure and just 5.3 at. % tungsten doping occurred on average. It was clear that the reactivity of $TiCl_4$ was far superior to that of WCl_6 under the conditions imposed. The average reaction rate of $TiCl_4$ corresponded to 1.21×10^{16}

molecules. 0.56$cm^{-2}s^{-1}$ and was more than 30 times greater than the average reaction rate of WCl_6 (3.3 x 10^{14} molecules. 0.56$cm^{-2}s^{-1}$). With these respective reaction rates and molar ratios in mind, $TiCl_4$ reacted *ca* 335 times more rapidly than WCl_6.

It has been documented that the blue coloration associated with tungsten doping arises from W^{5+} doping.[134] These W^{5+} states were identified as the prominent dopant environment across the combinatorial sample through XPS analysis. XRD and Raman mapping also confirmed the sole presence of the anatase TiO_2 phase. As CVD growth of the more thermodynamically stable rutile phase generally requires more elevated temperatures (≥ 600 °C), unitary anatase TiO_2 phase formation at the deposition temperature of 525 °C was as expected.[110] No presence of a separate tungsten oxide phase was observed in either Raman or XRD studies across Row 10. The systematic blue shifting of the principle E_g mode and increasing unit cell volume with increased tungsten dopant levels indicated that a solid solution had formed rather than a composite. From the increased lattice strain observed through XRD studies, the average ionic radii of the metal ions were derived; W^{5+} = 0.61 Å, Ti^{4+} = 0.55 Å. The disparity in ionic radii explained why increasing tungsten doping instigated a proportional decrease in crystallinity.

By culminating reaction rate data, the overall combinatorial APCVD reaction for the formation of anatase TiO_2 with a range of solid solution W-doping levels (0.38 ≤ W: Ti at. % ≤ 13.8) could be written as follows:

$$\mathrm{TiCl_4 + WCl_6 + \ MeCOOEt \ \rightarrow W_xTi_{1-x}O_2 + \ by\ products \ \ (12\ \%)} \qquad (4.6)$$

where 0.0038 ≤ x ≤ 0.138 (<x> = 0.053, σ = 0.032). An average molar ratio of $TiCl_4$: WCl_6: MeCOOEt = 1.0: 9.2: 1.1 was introduced in this combinatorial reaction over a glass substrate held at 525 °C (± 25 °C). As the reaction chemistry of 101 cm^2 over a total of 203 cm^2 of combinatorial film-space was investigated (Figure 4.4.11), the overall reaction efficiency in terms of the limit reagent was determined (12 %).

The results from our physical characterisations thus far were amalgamated into Table 4.4.2. Results from the upcoming functional property assessments are also included.

			A10	B10	C10	D10	E10	F10	G10	H10	I10	J10
Physical Properties	WDX (± 1 %)	W: Ti ratio (at. %)	0.42	0.87	2.27	3.93	5.20	6.40	6.65	6.95	8.13	10.3
	XPS (± 15 %)		2.05	1.88	2.18	2.13	2.20	2.47	3.78	5.41	13.5	28.8
	Raman	Principle E_g mode (cm^{-1} ± 0.1 %)	144.9	147.1	148.8	153.0	152.5	151.9	154.1	155.3	159.7	159.8
	XRD	Volume ($Å^3$ ± 0.1 %)	136.9	137.0	137.1	137.8	137.9	138.2	138.0	138.3	138.5	139.2
		Average crystallite size (nm ± 1 %)	19.5	19.9	18.7	18.7	18.1	17.3	16.9	16.3	16.4	14.2
	Reflectance	Thickness (± 1 %)	940	980	820	590	370	210	120	70	< 70	< 70
	AFM	Root mean squared (nm ± 0.1 %)	11.1	10.6	8.7	6.9	4.9	3.2	3.3	2.8	2.6	2.5
Functional Properties	Transmittance	Bandgap (± 1 %)	3.13	3.16	3.18	3.23	3.26	3.30	3.28	3.29	3.30	3.32
	Resistance	2 - point (10^4 Ω ± 10 %)	4.00	2.89	4.96	9.50	19.5	38.3	86.3	312	1390	-
		4 - point (10^4 Ω/□ ± 10 %)	2.05	1.94	2.61	4.74	10.1	17.3	35	78.3	-	-
		ρ (10^{-2} Ωm ± 10 %)	1.92	1.90	2.14	2.80	3.73	3.64	4.20	6.66	-	-
	Photocatalysis	Stearic (10^{-5} FQE ± 5 %)	5.21	4.95	3.75	2.55	2.53	2.48	1.22	1.14	1.93	0.99
		Resazurin (10^{12} molecules $cm^{-2}s^{-1}$ ± 10 %)	2.36	2.62	2.36	2.03	1.46	1.03	0.78	0.64	0.49	0.40
		Resazurin (10^{-4} FQE ± 10 %)	5.04	5.58	5.04	4.34	3.13	2.20	1.66	1.36	1.04	0.85
		Resazurin (10^{-4} FQY ± 10 %)	8.46	10.6	9.83	9.28	8.27	7.47	5.90	4.61	5.08	2.58
	Water Contact Angle	Pre – UV (° ± 10 %)	71	73	76	70	70	72	67	70	73	69
		Post- UV minimum (° ± 10 %)	4.6	7.9	5.4	8.0	8.2	6.0	10	16	16	18

Table 4.4.2: *List of physical and functional property data acquired from wavelength dispersive X-ray analysis (WDX), X-ray photoelectron spectroscopy (XPS), Raman spectroscopy, X-ray diffraction (XRD), transmittance/ reflectance spectroscopy, atomic force microscopy (AFM), four-point probe sheet resistance, intelligent ink photocatalysis (UVA light), stearic acid photocatalysis (UVC light) and water droplet contact angle measurements (UVC light) for the 10 grid positions along Row 10.*

4.4.3.8. Bandgap mapping

Transmittance spectroscopy showed a gradual blue-shift in the band edge from position A10 to J10, as shown in Figure 4.4.12(a).The bandgap was subsequently determined for each position through extrapolating Tauc plots of transmittance data.[195]

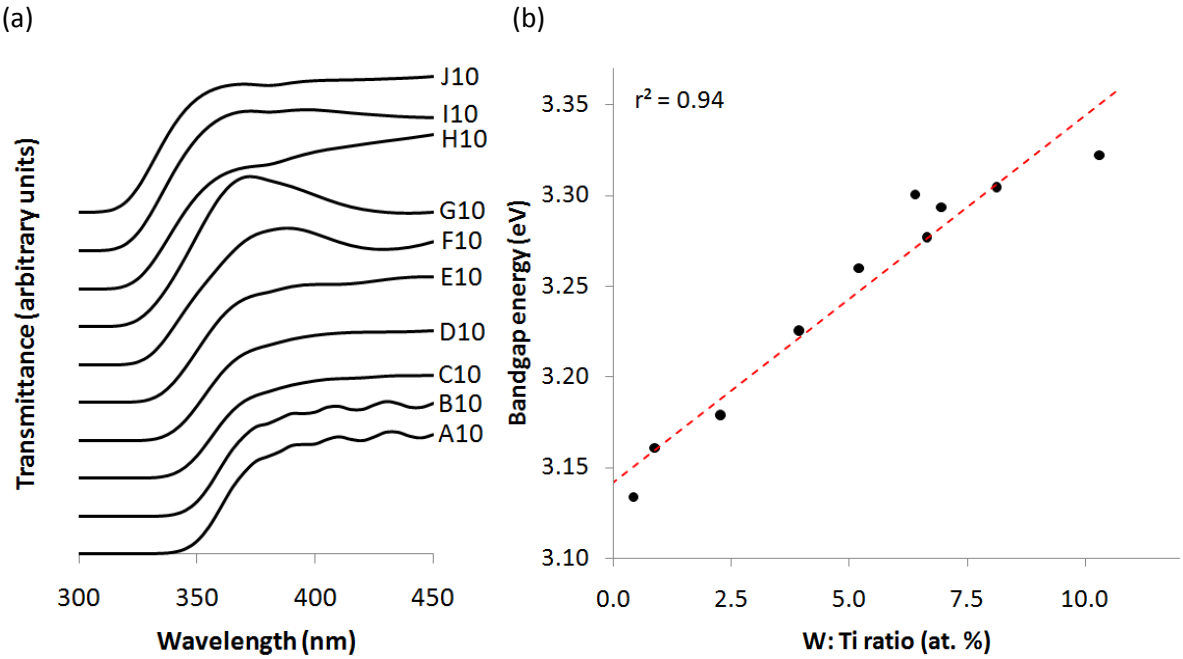

Figure 4.4.13: *(a) A stacked plot of the transmittance spectra focussed over the band-edge region and (b) a plot of Tauc plot derived bandgap energy against bulk W-doping level where a positive linear correlation with a strong degree of fit was observed (r^2 = 0.94) for positions analysed across Row 10.*

The bandgap energy increased relatively steadily from 3.13 eV at position A10 to 3.32 eV at positions J10. There are two phenomena that could cause such an effect: (i) the Moss-Burstein effect[270] or (ii) decreasing crystallinity. The Moss-Burnstein effect occurs when n-type doped semiconductors, such as W-doped anatase TiO_2, surpass a saturation limit in the number of charge carriers that are introduced into the system. As the conduction band fills, the energy required to excite electrons from the valence band to the lowest unoccupied state in the conduction band increases, causing a wider bandgap. Across Row 10, both the concentration of n-type dopants (W-doping level) as well as the degree of amorphousness increased. This made both explanations for the bandgap increase feasible. In order to determine which effect was playing the more dominant role, both the bulk tungsten doping level (WDX analysis) and average crystallite size (XRD analysis) were separately plotted against the bandgap energy. A stronger linear correlation was observed between the bulk tungsten doping level and the bandgap energy (Figure 4.3.13(b), r^2 = 0.94) than average crystallite size (r^2 = 0.79). This indicated that the Moss-Burstein effect was the primary cause for the bandgap increase across the material. The following relationship was observed:

$$bandgap\ increase\ (eV) = 0.020x \quad (4.7)$$

where *x* is the W: Ti ratio (at. %). This result was contrary to what was proposed by Takeuchi *et. al.*, where the introduction of W-dopants as a solid-solution in anatase TiO_2 create shallow states in the valence band that trap charge carriers.[282] A somewhat steady increase in bandgap energy was observed upon increased W-doping of anatase TiO_2 in our study that was best explained by a constant flow of charge carriers into the conduction band (Moss-Burstein effect).

4.4.3.9. Photo-induced wettability mapping

The water droplet contact angles along positions A10 to J10 were measured at several stages between its hydrophobic and hydrophilic extrema. Some example images of the change in contact angle over time at position A10 are shown in Figure 4.4.14(a).

(a)

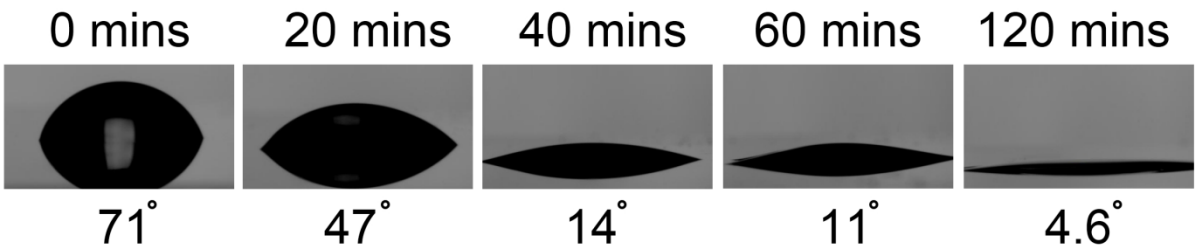

(b)

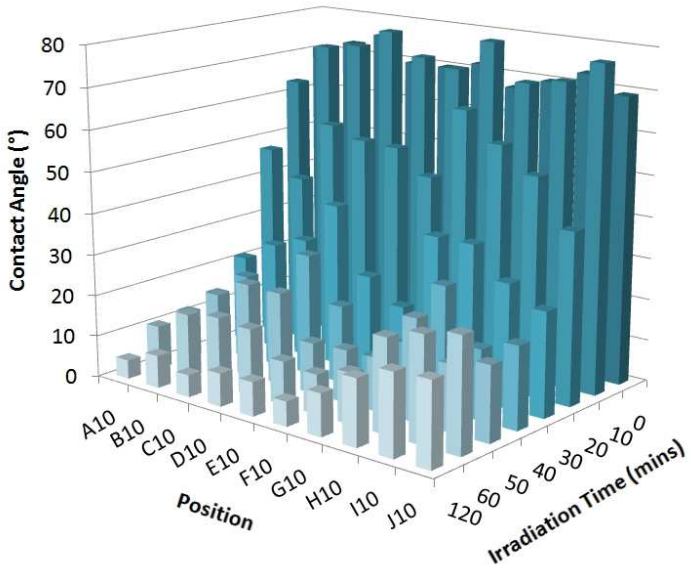

Figure 4.4.14: *(a) An image time-line of the water droplet contact angle (8.6 µl droplet) made against the surface at position A10 with UVC irradiation time and (b) a 3-dimensional bar chart stack of all contact angles measured along Row 10 with cumulative UVC irradiation time.*

At its maximum hydrophobic state, the water droplet made a contact angle of 71° with the surface. This decreased consistently as the surface was irradiated with UVC light (flux = 9.74 x 10^{15} photons $cm^{-2}s^{-1}$). This was attributed to the gradual formation of hydroxylated domains at the surface of the

film through the photo-induced hydrophilicity (PIH) mechanism. After 120 mins irradiation, the surface had most probably become inundated with hydroxyl groups as a water-droplet contact angle minimum of 4.6° was reached. A 3-dimensional bar chart of water droplet contact angle against cumulative UVC irradiations for all positions assessed across Row 10 is shown in Figure 4.4.14(b). Before the films were irradiated with UVC light, the initial contact angles observed across Row 10 were approximately equivalent; averaging 71°. A smooth progression to hydrophilicity was then observed for each position with cumulative irradiations. After saturating the films with UVC light (120 mins) and no further decrease in contact angle was observed, a trend in the maximum level of hydrophilicity was revealed, where from position A10 (4.6 °) to J10 (18 °) a decrease in maximum surface wettability was observed.

The mechanism of PIH has been well established for the rutile phase of TiO_2, where little work on the anatase phase has followed suit.[2] The PIH mechanism requires photo-excitations and the number of active sites at the surface of the material dictate the number of hydroxyl domains that can form. More specific to rutile TiO_2, it was found that the formation of hydroxyl domains was most pronounced on the (110) face of rutile TiO_2 crystals, where films with increased preferred orientation in this plane showed increased degrees of photo-induced wetting.[2] It is also worthy of note, that the process was found to be independent of film-crystallinity. Given the energy of the light source used (4.88 eV) far surpassed the bandgap energy of all positions tested (Table 4.4.2), the degree of photo-induced wetting would have primarily depended on the number of surface active sites. We first compared these saturated water droplet contact angle with surface roughness, a measure of surface area. A weak linear relationship was revealed ($r^2 = 0.50$). Given particular facets in rutile TiO_2 display more prominent degrees of photo-induced surface wetting than others, we compared the trend in saturated water droplet contact angles against the degree of preferred orientation in each crystal plane. The strongest relationship was observed upon comparing the degree of preferred orientation in the (211) crystal plane and saturated contact angle ($r^2 = 0.81$). Given the primary crystal plane for PSH processes in anatase TiO_2 is, to our knowledge, yet to be identified, these trends highlighted the importance of the (211) plane.

4.4.3.10. Photocatalytic activity mapping

The combinatorial film was sprayed with an even layer of a resazurin-based intelligent ink. The photo-reduction reaction was induced by UVA light (flux = 4.69×10^{15} photons $cm^{-2}s^{-1}$) and monitored solely through digital photography. A time-line of the reaction is shown in Figure 4.4.15(a). Before the reaction was initiated (0 mins), we see both the even layer of the royal blue coloured intelligent ink as well as some blue coloration from the W^{5+} ions, that was most intense along the left-middle

strip of the film due to the greater overall level of tungsten incorporated (Section 4.4.3.7). After 5 mins of UVA irradiation, the ink had changed colour from royal blue to pink solely along the left strip of the combinatorial film. This was due to the photo-reduction of resazurin (royal blue) to its intermediate resorufin (pink). A transitional change to pink, from left to right, was observed with further irradiations. After 100 mins total irradiation, the ink had fully degraded to bleached intermediates. The observed responses indicated that the film was increasingly more photocatalytically active towards the left side of the film.

(a)

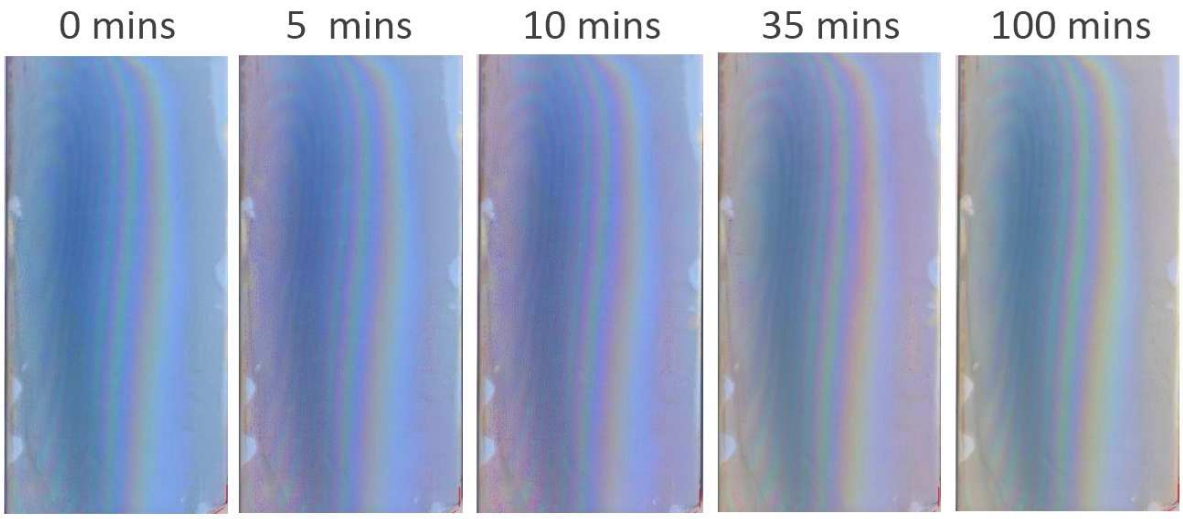

(b)

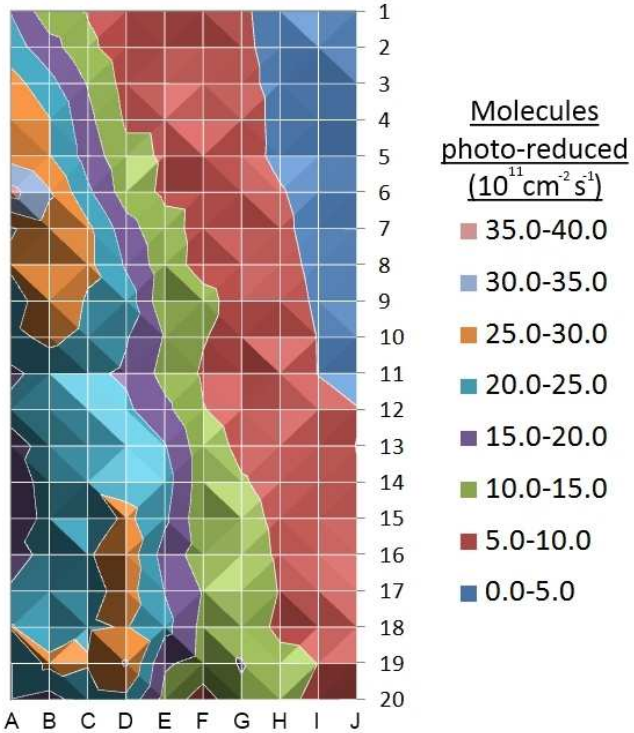

Figure 4.4.15: *(a) Timeline of the photocatalytic reduction of a resazurin-based intelligent ink that had been deposited evenly by an aerosol-spray over the entire combinatorial film and (b) a colour contour map of UVA photocatalysis of the resazurin-based intelligent ink (molecules photo-reduced 10^{11} $cm^{-2}s^{-1}$).*

The changes in the red component of digital colour were assessed for the 200 allotted grid positions (Section 2.6). Although the film alone showed a varying blue tinge (due to W^{5+} ions) this did not affect the digital colour analysis. This is because the time it takes for the components of digital colour to reach a plateau are assessed rather than any magnitude in the colour change. The times at which the red components of digital colour plateaued were determined by fitting data to a Boltzmann model. Each time represented the point at which the resazurin redox dye had been fully photo-reduced (Equation 2.20). As the thickness and concentration of the original ink layer were known, the photo-reduction rate (molecules photo-reduced $cm^{-2}s^{-1}$) at each grid position could be determined (Equation 4.3). A contour map of these rates is shown in Figure 4.4.15(b); quantifying the trends in colour change seen by eye. A general trend was observed, whereby the rate of UVA photocatalysis varied more substantially across rows and less so in columns. Thus for comparison, the UVC (flux = 9.74 x 10^{15} photons $cm^{-2}s^{-1}$) photo-oxidation of a stearic acid overlayer was assessed for positions across Row 10. The rates of UVC (stearic acid) and UVA (resazurin intelligent ink) photocatalysis were converted into formal quantum efficiencies (molecules destroyed per incident photon) and compared, where a linear correlation with a good degree of fit was observed (r^2 = 0.82). It was previously shown that the UVA photocatalytic response of pure anatase TiO_2 thin-films to resazurin-based intelligent ink was directly proportional to their UVC stearic acid photo-oxidation.[172] It was therefore unsurprising that such a good agreement between two separate tests were observed. However, these corroborating results added more weight to the observed general trend, where UV photocatalysis decreased from position A10 to J10.

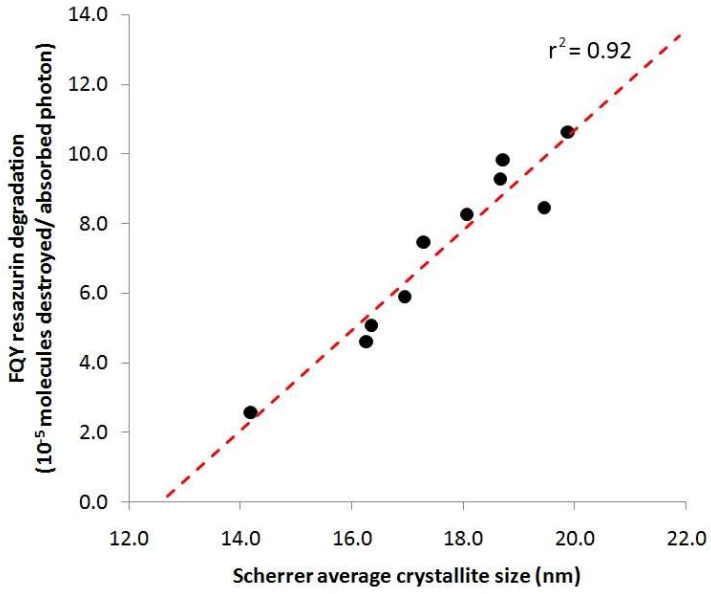

Figure 4.4.16: *A plot of average crystallite size (nm) against respective formal quantum efficiency (10^{-5} molecules/ absorbed photon) in the UVA photocatalysis of a resazurin-based intelligent ink for positions assessed along Row 10.*

When assessing the trends in photocatalysis across a number of samples, one must account for variations in thickness, bandgap energy, crystallinity, surface roughness and impurity dopant level; as the activity of a photocatalyst is dependent on these physical properties. The thickness and bandgap energy of a semiconductor will determine the number of UVA photons it will absorb. The formal quantum yield (FQY) accounts for the number of photons absorbed. Any change in thickness or bandgap energy can therefore be discounted when comparing FQYs. In trying to account for the decreasing trend in FQY across Row 10 from position A10 to J10, the average crystallite size, surface roughness and tungsten doping level were separately compared against this measure of photocatalysis. A weak relationship was observed between the increasing surface roughness and increasing FQY (r^2 = 0.66). This indicated that the number of surface sites available for the photo-reduction reaction to occur was not the primary cause for the variations in photocatalysis observed. A strong linear correlation between the increasing impurity dopant level and decreasing FQY was observed (r^2 = 0.81) and an even stronger degree of correlation between increasing average crystallite size and increasing FQY (r^2 = 0.92), as shown in Figure 4.4.16. This indicated two possible pathways that were causing detriment to the photocatalysis, where:

(i) an increased presence of tungsten impurities induced recombination of photo-excited electrons and holes and/ or

(ii) an increased presence of tungsten impurities disrupted the anatase TiO_2 lattice and decreased film-crystallinity

The strong degree of correlation observed between both the level of tungsten doping and film-crystallinity made it difficult to rule out one possible explanation or the other. However, given the strongest relationship was observed between film-crystallinity and photocatalysis, we suggest that this is primary cause of the variations in photocatalysis observed. In fact, the degree of film-crystallinity was entirely dictated by the level of tungsten doping in this system, so it may just be that the relationship between tungsten dopant level and photocatalysis is a remnant of this.

Previous studies on enhancing the photocatalytic activity of anatase through tungsten doping have entailed the formation of WO_3-TiO_2 composites consisting of WO_3 grains within a TiO_2 host matrix through a sol-gel synthesis.[23,287] Significant enhancements in the activity of these composite systems were discovered; where dopant levels between 2 - 3 atom % insertion were optimal.[23,285,287] The increase in activity was explained through a charge separation model where WO_3 sites could transfer photo-excited holes into the valence band of the anatase matrix and anatase could transfer photo-excited electrons into the conduction band of WO_3.[23] This mode hindered electron-hole recombination and drove photocatalytic processes. However, in this combinatorial study, tungsten

doping formed solid solutions in anatase TiO_2 that were incapable of such functionality. This was reflected in the photocatalytic activity, where the most active sample at position A10 showed a marginally lower FQE of 5.21 x 10^{-5} (stearic acid molecules degraded/ incident photon) compared with an optimized 2 atom % WO_3-TiO_2 sol-gel composite we tested previously with a FQE of 7.72 x 10^{-5}.[286] From observations across Row 10, increased W-doping induced lattice expansions and lowered film-crystallinity. This was found to be the primary cause for why increased W-doping as a solid solution in anatase TiO_2 caused detriment to the photocatalytic performance of the material.

4.4.3.11. Resistivity mapping

The electrical sheet resistance (Ω/□) was determined by applying the van der Pauw method[264] to electrical voltage and current measurements made between a four-point probe at all 200 allotted grid positions across the combinatorial film (Equation 4.1). The difference in sheet resistance differed by several orders of magnitude across the film. A trend was observed whereby a higher level of conductivity was observed where the film was thicker. The resistance along Columns I and J exceeded the detection limits of the apparatus so the sheet resistance could not be determined. A 3-dimnesional contour map of the $\log_{10}$(sheet resistance (Ω/□)) for all other columns is shown in Figure 4.4.17.

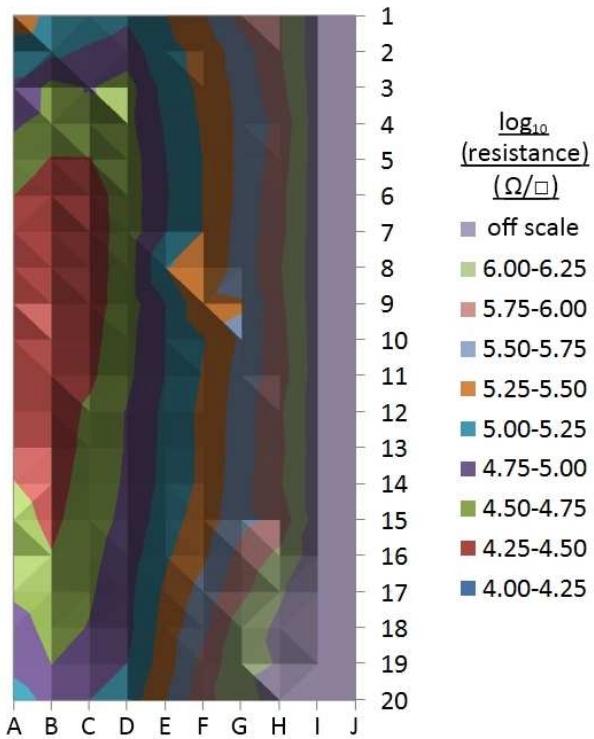

Figure 4.4.17: *A 3-dimensional colour contour map of the $\log_{10}$((sheet resistance (Ω/□)) across the combinatorial film. Columns I and J were omitted as resistances exceeded the detection limit of the measuring device.*

The conductivity of a thin-film material is dependent on film-thickness, as this determines the number of pathways in which charge carriers can flow. Film-thickness can therefore be accounted for by converting sheet resistance into resistivity (Equation 4.2). This was performed for positions across Row 10. The resistivities could not be determined for positions I10 and J10 given their off-scale resistance. However, a trend was observed across the row from A10 to H10, where the resistivity gradually increased.

In a previous study of a tungsten doped anatase TiO_2 solid solution, it was shown through computation and experiment that increased tungsten doping increases the number of charge carriers inserted into the material's conduction band.[149] Upon comparing the tungsten doping level with resistivity for all 180 positions across the combinatorial film (Columns I and J omitted as resistivity couldn't be determined), no direct relationship between the two properties was observed. However, a slight trend was observed, whereby increased tungsten doping increased film-resistivity, which was at odds with the literature.

The resistivity of an n-doped semiconductor such as tungsten doped anatase TiO_2 is dependent upon two factors:

(i) the charge carrier concentration (*n*) and
(ii) the mobility of charge carriers (μ)

Introducing small levels of tungsten into the anatase framework at position A10 decreased film-resistivity relative to pure anatase TiO_2 by several orders of magnitude. This was attributed to the introduction of charge carriers into the system with little disruption to the lattice. The increasing levels of tungsten doping seen across Row 10 should certainly have increased the number of charge carriers. However, a decrease in film-conductivity was observed. Therefore, the mobility of these charge carriers (μ) must have been impeded to counter this increase in charge carrier concentration (*n*). From XRD experiments, an increase in amorphousness was observed with increased tungsten doping (Section 4.4.3.4). This increased disruption of the TiO_2 lattice would have caused a decrease in the mobility of the charge carriers. From the decrease in resistivity seen across the group, it was clear that the detriment to charge carrier mobility was greater than the increase in charge carrier concentration. The most effective balance between these two counteracting properties was found at position A10, where a W-doping level of 0.42 at. % was present. A strong linear relationship between the underlying film crystallinity and resistivity was observed ($r^2 = 0.85$). This correlated with what has been observed in the literature for niobium doped anatase TiO_2[266,303,304] as well as what we observed through combinatorial investigation of Nb-doped anatase TiO_2 phase space (Section 4.3), where

mobility effects dominate. The combinatorial W-doped anatase TiO_2 system investigated here indicated that some optimum level of W-doping for increased film-conductivity lies between (0 < W: Ti at. % ≤ 0.42). However, these films were fully oxygenated, where it has been found that annealing similar materials under vacuum (3×10^{-3} Pa) at high temperatures (650 °C) can significantly decrease film-resistivity to levels as low as 1.5×10^{-4} Ωm for dopant levels as high as 6.3 atom %.[149] Their decrease in film-resistivity was attributed to an increase in the mobility of the charge carriers through oxygen vacancy formation and increased film-crystallinity.

4.4.4. Conclusions

A combinatorial thin-film comprised solely of the anatase TiO_2 phase with varying levels of tungsten (primarily W^{5+}) solid solution doping (0.38 ≤ W: Ti at. % ≤ 13.8) was formed by the combinatorial APCVD reaction of $TiCl_4$ (Ti source), WCl_6 (W source) and ethyl acetate (O source) at 525 °C. This was the first time in which thin-films of W-doped anatase TiO_2 solid solutions were formed by a CVD process. By pre-mixing each metal source with the oxygen source, a combinatorial film with a tungsten doping level that varied primarily in the lateral plane was formed. In applying high-throughput screening methods the physical and functional property inter-relationships were rapidly characterised.

A strong linear inter-relationship between the tungsten doping level, unit cell volume and degree of shift in the principle Raman active E_g vibrational mode was observed. The relationships provided simple routes to estimating the level of tungsten incorporated through either Raman spectroscopy or X-ray diffraction as opposed to the more time consuming direct method in wavelength dispersive X-ray analysis which requires pre-calibration of standards. It was also found that the degree of photocatalysis was most dependent on film-crystallinity, where increased tungsten doping disrupted the lattice and increased photo-generated electron and hole recombination processes. For film-resistivity, a similar relationship was observed, where increased tungsten doping disrupted the lattice and reduced charge carrier mobility. Under the experimental conditions imposed, the optimum balance between increased charge carrier concentration through W-doping and detrimental lattice disruptions was observed at a doping level of ≈ 0.42 at. %. The degree of photo-induced surface wetting was found to be most highly dependent on the level of preferred orientation in the (211) plane, where increased orientation in this plane increased the maximum degree of photo-induced surface wetting. Given the primary crystal plane for photo-induced wetting process in anatase TiO_2 is yet to be identified in the literature, these unique findings highlight the importance of the (211) plane.

In the following section we will compare the results from both our niobium and tungsten doped anatase TiO_2 combinatorial studies and try and conclude as to which is the better photocatalyst and transparent conductive oxide (TCO) material. After assessing the major physical and functional property relationships that operate in each system we will explain our choice.

4.5. Summary of metal-doped anatase TiO_2 systems explored

Combinatorial APCVD was used to produce two different metal-doped anatase TiO_2 solid-solution systems. Two niobium doped anatase TiO_2 solid solution systems were formed from the reaction of $TiCl_4$ and $NbCl_5$ and ethyl acetate at 500 °C, where:

(i) $Nb_xTi_{1-x}O_2$ ($0.0004 \leq x \leq 0.0011$)

(ii) $Nb_xTi_{1-x}O_2$ ($0.0017 \leq x \leq 0.0194$)

and one tungsten doped anatase TiO_2 solid solution was formed from the reaction of $TiCl_4$ and WCl_6 and ethyl acetate at 525 °C, where:

(iii) $W_xTi_{1-x}O_2$ ($0.0038 \leq x \leq 0.138$)

These systems were the first cases in which niobium and tungsten doped anatase TiO_2 solid solutions had been formed by a CVD process. By tailoring novel high-throughput screening methods to these systems in conjunction with traditional characterisation methods we were able to characterise the physical and functional properties of a large number of unique states across each combinatorial system.

When attempting to compare a particular functional property, one should be sure to account for the underlying physical properties that contribute. In the study of Nb-doped anatase TiO_2 (Section 4.3), positions along a central vertical strip were characterised in full so that well judged comparisons could be made. Their properties were tabulated in Table 4.3.2. In the study of W-doped anatase TiO_2, positions across a central lateral strip were fully characterised for the same reason. Their properties were tabulated in Table 4.4.2. For comparisons between the two systems, we will use the information contained in these tables.

The UVA photocatalysis of both W and Nb-doped TiO_2 systems was equivalently assessed using our photocatalytic activity mapping method and a resazurin-based intelligent ink (Section 2.6). The rate of photo-reduction was determined as the thickness of the ink layer was known (Section 4.2.2.4). The most active photocatalysts were observed in the Nb-doped anatase TiO_2 thin-films,

where the most active position (F1, $NbTiO_2$-A) photo-reduced 3.38 x 10^{12} molecules of resazurin $cm^{-2}s^{-1}$. The most active position in the W-doped anatase TiO_2 film (position A10) showed a photo-reduction rate that was almost 1.5 times slower than this of 2.36 x 10^{12} molecules $cm^{-2}s^{-1}$. These two positions also displayed the lowest resistances across each system, where the W-doped material showed a marginally lower resistivity of 1.92 x 10^{-2} Ωm compared with 2.20 x 10^{-2} Ωm for the Nb-doped material. The physical properties of these two positions are shown in the table below:

		W-doped	Nb-doped
Physical properties	Doping level (at. %)	0.42	0.11
	Average crystallite size (nm)	19.5	20.4
	Thickness (nm)	940	836
	Surface area per μm^2 (μm^2)	1.15	1.21
Functional properties	Bandgap (eV)	3.13	3.23
	ρ (10^{-2} Ωm)	1.92	2.20
	Resazurin (10^{12} molecules $cm^{-2}s^{-1}$)	2.36	3.38

Table 4.5.1: *List of the physical and functional properties at the positions which showed the greatest level of UVA photocatalysis in each W and Nb-doped anatase TiO_2 combinatorial system investigated. It so happened that these positions also showed the lowest resistivity in each set as well.*

The photocatalysis of a thin-film semiconductor is dependent on film-crystallinity, thickness, surface roughness and impurity dopant level. Each of these physical properties was quantified in the table above. With the exception of impurity doping level, the physical properties of these two photocatalysts differed by less than 5 %. So the large discrepancy observed in the level of UVA photocatalysis was attributed to the effect of the impurity dopant ion. From evaluating a range of Nb (0.04 ≤ Nb: Ti at. % ≤ 1.94) and W (0.38 ≤ W: Ti at. % ≤ 13.8) doping levels in each system, there was no clear indication that these impurities acted as sites for the lower energy recombination of photo-generated electrons and holes that mediate photocatalysis. Through investigating the W-doped series, it was established that the degree of photocatalysis was most dependent on film-crystallinity. As the W ions that replaced the Ti ions in the lattice were significantly larger (W^{5+} = 0.61 Å, Ti^{4+} = 0.55 Å), higher levels of W doping disrupted the lattice more greatly, decreasing film-crystallinity and the degree of UVA photocatalysis. This indicated that W doping did nothing but cause detriment to the level of UVA photocatalysis in anatase TiO_2. However, Nb doping caused no significant disruption to the TiO_2 lattice. In fact, no direct relationship between the level of Nb doping and UVA photocatalysis was observed. Instead, our experiments suggested that the concentration of oxygen vacancies present in the lattice was responsible for the observed increase in UVA photocatalysis. The fact that a more active photocatalyst could be induced by oxygen vacancies is not a novel concept, where it has

been postulated to play a key role in nitrogen doping anatase TiO_2 as well.[194,279] It was computational shown that Nb-doping TiO_2 provides lower energy pathways for oxygen vacancies to form.[265] It was also shown that the oxygen concentration present during growth of Nb-doped TiO_2 would impact upon the number oxygen vacancies incorporated into the lattice.[261] In our Nb-doped TiO_2 films, the most photocatalytically active positions were observed where film growth was most rapid. This was attributed to two factors:

(i) some presence of Nb that induced a lower energy pathway for oxygen vacancies to form and
(ii) a more rapidly growing film that encouraged the formation of a greater level of oxygen vacancy defects.

In aiming to produce an enhanced UVA photocatalyst, our results suggest that Nb doping, rather W doping, TiO_2 as a solid solution would be the better option. Our results also suggest that the level of Nb doping is not as important as the growth conditions, where a more reducing growth environment is recommended.[261] However, some presence of Nb doping may be vital as computational studies not only suggested that they provide lower energy pathways to the formation of oxygen vacancies but stabilised them to oxidation as well.[265]

X-ray photoelectron studies of both W and Nb doped anatase TiO_2 systems showed the dopant ions to both be in the +5 oxidation state. As both form n-type semiconductors,[149,261] this suggested that each dopant ion provided a single charge carrier per insertion. Nevertheless, the resulting conductivity within each system was found to heavily depend on the mobility of these charge carriers rather than their concentration. The best W-doped material showed a marginally lower resistivity (1.92×10^{-2} Ωm) than the best Nb-doped material (2.20×10^{-2} Ωm). However, the level of visible light transparency was significantly lower in the W-doped material (≈ 55 %) compared with the Nb-doped material (≈ 70 %) even though both films were of a similar thickness. This increased absorption in the visible for the W-doped material may have been due to the presence of shallow W^{5+} valence states.[282] When choosing a TCO material for optoelectronics applications, a high transparency in the visible is often a prerequisite. We therefore suggest that Nb-doping anatase TiO_2 would make a marginally better TCO material than W-doping because of the higher degree of visible light transparency and similar resistivity. Nevertheless, the resistivities observed in our studies were far too high for what is generally required of TCOs (10^{-6} Ωm). We also recommend that these materials be produced in a more reducing environment,[261] or post-processed in a reduced environment,[266] to increase film-conductivity.

The lowest contact angle that a water-droplet made with the surface of a W-doped thin-film after being saturated with UVC light was 4.6°. However, the lowest contact angle achieved in our Nb-doped thin-films was 1.5°. Across both series, the average contact angle in our W-doped TiO_2 thin-film was 10° (σ = 4.9°) and 2.7° (σ = 0.91°) in our Nb-doped TiO_2 films. The variation in contact angle in our W-doped TiO_2 thin-film was attributed to the variation in the degree of preferred orientation in the (211) plane across the film, where the lowest contact angle was observed where the growth in this plane was strongest (57 % increase relative to a single crystal). However, in our Nb-doped TiO_2 thin-films, not only did the preferred orientation change very little across the film but there was also heavy preferred orientation in the (211) plane (≈ 400 % increase relative to a single crystal, Figure 4.3.5(a)). We therefore propose that the higher degree of photo-induced surface wetting observed in Nb-doped TiO_2 was due to the high degree of preferred growth in this plane. We also suggest that for highly photo-induced wettable surfaces that Nb-doped, rather than W-doped, solid solutions of anatase TiO_2 is a better choice as the introduction of Nb seemingly mediates the increased preference for growth in the (211) plane. In comparing these two systems, the importance of the (211) plane in the photo-induced hydrophilicity (PIH) mechanism is highlighted further.

In the following Chapter we will provide a brief conclusion of this work. We will scrutinise combinatorial thin-film methods as a route to optimising the functional properties of systems with a focus on CVD methods. From the literature we will then suggest what we feel is required of the field to make it a leading method for new materials discovery and functional property optimisation.

5. Conclusions

The publication rate for research papers devoted to thin-film combinatorial science has steadily increased from 31 publications in 1996-2000, to 201 publications in 2001-2005 to 311 publications in 2006-2010. Although some groups have applied the combinatorial thin-film approach in producing and characterising more than 1000+ unique materials, smaller sample libraries containing only 10 – 20 unique members were more common. For the true benefits of the combinatorial approach to take root, more unique states should be evaluated in any given study. This would ensure that true optimum compositions are established and previously unexplored phase space is not missed for new materials discovery. With the vast number of unique states that can be deposited, the limiting factor of this approach is indeed the speed of characterisation. The development of new high-throughput methods for screening the functional properties of combinatorial libraries has led to the progression of this field into at least 14 areas of materials science spanning dielectric,[57-59] ferroelectric,[60,61] H_2 storage,[62-65] fuel cell anode and cathode,[66-72] hardness,[73-76] Li-ion battery electrode,[77-79] luminescence,[80,81] transparent ferromagnetic,[55,56] photovoltaic,[82-85] transparent conducting oxide,[86-91] shape-memory[92-95] and thermoelectric[96-100] materials optimisation. Using such methods, a wide-range of material compositions were optimised for a variety of functions. Nevertheless, most functional properties depend on more than just composition. For instance, in the field of photocatalysis, the activity also depends upon the bandgap energy, crystallinity, surface roughness and film-thickness. Although most groups using the combinatorial thin-film approach as a route to optimising functional properties have used precise deposition methods to produce highly epitaxial and evenly smooth films; slight variations in film crystallinity, surface roughness *etc* were not always accounted for. In order for combinatorial methods to carry more weight as a leading materials approach, a characterisation that covers all of the physical properties related to the specific functional property under investigation should be consistently addressed. By developing an arsenal of high-throughput screening methods (Chapter 2) we were able to account for most, if not all underlying physical properties that contributed to the observed functional effect. In addition, we were also able to develop a method for rapidly screening the UVA photocatalysis of a large number of states. In doing so we were able to apply combinatorial thin-film methods in investigating the photocatalytic activity of a large number of unique states for the first time.

Combinatorial CVD has been used on just a few occasions to investigate the functional properties of thin-film systems.[57-60,109-111] More specifically, the combinatorial APCVD approach to optimising functional properties has been used just three times. Once by Kuykendall *et. al.* to produce the full range of $In_xGa_{1-x}N$ materials in a single deposition and investigate the change in bandgap energy[109]

and twice by Hyett *et. al.* to investigate the heat-mirror properties of $Ti_xV_{1-x}N$ alloys[111] and UVC photocatalysis of anatase TiO_2: rutile TiO_2 composites.[110] Given APCVD is the native method in which thin-films of TiO_2 are mass-produced, we used combinatorial APCVD to investigate the photocatalytic activity and other functional properties of N, Nb and W doped TiO_2 thin-film systems. In one of our N-doped titania studies, a new route to forming the recently discovered pseudo-brookite $Ti_{3-\delta}O_4N$ phase was established and was also the first case in which a composite between the pseudo-brookite $Ti_{3-\delta}O_4N$ phase and anatase TiO_2 was formed. In addition, our Nb and W doped titania studies were the first cases in which solid solutions of these materials had been formed by a CVD process. In tailoring high-throughput screening methods to these systems we were able to characterise large numbers of unique states across each combinatorial system and inter-relate their physical and functional properties. Many interesting relationships were revealed, which were highlighted in our summary sections (3.6 and 4.5). For instance, in the field of N-doped TiO_2, there is little consensus as to which type of doping (substitutional or interstitial) or dopant concentration yields the more active visible light photocatalyst. However, our studies suggested that solely N_i-doped TiO_2 yielded the more active photocatalyst. In the field of TiO_2 research, there is also some debate as to whether or not anatase TiO_2: rutile TiO_2 composites produce a synergistic effect on photocatalysis. After investigating a wide range of phase-space, we were also able to suggest that pure anatase TiO_2 is the more active photocatalyst with no indication of synergy. After investigating a range of Nb and W-doping levels in anatase TiO_2, our results suggested that Nb-doping was the better route to forming more active UVA photocatalysts, practical TCOs and photo-induced wettable surfaces. In addition, from studying these metal doped systems, an importance for growth in the (211) plane for increased photo-induced surface wetting was revealed. Given the primary crystal plane for photo-induced wetting process in anatase TiO_2 is yet to be identified in the literature, these unique findings highlighted the importance of the (211) plane.

Within the field of thin-film combinatorial optimisation, PVD techniques have been applied in predominance over CVD or wet-chemical methods. Although thin-film combinatorial PVD methods have the advantage of tailoring compositional gradients with high precision, these materials inherently suffer from epitaxial stresses and strains due to lattice mismatch with the underlying substrate. However, films formed from CVD suffer less from these effects as the process relies upon the chemical reaction of precursors. CVD can also produce films with excellent conformal coverage on non-flat substrates; where PVD methods typically fail. There are also a multitude of CVD variants each with specific benefits. For instance, aerosol-assisted CVD (AACVD) can introduce heavy precursors or even nanoparticles within depositions and could provide an avenue for the combinatorial investigation to the intrinsic effect of nanoparticle concentration, size distribution *etc*

within a host medium. Also, equipment start-up costs are typically far cheaper for CVD apparatus over PVD. Indeed, the combinatorial CVD method is yet to be explored in as much depth as PVD methods and is certainly an open canvas. The difficulty of CVD is getting precise compositional gradients, something to which PVD excels.

Most research groups have used the thin-film combinatorial approach to investigate phase-space already covered by individual synthetic operations. Although the combinatorial approach can refine compositions for an optimised functional performance it has the unique power of being able to rapidly unravel previously unexplored phase-space. As shown by Van Dover *et. al.* in their discovery and optimisation of $Zr_{0.2}Sn_{0.2}Ti_{0.6}O_2$ di-electric thin-films for DRAM applications, the combinatorial exploration and optimisation approach should be more frequently unified in discovering new promising materials and maximising their functional benefit.

5.1. Future work

We feel that we are yet to scratch the surface of the potential applications of the combinatorial APCVD approach, let alone the multitude of CVD variants, where combinatorial AACVD has just recently been used to investigate the resistance of a range of gallium-indium-oxide thin-films.[305] Although being a relatively new technique, combinatorial APCVD has already led to the discovery of a new material, pseudo-brookite $Ti_{3-\delta}O_4N$ ($0.06 < \delta < 0.25$).[112] We feel that continued application of this method could certainly lead to further materials discoveries, especially if new combinations of precursors are applied. However, in terms of our research, we would like to try and use combinatorial APCVD for discovering new photocatalytic materials. From looking at the literature, there are an array of non-titania based photocatalysts including titanates, nickel oxides, zinc oxides *etc* that have been suggested to be highly active, especially for visible light functions. Rather than trying new combinations of elements, we would also like to apply combinatorial APCVD in studying the underlying physical factors that contribute towards photocatalysis in greater depth. For instance, we recently observed that the photocatalytic activity for an un-doped anatase TiO_2 thin-film system with graded thickness plateaued above ≈ 200 nm in thickness. The result surprised us as the thicker sections of the film were absorbing a greater fraction of photons from the UVA light source. This hinted that the average distance in which the photo-excited electrons and holes could travel before recombination occurred was ≈ 200 nm. This was further supported by a recent investigation of Pt-TiO_2 photo-diodes that were observed to be most effective when the TiO_2 layer was ≈ 200 nm thick.[280] The phenomenon was attributed to the distance in which the photo-generated electrons

could travel through the material, where 200 nm was the optimum balance between how far the electrons could travel to the Pt layer and the level of UVA light absorbed. Using combinatorial APCVD we would like to assess the validity of this phenomenon by simultaneously testing a range of anatase TiO_2 materials with varying thickness and crystallinity with a range of light sources. We would also like to use the combinatorial APCVD approach to better answer the question of anatase TiO_2: rutile TiO_2 composite synergy by investigating the full range of states. Moreover, we would also like to further develop our photocatalytic activity mapping method. The intelligent inks that we currently use in this method function by scavenging the photo-generated holes at the surface of the material, as the hole scavenger (glycerol) is in excess. The electrons which remain then reduce the redox dyes that are present in low concentration in the dye. It would be interesting if the mode of operation of the intelligent ink was reversed, where an indicator that changes colour upon reaction with photo-generated holes is used in conjunction with a photo-generated electron scavenger instead. This might reveal differences in the reactivity of photo-generated electrons and holes at the material surface, as indicated by their reactivity lifetimes.[2]

Acknowledgements

I would first like to thank my supervisor Professor Ivan Parkin for giving me this opportunity and providing his guidance and knowledge in abundance. I couldn't have asked for a more helpful or supportive supervisor. I would next like to thank my wife, Madeeha Uppal, for her love and patience. I would also like to thank all of my colleagues for their friendship and advice. I would like the thank Professor Andrew Mills for our occasional chats and Dr Geoff Hyett for taking me under his wing when I first started. Lastly I would personally like to thank Mr Kevin Reeves for his technical support which went above and beyond the call of duty on many occasions.

References

(1) Mills, A.; Hunte, S. Le *Journal of Photochemistry and Photobiology A: Chemistry* **1997**, *108*, 1.

(2) Fujishima, A. Zhang, X.; Tryk, D. *Surface Science Reports* **2008**, *63*, 515.

(3) Selli, E. Chiarello, G. L. Quartarone, E. Mustarelli, P. Rossetti, I.; Forni, L. *Chemical Communications* **2007**, *1*, 5022.

(4) Mills, A.; Valenzuela, M. *Journal of Photochemistry and Photobiology A: Chemistry* **2004**, *165*, 25.

(5) Osterloh, F. E. *Chemistry of Materials* **2008**, *20*, 35.

(6) Savage, N. *Sensors and Actuators B: Chemical* **2001**, *79*, 17.

(7) Bach, U. Lupo, D. Comte, P. Moser, J. E. Weissortel, F. Salbeck, J. Spreitzer, H.; Gratzel, M. *Nature* **1998**, *395*, 583.

(8) Huang, S. Y. Schlichthörl, G. Nozik, A. J. Grätzel, M.; Frank, A. J. *The Journal of Physical Chemistry B* **1997**, *101*, 2576.

(9) Hashimoto, K. Irie, H.; Fujishima, A. *Japanese Journal of Applied Physics* **2005**, *44*, 8269.

(10) Zhang, H. Chen, G.; Bahnemann, D. W. *Journal of Materials Chemistry* **2009**, *19*, 5089.

(11) Page, K. Palgrave, R. G. Parkin, I. P. Wilson, M. Savin, S. L. P.; Chadwick, A. V. *Journal of Materials Chemistry* **2007**, *17*, 95.

(12) Hajkova, P. Spatenka, P. Horsky, J. Horska, I.; Kolouch, A. *Plasma Processes and Polymers* **2007**, *4*, S397.

(13) Kubota, Y. Shuin, T. Kawasaki, C. Hosaka, M. Kitamura, H. Cai, R. Sakai, H. Hashimoto, K.; Fujishima, A. *British Journal of Cancer* **1994**, *70*, 1107.

(14) Fujishima, A. Rao, T. N.; Tryk, D. *Journal of Photochemistry and Photobiology C: Photochemistry Reviews* **2000**, *1*, 1.

(15) Goodeve, C. F.; Kitchener, J. A. *Transactions of the Faraday Society* **1938**, *34*, 570.

(16) Arntz, F. O. Myamlin, V. A.; Pleskov, Y. V. *Science* **1968**, *160*, 984.

(17) Wang, R. Sakai, N. Fujishima, A. Watanabe, T.; Hashimoto, K. *The Journal of Physical Chemistry B* **1999**, *103*, 2188.

(18) Mills, A. Elliott, N. Parkin, I. P. O'Neill, S. A.; Clark, R. J. H. *Journal of Photochemistry and Photobiology A: Chemistry* **2002**, *151*, 171.

(19) Lee, J.; Choi, W. *Environmental Science & Technology* **2004**, *38*, 4026.

(20) Dunnill, C. W. Page, K. Aiken, Z. A. Noimark, S. Hyett, G. Kafizas, A. Pratten, J. Wilson, M.; Parkin, I. P. *Journal of Photochemistry and Photobiology A: Chemistry* **2011**, *220*, 113.

(21) Li, X. Z.; Li, F. B. *Environmental Science & Technology* **2001**, *35*, 2381.

(22) Kafizas, A. Kellici, S. Darr, J. A.; Parkin, I. P. *Journal of Photochemistry and Photobiology A: Chemistry* **2009**, *204*, 183.

(23) Rampaul, A. Parkin, I. P. O'Neill, S. A. Desouza, J. Mills, A.; Elliott, N. *Polyhedron* **2003**, *22*, 35.

(24) Wang, J.-Y. Liu, Z.-H. Zheng, Q. He, Z.-K.; Cai, R.-X. *Nanotechnology* **2006**, *17*, 4561.

(25) Wu, L. Yu, J. C.; Fu, X. *Journal of Molecular Catalysis A: Chemical* **2006**, *244*, 25.

(26) Rajh, T. Nedeljkovic, J. M. Chen, L. X. Poluektov, O.; Thurnauer, M. C. *The Journal of Physical Chemistry B* **1999**, *103*, 3515.

(27) Zhao, D. Chen, C. Wang, Y. Ji, H. Ma, W. Zang, L.; Zhao, J. *Journal of Physical Chemistry C* **2008**, *112*, 5993.

(28) Makarova, O. V. Rajh, T. Thurnauer, M. C. Martin, A. Kemme, P. A.; Cropek, D. *Environmental Science & Technology* **2000**, *34*, 4797.

(29) Dunnill, C. W. Aiken, Z. A. Kafizas, A. Pratten, J. Wilson, M. Morgan, D. J.; Parkin, I. P. *Journal of Materials Chemistry* **2009**, *19*, 8747.

(30) Dunnill, C. W. Aiken, Z. A. Pratten, J. Wilson, M. Morgan, D. J.; Parkin, I. P. *Journal of Photochemistry and Photobiology A: Chemistry* **2009**, *207*, 244.

(31) Klosek, S.; Raftery, D. *The Journal of Physical Chemistry B* **2001**, *105*, 2815.

(32) Yoong, L. S. Chong, F. K.; Dutta, B. K. *Energy* **2009**, *34*, 1652.

(33) Osterwalder, J. Droubay, T. Kaspar, T. Williams, J. Chambers, S. A.; Wang, C. M. *Thin Solid Films* **2005**, *484*, 289.

(34) Gracia, F. Holgado, J. P. Caballero, A.; Gonzalez-Elipe, A. R. *The Journal of Physical Chemistry B* **2004**, *108*, 17466.

(35) Egerton, T. A. Harris, E. Lawson, E. J. Mile, B.; Rowlands, C. C. *Physical Chemistry Chemical Physics* **2001**, *3*, 497.

(36) Dvoranova, D. Brezova, V. Mazur, M.; Malati, M. A. *Applied Catalysis B: Environmental* **2002**, *37*, 91.

(37) Jing, D. Zhang, Y.; Guo, J. *Chemical Physical Letters* **2005**, *415*, 74.

(38) Yang, Y. Li, X. Chen, J.; Wang, L. *Journal of Photochemistry and Photobiology A: Chemistry2* **2004**, *163*, 517.

(39) Lin, L. Lin, W. Zhu, Y. Zhao, B.; Xie, Y. *Chemical Letters* **2005**, *34*, 284.

(40) Yu, J. C. *Chemistry of Materials* **2002**, *14*, 3808.

(41) Zhao, W. Ma, W. Chen, C. Zhao, J.; Shuai, Z. *Journal of the American Chemical Society* **2004**, *126*, 4782.

(42) Neumann, B. Bogdanoff, P. Tributsch, H. Sakthivel, S.; Kisch, H. *The Journal of Physical Chemistry B* **2005**, *109*, 16579.

(43) Jurgen, D. *Science* **2000**, *287*, 1960.

(44) Zhao, J. *Progress in Materials Science* **2006**, *51*, 557.

(45) Xiang, X.-D. *Annual Review of Materials Science* **1999**, *29*, 149.

(46) Woo, S. I. Kim, K. W. Cho, H. Y. Oh, K. S. Jeon, M. K. Tarte, N. H. Kim, T. S.; Mahmood, A. *QSAR & Combinatorial Science* **2005**, *24*, 138.

(47) Barber, Z. H.; Blamire, M. G. *Materials Science and Technology* **2008**, *24*, 757.

(48) Boettcher, A. Haase, G.; Thun, R. *Zeitschrift fur Metallkunde* **1955**, *46*, 386.

(49) Hanak, J. J. *Journal of Materials Science* **1970**, *5*, 964.

(50) Hanak, J. J. *Journal of Applied Physics* **1972**, *43*, 1666.

(51) Briceno, G. Chang, H. Sun, X. Schultz, P. G.; Xiang, X.-D. *Science* **1995**, *270*, 273.

(52) Xiang, X.-D. Sun, X. Briceño, G. Lou, Y. Wang, K. Chang, H. Wallace-Freedman, W. G. Chen, S. W.; Schultz, P. G. *Science* **1995**, *268*, 1738.

(53) Danielson, E. Golden, J. H. Mcfarland, E. W. Reaves, C. M. Weinberg, W. H.; Wu, X. D. *Nature* **1997**, *389*, 2331.

(54) Dover, R. B. Van; Schneemeyer, L. F. Fleming, R. M.; Huggins, H. A. *Biotechnology and Bioengineering* **1999**, *61*, 217.

(55) Matsumoto, Y. Murakami, M. Hasegawa, T. Fukumura, T. Kawasaki, M. Ahmet, P. Chikyow, T. Nakajima, K.; Koinuma, H. *Applied Surface Science* **2002**, *189*, 344.

(56) Matsumoto, Y. Murakami, M. Shono, T. Hasegawa, T. Fukumura, T. Kawasaki, M. Ahmet, P. Chikyow, T. Koshihara, S.; Koinuma, H. *Science* **2001**, *291*, 854.

(57) Smith, R. C. Hoilien, N. Roberts, J. T. Campbell, S. A.; Gladfelter, W. L. *Chemistry of Materials* **2002**, *14*, 474.

(58) Xia, B. Chen, F. Campbell, S. A. Roberts, J. T.; Gladfelter, W. L. *Chemical Vapor Deposition* **2004**, *10*, 195.

(59) Zhong, L. Zhang, Z. Campbell, S. A.; Gladfelter, W. L. *Journal of Materials Chemistry* **2004**, *14*, 3203.

(60) Kim, K. W. Jeon, M. K. Oh, K. S. Kim, T. S. Kim, Y. S.; Woo, S. I. *Proceedings of the National Academy of Sciences of the United States of America* **2007**, *104*, 1134.

(61) Kim, K. W. Kim, T. S. Jeon, M. K. Oh, K. S. Jung, C. H.; Woo, S. I. *Applied Physics Letters* **2008**, *92*, 052911.

(62) Olk, C. H. *Measurement Science and Technology* **2005**, *16*, 14.

(63) Olk, C. H. Tibbetts, G. G. Simon, D.; Moleski, J. J. *Journal of Applied Physics* **2003**, *94*, 720.

(64) Dam, B. Gremaud, R. Broedersz, C.; Griessen, R. *Scripta Materialia* **2007**, *56*, 853.

(65) Gremaud, R. Broedersz, C. P. Borsa, D. M. Borgschulte, A. Mauron, P. Schreuders, H. Rector, J. H. Dam, B.; Griessen, R. *Advanced Materials* **2007**, *19*, 2813.

(66) Cooper, J.; Mcginn, P. *Journal of Power Sources* **2006**, *163*, 330.

(67) Strasser, P. Fan, Q. Devenney, M. Weinberg, W. H. Liu, P.; Nørskov, J. K. *The Journal of Physical Chemistry B* **2003**, *107*, 11013.

(68) Lu, G. Cooper, J. S.; McGinn, P. J. *Journal of Power Sources* **2006**, *161*, 106.

(69) Whitacre, J. F. *Electrochimica Acta* **2008**, *53*, 3680.

(70) Cooper, J.; Mcginn, P. *Applied Surface Science* **2007**, *254*, 662.

(71) Easton, E. B. Bonakdarpour, A. Yang, R. Stevens, D. A.; Dahn, J. R. *Journal of The Electrochemical Society* **2008**, *155*, B547.

(72) Garsuch, A. Yang, R. Bonakdarpour, A.; Dahn, J. R. *Electrochimica Acta* **2008**, *53*, 2423.

(73) Borgia, C. Scharowsky, T. Furrer, A. Solenthaler, C.; Spolenak, R. *Acta Materialia* **2011**, *59*, 386.

(74) Diechle, D. Stuber, M. Leiste, H. Ulrich, S.; Schier, V. *Surface and Coatings Technology* **2010**, *204*, 3258.

(75) Stuber, M. Albers, U. Leiste, H. Seemann, K. Ziebert, C.; Ulrich, S. *Surface and Coatings Technology* **2008**, *203*, 661.

(76) Rar, A. Frafjord, J. J. Fowlkes, J. D. Specht, E. D. Rack, P. D. Santella, M. L. Bei, H. George, E. P.; Pharr, G. M. *Measurement Science and Technology* **2005**, *16*, 46.

(77) Fleischauer, M. D. Hatchard, T. D. Bonakdarpour, A.; Dahn, J. R. *Measurement Science and Technology* **2005**, *16*, 212.

(78) Dahn, J. R. Mar, R. E.; Abouzeid, A. *Journal of The Electrochemical Society* **2006**, *153*, A361.

(79) Todd, A. D. W. Mar, R. E.; Dahn, J. R. *Journal of The Electrochemical Society* **2006**, *153*, A1998.

(80) Sano, H. Matsumoto, T. Matsumoto, Y.; Koinuma, H. *Applied Surface Science* **2006**, *252*, 2493.

(81) Danielson, E. Devenney, M. Giaquinta, D. M. Golden, J. H. Haushalter, R. C. McFarland, E. W. Poojary, D. M. Reaves, C. M. Weinberg, W. H.; Wu, X. D. *Science* **1998**, *279*, 837.

(82) Wang, Q. Moutinho, H. To, B. Perkins, J. Ginley, D. S. Branz, H. M.; Han, D. *National Renewable Energy Laboratory* **2003**, 1.

(83) Wang, Q. *Thin Solid Films* **2003**, *430*, 78.

(84) Hänsel, H. Zettl, H. Krausch, G. Schmitz, C. Kisselev, R. Thelakkat, M.; Schmidt, H. *Applied Physics Letters* **2002**, *81*, 2106.

(85) Wang, Q. Liu, F.; Han, D. *Macromolecular Rapid Communications* **2004**, *25*, 326.

(86) Joshi, U. S.; Koinuma, H. *Indian Journal of Pure & Applied Physics* **2007**, *45*, 62.

(87) Akazawa, H. *Journal of Vacuum Science & Technology A: Vacuum, Surfaces and Films* **2010**, *28*, 314.

(88) Perkins, J. Cueto, J. A. del; Alleman, J. L. Warmsingh, C. Keyesa, B. M. Gedvilasa, L. M. Parilla, P. A. To, B. Readey, D. W.; Ginley, D. S. *Thin Solid Films* **2002**, *411*, 152.

(89) Kukuruznyak, D. Ahmet, P. Chikyow, T. Yamamoto, A.; Ohuchi, F. *Applied Surface Science* **2006**, *252*, 3828.

(90) Martel, A. Caballero-Briones, F. Castro-Rodríguez, R. Méndez-Gamboa, J. Romeo, N. Bosio, A.; Peña, J. L. *Thin Solid Films* **2009**, *518*, 413.

(91) Wakisaka, T. Koida, T. Matsumoto, Y. Itaka, K.; Koinuma, H. *Applied Surface Science* **2004**, *223*, 264.

(92) Lobel, R. Thienhaus, S. Savan, A.; Ludwig, A. *Materials Science and Engineering: A* **2008**, *481-482*, 151.

(93) Cui, J. Chu, Y. S. Famodu, O. O. Furuya, Y. Hattrick-Simpers, J. James, R. D. Ludwig, A. Thienhaus, S. Wuttig, M. Zhang, Z.; Takeuchi, I. *Nature materials* **2006**, *5*, 286.

(94) Zarnetta, R. Savan, A. Thienhaus, S.; Ludwig, A. *Applied Surface Science* **2007**, *254*, 743.

(95) Borgia, C. Olliges, S. Dietiker, M. Pigozzi, G.; Spolenak, R. *Thin Solid Films* **2010**, *518*, 1897.

(96) Wang, Q. Itaka, K. Minami, H. Kawaji, H.; Koinuma, H. *Science and Technology of Advanced Materials* **2004**, *5*, 543.

(97) Watanabe, M. Kita, T. Fukumura, T. Ohtomo, A. Ueno, K.; Kawasaki, M. *Applied Surface Science* **2007**, *254*, 777.

(98) Yamada, Y. Ohtomo, A.; Kawasaki, M. *Applied Surface Science* **2007**, *254*, 768.

(99) Minami, H. Itaka, K. Kawaji, H. Wang, Q. Koinuma, H.; Lippmaa, M. *Applied Surface Science* **2002**, *197-198*, 442.

(100) Gregory, O. J.; Amani, M. *Journal of The Electrochemical Society* **2011**, *158*, J15.

(101) Marin, V. Holder, E. Wienk, M. M. Tekin, E. Kozodaev, D.; Schubert, U. S. *Macromolecular Rapid Communications* **2005**, *26*, 319.

(102) Okamura, S. Takeuchi, R.; Shiosaki, T. *Japanese Journal of Applied Physics* **2002**, *41*, 6714.

(103) Jas, G.; Kirschning, A. *Chemistry- A European Journal* **2003**, *9*, 5708.

(104) Walter, H. Basset, G. Beierlein, T. Muhlenen, A. Von; Nisato, G. *Journal of Polymer Science Part B: Polymer Physics* **2010**, *48*, 1587.

(105) Simon, C. G. Eidelman, N. Kennedy, S. B. Sehgal, A. Khatri, C. A.; Washburn, N. R. *Biomaterials* **2005**, *26*, 6906.

(106) Hatchard, T. D.; Dahn, J. R. *Journal of The Electrochemical Society* **2004**, *151*, A1628.

(107) Pilkington Activ. *http://www.pilkington.com/resources/datasheet4coatingtechnologyproducts.pdf*.

(108) Choy, K. *Progress in Materials Science* **2003**, *48*, 57.

(109) Kuykendall, T. Ulrich, P. Aloni, S.; Yang, P. *Nature Materials* **2007**, *6*, 951.

(110) Hyett, G. Green, M.; Parkin, I. P. *Journal of the American Chemical Society* **2006**, *128*, 12147.

(111) Hyett, G. Green, M.; Parkin, I. P. *Chemical Vapor Deposition* **2008**, *14*, 309.

(112) Hyett, G. Green, M.; Parkin, I. P. *Journal of the American Chemical Society* **2007**, *129*, 15541.

(113) Livraghi, S. Chierotti, M. R. Giamello, E. Magnacca, G. Paganini, M. C. Cappelletti, G.; Bianchi, C. L. *Journal of Physical Chemistry C* **2008**, *112*, 17244.

(114) Livraghi, S. Elghniji, K. Czoska, A. M. Paganini, M. C. Giamello, E.; Ksibi, M. *Journal of Photochemistry and Photobiology A: Chemistry* **2009**, *205*, 93.

(115) Mahalingam, S.; Edirisinghe, M. J. *Journal of Physics D: Applied Physics* **2008**, *41*, 215406.

(116) Pomoni, K. Vomvas, A.; Trapalis, C. *Journal of Non-Crystalline Solids* **2008**, *354*, 4448.

(117) Irie, H. Watanabe, Y.; Hashimoto, K. *The Journal of Physical Chemistry B* **2003**, *107*, 5483.

(118) Asahi, R. Morikawa, T. Ohwaki, T. Aoki, K.; Taga, Y. *Science* **2001**, *293*, 269.

(119) Cuevas, F. *Journal of Alloys and Compounds* **1997**, *253-254*, 158.

(120) Wang, J. Yoo, Y. Gao, C. Takeuchi, I. Sun, X. Chang, H. Xiang, X.-D.; Schultz, P. G. *Science* **1998**, *279*, 1712.

(121) Rende, D. Maier, W. F. Schwarz, K.; Rabe, U. *Advances in Mass Data Analysis of Signals and Images in Medicine, Biotechnology and Chemistry* **2007**, *4826*, 80.

(122) Swanepoel, R. J. *Journal of Physics E: Scientific Instruments* **1983**, *16*, 1214.

(123) Xia, B. Chu, Y. S.; Gladfelter, W. L. *Surface and Coatings Technology* **2007**, *201*, 9041.

(124) Rietveld, H. M. *Journal of Applied Crystallography* **1969**, *2*, 65.

(125) Dollase, W. A. *Journal of Applied Crystallography* **1986**, *19*, 267.

(126) Rigby, S. Alobaidi, A. Lee, S. Mcstay, D.; Robertson, P. *Applied Surface Science* **2006**, *252*, 7948.

(127) Hibben, J. H. *Industrial and Engineering Chemistry* **1939**, *17*, 556.

(128) Capwell, R. J. Spagnolo, F.; DeSesa, M. A. *Applied Spectroscopy* **1972**, *26*, 537.

(129) Ushanov, V. Z. Kolodina, I. S. Sembaev, D. K.; Agashkin, O. V. *Journal of Analytical Chemistry* **1992**, *47*, 553.

(130) Murad, E. *American Mineralogist* **1997**, *82*, 203.

(131) Casa Software Ltd. *http://www.casaxps.com/*.

(132) Patterson, A. *Physical Review* **1939**, *56*, 978.

(133) Sayers, D. Stern, E.; Lytle, F. *Physical Review Letters* **1971**, *27*, 1204.

(134) Hyett, G.; Parkin, I. P. *Surface and Coatings Technology* **2007**, *201*, 8966.

(135) Mendive, C. B. Bredow, T. Blesa, M. A.; Bahnemann, D. W. *Physical Chemistry Chemical Physics* **2006**, *8*, 3232.

(136) Wang, Y. Deng, K.; Zhang, L. *The Journal of Physical Chemistry C* **2011**, *115*, 14300.

(137) Wang, H. Wang, T.; Xu, P. *Journal of Materials Science: Materials in Electronics* **1998**, *9*, 327.

(138) Kim, B. Byun, D. Lee, J. K.; Park, D. *Japanese Journal of Applied Physics* **2002**, *41*, 222.

(139) Jang, E. S. Won, J. H. Hwang, S. J.; Choy, J. H. *Advanced Materials* **2006**, *18*, 3309.

(140) Nolan, M. G. Hamilton, J. A. O'Brien, S. Bruno, G. Pereira, L. Fortunato, E. Martins, R. Pemble, M. E.; Poveya, I. M. *Journal of Photochemistry and Photobiology A: Chemistry* **2011**, *219*, 10.

(141) Chen, D. *Recent Patents on Nanotechnology* **2008**, *2*, 183.

(142) Richtera, C. Pluijma, B. A. van der; Housen, B. A. *Journal of Structural Geology* **1993**, *15*, 113.

(143) Aerden, D. *Journal of Structural Geology* **2003**, *25*, 923.

(144) Roe, R. J. *Journal of Applied Physics* **1965**, *36*, 2024.

(145) Bragg, W. H. *Proceedings of the Royal Society of London- Series A* **1913**, *89*, 248.

(146) Burdett, J. K. Hughbanks, T. Miller, G. J. Richardson, J. W.; Smith, J. V. *Journal of the American Chemical Society* **1987**, *109*, 3639.

(147) Chen, T. L. Furubayashi, Y. Hirose, Y. Hitosugi, T. Shimada, T.; Hasegawa, T. *Journal of Physics D: Applied Physics* **2007**, *40*, 5961.

(148) Liu, G. Wolfman, J. Autret-Lambert, C. Sakai, J. Roger, S. Gervais, M.; Gervais, F. *Journal of Applied Physics* **2010**, *108*, 114108.

(149) Chen, D. Xu, G. Miao, L. Chen, L. Nakao, S.; Jin, P. *Journal of Applied Physics* **2010**, *107*, 063707.

(150) Neumann, B. Bierau, F. Johnson, B. Kaufmann, C. A. Ellmer, K.; Tributsch, H. *Physica Status Solidi (B)* **2008**, *245*, 1849.

(151) Stout, K. J.; Blunt, L. *Three-dimensional surface topography (2nd edition)*; Elsevier, 2000.

(152) Kafizas, A. Hyett, G.; Parkin, I. P. *Journal of Materials Chemistry* **2009**, *19*, 1399.

(153) Perkins, J. *Applied Surface Science* **2004**, *223*, 124.

(154) Okato, T. Sakano, T.; Obara, M. *Physical Review B* **2005**, *72*, 115124.

(155) Bao, N. N. Fan, H. M. Ding, J.; Yi, J. B. *Journal of Applied Physics* **2011**, *109*, 07C302.

(156) Livraghi, S. Elghniji, K. Czoska, A. M. Paganini, M. C. Giamello, E.; Ksibi, M. *Journal of Photochemistry and Photobiology A: Chemistry* **2009**, *205*, 93.

(157) Briggs, D.; Seah, M. P. *Practical Surface Analysis by Auger and X-ray Photoelectron Spectroscopy (2nd edition)*; John Wiley and Sons, 1992.

(158) Climent-Font, A. Cervera, M. Hernandez, M. J. Munoz-Martin, A.; Piqueras, J. *Nuclear Instruments and Methods in Physics Research Section B: Beam Interactions with Materials and Atoms* **2008**, *266*, 1498.

(159) Photon energies and relative intensities of K-, L-, and M-shell lines - Center for X-ray Optics and Advanced Light Source **2008**.

(160) Leite, B. Camus, P.; Rohde, D. Peak Deconvolution of Ti-L and O-K in the Presence of Iron Oxide - Thermo Fisher Scientific **2009**.

(161) Mills, A.; Mcfarlane, M. *Catalysis Today* **2007**, *129*, 22.

(162) Mills, A.; Wang, J. *Journal of Photochemistry and Photobiology A: Chemistry* **2006**, *182*, 181.

(163) Remillard, J. T. McBride, J. R. Nietering, K. E. Drews, A. R.; Zhang, X. *The Journal of Physical Chemistry B* **2000**, *104*, 4440.

(164) Mills, A. Lepre, A. Elliott, N. Bhopal, S. Parkin, I. P.; O'Neill, S. A. *Journal of Photochemistry and Photobiology A: Chemistry* **2003**, *160*, 213.

(165) Mills, A. Elliott, N. Parkin, I. P. O'Neill, S. A.; Clark, R. J. H. *Journal of Photochemistry and Photobiology A: Chemistry* **2002**, *151*, 171.

(166) Jung, S.-C. Kim, B.-H. Kim, S.-J. Imaishi, N.; Cho, Y.-I. *Chemical Vapor Deposition* **2005**, *11*, 137.

(167) Tayade, R. J. Surolia, P. K. Kulkarni, R. G.; Jasra, R. V. *Science and Technology of Advanced Materials* **2007**, *8*, 455.

(168) Fabiyi, M. E.; Skelton, R. L. *Journal of Photochemistry and Photobiology A: Chemistry* **2000**, *132*, 121.

(169) Houas, A. Lachheb, H. Ksibi, M. Elaloui, E. Guillard, C.; Herrmann, J. *Applied Catalysis B: Environmental* **2001**, *31*, 145.

(170) Lewis, G. N. Goldschmid, O. Magel, T. T.; Bigeleisen, J. *Journal of the American Chemical Society* **1943**, *65*, 1150.

(171) Doushita, K.; Kawahara, T. *Journal of Sol-Gel Science and Technology* **2001**, *22*, 91.

(172) Mills, A. Wang, J. Lee, S.-K.; Simonsen, M. *Chemical Communications* **2005**, *21*, 2721.

(173) Mills, A.; McGrady, M. *Journal of Photochemistry and Photobiology A: Chemistry* **2008**, *193*, 228.

(174) Mills, A. McGrady, M. Wang, J.; Hepburn, J. *International Journal of Photoenergy* **2008**, *2008*, 1-6.

(175) Mills, A. Wang, J.; McGrady, M. *The Journal of Physical Chemistry B* **2006**, *110*, 18324.

(176) Microsoft Visual Basic 6.0. *http://www.microsoft.com/download/en/details.aspx?id=20429* **2001**.

(177) OriginLab Origin 8.0. *http://www.originlab.com/* **2009**.

(178) Dai, Q. X. Xiao, H. Y. Li, W. S. Na, Y. Q.; Zhou, X. P. *Journal of Combinatorial Chemistry* **2005**, *7*, 539.

(179) Xiao, H. A. Dai, Q. X. Li, W. S. Na, Y. Q.; Zhou, X. P. *Applied Catalysis A: General* **2005**, *290*, 25.

(180) Xiao, H. A. Dai, Q. X. Li, W. S. Au, C. T.; Zhou, X. P. *Journal of Molecular Catalysis A: Chemical* **2006**, *245*, 17.

(181) Ohsawa, T. Nakajima, K. Matsumoto, Y.; Koinuma, H. *Applied Surface Science* **2006**, *252*, 2603.

(182) Sun, S. Ding, J. Bao, J. Luo, Z.; Gao, C. *Combinatorial Chemistry and High Throughput Screening* **2011**, *14*, 160.

(183) Parkin, I. P.; Palgrave, R. G. *Journal of Materials Chemistry* **2005**, *15*, 1689.

(184) O'Neill, S. A. Parkin, I. P. Clark, R. J. H. Mills, A.; Elliott, N. *Journal of Materials Chemistry* **2003**, *13*, 56.

(185) Kim, S.; Ehrman, S. H. *Journal of Colloid and Interface Science* **2009**, *338*, 304.

(186) Ohno, T. Sarukawa, K. Tokieda, K.; Matsumura, M. *Journal of Catalysis* **2001**, *203*, 82.

(187) Ray, K. J. A.; Viswanathan, B. *Indian Journal of Chemistry* **2009**, *48A*, 1378.

(188) Bird, R. E. Hulstrom, R. L.; Lewis, L. J. *Solar Energy* **1983**, *30*, 563.

(189) Lopez-Luke, T. Wolcott, A. Xu, L.-P. Chen, S. Wen, Z. Li, J. La Rosa, E. De; Zhang, J. Z. *Journal of Physical Chemistry C* **2008**, *112*, 1282.

(190) Wong, M.-S. Hsu, S.-W. Rao, K. K.; Kumar, C. P. *Journal of Molecular Catalysis A: Chemical* **2008**, *279*, 20.

(191) Sonawane, R. S.; Dongare, M. K. *Journal of Molecular Catalysis A: Chemical* **2006**, *243*, 68.

(192) Celik, E. Gokcen, Z. Azem, N. F. A. Tanoglu, M.; Emrullahoglu, O. F. *Materials Science and Engineering: B* **2006**, *132*, 258.

(193) Sharma, S. D. Singh, D. Saini, K. K. Sharma, V. Jain, S. C.; Sharma, C. P. *Applied Catalysis* **2006**, *314*, 40.

(194) Zhao, L. Jiang, Q.; Lian, J. *Applied Surface Science* **2008**, *254*, 4620.

(195) Tauc, J. *Materials Research Bulletin* **1968**, *3*, 37.

(196) Hyett, G. Green, M. A.; Parkin, I. P. *Journal of Photochemistry and Photobiology A: Chemistry* **2009**, *203*, 199.

(197) Mo, S.-D.; Ching, W. *Physical Review B* **1995**, *51*, 13023.

(198) Mi, L. Xu, P. Shen, H.; Wang, P.-N. *Journal of Photochemistry and Photobiology A: Chemistry* **2008**, *193*, 222.

(199) Bohman, O. Ahlberg, P. Nyholm, R. Martensson, N. Siegbahn, K.; Lehn, J. M. *Chemica Scripta* **1981**, *18*, 44.

(200) Betsch, R. J. *Journal of Crystal Growth* **1986**, *77*, 210.

(201) Ralph, J.; Chau, I. The Mineral Database. *The Mineral Database* **2011**.

(202) Evans, P. Pemble, M. E.; Sheel, D. W. *Chemistry of Materials* **2006**, *18*, 5750.

(203) Torres, G. R. Lindgren, T. Lu, J. Granqvist, C.-G.; Lindquist, S.-E. *The Journal of Physical Chemistry B* **2004**, *108*, 5995.

(204) Nambu, A. Graciani, J. Rodriguez, J. A. Wu, Q. Fujita, E.; Sanz, J. F. *The Journal of Chemical Physics* **2006**, *125*, 094706.

(205) Beranek, R.; Kisch, H. *Electrochemistry Communications* **2007**, *9*, 761.

(206) Valentin, C. Di; Finazzi, E. Pacchioni, G. Selloni, A. Livraghi, S. Paganini, M. C.; Giamello, E. *Chemical Physics* **2007**, *339*, 44.

(207) Sato, S. *Chemical Physics Letters* **1986**, *123*, 126.

(208) Prabakar, K. Takahashi, T. Nezuka, T. Takahashi, K. Nakashima, T. Kubota, Y.; Fujishima, A. *Renewable Energy* **2008**, *33*, 277.

(209) Dunnill, C. W.; Parkin, I. P. *Chemical Vapor Deposition* **2009**, *15*, 171-174.

(210) Sakthivel, S.; Kisch, H. *ChemPhysChem* **2003**, *4*, 487.

(211) Sakthivel, S. Janczarek, M.; Kisch, H. *The Journal of Physical Chemistry B* **2004**, *108*, 19384.

(212) Baur, W. H.; Khan, A. A. *Acta Crystallographica Section B* **1971**, *B27*, 2133.

(213) Badrinarayanan, S. Sinha, S.; Mandale, A. B. *Journal of Electron Spectroscopy and Related Phenomena* **1989**, *49*, 303.

(214) Kafizas, A. Dunnill, C. W.; Parkin, I. P. *Journal of Materials Chemistry* **2010**, *20*, 8336.

(215) Diwald, O. Thompson, T. L. Goralski, E. G. Walck, S. D.; Yates, J. T. *The Journal of Physical Chemistry B* **2004**, *108*, 52.

(216) Miyauchi, M. Ikezawa, A. Tobimatsu, H. Irie, H.; Hashimoto, K. *Physical Chemistry Chemical Physics* **2004**, *6*, 865.

(217) Nakamura, R. Tanaka, T.; Nakato, Y. *The Journal of Physical Chemistry B* **2004**, *108*, 10617.

(218) Dunnill, C. W. Ansari, Z. Kafizas, A. Perni, S. Morgan, D. J. Wilson, M.; Parkin, I. P. *Journal of Materials Chemistry* **2011**, 11854-11861.

(219) Pradhan, S. K.; Reucroft, P. J. *Journal of Crystal Growth* **2003**, *250*, 588.

(220) Duminica, F.-D. Maurya, F.; Hausbrand, R. *Surface and Coatings Technology* **2007**, *201*, 9349.

(221) Yates, H. M. Nolan, M. G. Sheel, D. W.; Pemble, M. E. *Journal of Photochemistry and Photobiology A: Chemistry* **2006**, *179*, 213.

(222) Valentin, C. Di; Pacchioni, G. Selloni, A. Livraghi, S.; Giamello, E. *The Journal of Physical Chemistry B* **2005**, *109*, 11414.

(223) Diwald, O. Thompson, T. L. Zubkov, T. Walck, S. D.; Yates, J. T. *The Journal of Physical Chemistry B* **2004**, *108*, 6004.

(224) Mrowetz, M. Balcerski, W. Colussi, A. J.; Hoffmann, M. R. *The Journal of Physical Chemistry B* **2004**, *108*, 17269.

(225) Lin, Z. Orlov, A. Lambert, R. M.; Payne, M. C. *The Journal of Physical Chemistry B* **2005**, *109*, 20948.

(226) Kisch, H. Sakthivel, S. Janczarek, M.; Mitoraj, D. *Journal of Physical Chemistry C* **2007**, *111*, 11445.

(227) Tokudome, H.; Miyauchi, M. *Chemistry Letters* **2004**, *33*, 1108.

(228) Cong, Y. Zhang, J. Chen, F.; Anpo, M. *Journal of Physical Chemistry C* **2007**, *111*, 6976.

(229) Aita, Y. Komatsu, M. Yin, S.; Sato, T. *Journal of Solid State Chemistry* **2004**, *177*, 3235.

(230) Peng, F. Cai, L. Yu, H. Wang, H.; Yang, J. *Journal of Solid State Chemistry* **2008**, *181*, 130.

(231) Vinodgopal, K. Wynkoop, D. E.; Kamat, P. V. *Environmental Science & Technology* **1996**, *30*, 1660.

(232) Sovány, T. Nikowitz, K. Regdon Jr., G. Kása Jr., P.; Pintye-Hódi, K. *Polymer Testing* **2009**, *28*, 770.

(233) Wu, K.-R.; Hung, C.-H. *Applied Surface Science* **2009**, *256*, 1595.

(234) Ledinsky, M. Vetushka, A. Stuchlik, J. Mates, T. Fejfar, A. Kocka, J.; Stepanek, J. *Journal of Non-Crystalline Solids* **2008**, *354*, 2253.

(235) Nefedov, V. Salyn, Y. V. Scheibe, R.; Leonhardt, G. *Journal of Electron Spectroscopy and Related Phenomena* **1977**, *10*, 121.

(236) Maeda, M.; Watanabe, T. *Journal of The Electrochemical Society* **2006**, *153*, C186.

(237) Serpone, N. Lawless, D.; Khairutdinov, R. *The Journal of Physical Chemistry* **1995**, *99*, 16646.

(238) Ananpattarachai, J. Kajitvichyanukul, P.; Seraphin, S. *Journal of Hazardous Materials* **2009**, *168*, 253.

(239) Yuan, J. Wang, E. Chen, Y. Yang, W. Yao, J.; Cao, Y. *Applied Surface Science* **2011**, *257*, 7335.

(240) Cardon, F.; Gomest, W. P. *Journal of Physics D: Applied Physics* **1978**, *63*, L63.

(241) Wu, P.-G. Ma, C.-H.; Shang, J. K. *Applied Physics A* **2004**, *81*, 1411.

(242) Jiang, X. Wang, Y.; Pan, C. *Journal of the American Ceramic Society* **2011**, 1.

(243) Highfield, J. G.; Pichat, P. *New Journal of Chemistry* **1989**, *13*, 61.

(244) Bettinelli, M. Speghini, A. Falcomer, D. Daldosso, M. Dallacasa, V.; Romanò, L. *Journal of Physics: Condensed Matter* **2006**, *18*, S2149.

(245) Xu, A. *Journal of Catalysis* **2002**, *207*, 151.

(246) Serpone, N. Lawless, D. Disdier, J.; Herrmann, J.-M. *Langmuir* **1994**, *10*, 643.

(247) Karakitsou, K. E.; Verykios, X. E. *The Journal of Physical Chemistry* **1993**, *97*, 1184.

(248) Carp, O. *Progress in Solid State Chemistry* **2004**, *32*, 33.

(249) Wilke, K. *Journal of Photochemistry and Photobiology A: Chemistry* **1999**, *121*, 49.

(250) Arpaç, E. Sayilkan, F. Asiltürk, M. Tatar, P. Kiraz, N.; Sayilkan, H. *Journal of Hazardous Materials* **2007**, *140*, 69.

(251) Yu, J. Zhou, M. Yu, H. Zhang, Q.; Yu, Y. *Materials Chemistry and Physics* **2006**, *95*, 193.

(252) Zhu, J. Deng, Z. Chen, F. Zhang, J. Chen, H. Anpo, M. Huang, J.; Zhang, L. *Applied Catalysis B: Environmental* **2006**, *62*, 329.

(253) Zhou, M. Yu, J.; Cheng, B. *Journal of hazardous materials* **2006**, *137*, 1838.

(254) Graetzel, M.; Howe, R. F. *The Journal of Physical Chemistry* **1990**, *94*, 2566.

(255) Fuerte, A. Hernández-Alonso, M. D. Maira, A. J. Martínez-Arias, A. Fernández-García, M. Conesa, J. C.; Soria, J. *Chemical Communications* **2001**, 2718.

(256) Yu, J. Yu, H. Ao, C. Lee, S.; Ho, W. *Thin Solid Films* **2006**, *496*, 273.

(257) Dvoranová, D. Brezová, V. Mazúr, M.; Malati, M. A. *Applied Catalysis B: Environmental* **2002**, *37*, 91.

(258) Furubayashi, Y. Hitosugi, T. Yamamoto, Y. Inaba, K. Kinoda, G. Hirose, Y. Shimada, T.; Hasegawa, T. *Applied Physics Letters* **2005**, *86*, 252101.

(259) Bally, A. R. Korobeinikova, E. N. Schmid, P. E. Lévy, F.; Bussy, F. *Journal of Physics D: Applied Physics* **1998**, *31*, 1149.

(260) Janisch, R. Gopal, P.; Spaldin, N. A. *Journal of Physics: Condensed Matter* **2005**, *17*, R657.

(261) Sheppard, L. R. Bak, T.; Nowotny, J. *Journal of Physical Chemistry C* **2008**, *112*, 611.

(262) Lee, M.-K. Shih, C.-M. Fang, S.-C. Tu, H.-F.; Ho, C.-L. *Japanese Journal of Applied Physics* **2007**, *46*, 1653.

(263) First Ten Angstroms. *http://www.firsttenangstroms.com/*.

(264) Pauw, L. J. van der *Philips Research Reports* **1958**, *13*, 1.

(265) Kamisaka, H. Hitosugi, T. Suenaga, T. Hasegawa, T.; Yamashita, K. *The Journal of Chemical Physics* **2009**, *131*, 034702.

(266) Zhang, S. X. Dhar, S. Yu, W. Xu, H. Ogale, S. B.; Venkatesan, T. *Applied Physics Letters* **2007**, *91*, 112113.

(267) Yang, J. Y. Li, W. S. Li, H. Sun, Y. Dou, R. F. Xiong, C. M. He, L.; Nie, J. C. *Applied Physics Letters* **2009**, *95*, 213105.

(268) Golego, N. Studenikin, S. A.; Cocivera, M. *Journal of Materials Research* **2011**, *14*, 698.

(269) Pehlivan, E. Tepehan, F. Z.; Tepehan, G. G. *Solar Energy Materials and Solar Cells* **2005**, *87*, 317.

(270) Moss, T. S. *Proceedings of the Physical Society: Section B* **1954**, *67*, 775.

(271) Burstein, E. *Physical Review* **1954**, *93*, 632.

(272) Sheppard, L. Bak, T. Nowotny, J. Sorrell, C. Kumar, S. Gerson, A. Barnes, M.; Ball, C. *Thin Solid Films* **2006**, *510*, 119.

(273) Atashbar, M. Sun, H. T. Gong, B. Wlodarski, W.; Lamb, R. *Thin Solid Films* **1998**, *326*, 238.

(274) Maruyama, T. *Journal of The Electrochemical Society* **1994**, *141*, 2868.

(275) O'Neill, S. A. Parkin, I. P. Clark, R. J. H. Mills, A.; Elliott, N. *Journal of Materials Chemistry* **2003**, *13*, 2952.

(276) Smith, D. L. *Thin Film Deposition: Principles and Practice*; 1st ed. McGraw Hill Inc, 1995.

(277) O'Neill, S. A. Clark, R. J. H. Parkin, I. P. Elliott, N.; Mills, A. *Chemistry of Materials* **2003**, *15*, 46.

(278) Zhang, S. X. Kundaliya, D. C. Yu, W. Dhar, S. Young, S. Y. Salamanca-Riba, L. G. Ogale, S. B. Vispute, R. D.; Venkatesan, T. *Journal of Applied Physics* **2007**, *102*, 013701.

(279) Dunnill, C. W.; Parkin, I. P. *Dalton Transactions* **2011**, *40*, 1635-40.

(280) Kundu, S. Kafizas, A. Hyett, G. Mills, A. Darr, J. A.; Parkin, I. P. *Journal of Materials Chemistry* **2011**, *21*, 6854.

(281) Suchea, M. Christoulakis, S. Tudose, I. V. Vernardou, D. Lygeraki, M. I. Anastasiadis, S. H. Kitsopoulos, T.; Kiriakidis, G. *Materials Science and Engineering: B* **2007**, *144*, 54.

(282) Takeuchi, U. Chikamatsu, A. Hitosugi, T. Kumigashira, H. Oshima, M. Hirose, Y. Shimada, T.; Hasegawa, T. *Journal of Applied Physics* **2010**, *107*, 023705.

(283) Garzella, C. *Sensors and Actuators B: Chemical* **2003**, *93*, 495.

(284) Hsu, C. Lin, C. Chan, C. Chang, C.; Tsay, C. *Thin Solid Films* **2006**, *494*, 228.

(285) Lee, Y. C. Hong, Y. P. Lee, H. Y. Kim, H. Jung, Y. J. Ko, K. H. Jung, H. S.; Hong, K. S. *Journal of Colloid and Interface Science* **2003**, *267*, 127.

(286) Kafizas, A. Kellici, S. Darr, J. A.; Parkin, I. P. *Journal of Photochemistry and Photobiology A: Chemistry* **2009**, *204*, 183.

(287) Li, X. Z. Li, F. B. Yang, C. L.; Ge, W. K. *Journal of Photochemistry and Photobiology A: Chemistry* **2001**, *141*, 209.

(288) Slink, W. E.; DeGroot, P. B. *Journal of Catalysis* **1981**, *68*, 423.

(289) Ashraf, S. Binions, R. Blackman, C. S.; Parkin, I. P. *Polyhedron* **2007**, *26*, 1493.

(290) Bathe, S.; Patil, P. *Solid State Ionics* **2008**, *179*, 314.

(291) McGuire, G. E. Schweitzer, G. K.; Carlson, T. *Inorganic Chemistry* **1973**, *12*, 2450.

(292) Occhiuzzi, M. Cordischi, D. Gazzoli, D. Valigi, M.; Heydorn, P. C. *Applied Catalysis A: General* **2004**, *269*, 169.

(293) Sarma, D.; Rao, C. *Journal of Electron Spectroscopy and Related Phenomena* **1980**, *20*, 25.

(294) Schiavello, M. *Journal of Solid State Chemistry* **1977**, *72*, 67-72.

(295) Ohsaka, T. Izumi, F.; Fujiki, Y. *Journal of Raman Spectroscopy* **1978**, *7*, 321.

(296) Harunsani, M. H. Oropeza, F. E. Palgrave, R. G.; Egdell, R. G. *Chemistry of Materials* **2010**, *22*, 1551.

(297) Kim, D.-S. Yang, J.-H. Balaji, S. Cho, H.-J. Kim, M.-K. Kang, D.-U. Djaoued, Y.; Kwon, Y.-U. *CrystEngComm* **2009**, *11*, 1621.

(298) Toby, B. H. *Journal of Applied Crystallography* **2001**, *34*, 210.

(299) Chan, T. S. Lee, J.-F.; Liu, R. S. *Journal of Physics: Conference Series* **2009**, *190*, 012095.

(300) Carvajal, J. J. Solé, R. Gavaldà, J. Massons, J. Díaz, F.; Aguiló, M. *Chemistry of Materials* **2003**, *15*, 2730.

(301) Kr, J. Smole, F.; Topi, M. *Journal of Non-Crystalline Solids* **2004**, *338-340*, 673.

(302) Brunauer, S. Emmett, P. H.; Teller, E. *Journal of the American Chemical Society* **1938**, *60*, 309.

(303) Sheppard, L. R. Bak, T.; Nowotny, J. *The Journal of Physical Chemistry C* **2008**, *112*, 611.

(304) Kamisaka, H. Hitosugi, T. Suenaga, T. Hasegawa, T.; Yamashita, K. *The Journal of Chemical Physics* **2009**, *131*, 034702.

(305) Knapp, C. E. Kafizas, A. Parkin, I. P.; Carmalt, C. J. *Journal of Materials Chemistry* **2011**, *21*, 12644.